PREDICTION OF MASS TRANSFER COEFFICIENT IN BUBBLE COLUMN USING ARTIFICIAL NEURAL NETWORK

Dr. Adil A. Al-Hemiri and Salih A. Salih

Chemical Engineering Department-Baghdad University

ABSTRACT

The volumetric mass transfer coefficient $k_L.a$ was calculated using two gases (air and CO_2) in water and NaOH solution. The experiments were carried out using 0.1 m column diameter. Empirical and Artificial Neural Network (ANN) correlation were developed to predicted mass transfer coefficient in form of dimensionless groups (Sh, Re,Bo and We). The use of Back Propagation Neural Network (BPNN) gave better results than other correlations found in literature and than the empirical one found in this study.

الخلاصة

تمت دراسة معامل الانتقال الحجمي في عمود فقاعي ذو قطر 0.1 متر يحتوي على موزع للغاز ذو 79 فتحة بقطر 2 مليمتر لكل فتحة باستخدام الهواء و ثاني اوكسيد الكاربون للطور الغازي و الماء ومحلول هيدروكسيد الصوديوم للطور السائل.

تم تطوير معادلة عامة وإستخدام الشبكة الذكية المصطنعة (ANN) لحساب معامل انتقال الكتلة الحجمي من خلال استخدام مجاميع عديمة الوحدات (We,Sh,Re,Bo). إستخدام الشبكة الذكية من نوع التوالد العكسي (BPNN) اعطى نتائج متميزة احسن من تلك الموجودة في الادبيات.

KEYWORDS

Bubble column, Mass transfer coefficient, Artificial neural network.

INTRODUCTION

One of the most important applications of the gas-liquid reaction is the bubble column reactor. Bubble columns are widely used in industry for carrying out a variety of chemical reactions such as hydrogenations, oxidations and the Fischer–Tropsch synthesis. Mass transfer is one of the key parameters determining the design and scale up of bubble column reactors used in a wide spectrum of industrial process(Kantarci,et al;2005).

Mass transfer coefficients depend strongly on the fluid dynamics and are mostly quantified through correlation in which the gas holdup plays an important role. Gas holdup is a dimensionless key parameter for design purposes that characterizes transport phenomena of bubble column systems. It is basically defined as the volume fraction of gas phase occupied by the gas bubbles. Gas holdup for the two phase bubble column reactor can be estimated using the following relation (Pandit and Doshi, 2005; Vandu and Krishna R., 2004):

$$\varepsilon_G = \frac{H_D - H_C}{H_D} \qquad (1)$$

Anther factor that effecting mass transfer is the superficial gas velocity, which is the average velocity of the gas that is sparged into the column, and it is simply expressed as the volumetric flow rate divided by the cross-sectional area of the column (Lakota et. al. 2002, Bouaifi et. al. 2001). The volumetric gas to liquid (GL) mass transfer coefficient (k_L.a) in bubble column reactor is mainly determined by (i) the GL interfacial area (a) determined by the bubble diameter (d_b) and the gas holdup ε_G and (ii) the liquid side mass transfer coefficient (k_L) is determined by the slip velocity between bubble and liquid phase (U_b) and the bubble diameter. Gas-liquid interfacial area (a) is determined by the gas holdup and the bubble diameter (equation 2).The gas-liquid interfacial area (a) is calculated too from video imaging (Mouza et. al., 2004, Krishna and van Baten 2003).

$$a = \frac{6\,\varepsilon_G}{d_b} \qquad (2)$$

ARTIFICIAL NEURAL NETWORK MODEL

Artificial Neural Network (ANN) models have been recently given an increasing attention in chemical engineering applications, including parameters prediction, modeling, process optimization, process simulation and process control. Back Propagation Neural Network (BPNN) and radial biasis function are employed, whereas for problems involving data clustering, adaptive resonance theory, network for binary signals and Kohonen self-organizing map are used (Shaikh A., Al-Dahhan M. 2003). A back propagation network with a single hidden layer of processing elements can model any continuous function to any degree of accuracy. , since back propagation is based on a relatively simple form of optimization known as gradient descent, mathematically astute observers soon proposed modifications using more powerful techniques such as conjugate gradient and Newton’s methods. Back propagation is still the most widely used variant. Its two primary virtues are that it is simple and easy to understand, and it works for a wide range of problems. (Bao, 2005; Young 2001). The basic back propagation algorithm consists of three steps. The input pattern is presented to the input layer of the network. These inputs are propagated through the network until they reach the output units. This forward pass produces the actual or predicted output pattern. Because back propagation is a supervised learning algorithm, the desired outputs are given as part of the training vector. The actual network outputs are subtracted from the desired outputs and an error signal is produced. This error signal is then the basis for the back propagation step, whereby the errors are passed back through the neural network by computing the contribution of each hidden processing unit and deriving the corresponding adjustment needed to produce the correct output. The connection weights are then adjusted and the neural network has just “learned” from an experience (Rzempoluck E. J. 1998).

Adding a single layer of hidden units turns the linear neural network into a nonlinear one, capable of performing multivariate logistic regression, but with some distinct advantages over the traditional statistical technique (Wu R. C. 1997, You X. Y. and Yang Z. S. 2003).

EXPERIMENTAL WORK

The schematic of the bubble column reactor setup is illustrated in Fig1. The column is constructed from QVF Pyrex glass. The inside diameter of bubble column reactor is (0.1 m) and its height is (1.5 m).

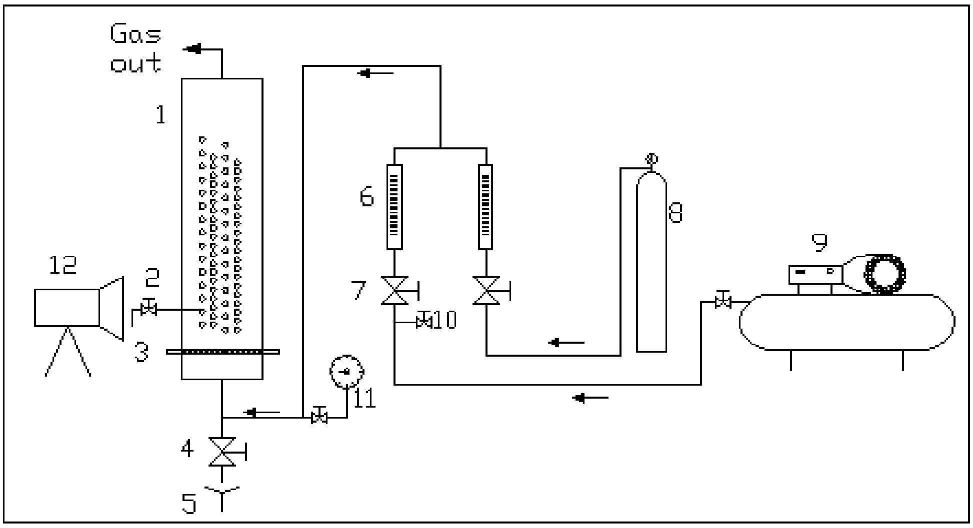

1- QVF bubble column
2- Sampling valve
3- Gas distributor
4- Drain valve
5- Drain
6- Rotameters
7- Regulating valves
8- CO_2 cylinder
9- Air compressor
10- Vent valve.
11- Pressure Gauge
12- Photo camera

Fig. 1, Typical experimental set-up for 0.1 m diameter column

The perforated plate used in the bubble column is constructed from aluminum of (2 mm) thickness with perforated holes of 2 mm diameter on a triangular pitch of 11 mm. The total holes were 79 holes as shown in Fig.2.

EXPERIMENTAL PROCEDURE

(i) Using a stationary liquid phase of 2500 ml tap water containing 0.7 gm sodium sulfate and 0.0025 gm cobalt for oxygen scavenging from the water, air was introduced into the bubble column and at varying flow rates of 0.886,2,3,5 and 7 m^3/hr. Samples of water from the column were taken every 30 seconds and were tested for dissolved oxygen using Winkler titration.

(ii) Same as above except that the gas was 50-50 air and carbon monoxide and the liquid was sodium hydroxide solution. And the liquid samples were analyzed for sodium carbonate content using standard method.

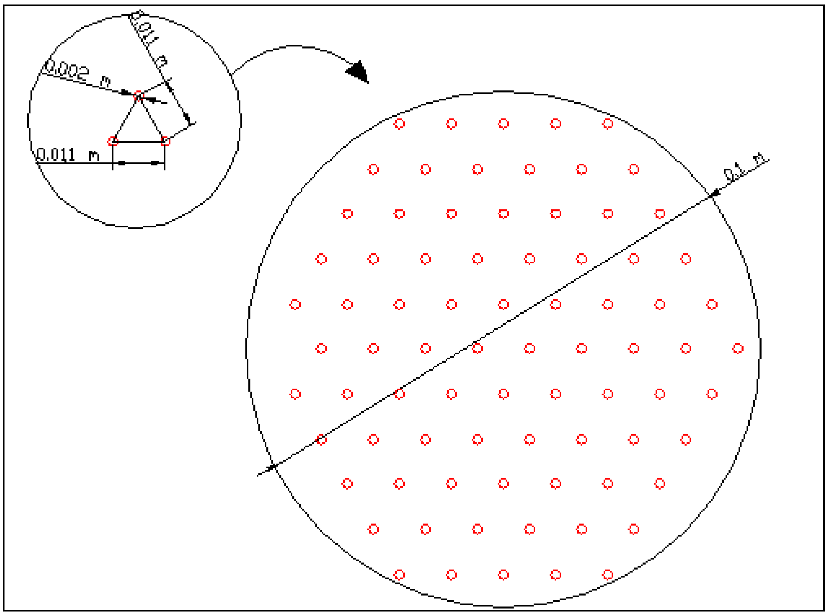

Fig.2, Gas Distributor.

RESULTS AND DISCUSSION

For air-water system, Fig.3, shows the relation between the ratio C/C* and time for different gas velocities. It's obvious that increasing air velocity decreases the time needed for saturation.

For carbon dioxide- sodium hydroxide system, Fig.4, illustrates the variation of CO_2 concentration profile with time. It can be seen that increasing normality causes an increase in CO_2 absorption due to increasing the reaction rate

CALCULATION OF GAS HOLDUP

Gas holdup was determined using visual measurements. For each run, the gas flow rate was adjusted with sufficient time given for steady state to be reached in the column after which the increase in dispersion height was recorded; Fig. 5, shows the change of gas holdup with superficial gas velocity.

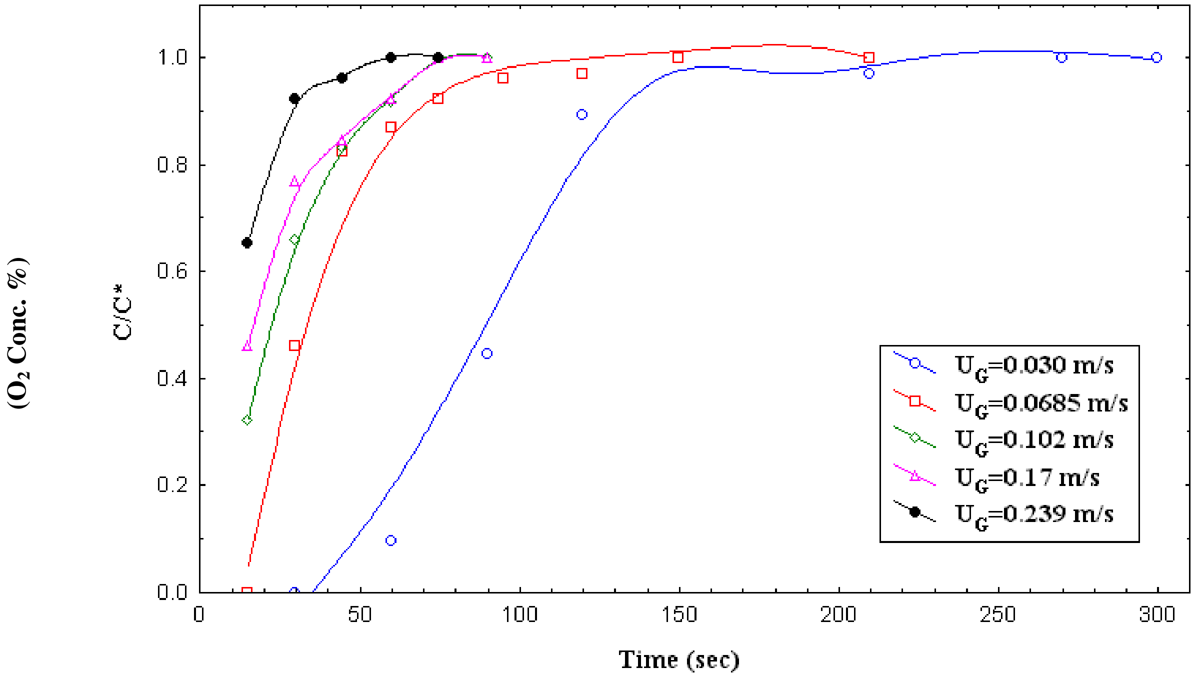

Fig. 3, Transient approach to steady state in bubble column reactor (For air- water system.

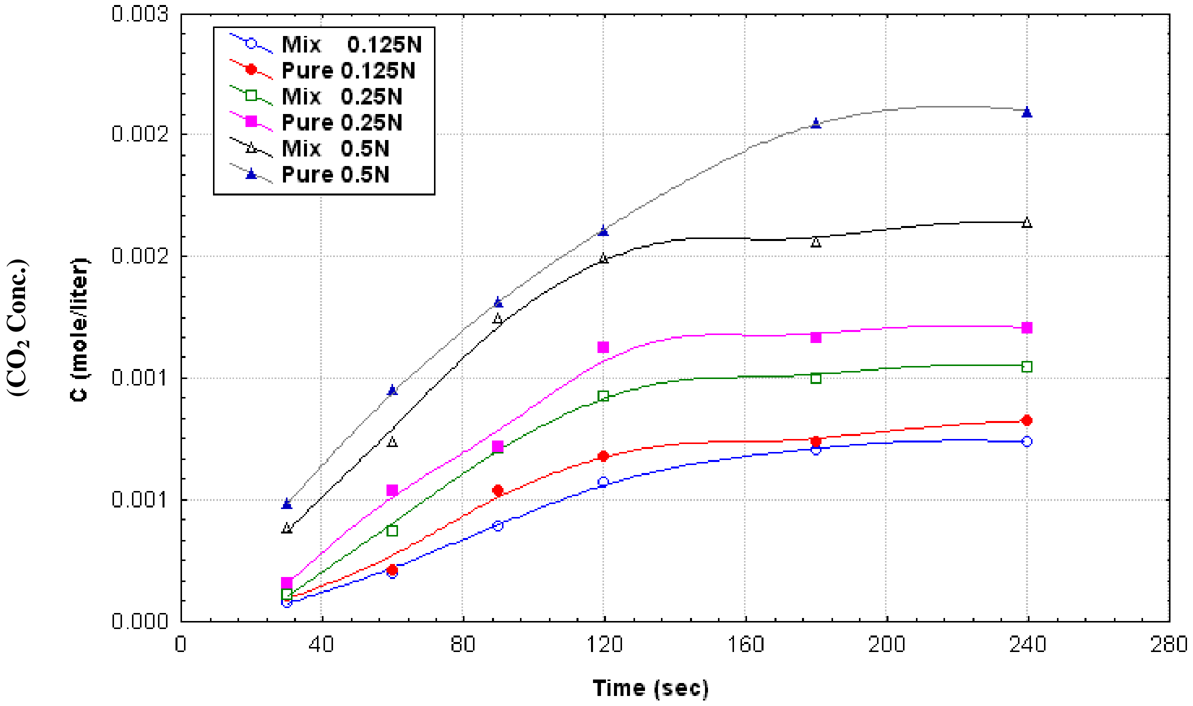

Fig.4, CO_2 absorption in NaOH solution. (Mix: mean Air-CO_2 gas mixtures).

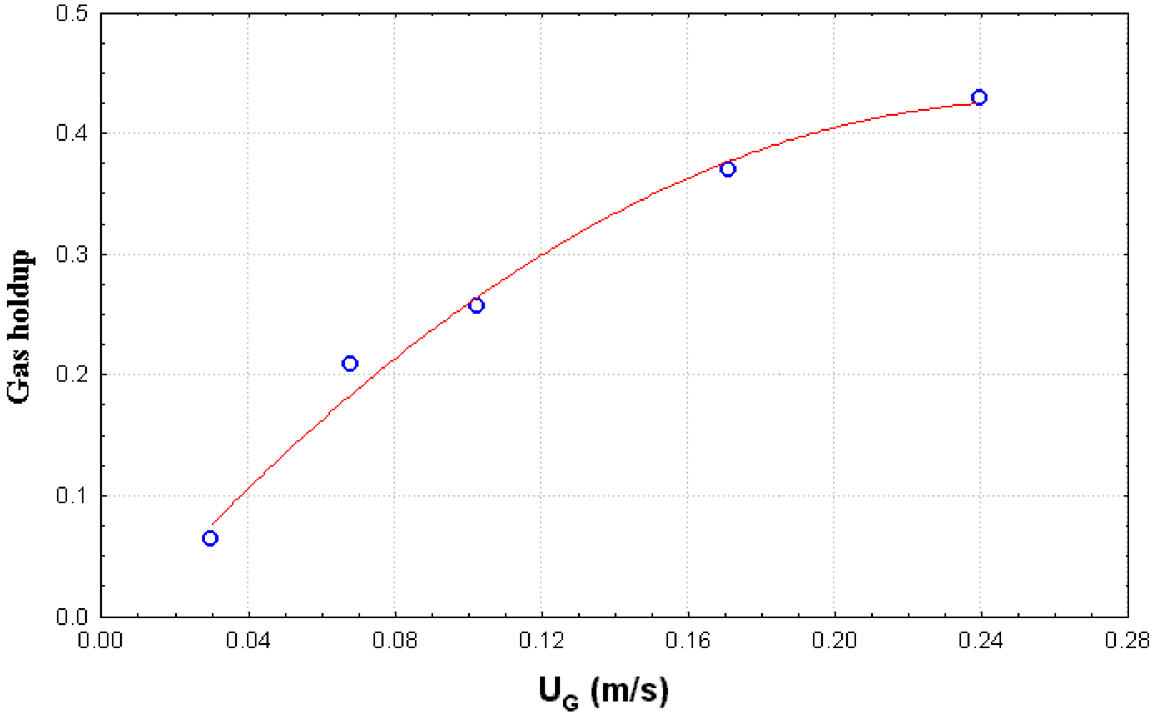

Fig. 5, Gas holdup ε_G as a function of superficial gas velocity (Air-water).

Calculation of Bubble Diameter

With the aid of the Bhavaraju et al. (1978) correlation that shows below, the bubble size diameter was calculated.

$$\frac{d_b}{d_o} = 3.23\left(\frac{4\rho_L Q}{\pi\mu_L d_o}\right)^{-0.1}\left(\frac{Q^2}{d_o^5 g}\right)^{0.21} \qquad (3)$$

Fig. 6 shows the bubble distribution in the bubble column reactor with the superficial gas velocity.

Calculation of Mass Transfer Coefficient

For calculating volumetric mass transfer coefficient; an equation developed by Vandu and Krishna (2003) based on two film theory was used:

$$\frac{C_L}{C_L^*} = 1 - \exp\left(-\frac{k_L.a}{1-\varepsilon_G}t\right) \qquad (4)$$

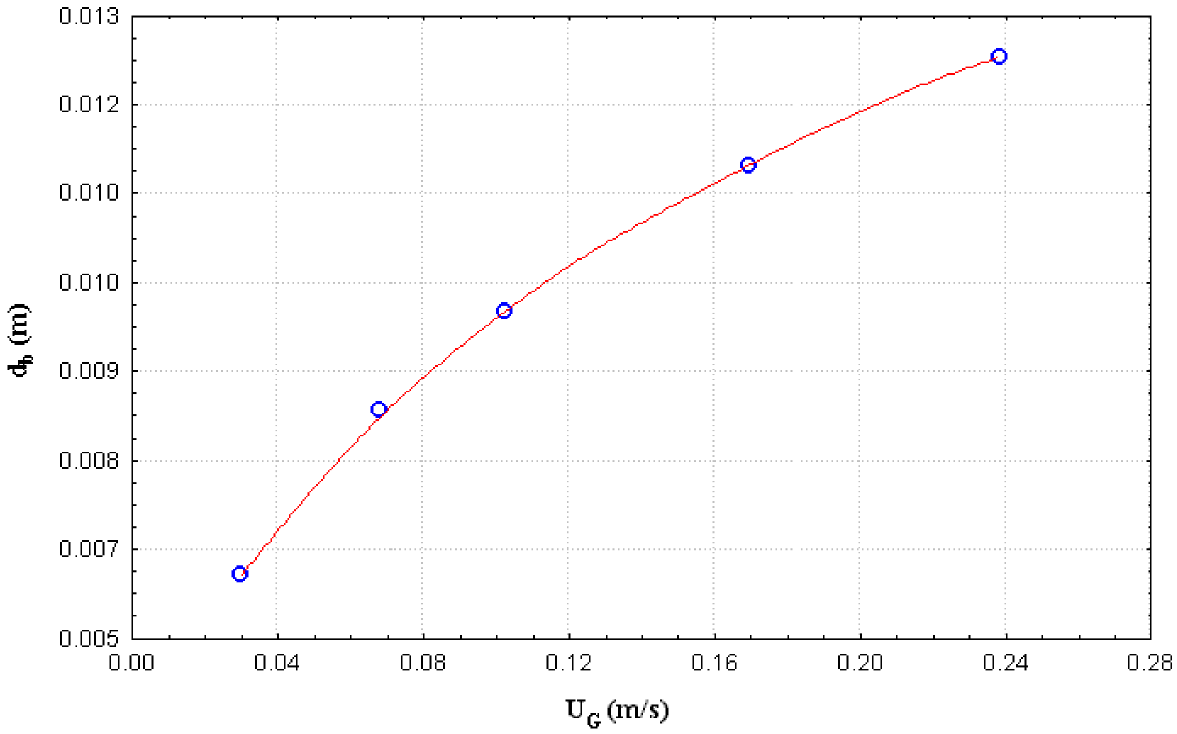

Fig. 6, Bubble size vs. superficial gas velocity (Air-water).

The only unknown constant in equation (4) is k_L.a; which can be determined by a regression of equation (4) to the actual concentration data. With the aid of STATISTCA for Window Release 5, (1995), equation (4) can be solved to find k_L.a. Fig. 7, shows the volumetric mass transfer coefficient k_L.a in relation to superficial gas velocity. Increasing the superficial gas velocity leads to increasing in k_L.a. With the aid of equation (2), interfacial area and mass transfer coefficient k_L were calculated. Fig. 8, and 9 show k_L and (a) as a function to superficial gas velocity. Comparison between the two figures shows no significant variation of k_L with gas superficial gas velocity but (a) increases significantly with increasing U_G. Similar findings were reported by Behkish, (2004); Kantarci et. al.,(2005); and Ruthiya, (2005).

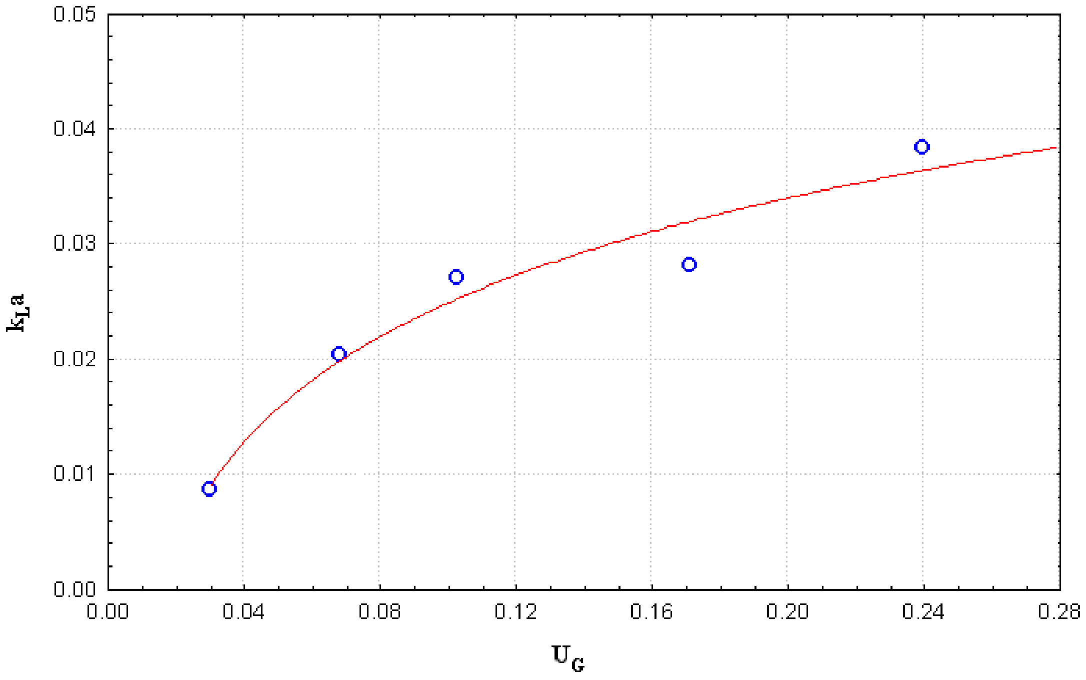

Fig. 7, $k_L.a$ (s^{-1}) vs. superficial gas velocity U_G (m/s) (Air-water).

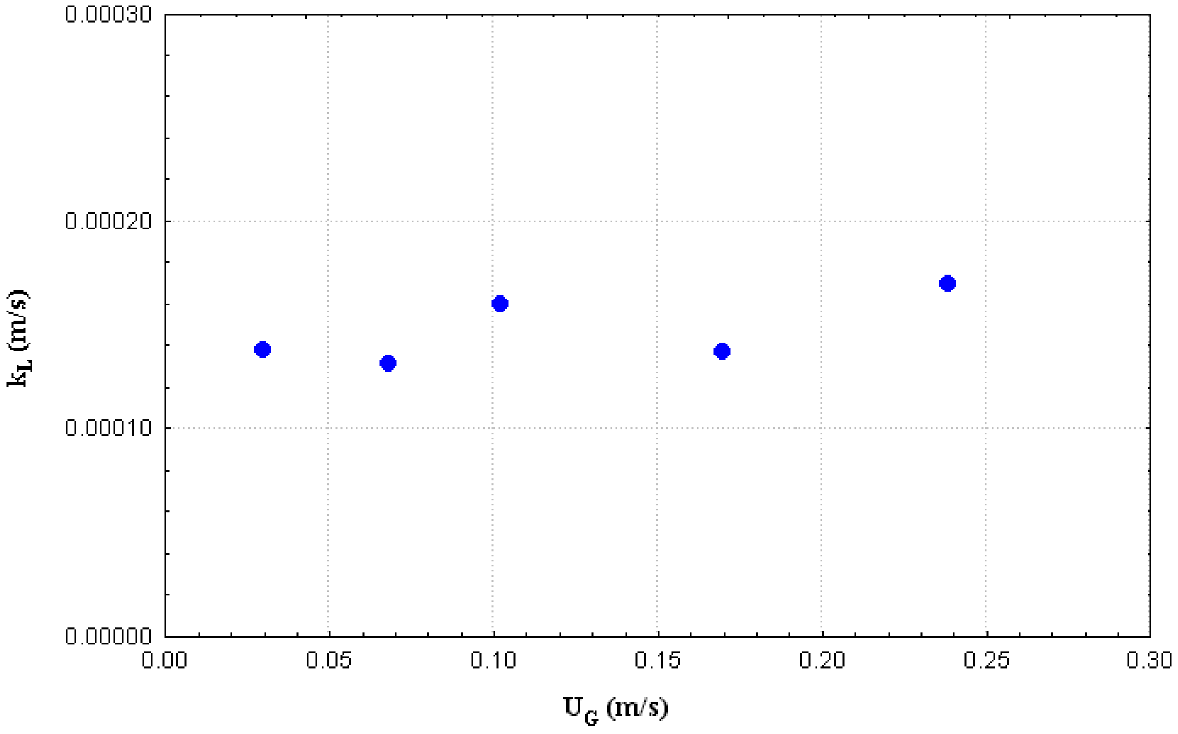

Fig. 8, Variation of k_L with superficial gas velocity (Air-water).

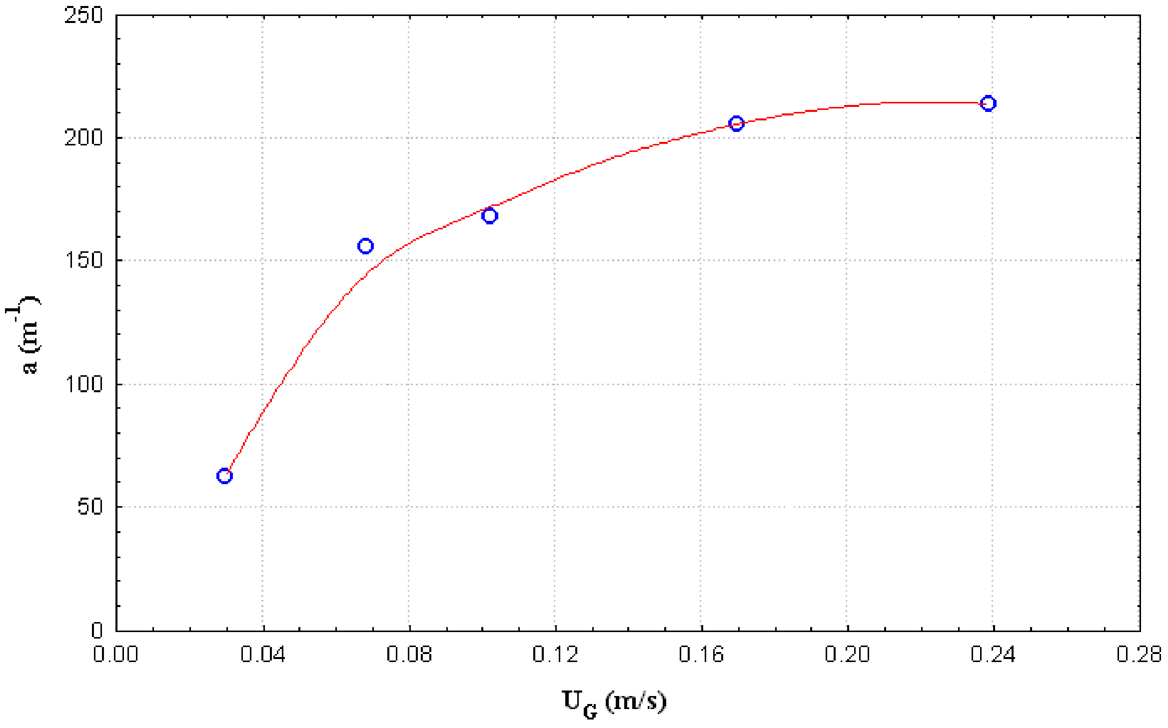

Fig. 9, Variation of interfacial area with superficial gas velocity (Air-water).

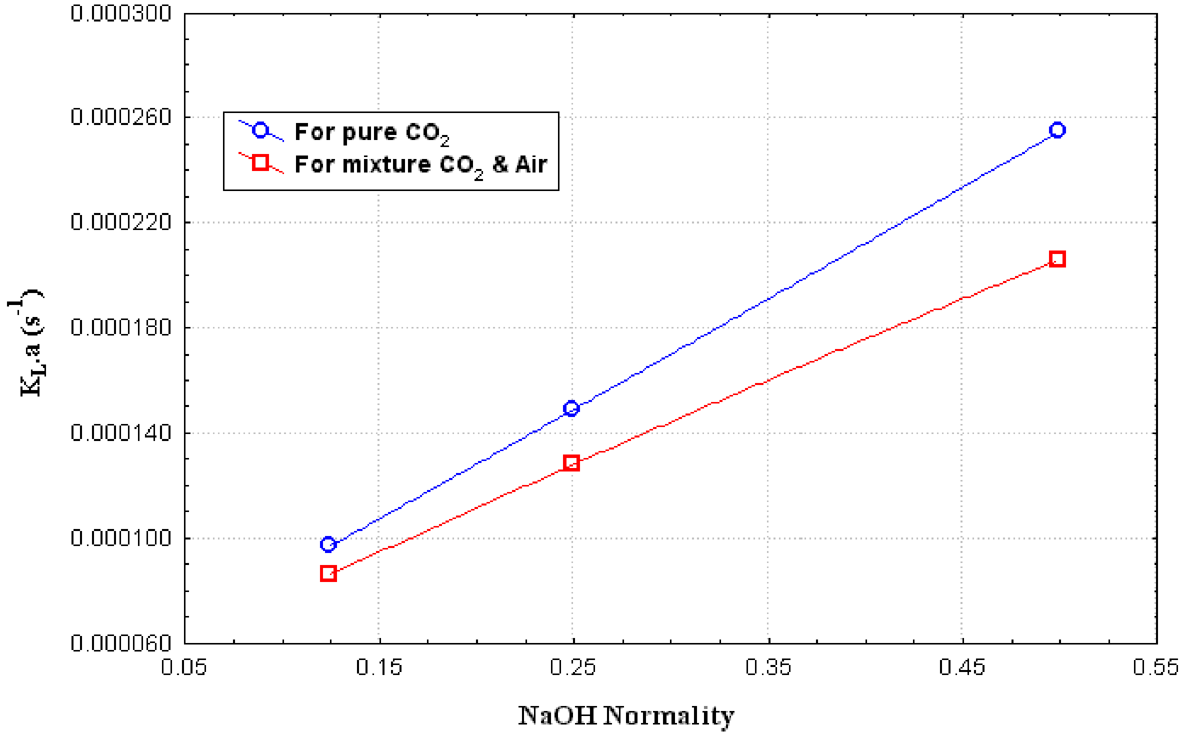

Fig.10, $k_L.a$ as a function of NaOH normality (CO_2- NaOH).

For CO_2- NaOH system, Fig. 10, shows the volumetric mass transfer coefficient calculated using equation (4) and STATISTCA for Window Release 5, (1995).

CORRELATION OF MASS TRANSFER COEFFICIENT

Two approaches were used to correlate the experimental mass transfer data obtained in this search. The first method was to develop empirical correlations, and the second was to use ANN correlation. A literature search as listed in Table (1) for bubble column reactor was conducted to obtain mass transfer data.

Table 1, Literature search for air-water system and 0.1 m column diameter

No.	Authors	Operating Condition	No. of points
1	(Krishna and Van Baten, 2003).	d_o=0.5 mm N_o=1200	7
2	(Vandu, 2004)	d_o=0.5 mm N_o=199	21

EMPIRICAL CORRELATION

The k_L values obtained in this study for oxygen dissolved in water in bubble column reactor along with the literature data given in the references listed in Table (1) were correlated using dimensionless groups; the correlation was calculated using STATISTCA for Window Release 5, (1995):

$$\mathrm{Sh} = 1.63\,\mathrm{Re}^{0.88}\,\mathrm{Bo}^{-0.04}\,\mathrm{We}^{0.268} \qquad (5)$$

It should be noted that all dimensionless groups in equation (5) are based on the physical properties of fluid which listed in Table (2), also Table (3) showes The limits of dimensionless groups.

Table 2, physical properties of air-water system (Ruthiya, 2005)

Fluid	Density Kg/m^3	Viscosity Pa.s	Surface Tension N/m	Diffusivity m^2/s
Water	998	$1*10^{-3}$	$72*10^{-3}$	$2.11*10^{-9}$
Air	1.3	$1.7*10^{-3}$	$72*10^{-3}$	$1*10^{-5}$

Table 3, The limits of Dimensionless groups.

No.	Variable	Minimum	Maximum
1	Bo	0.247	19.3
2	We	0.0003	49.93
3	Re	110	2887.4
4	Sh	87.94	3121.9

ARTIFICIAL NEURAL NETWORK CORRELATION

Using the Simulent version 3.05 (1997) computer software, ANN correlation were developed to predicte the mass transfer coefficient in bubble column using k_L values obtained in this study for oxygen dissolved in water in bubble column reactor along with the literature data given in the references listed in Table 1. Fig.11, shows the architecture of the BPNN with three inputs, one hidden layer with four nodes and one output. Table 4 shows the weighting parameters produced by training the net.

Table 4, Weighted parameters for trained BPNN.

	w_{ij}				
	1	2	3	4	5
1	-45.716	23.269	-69.555	11.38	
2	8.695	1.8127	2.7085	-1.71227	
3	19.0316	-5.265	15.374	1.0333	
4	8.257	2.096	3.393	-1.097	
	w_{jk}				
1	-0.7308	-5.0748	1.67166	6.8745	1.312057

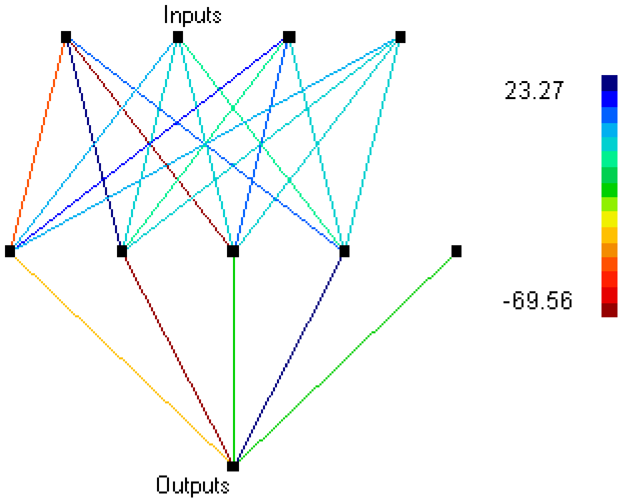

Fig. 11, ANN architecture

Comparison of the ANN Correlation with the Published Correlations

The literature correlations listed in Table 5 along with equation (5) were used to predict the mass transfer through Sherwood number. Fig.12, shows the comparison between the experimental and predicate Sherwood number of different correlations. Table 6 shows the comparison between the AARE and σ for the different correlations. It is obvious that ANN correlation is a better choice to correlate the experimental data through its lower values of AARE and σ (12.79% and 10%).

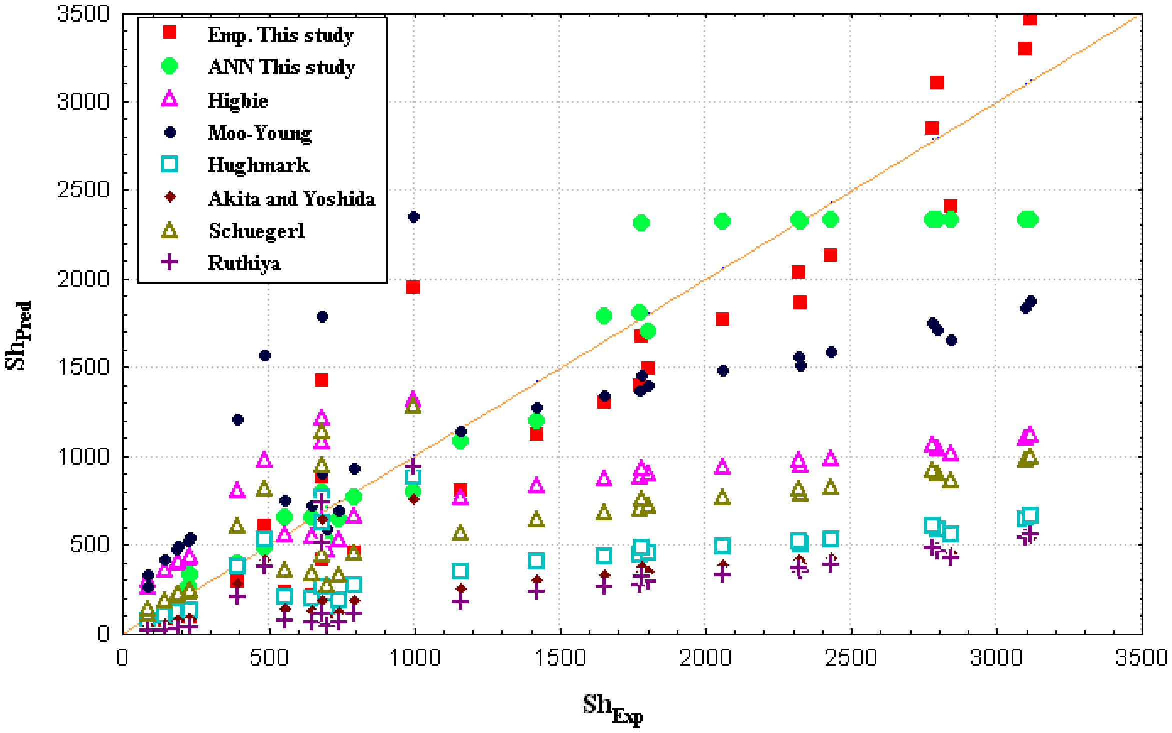

Fig. 12, comparison between the experimental and predicted Sherwood number of different correlations.

Table 5, Various correlations to predicate Sh No.(adopted from Ruthiya, 2005)

No.	Authors	Correlations
1	Higbies (1960)	$Sh = 1.13 Re^{1/2} Sc^{1/2}$
2	Moo-Young and Calerbank (1961)	$Sh = 0.53\, Re^{2/3}\, Sc^{1/2}$
3	Hughmark (1967)	$Sh = 2 + 0.0192\, Re^{0.86}\, Sc^{0.63}$
4	Akita and Yoshida, (1974)	$Sh = 0.6\, Re^{1/2}\, Sc^{1/3}\, Bo^{3/8}$
5	Schuegerl, (1977)	$Sh = 0.15\, Re^{3/4}\, Sc^{1/2}$
6	Ruthiya, (2005)	$Sh = 0.083 Re^{1/2} Sc^{1/2} Bo^{0.768}$

Table 6, Comparison between the AARE and σ for the different correlations.

No.	Correlations	AARE %	σ %
1	Higbie	68.3	49.2
2	Moo-Young	80.7	78.6
3	Hughmark	56.5	25.9
4	Akita and Yoshida	67.85	22.1
5	Schuegerl	48.9	20.8
6	Ruthiya	79.2	26.3
7	Empirical (This study)	41.2	30.17
8	ANN (This study)	12.79	10.0

CONCLUSIONS

The study of mass transfer parameters led to the following conclusions:

❶ $k_L.a$ increased with superficial gas velocity.

❷ The gas-liquid bubble interfacial area (a) increased as superficial gas velocity increased, while no significant increase of k_L with superficial gas velocity was observed.

❸ The volumetric mass transfer coefficient $k_L.a$ for CO_2-NaOH system increased with increasing the normality of NaOH solution and more increased when pure gas was used

❹. The correlation proposed by using BPNN shows less AARE and σ (12.79% & 10.0%) respectively ,than other empirical correlations found in literature. An empirical correlation was proposed with AARE, σ and R equal to (41.2 %, 30.17% and 93%) respectively. From above, the use of BPNN is a good choice for predicting mass transfer coefficient.

NOMENCLATURE

a	Gas-liquid interfacial area per unit volume of liquid, m^{-1};
A_C	Cross sectional area of the reactor column, m^2 ;
C_A	Concentration of the gas A in the liquid bulk, kmol m^{-3};
C*	Solubility of the gas at equilibrium, kmol m^{-3};
C_L	Concentration of the gas in the liquid bulk, kmol m^{-3};
D_{AB}	Diffusivity of gas A in the liquid B, m^2 s^{-1};

d_b	Gas bubble diameter, m ;
D_C	Diameter of the reactor column, m;
d_o	Orifice diameter, m;
g	Gravitational constant, m s^{-2};
H	Henry's Law Constant, bar m^3 $kmol^{-1}$;
H_C	Clear liquid height, m;
H_D	Dispersed liquid height, m;
$K_{o.a}$	Over all mass transfer coefficients, m s^{-1};
k	Phase mass transfer coefficient, m s^{-1};
$k_L.a$	Volumetric liquid-side mass transfer coefficient, s^{-1};
N	number of input data for train;
N_o	Number of openings on the gas sparger;
P	Pressure, bar;
P_T	Total pressure, bar;
Q	Phase flow rate, m^3 s^{-1};
R	gas constant: 8.314 KPa.m^3 $Kmol^{-1}$. $^oK^{-1}$;
t	Time, s;
T	Temperature, ^oK;
U	Superficial velocity, m s^{-1};
U_b	Bubble rise velocity, m s^{-1};
V	Volume, m^3;

GREEK SYMBOLS

ε	Phase holdup;
μ	Phase viscosity, kg m^{-1} s^{-1};
ν	Kinematic viscosity, m^2 s^{-1};
ρ	Phase density, kg m^{-3};
σ	Standard of deviation ;
σ_L	Surface tension of the liquid, Nm^{-1};
υ	Molar volume, m^3 $kmol^{-1}$;

SUBSCRIPTS

A	Gas specie;
B	Liquid specie;
G	Gas phase;
i	Initial condition or interface;
L	Liquid phase;

O	Orifice;
T	whole column;

DIMENSIONAL NUMBERS

Bo	Bond number, $gd_b^2\rho_L/\sigma_L$;
Re	Reynolds number, gas $U_G D_c \rho_L/\mu_L$, gas bubble $U_b d_b \rho_L/\mu_L$;
Sc	Schmidt number, $\mu_L/\rho_L D_{AB}$;
Sh	Sherwood number, $k_L d_b/D_{AB}$;
We	Webber number, $\rho_G U_G^2 D_c^4/N_o^2 d_o^3 \sigma_L$;

ABBREVIATIONS

AARE	Absolute average relative error;
ANN	Artificial neural network;
BPNN	Back propagation neural network;
GL	Gas-Liquid;

REFERENCES

- Akita, K., and Yoshida, F., (1973) “Gas Holdup and Volumetric Mass Transfer Coefficient in Bubble Columns”, Ind. Eng. Chem. Process Design and Develop, 12, 76-80, cited from (Behkish, 2004).
- Bahavaraju SM, Mashelkar RA, Blanch HW, (1978) “Bubble motion and mass transfer in non-Newtonian fluids.” AIChE J.; 24; 1063-1076, cited from Behkish A., (2004).
- Bao H. T. , (2005) “Knowledge Discovery and data mining Techniques and Practice ” Department of Pattern Recognition and Knowledge Engineering, Japan Advanced Institute of Science and Technology, available online from: http://www.netnam.vn/unescocourse/knowlegde/knowlegd.htm
- Behkish A., (2004), “Hydrodynamic and mass transfer parameters in large-scale slurry bubble column reactor “, PhD thesis, University of Pittsburgh.
- Botton R., Cosserat O. and Charpentier J. C. (1980) “Mass transfer in bubble columns operating at high gas throughputs” Chem. Eng. J., 20, 87-94.
- Bouaifi M., Hebrard G., Bastoul D. and Roustan M. (2001) “A comparative study of gas hold-up, bubble size, interfacial area and mass transfer coefficients in stirred gas–liquid reactors and bubble columns” Chem. Eng. & Procc, 40, 97-111.
- Kantarci N., Borak F. and Ulgen K. O., (2005) “Bubble column reactor “, Process Biochem., 40, 2263-2283.
- Krishna R. and van Baten J. M. (2003) “Mass transfer in bubble columns“ Catal. Today, 79-80, 67-75.
- Lakota A., Jazbec M. and Levec J.(2002) “Impact of structured packing on bubble column mass transfer charasteristics. part 2. Analysis of gas-liquid mass transfer measurements” Acta. Chim. Slov., 49, 587-604.

- Mouza K.A., Kazakis N.A., and Paras. S.V. (2004) "Bubble column reactor design using CFD code" International Conference " from Scientific Computing to Computational Engineering, Athens, 8-10 September.
- Pandit A. B. and Doshi Y. K. (2005) "Mixing time studies in bubble column reactor with and without internals" Int. J. Chem. Reactor Eng., 3, article A22, 1-23.
- Perry R. H. (1984) "Perrys chemical engineering handbook" McGraw-Hill book comp.
- Ruthiya, K. C. (2005) "Mass Transfer and Hydrodynamics in Catalytic Slurry Reactors" PhD thesis, Technische University of Eindhoven.
- Rzempoluck E. J. (1998) "Neural Network Data Analysis using Simulnet" Springer-Verlag, NewYork.
- Schügerl, K., Lücke, J., and Oels, U., (1977) "Bubble Column Bioreactors," Adv. Biochem. Eng., 7,1-84, cited from (Behkish, 2004).
- Shaikh A., Al-Dahhan M. (2003) "Development of an artificial neural network correlation for prediction of overall gas holdup in bubble column reactors" Chem. Eng. and Processing, 42, 599- 610.
- Simulent version 3.05 (1997), Springer-Verlag, NewYork.
- STATISTCA for Window Release 5, (1995), Stat Soft Ins., Tulsa, USA.
- van Baten J. M. and Krishna R. (2004) "CFD modeling of a bubble column reactor carrying out consecutive A→B→C reaction" Chem. Eng. Techno., 27, No. 4, 398-406.
- Vandu C. O. and Krishna R. (2003) "Gas Hold and Volumetric Mass Transfer Coefficient in a Slurry Bubble Column", Chem. Eng. Tech., 26, NO.6 , 779-782.
- Vandu C. O. and Krishna R. (2004), "Influence of scale on the volumetric mass transfer", Chem. Eng & Pro., 43, 575-579.
- Wu R. C. (1997)"Neural Network models: Foundation and application to an audit decision problem" Annals of Operation Resea., 75, 291-301.
- You X. Y. and Yang Z. S. (2003) "Estimation the relative tray efficiency of sieve distillation trays by applying Artificial Neural Networks" Chem. Biochem. Eng. Q, 17, No. 2, 153-158.
- Young D. (2001) "Formal Computational skills "School Cognitive and Computing Science, Sussex University, section 2, 7-13.
- Young D. (2001) " Formal Computational skills " School Cognitive and Computing Science , Sussex University , section 2, 7- 13.

Number 2 Volume 13 June 2007 Journal of Engineering

COPPER RECOVERY FROM SPENT ETCHANT CUPRIC CHLORIDE SOLUTION BY ELECTROWINNING METHOD

Dr. Aprael S. Yaro and Zuhaira N. Hanna
Chemical Engineering Department – College of Engineering - University of Baghdad

ABSTRACT

Recovery of copper from actual spent etchant cupric chloride solution used in manufacturing of printed circuit board (PCB) containing 124 g/l Cu^{+2} ions concentration and 60 g/l hydrochloric acid was investigated in a batch mode jacketed tank. This tank was constructed with inner dimensions of 19×10×15 cm^3. Cylindrical rode-shape titanium was used as cathode, while two rectangular shaped graphite were used as anodes. The parameters studied were: current density (0.16-0.30 A/cm^2), copper concentration in etchant solution (30-124 g/l) and the temperature (25-45^o C). The highest current efficiency obtained was about 92% and the lowest power consumption achieved was about 2.7 W.h/g within the temperature range 25-35^o C.

الخلاصة

يهدف البحث الى استعادة النحاس بطريقة الترسيب الالكتروليتي من محلول كلوريد النحاس الفائض (المتخلف) من انتاج البطاقات الالكترونية، يحتوي المحلول على ايونات النحاس بتركيز 124 غم\لتر و حامض الهيدروكلوريك بتركيز 60 غم\اتر. تم البحث باستخدام نظام الوجبات في خزان ذو جاكيت لغرض التبريد و بابعاد داخلية 19×10×15 سم^3. استخدم قطب كاثود اسطواني الشكل من التيتانيوم و قطبي الانود مستطيلي الشكل من مادة الكرافيت. درست الظروف التشغيلية التالية: كثافة تيار (0.30-0.16 امبير\سم^2) و تركيز ايونات النحاس بالمحلول (124-31 غم\لتر) و درجة الحرارة (45-25 ^{5} م). اعلى كفاءة تيار تم الحصول عليها كانت حوالي 92 % و اقل طاقة مستهلكة لترسيب النحاس على سطح الكاثود بالساعة كانت حوالي 2.7 واطزساعة\غم ضمن درجة الحرارة 35-25 ^{5} م.

KEY WORD

Electro winning, copper recovery, spent etchant, cupric chloride.

INTRODUCTION

Metals contaminations in waste streams are serious problem for several industries. .these streams containing a metal concentration higher than the acceptable limit set by law. Therefore, the treatment of contaminated streams is required in order to reduce the amount of metal to an acceptable level. The prospect of recovery has attracted interest among industries for environmental and economic reasons.

Many previous studies have attempted to find reasonable ways to recover heavy metals. Electrochemical technology offers an efficient means of controlling pollution as it provides removing of heavy metals via redox reactions (Tenterio, 1978, Sioda, 1980 and Simonson, 1984).

The aim of the present study was to establish an electrolytic deposition method for the recovery of copper (II) from spent etchant cupric chloride solution taken as waste stream from Electronic Industries Company by electrowinning.

Operating conditions are very important to specify the typical deposition of the metal on the cathode surface (Parikh, 1974).

Any condition that increases the rate of formation of nuclei tends to increase the number of crystals and the deposit will be fine grain spongy or as powder (Mantel, 1960).

The following factors have been found to significantly affect the character of the metal (copper) deposits on the cathode: quantity and concentration of copper ion, current density, temperature, shape of the electrodes, and ratio of anode to cathode surface area (Parikh, 1974).

Materials and Experimental Method

This study illustrates the laboratory design of electrowinning system as well as the experimental work to investigate the best conditions of copper recovery from spent etchant cupric chloride solution which was brought from Electronic Industries Company (EIC) / printed circuit boards' production factory.

The test solution contains 124.5 g/l (124,500 ppm) copper ions and 60 g/l (60,000 ppm) hydrochloric acid (HCl).

Experiments were studied in a batch mode using D.C. power supply (HP 6269B) operated at a constant current mode.

A cylindrical rode-shaped cathode of titanium and two rectangular-shaped of graphite anodes were used. The ratio of anode to cathode surface area was 4.6. Cathodic and anodic potential recorded versus a saturated calomel electrode (SCE).

One litter of solution was electrochemically treated for 30 minutes with mixer speed of 120 rpm in a jacketed tank with inner dimensions of 19×10×15 cm^3 and outer dimensions of 21×12×17.5 cm^3. Chiller was used to supply water to electrolytic cell through the tank's jacket to maintain the electrolyte at a desired temperature. Figure 1 shows the schematic layout of the experimental apparatus.

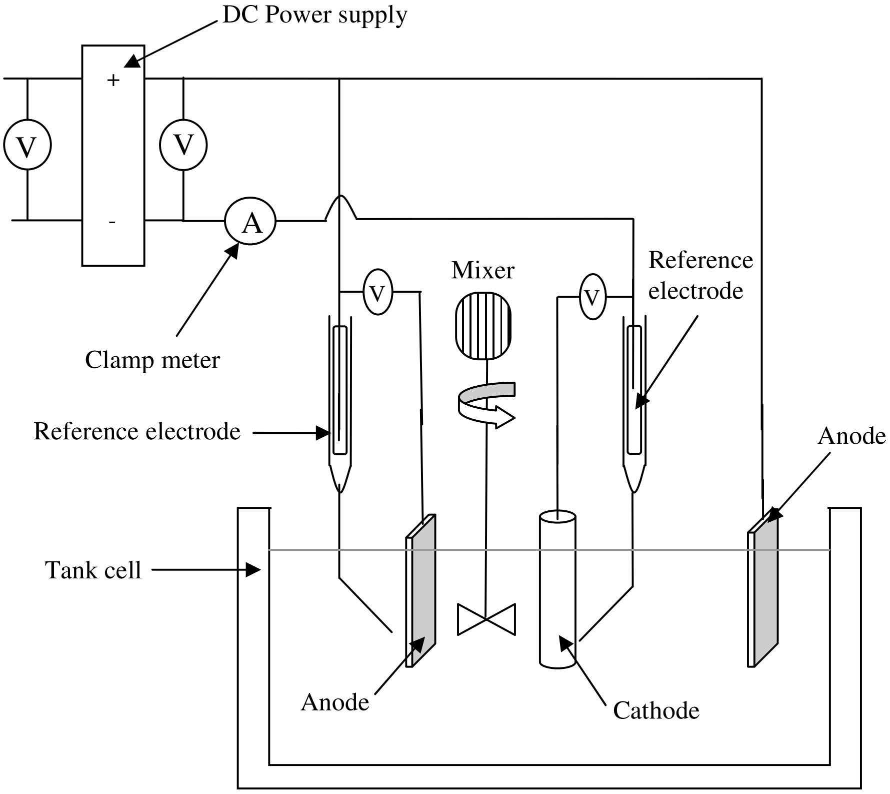

Fig. (1). Schematic layout of the electrical circuit

Results and Discussion

This study concerned with simple formulas based on Faraday's law of electrolysis and energy consumption for producing high purity copper metal from electrolytes through an aqueous electrolysis. The economics of electrowinning is not introduced since this is not the main subject in this study.

$$C.E.\% = 100 \times \frac{\text{Total weight deposited, g}}{\text{Theoretical weight deposited, g}} \qquad \ldots 1$$

Figure 2 represent the relationship between cathodic current efficiency and Cu^{+2} ion concentration for different temperatures.

It is clear that current efficiency decreases with increasing Cu+2 ion concentration when other conditions remained constant. Low ionic metal concentration is in general used for production of fine grained deposits (Mental, 1960).

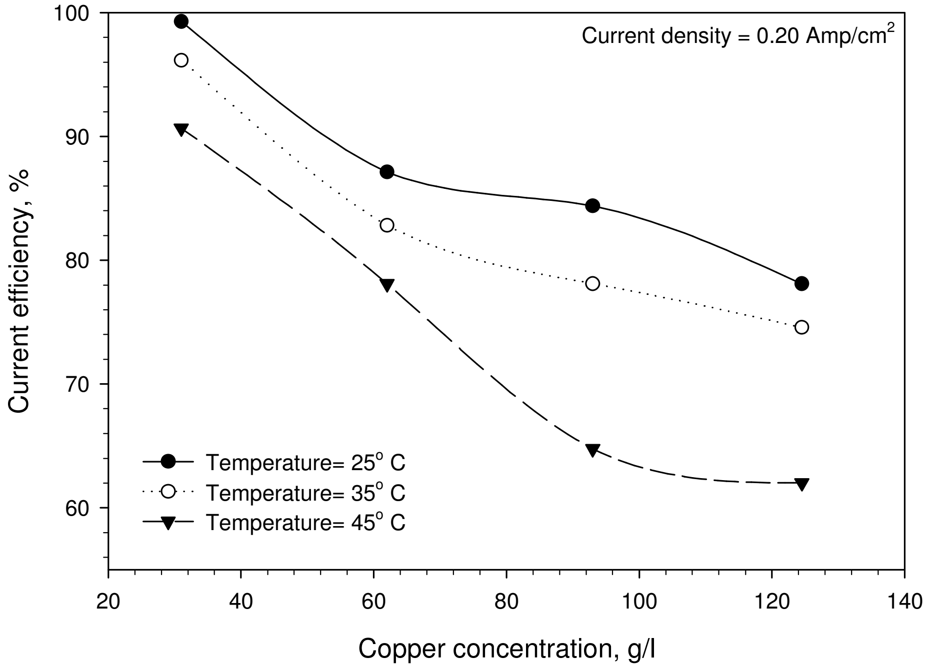

Fig.(2)., Current efficiency versus copper concentration at different temperatures and current density = 0.20 Amp/cm^2

Figure 3 shows the effect of increasing temperature on current efficiency at different current densities and copper ion concentration.

Current efficiency decreases as temperature increases. Decreasing the temperature decreasing the ionic migration, diffusion and convection, which promote the rate of formation of crystal nuclies.

Figure 4 shows that current efficiency decreases with increasing current density. Increasing the current density increases the capacity or output of product.

Because of high current densities are employed, so that the concentration of the discharging ion declines considerably in the cathodic layer, the temperature increase may be ascribed, in this case to an appreciable increase of ohmic resistance of the cathodic layer following ion discharge, so part of current converts to heat which causes decreasing of current efficiency (Calusaru, 1979).

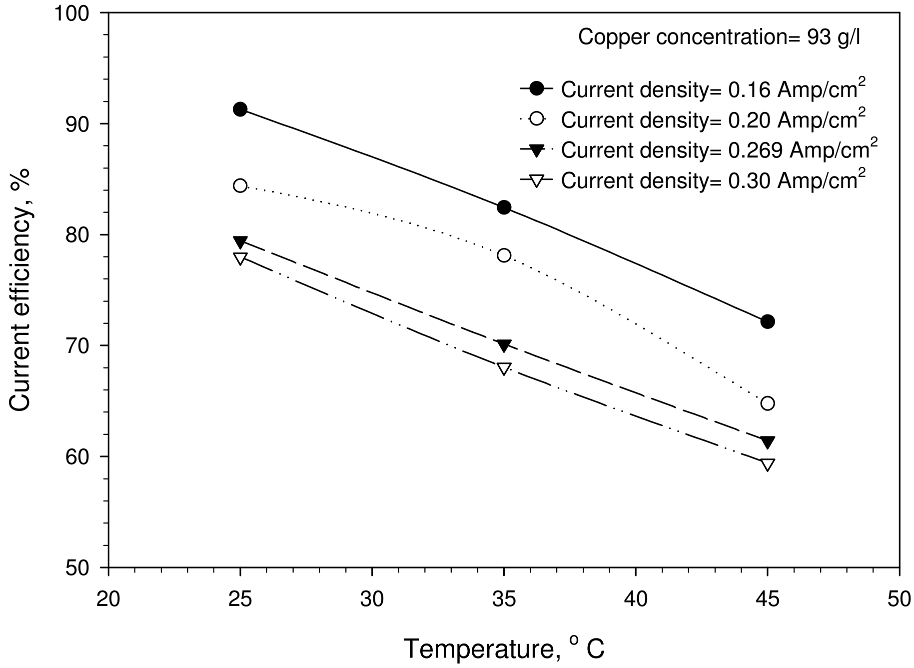

Fig. (3)., Current efficiency versus temperature at different current densities and copper concentration= 93 g/l

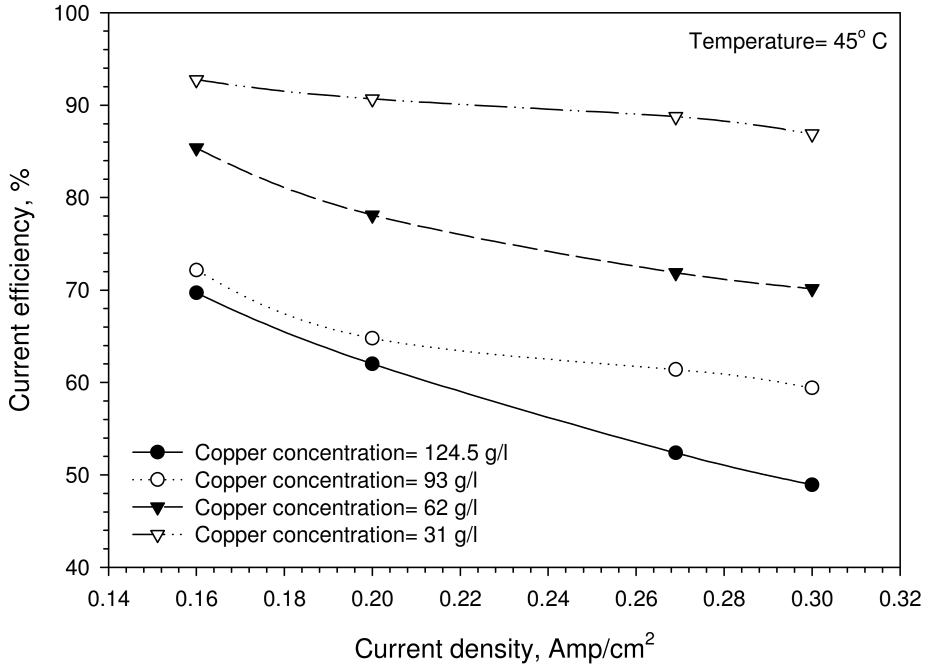

Fig.(4)., Current efficiency versus current density at different copper concentrations and at 45° C

Power consumption is a vital to the economic justification of the method; it depends on current applied, cell voltage, time and weight of copper recovered.

$$\text{Power consumption} = \frac{\mathrm{I\,V\,h}}{\mathrm{g}} \qquad \ldots 2$$

Power consumption is electrical power required to deposit one gram of metallic ions as metal on the electrode in one hour Mantel, 1960).

The cell potential is the sum of a number of components.

$$V_{cell} = V_c + V_a + V_s \qquad \ldots 3$$

Potential drop across the solution (*Vs*) depends upon the conductivity of solution. As the conductivity of solution decreases, *Vs* increases due to the increasing in the resistance of solution and leads to increase in power consumption (Canning, 1970), which means increasing the cost of copper recovery.

Figure 5 shows at minimum Cu^{+2} ion concentration, higher power consumption is recorded because the solution of low conductivity causes an increase in the resistance of solution, accordingly the voltage of the cell increases leading to increase in power consumption. As Cu^{+2} ion increase above 80 g/l, power consumption raises because at high Cu^{+2} ion concentration current efficiency decreases leading to decrease the weight of copper recovered.

Figure 6 shows that the higher the temperature the higher the power consumption because increasing the temperature decreases the weight of copper recovered due to a decrease in current efficiency compared with cell voltage.

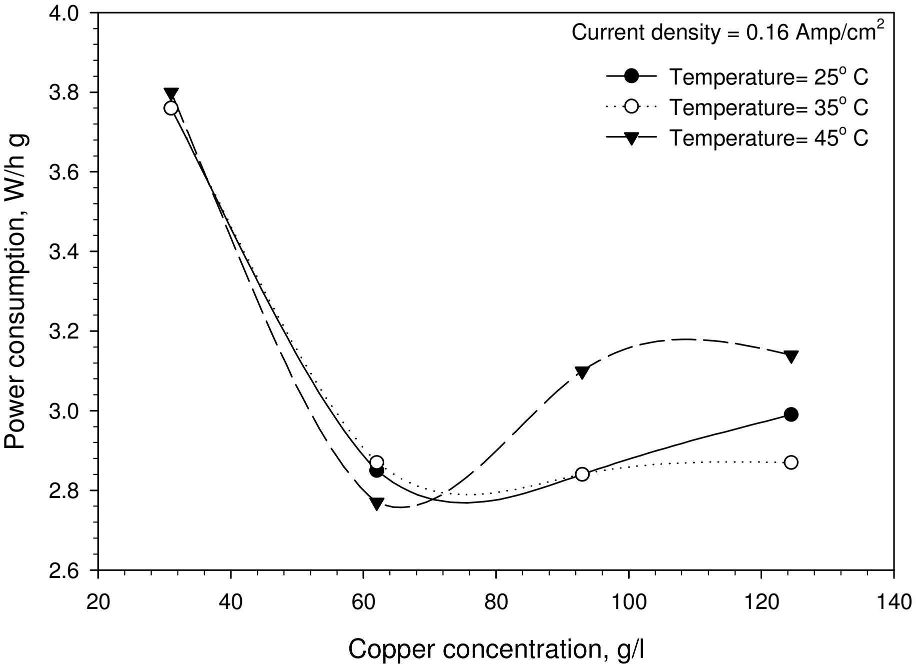

Fig. (5)., Power consumption versus copper concentration at different temperatures and current density = 0.16 Amp/cm^2

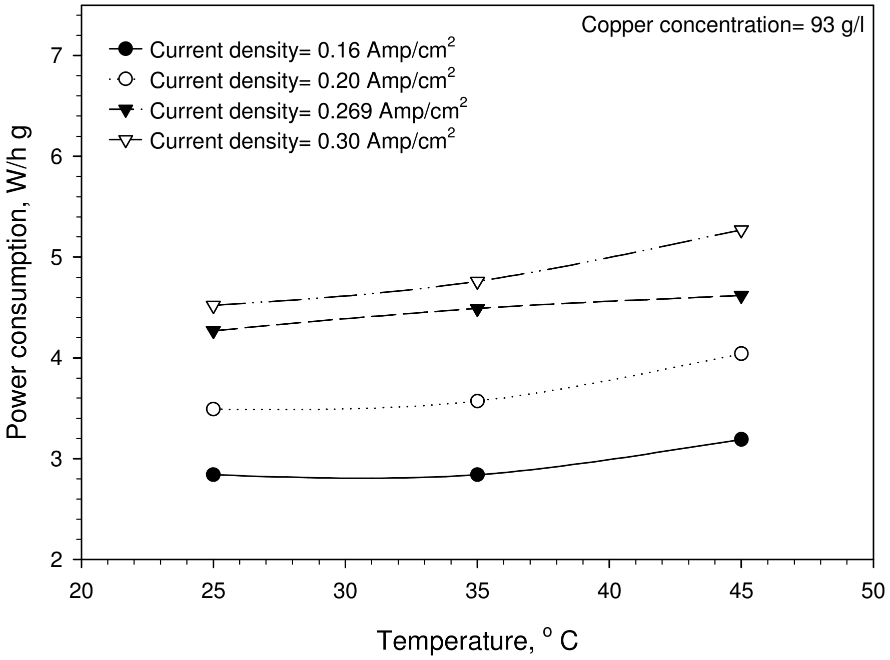

Fig. (6)., Power consumption versus temperature at different current densities and copper concentration= 93 g/l

Figure 7 shows that power consumption increases as current density increases. Current density has the greatest effect because as current applied increases, cell voltage increases and also current efficiency decreases which leads to decrease in the weight of copper recovery, accordingly power consumption increases.

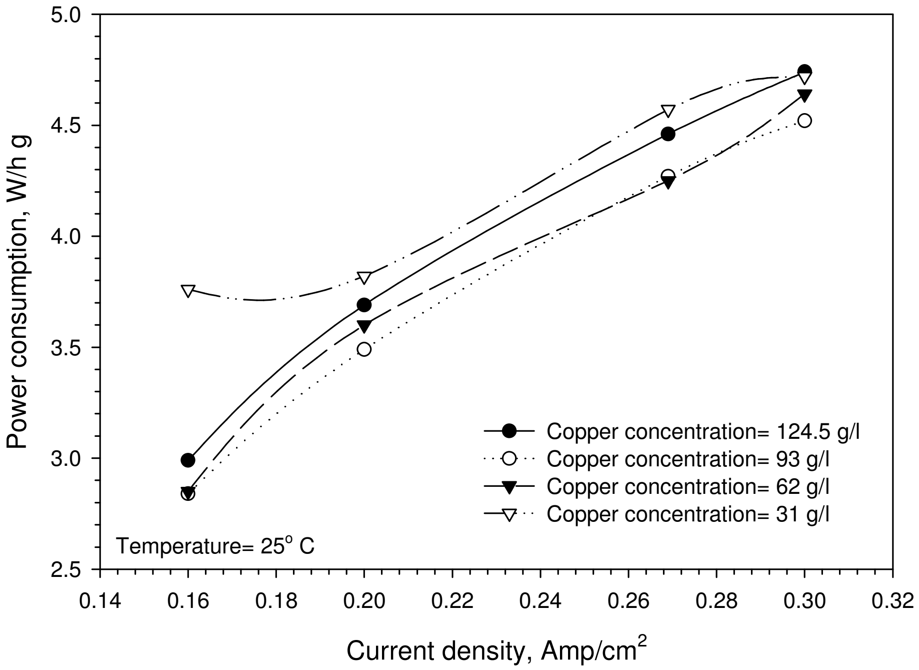

Fig. (7)., Power consumption versus current density at different copper concentrations and at 25° C

CONCLUSIONS

1. Current efficiency increases with decreasing Cu^{+2} ion concentration for all current densities and temperatures. The highest current efficiency between 75 to 92 % and lowest power consumption is about 2.7 to 3.7 Watt. h/g, within 60-124 g/l Cu^{+2} ion concentration, were achieved under the conditions of 0.16 to 0.2 Amp./cm^2 current density and 25-35° C temperature.
2. Although the highest current efficiency had been achieved at minimum Cu^{+2} ion concentration of 31 g/l, the operation was not economic, because of high power consumption.

REFERENCES

- Calusaru, A., 1979, "*Electrodeposition of metal powder*", Elsevier Scientific Company, New York.
- Canning, W., 1970, "*Canning handbook on electroplating*", Birmingham, England.
- Mantell, C. L., 1960, "*Electrochemical engineering*", McGraw-Hill Book Company, New York.
- Parikh, G. D. and Wittard, W. C., 1974, US patent 3,784,455.

- Simonsom, D., 1984, J. Appl. Electrochemistry, **14**, p. 595.
- Sioda, R. E. and Piotroska, H., 1980, Electrrochemical Acta, **25**, p. 331.
- Tenterio, A. and Casolo-Ginelli, U., 1978, J. Appl. Electrochemistry, **8**, p. 195.

DESIGN AND IMPLEMENTATION OF COMPUTER AIDED SYSTEM FOR QUALITY IMPROVEMENT INSPECTION AND TESTING FOR BOILER IN THERMAL ELECTRIC POWER STATION

ABSTRACT

There is a problem, in Iraq, due to the multitude of malfunction after the overall annual maintenance has been achieved, and that raises the cost of continuous repairs, one of the reasons of this problem, is the absence of planned testing and automation for testing devices, the second reason is the neglect of concentrating on a database, the third one is not following an integrated testing system for all parts, as well as, there are no documented reports for inspected parts. Most of various nondestructive inspection techniques have been achieved random selection steps.

The lack of a documentation system leads to lack of historical information a bout failures parts of a boiler that affect inspection decision process.

This paper summarizes Programmed system designing and computerized for internal inspection of boiler heatsurfaces (IIBHS) at Nassyriah power station as an example.

KEYWORDS

Internal Inspection of Boiler, Inspection and test for boiler in thermal power station, Inspection of Heat surfaces in thermal power.

الخلاصة

في العراق هناك مشكلة في كثرة الأعطال بعد القيام بالصيانة السنوية الشاملة وزيادة كلفة التصليح باستمرار وكان أحد أسباب هذه المشكلة غياب الفحص المبرمج والأتمتة في أجهزة الفحص مع عدم التركيز على قاعدة معلومات وعدم إتباع نظام فحص متكامل لكل أجزاء المنظومة وغيرها من الأسباب الكثيرة جداً والتي لا مجال لذكرها أو ذكر أهميتها.في هذا البحث تم التركيز على وضع نظام فحص داخلي واختبار للسطوح الحرارية في مرجل محطة كهرباء الناصرية.

INTRODUCTION

There are a wide range of reasons that cause failures to occur in the critical parts of a boiler in TPS, the type and amount of inspection needed for repairs will be determined on an individual system basis. The internal surfaces of a boiler in contact with water and steam which cause many problems lead to failures. Basic problems due to scale, generally the critical parts are those whose failure will directly affect the reliability of the boiler. The critical parts include:

- Drum.
- Furnace – tubes.
- Supperheater – tubes.
- Economizer tubes [M.N. Hoving and GLNakoneczy , 2000].

The main problems caused by boiler scales are:

- Increase in tube wall temperature, hence, boiler tube ruptures.
- Decrease in overall boiler efficiency, hence, increase in energy cost and loss of reliability [MoD. Majnouni and Arif E. jaffer, 2003]

Ever part contains components which need an internal inspection system which includes.

- Knowledge of environment of working conditions.
- Historical, current, and manufacturing data for boiler.
- Expected failure based on lessons learned from failure history.
- Selection of nondestructive test (NDT) & destructive test (DT) methods of inspection[ASME Sec . V, 1980].
- Failure analysis and recovery with recommendation for correct actions.
- determination of time frame consuming through the inspection process.
- Documentation involving reports, and recordings for future analysis.

EXPECTED FAILURES:

A SYSTEM DESIGN FOR IIHSB:

In general, system design means deciding what information is needed by the end user. It includes logical and physical design activities, and user's interface, data, and process design activities. Also what procedure system requirements developed in the stages of system analysis[James A. Obrien, 1997].

A system design for IIHSB by analyzing in details the process which includes the activities of IIBHS and deals with all problems, then puts the systematic solution programmed by writing a set of instructions that cause a computer to perform a particular task.

In the fig. (1) the system design concept is applied on IIBHS process in TPS of Nassirya in south of Iraq.

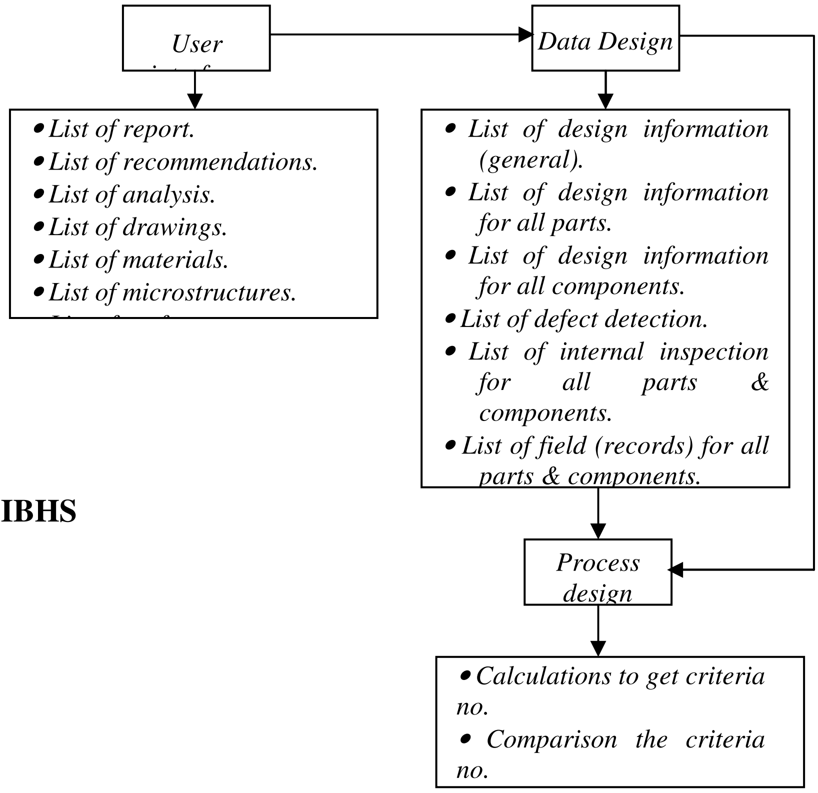

Fig. (1)

A system design of IIBHS

The system covers the main parts and components as in fig. (2)

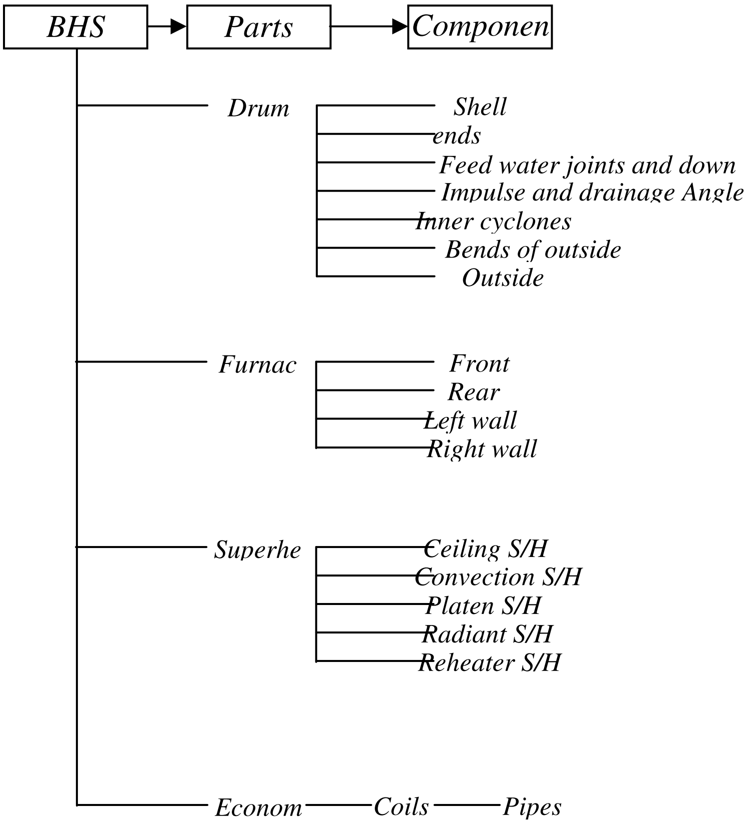

Fig (2) The tree diagram of BHS illustrates parts & components

FEATURES OF PARTS:

Features of parts or components and the condition of operation define the factor which governs the designing of lists.

- Drum shell is inspected in longitudinal and circumference tial welds. All welded attachment in the inner drum and the ends.
- Furnace tubes on the lists are inspected in levels to consider the area near burners which has suffered from exposure to direct impinged fire-or dissimilar materials which defines the level of pipe.
- Superheater has tubes made of alloy steel and subjected to creep failure, the lists include **OD** measurement to help the inspector if there is any failure caused by creep effect in the metal.
- Economizer, external water tubes are subjected to damage of erosion on tube surface[David N. French, 1993].

DOCUMENTS IN SYSTEM DESIGNING:

Two types of documents are used for designing a system of inspection and testing to cover principles and requirements of process.

The first type is the information documents as specifications, design information and defect detection.

The second type is the documents which express the process of (I & T) with decision making for each inspected part and components throughout lists such as:

- List of internal inspection & testing.
- List of internal inspection & testing (record) as in fig. (3).
- List of reports of internal inspection & testing.
- List of defects code.
- List of recommendations.
- List of analysis.
- List of work time.

In each part or component the list designed according to Russian and American which consider the feature of parts.

In addition two types of documents required for the calculations which give the number to achieve the process, such as:

Calculations of criterion number to limit the dependent thickness or allowable thickness, number of hardness allowable and other mechanical properties, out diameter (OD) allowable calculations, and time standard for all activities in each part.

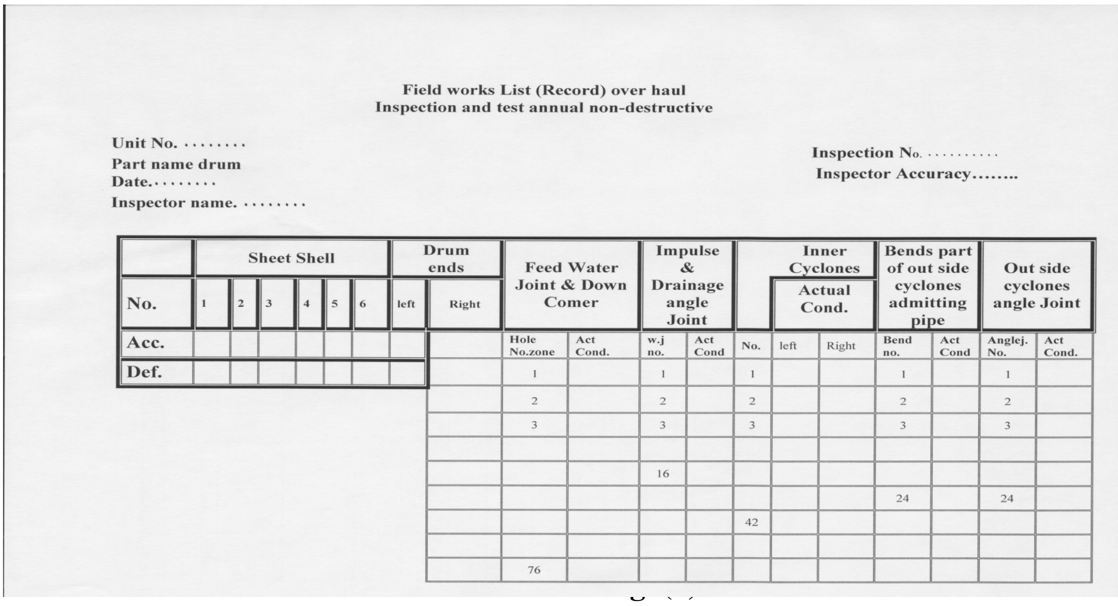

Field works List (Record) over haul
Inspection and test annual non-destructive

Unit No. ....
Part name drum
Date.........
Inspector name. ....

Inspection No. ....
Inspector Accuracy........

	Sheet Shell						Drum ends	
No.	1	2	3	4	5	6	left	Right
Acc.								
Def.								

Feed Water Joint & Down Comer		Impulse & Drainage angle Joint		Inner Cyclones			Bends part of out side cyclones admitting pipe		Out side cyclones angle Joint	
				Actual Cond.						
Hole No.zone	Act Cond.	w.j no.	Act Cond	No.	left	Right	Bend no.	Act Cond	Anglej. No.	Act Cond.
1		1		1			1		1	
2		2		2			2		2	
3		3		3			3		3	
		16								
							24		24	
				42						
76										

List of field record for drum

A SYSTEM BUILDING STEPS:

The steps to build the system are as follows:

1. Identifies the data needed from a huge data pool which include: parts, material, dimensions, drawing specification, working hours… etc, then designs lists for all informations to all parts.
2. Identifies the expected defects in all parts in a separate list.
3. Selecting a dependent procedure of nondestructive test and destructive, and designing lists of inspection & test which include the list of mechanical test.
4. Design lists of field (records) for all parts.
5. Finding the criteria number and allowable limit of all parts, by calculation, as thickness or OD allowable.
6. The lists of reports designing easy form to user which separates the rejected component, and fitting the lists of recommendations to repairs or treatments.
7. Designs analysis lists after type defect classifications.
8. Calculations of the standard time to estimate the performance of each activity are achieved.
9. Setting the materials compositions for all parts to help the inspector to take a decision and setting microstructure in picture with limits of work hours to help the inspector to achieve the comparisons and take a decision for validity as in.
10. Identifies the methods of water chemical analysis with designing the lists of chemical analysis.

CALCULATIONS:

The calculations involve equations to define the numbers needed by inspector after comparison to take a decision for repairing or changing or leaving the inspected part in the work.

1. According to Russion standard the equation was used to define the allowable thickness of pipe for furnace, superheater, and economizer is [Dr.Markov , Dr.plastoy]:

$$\text{tmin} = \frac{\text{Pw} \times \text{Dm}}{200\ \psi\ \sigma\text{act} + \text{Pw}}$$

Where:

tmin = minimum thickness allowable (mm).

Pw = working pressure kgf / mm2.

Dm = Nominal diameter (OD) mm.

ψ = Welding coefficient.

= 1 for seamless pipe.

σact = Ultimate stress at working temperature kgf / cm2.

For example:

The allowable thickness for water wall pipe of front wall of furnace:

First step the material defines, the pipe made of 15XM.

From the standards the minimum thickness is:

$$t_{\min} = \frac{155.5 \times 60}{200 \times 1 \times 13.085 + 155.5} = 3.36 \text{ mm} \qquad = 3.4 \text{ mm}$$

This number means the criterion number to inspect the thickness of all pipes made of alloy steel 15XM, under working pressure 155.5 kgf / mm^2 and out side diameter 60 mm, design thickness 6mm – and accepted thickness number after working hours > 3.4 mm.

2. According to American standard the equation was used to define the criterion number of (OD) in sperheater, which gives the indication about thermal effect on the metal (creep failure)[ASME, 1971].

$$\text{OD criterion} = \frac{\text{OD original} \times 3.5}{100 + \text{OD}}$$

Where

OD criterion = out side diameter of pipe.

OD original = out side diameter of pipe in design condition.

Then OD allowable < OD criterion

For example:

The pipe of platen superheater which is made of alloy steel (12X IMΦ) with dimension of OD = 42 mm.

$$\text{OD criterion} = \frac{42 \times 3.5}{100 + 42} = 43.47 \text{ mm}$$

OD allowable < 43.47 mm

3. Stresses in the drum shell calculated from hardness number of test.

By measuring hardness Brinel number (HB) (used portable digital hardness tester) then calculate σ number from equation:

$$\sigma = \left(\frac{HB}{3 \text{ or } 3.5} \right)$$

Then σ allowable > 50 kgf / mm2 accepted.

4. According to Japanes standard the equation which gives the indication about the scale in the water of boiler[JIS, 1966]:

W2 – W1 < 400 g / mm2

Where

W2 = the weight of pipe with scale.

W1 = the weight of pipe without scale (after washing).

Then (w2 – W1) allowable < 400g / mm2

This test helps the inspector to give his decision about washing the boiler.

5. Time standard calculation:

Time consumer in all types of (I & T) NDT and DT calculates by means of data numbers after analysis in normal distributed curve.

The data numbers divided to classes **[G.M. Clarke and D. Cooke , 1978].**

$$\text{Length of class} = \frac{HV - LV}{6}$$

Where

HV – LV = range

HV = high value number in data

LV = Low value number in data

6 = number of classes

then apply the equation.

$$\overline{X} = \frac{\sum f\,\overline{x}}{\sum f}$$

Where

f= frequency (data numbers)

X = mean value

The equation of $S = \sqrt{\frac{\sum fx^{2}}{\sum f} - \left(\overline{X}\right)^{2}}$

Where S standard deviation

The analysis covers all type of DT & NDT like ULT, RL, MPT, PT… etc.

For example ultrasonic data submitted to analysis as below

Range = HV – LV

= 5.33 – 4.88

= 0.45

$$\text{Length of class} = \frac{\text{Range}}{\text{Number of classes}} = \frac{0.45}{6} = 0.075$$

No.	class	Freq.	mid point X	$(X)^2$	fx	fx^2
1.	**4.88-4.4955**	**3**	**4.91**	**24.10**	**14.73**	**72.32**
2.	**4.956-5.031**	**5**	**4.99**	**24.90**	**24.95**	**124.50**
3.	**5.032-5.107**	**7**	**5.06**	**25.60**	**35.42**	**179.22**
4.	**5.108-5.183**	**6**	**5.14**	**26.41**	**30.84**	**158.51**
5.	**5.184-5.259**	**5**	**5.21**	**27.14**	**26.05**	**135.72**
6.	**5.26-5.335**	**4**	**5.29**	**27.98**	**21.16**	**111.93**
		30			**153.15**	**782.20**

$$= \frac{153.15}{30} = 5.10$$

$$S = \sqrt{\frac{\sum fx^{2}}{\sum f} - \left(\overline{X}\right)^{2}}$$

$$= \sqrt{\frac{782.20}{30} - (5.10)^{2}}$$

= 0.25165

IMPLEMENTATION (DBMS) COMPUTER AIDED OF IIBHS IN TPS

The software involves three basic activities:

1. Updating and maintaining common data base to reflect new events requiring changes to an organizations record.
2. Providing information needed for end users application by using application programs that share the data in common databases. This sharing of data supported by the common software interface provided by (DBMS) package.

Thus, end users and programmers do not have to know where or how data are physically stored.

3. Providing an inquiry / response and reporting capability through a DBMS package, so that endurance can easily interrogate data bases, generate reports, and receive quick responses to their special requests for information.

The software of a database management system (DBMS) is implemented to record and supervise the IIBHS in Al- Nassryiah power station in south of Iraq. Since all four units of power station, have the same type of boiler then the options in this system applies for all four boiler.

Computer specification for system requirements:

Central process unit (CPU): Pentium III 633 MHz or higher.

RAM memory: 128 MB, 256 MB recommended.

Hard disk space: 200 MB

Operating system: windows XP.

For printing a laser with A4 paper size is recommended.

As in fig. (8) these options are:

1. Boiler specifications: displays the boiler specifications window.
2. Drum: displays the drum list.
3. Furnace: displays the furnace list.
4. Super heater: displays the super heater list.
5. Economizer: displays the economizer list.
6. Materials: displays the window containing the materials used in the boiler and there chemical composition.
7. Help: to execute this help file.
8. Exit: to end the system and return to windows.

After having a good look on the existing option with high + light which moves to choose any required one.

If the user selects the drum second menu will appear which contains four options, then if the user selects list option the third menu will appear etc. for example the list in fig. (3) in the computer will appear as in fig (9-a) fig. (9-b), and fig. (9-c), also the list of report in fig. (4) it will appear by the window of computer as in fig. (10).

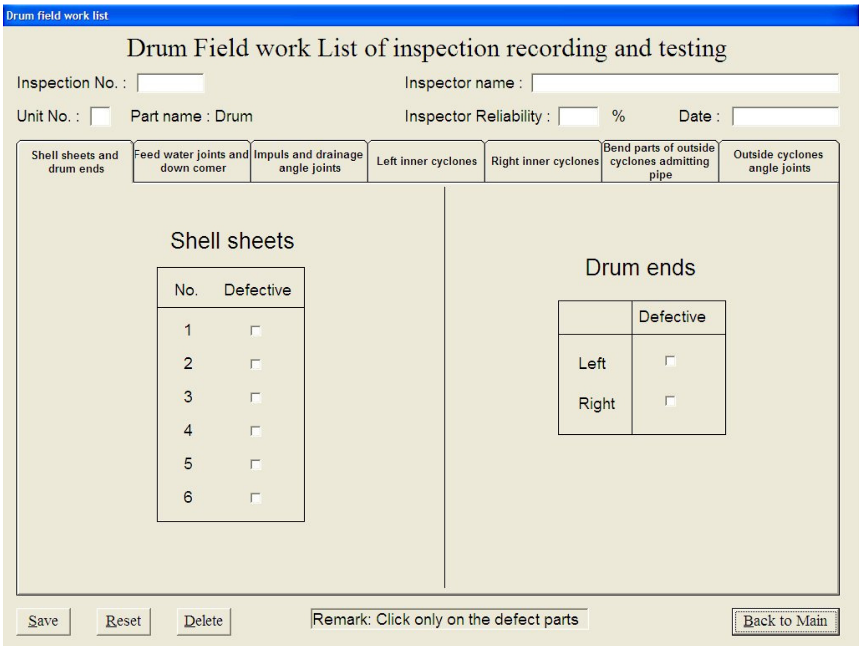

Drum Field work List of inspection recording and testing

Inspection No. :

Inspector name :

Unit No. :

Part name : Drum

Inspector Reliability : %

Date :

Shell sheets

No.	Defective
1	☐
2	☐
3	☐
4	☐
5	☐
6	☐

Drum ends

	Defective
Left	☐
Right	☐

Remark: Click only on the defect parts

Fig(8)

All the system will display as window in the computer to achieve the activities of IIBHS and give the user results, and recommendations in a simple method.

Fig (9)

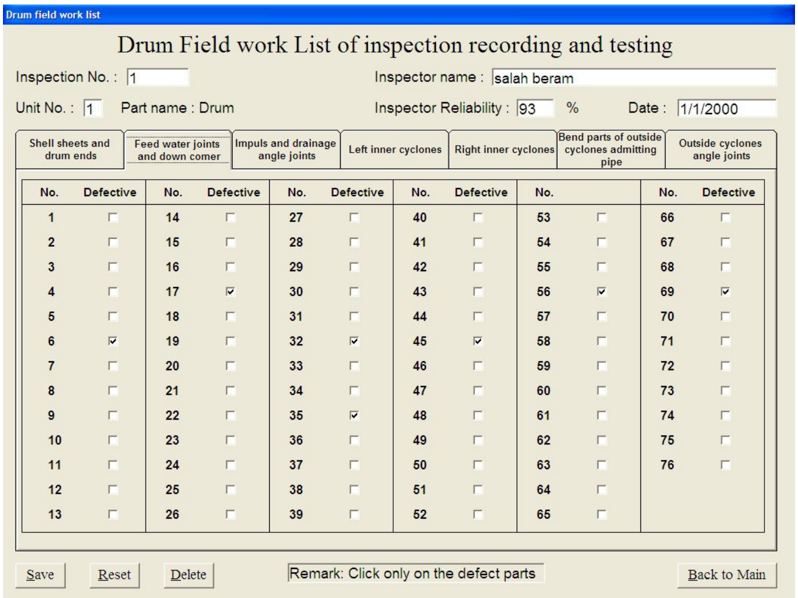

Drum Field work List of inspection recording and testing

Inspection No. : 1

Inspector name : salah beram

Unit No. : 1

Part name : Drum

Inspector Reliability : 93 %

Date : 1/1/2000

No.	Defective	No.	Defective	No.	Defective	No.	Defective	No.		No.	Defective
1	☐	14	☐	27	☐	40	☐	53	☐	66	☐
2	☐	15	☐	28	☐	41	☐	54	☐	67	☐
3	☐	16	☐	29	☐	42	☐	55	☐	68	☐
4	☐	17	☑	30	☐	43	☐	56	☑	69	☑
5	☐	18	☐	31	☐	44	☐	57	☐	70	☐
6	☑	19	☐	32	☑	45	☑	58	☐	71	☐
7	☐	20	☐	33	☐	46	☐	59	☐	72	☐
8	☐	21	☐	34	☐	47	☐	60	☐	73	☐
9	☐	22	☐	35	☑	48	☐	61	☐	74	☐
10	☐	23	☐	36	☐	49	☐	62	☐	75	☐
11	☐	24	☐	37	☐	50	☐	63	☐	76	☐
12	☐	25	☐	38	☐	51	☐	64	☐		
13	☐	26	☐	39	☐	52	☐	65	☐		

Remark: Click only on the defect parts

CONCLUSION:

By using the computerized system, the efforts and time will be saved, also the successful results which introduce by implementing the system gives the benefits as follows:

- Standardization of methods, procedures, for selection the NDT and DT.
- Reducing of paper work and form.
- Providing database from a huge data in a short time.
- Better documentation by recording the stages of inspection and reports.
- Historical data is given with time which assists both manager and inspection staff.
- Enlarging the capabilities of analysis.
- Avoiding the undeliberating errors.
- Training become more easy by using the programmed system.

The recommendations listed in this system are minimum guideline for inspecting the critical components of the boiler island. Based on problems encountered during the day-to-day boiler operation, additional inspections may be recommended.

The steps in this system will help to know the amount, type and specific location of inspection performed at any outage, either planned or forced.

References

1. American Society of Mechanical Engineers “Nondestructive Examination” Sec. V. printed in the United States of American in 1980.
2. American Society of Mechanical Engineers Center “Rules of Construction of Power Boiler” printed in New York at 1971.
3. David N. French “Metallurgical Failures in Fossil Fired Boilers” printed by John Wiley & Sons, Inc. published in Canada at 1993.
4. Dr.Markov N.M & Dr. Plastov vp "Steam boilers , water superheaters and pipelines for steam and heated water"published by polznova institute of USSR at October of 1975.
5. G. M. Clarke and D. Cooke “A Basic Course In Statistics” printed by photolithography in Great British at the pitman press, published by Edward Arnold Ltd. in 1978.
6. John Carter “Data base Design and Programming With Access, SQL and Visual Basic” printed in Mc Graw Hill International (UK) Limited, published by Mc Graw - Hill Company at 2000.
7. James A. O. Brien “ Introduction To Information System” printed by Mc Graw Hill New York at 1997.

8. Japanese Industrial standards Committee (JIS) “Test Methods for Water Content of Chemical Products” printed in Japan Translated and published by Japanese standards Association at 1966.

9. M. N. Hovinga G.L. Nakoneczny “Standard Recommendation for Pressure Part Inspection During A Boiler Life Extension Program” published by Babcock & Wilcox company in (USA) at May 2000.

10. M. M. Joshi “Inspection For Coal Handling Plant Of Thermal Power Station Using NDT” NDT net January 2003. Vol. 8 No. 01.

11.. Mo D. Majnouni, and Arif E. jaffer, "Chemical cleaning of industrial Boiler-Anoverview paper was presented at Annual conference in Pittsburgh" Oct. 19 to 23. 2003

12. Robert D. Port & Harvey M. Herro “The Naclo Guide To Boiler Failure Analysis” print by Mc Graw-Hill, USA published at 1991.

www.file://A:\I-service%20Inspection%20for%20coal%20handling%20lpant%20of%20then

SYSTOLIC ARRAY FOR REALIZATION OF DISCRETE WAVELET TRANSFORM

Dr.Waleed A. Mahmoud,
University of Baghdad
College of Eng.\ Electrical Dept.

Ahmed S. Hadi
University of Baghdad
Al_Khawarizmy College of Eng.\Information Dept.

ABSTRACT:

This paper introduce a new method for using a systolic array to perform the one, and two dimension discrete wavelet transform (1-D DWT, and 2-D DWT).

The 1-D needs only a semi-systolic array for its realization. However, it was found that the 2-D method needs the combination of two types of semi-systolic array into one systolic array to achieve its implementation.

الخلاصه:

في هذا البحث تم تقديم طريقة جديدة لايجاد تحويل ال"wavelet" المتقطع احادي البعد (1-D DWT) وثنائي البعد (2-D DWT)
باستخدام مصفوفة ال" systolic ".
في تحويل ال"wavelet" المتقطع احادي البعد (1-D DWT) استخدمنا شبه مصفوفة ال"systolic". بينما في تحويل
ال"wavelet" المتقطع ثنائي البعد (2-D DWT) تم دمج مصفوفتان من شبه ال"systolic" لانتاج مصفوفة "systolic" كاملة.

KEYWORDS:
1-D DWT, 2-D DWT , Semi-systolic array, and Systolic array.

INTRODUCTION

One of the signal-processing problems is the efficient implementation in VLSI of the discrete wavelet transform (DWT). The DWT is important in many applications such as spectral analysis, digital filtering, image processing . . . etc. There is a much interest in two dimension discrete wavelet transform (2-D DWT), to gain a better understanding for pattern analysis [Martin 1999].

For VLSI implementation, systolic arrays are attractive because they are constructed with a repetitive array of identical cells. The use of identical cells simplifies the design process. Further, if the interconnection between cells can be restricted to the nearest neighbor connections (i.e., only adjacent cells communicate with each other), high speed is possible [Swartzlander 1987].

The DWT is better suited to realization with a systolic array, due to the high density, and high speed processors of the systolic array that result from the short and systematic wire routing and concurrency [Lee 1992, O'Brien 1989].

This paper is organized as follows: Section II presents a computation of 1-D DWT and 2-D DWT. Section III describes semi-systolic array for matrix multiplication. Section IV presents a systolic array for computing 1-D DWT, and 2-D DWT. Section V presents conclusions.

COMPUTATION OF DWT:

The structure of a one dimensional DWT is shown in fig. (1). X(n) is the 1-D input signal. H(n) and g(n) are the analysis lowpass and high pass filters which, split the input signal into two subbands: lowpass and highpass. The lowpass and highpass subbands are then downampled generating $X_L(n)$ and $X_H(n)$ respectively [Goswami 1999]. The 1-D DWT can compute as follows:

1. Checking input dimensions: input vector should be of length N, where N must be power of two.
2. Construct a transformation matrix T: using transformation such as Haarr, or Daubechies Db4 [Burrus 1998]. As shown below for N=4:

$$T_{Haar} = \begin{bmatrix} h_0 & h_1 & 0 & 0 \\ 0 & 0 & h_0 & h_1 \\ h_1 & -h_0 & 0 & 0 \\ 0 & 0 & h_1 & -h_0 \end{bmatrix}$$

$$T_{Db4} = \begin{bmatrix} h_0 & h_1 & h_2 & h_3 \\ h_2 & h_3 & h_0 & h_1 \\ h_3 & -h_2 & h_1 & -h_0 \\ h_1 & -h_0 & h_3 & -h_2 \end{bmatrix}$$

3. Transformation of input vector: which can be done by multiplying the N×N constructed transformation matrix by the N×1 input vector.

$$Y_{N\times 1} = T_{N\times N}.X_{N\times 1} \qquad [1]$$

There are two main types of methods for computing DWT for 2-D signals, which are separable and non-separable algorithms. Separable methods simply work on each dimension in series. The typical approach is to process each of the rows in order and then process each column of the result. Non-separable methods work in both signal dimensions at the same time [Strela 1996]. Because the non-separable method can save time and computation, it will be use here.

The 2-D DWT can compute using non-separable method as follows:

1. Checking input dimensions: input matrix, X, should be of length N×N, where N must be power of two.
2. For an N×N matrix input 2-D signal, X construct an N×N transformation matrix, T, using Haarr, or Daubechies Db4 [Burrus 1998].
3. Apply transformation by multiplying the transformation matrix by the input matrix by the transpose of the transformation matrix.

$$Y_{N\times N} = T_{N\times N}.X_{N\times N}.T^{T}_{N\times N} \qquad [2]$$

This multiplication of the three matrices result in the final discrete wavelet transformed matrix.

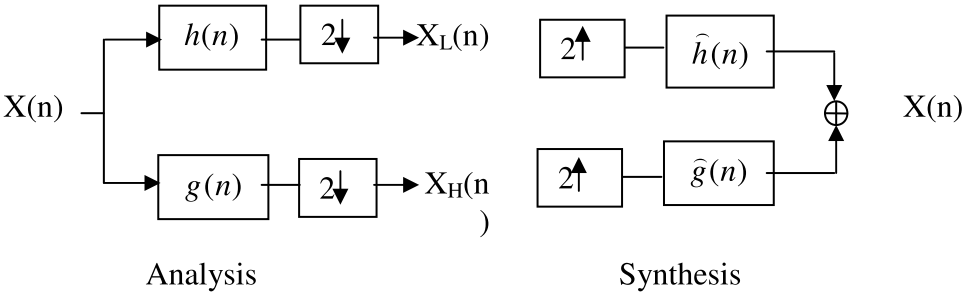

Fig. (1): Analysis and synthesis stages of a 1-D DWT

SEMI-SYSTOLIC ARRAY FOR MATRIX MULTIPLICATION:

Since matrix multiplication is the basic operation for the DWT it will describe here. Our approach is based on systolic arrays for matrix multiplication. Kung [Kung 1988] has identified two types of semi-systolic arrays for the multiplication of two N × N matrices. An array is semi-systolic if the output data is not produced in the boundary cells of the array (type 1) or if the input data has to be preloaded into the array (type 2).

The type 1 array and the type 2 array and their cell structure are shown for N=4 on fig.(2) for matrix multiplication C=AB. Where H_{in}, H_{out}, V_{in}, and V_{out} represent the horizontal input, the horizontal output, the vertical input, and the vertical output respectively. R_{ij} is a value saved in a register of each semi-systolic cell.

In the type 1 array shown in fig. (2 a). Each semi-systolic cell perform a multiply-accumulator operation. Where the horizontal and vertical inputs are are multiplied and added to the register in semi-systolic cell. In N cycles, each semi-systolic cell computes an inner product of row of A and column of B. Here type 1 computation is done as follows from type 1 array in fig. (2 a):

$$H_{out} \leftarrow H_{in}$$

$$V_{out} \leftarrow V_{in}$$

$$R_{ij} \leftarrow R_{ij} + H_{in} V_{in}$$

The computational sequence of this array is shown in table (1 a), where $x \leftarrow y$ indicates that the value of x is replaced by the value of y. this array is semi-systolic since the output data is produced throughout the array and not at in the boundary cells. This requires overhead for the output to be shifted out of the array.

In the type 2 semi-systolic array shown in fig. (2 b), to compute C=AB, the components of matrix B are preloaded into register in the semi-systolic cells, and matrix A stream into the array. Each cell multiplies the horizontal input times the register value and adds this to the vertical input to produce the vertical output. The inner product of a row of input matrix A and a column of the array (a column of matrix B) is computed in N cycles. Type 2 semi-systolic computation is defined as follows from the type 2 array in fig. (2 b):

$$H_{out} \leftarrow H_{in}$$

$$V_{out} \leftarrow V_{in} + R_{ij} H_{in}$$

The computational sequence of this array is given in table (1 b). The value of C_{ij}(i=1, 2, 3, 4) is generated by semi-systolic cell (4, j) for j=1, 2, 3, 4.

Inputs for type 1 matrix multiplication array are stream inputs, whereas one of the inputs of the type 2 matrix multiplication array is preloaded input. On the other hand, in the type 1 matrix multiplication array, each element of matrix C is saved in a semi-systolic cell, where as in type 2 matrix multiplication array, each element of matrix C is generated in the bottom boundary semi-systolic cell's of the array as stream outputs.

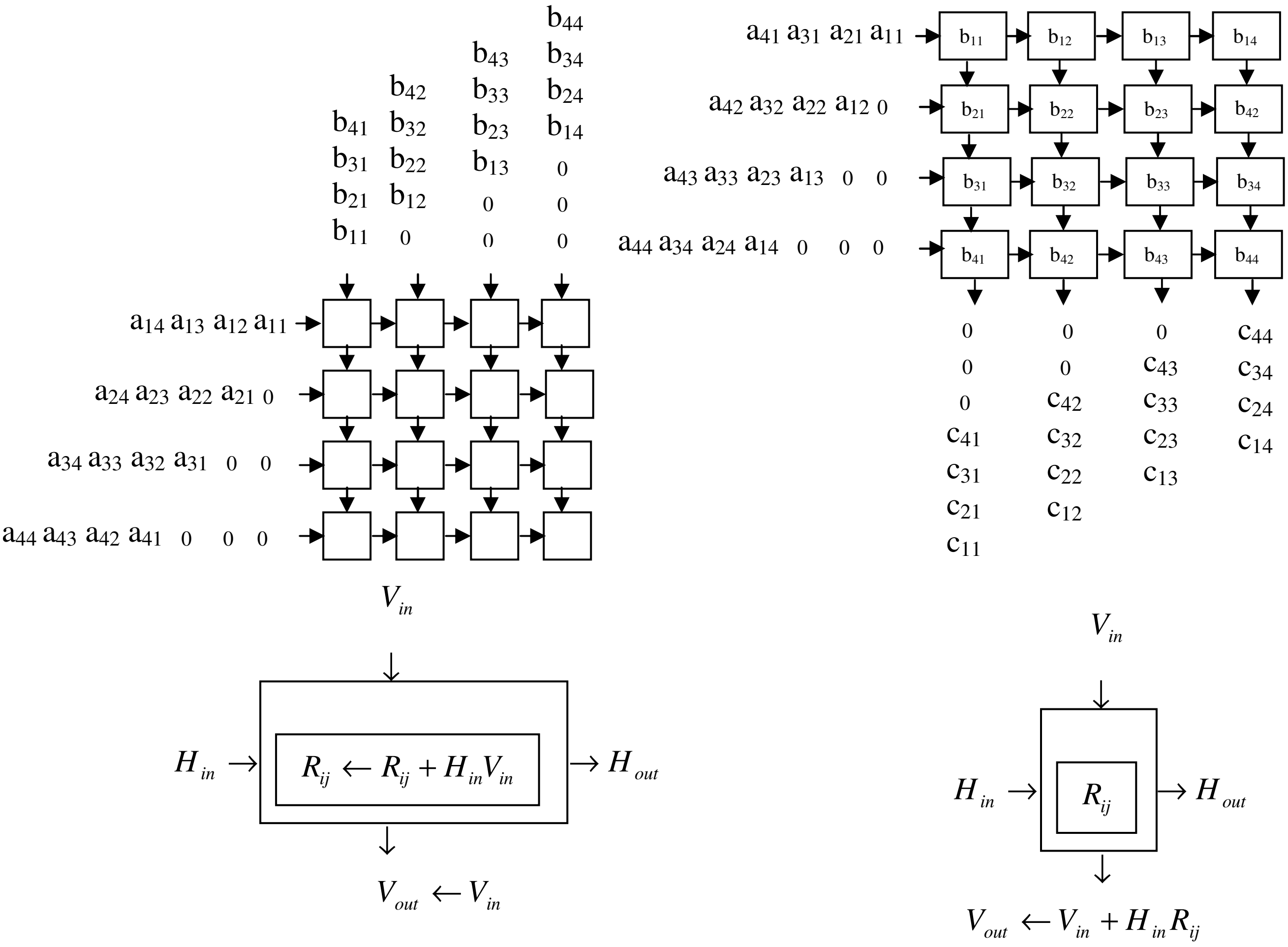

(a) Type 1 array

(b) Type 2 array.

Fig. (2): Semi-systolic arrays for matrix multiplication.

Table 1

Coputational sequences for type 1 and type 2 semi-systolic arrays. (a) for the type 1 semi-systolic array. (b) for the type 2 semi-systolic array.

	cell(1,1)	cell(2,1)	cell(3,1)	cell(4,1)
1	$R_{11} \leftarrow a_{11}b_{11}$			
2	$R_{11} \leftarrow R_{11} + a_{12}b_{21}$	$R_{12} \leftarrow a_{21}b_{11}$		
3	$R_{11} \leftarrow R_{11} + a_{13}b_{31}$	$R_{21} \leftarrow R_{21} + a_{22}b_{21}$	$R_{31} \leftarrow a_{31}b_{11}$	
4	$R_{11} \leftarrow R_{11} + a_{14}b_{41}$	$R_{21} \leftarrow R_{21} + a_{23}b_{31}$	$R_{31} \leftarrow R_{31} + a_{32}b_{21}$	$R_{41} \leftarrow a_{41}b_{11}$
5		$R_{21} \leftarrow R_{21} + a_{24}b_{41}$	$R_{31} \leftarrow R_{31} + a_{33}b_{31}$	$R_{14} \leftarrow R_{41} + a_{42}b_{21}$
6			$R_{31} \leftarrow R_{31} + a_{34}b_{41}$	$R_{14} \leftarrow R_{41} + a_{43}b_{31}$
7				$R_{14} \leftarrow R_{41} + a_{44}b_{41}$

(b)

	cell(1,1)	cell(2,1)	cell(3,1)	cell(4,1)
1	$V_{out} \leftarrow a_{11}b_{11}$			
2	$V_{out} \leftarrow a_{21}b_{11}$	$V_{out} \leftarrow V_{in} + a_{12}b_{21}$		
3	$V_{out} \leftarrow a_{31}b_{11}$	$V_{out} \leftarrow V_{in} + a_{22}b_{21}$	$V_{out} \leftarrow V_{in} + a_{13}b_{31}$	
4	$V_{out} \leftarrow a_{41}b_{11}$	$V_{out} \leftarrow V_{in} + a_{32}b_{21}$	$V_{out} \leftarrow V_{in} + a_{23}b_{31}$	$V_{out} \leftarrow V_{in} + a_{14}b_{41}$
5		$V_{out} \leftarrow V_{in} + a_{42}b_{21}$	$V_{out} \leftarrow V_{in} + a_{33}b_{31}$	$V_{out} \leftarrow V_{in} + a_{24}b_{41}$
6			$V_{out} \leftarrow V_{in} + a_{43}b_{31}$	$V_{out} \leftarrow V_{in} + a_{34}b_{41}$
7				$V_{out} \leftarrow V_{in} + a_{44}b_{41}$

COMPUTATION OF DWT USING SYSTOLIC ARRAY:

The 1-D DWT can be implement by using type 2 semi-systolic array. Where Rij will content the elements of the transformation matrix T after transposition (Which is either Haar, or Db4 transformation matrix). X is the input signal. As shown in fig. (3). Which implement equation 1. Where Fig. (3 a) implement this equation by using the Haar transformation. While Fig. (3 b) implement this equation by using the Db4 transformation.

$$\begin{bmatrix} Y_0 \\ Y_1 \\ Y_2 \\ Y_3 \end{bmatrix} = \begin{bmatrix} h_0 & h_1 & 0 & 0 \\ 0 & 0 & h_0 & h_1 \\ h_1 & -h_0 & 0 & 0 \\ 0 & 0 & h_1 & -h_0 \end{bmatrix} \begin{bmatrix} X_0 \\ X_1 \\ X_2 \\ X_3 \end{bmatrix} = \begin{bmatrix} X_0h_0 + X_1h_1 \\ X_2h_0 + X_3h_1 \\ X_0h_1 - X_1h_0 \\ X_2h_1 - X_3h_0 \end{bmatrix}$$

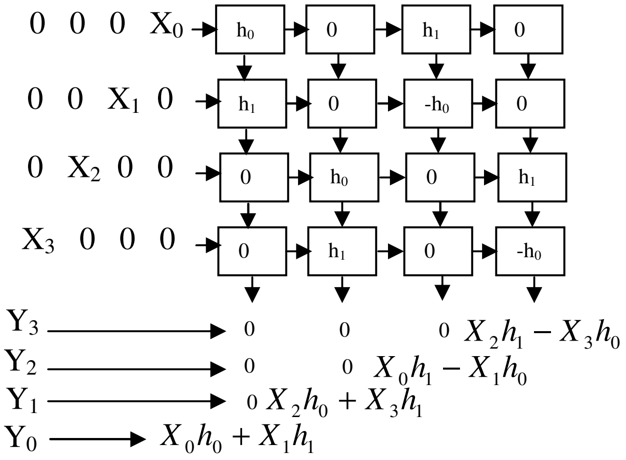

Fig. (3, a): Implementation of 1-D DWT using Haar.

$$\begin{bmatrix} Y_0 \\ Y_1 \\ Y_2 \\ Y_3 \end{bmatrix} = \begin{bmatrix} h_0 & h_1 & h_2 & h_3 \\ h_2 & h_3 & h_0 & h_1 \\ h_3 & -h_2 & h_1 & -h_0 \\ h_1 & -h_0 & h_3 & -h_2 \end{bmatrix} \begin{bmatrix} X_0 \\ X_1 \\ X_2 \\ X_3 \end{bmatrix} = \begin{bmatrix} X_0h_0 + X_1h_1 + X_2h_2 + X_3h_3 \\ X_0h_2 + X_1h_3 + X_2h_0 + X_3h_1 \\ X_0h_3 - X_1h_2 + X_2h_1 - X_3h_0 \\ X_0h_1 - X_1h_0 + X_2h_3 - X_3h_2 \end{bmatrix}$$

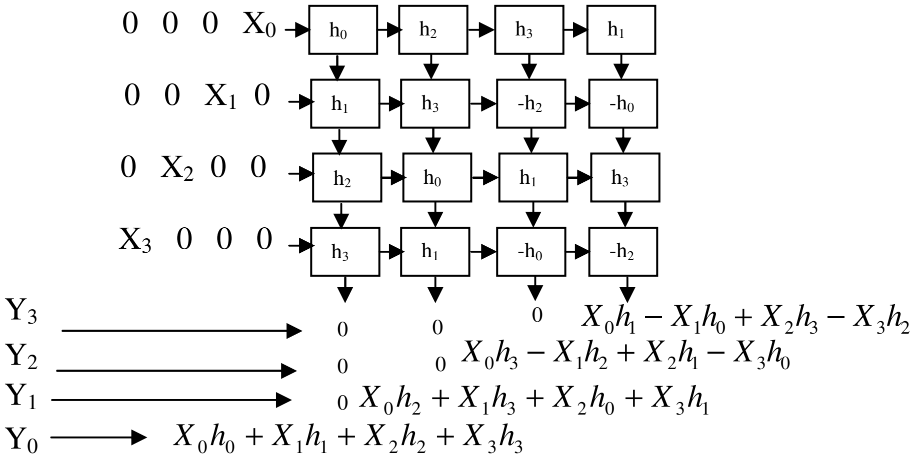

Fig. (3, b): The implementation of 1-D DWT using Db4.

Fig. (3): Implementation of 1-D DWT using type 2 semi-systolic array.

Equation 2, which represent the 2-D DWT can be implemented by using type 1, and type 2 semi-systolic array. As shown in fig. (4), which represent a fully systolic array. Where first a type 1 semi-systolic array is used to implement the first part of equation 2 (Z=T.X), and store it inside it. Then type 2 is used to implement the second part of equation 2 ($Y=Z.T^T$), but with some change as shown below:

$$H_{out} = H_{in} + V_{in} R_{ij} \quad \text{instead of} \quad V_{out} = V_{in} + H_{in} R_{ij}$$

$$V_{out} = V_{in} \quad \text{instead of} \quad H_{out} = H_{in}$$

Note that due the rearrangement of T in type 2, the result obtained in reverse order. The overall fully systolic array is shown in fig. (4 c).

$$R_{ij} \leftarrow R_{ij} + H_{in} V_{in}$$
$$V_{out} \leftarrow V_{in}$$
$$H_{out} \leftarrow H_{in}$$

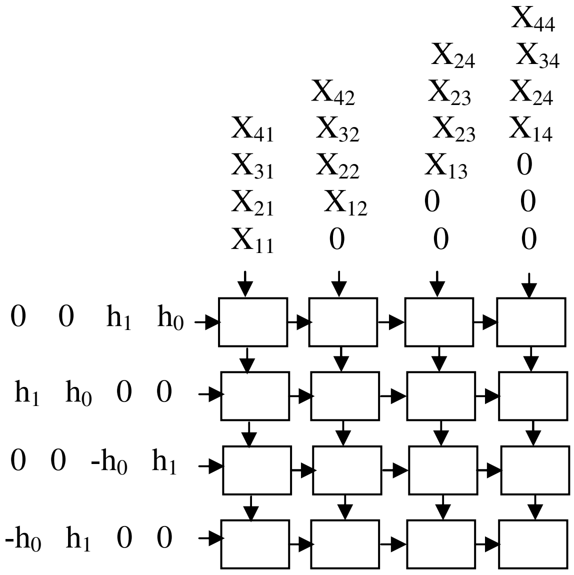

Fig. (4, a): Represent type 1 semi-systolic array to implement Z=T.X

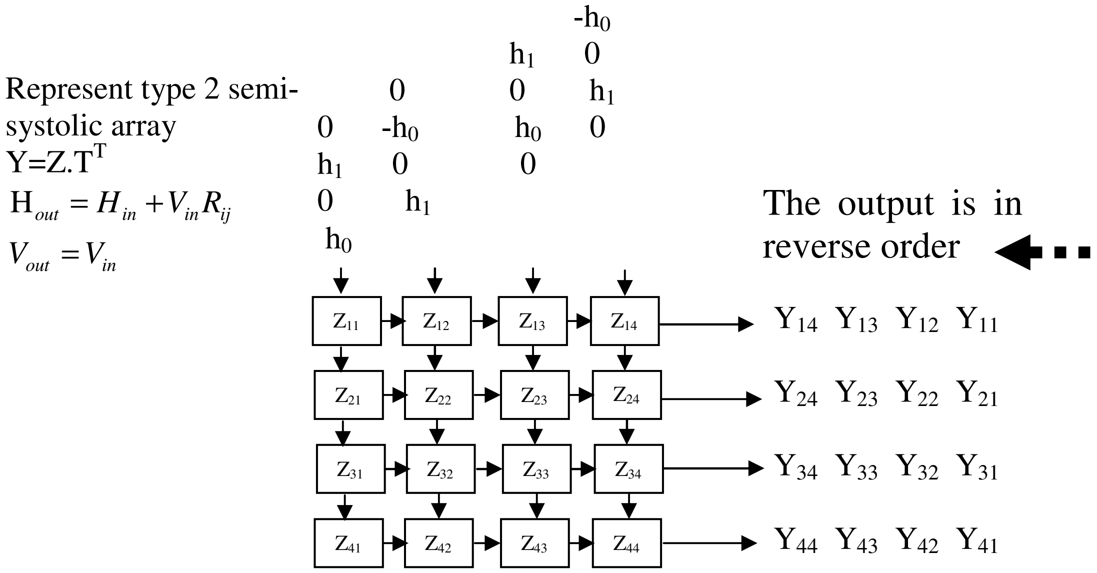

Fig. (4, b): Represents type 2 semi-systolic array to implement $Y=Z.T^T$.

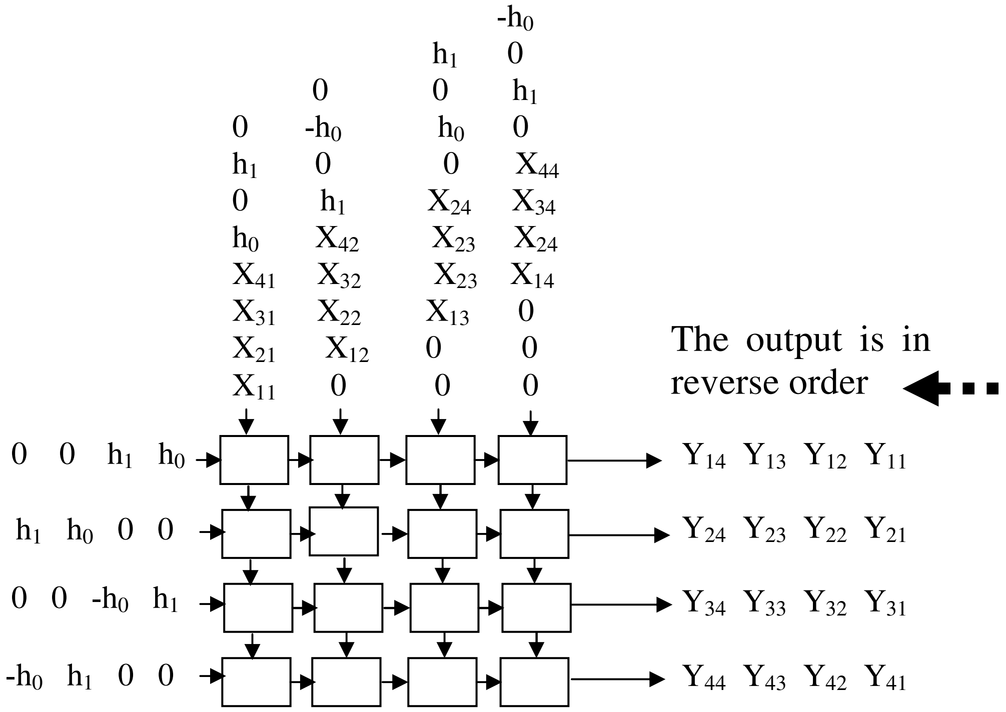

Fig. (4, c): The overall fully systolic array, to implement $Y=T.X.T^T$.

Fig. (4): The implementation of 2-D DWT using systolic array with Haar Transformation.

CONCLUSION

This paper presents a systolic array realization of the 1-D DWT, and 2-D DWT. The 1-D needs only a semi-systolic array for its realization, which need a preloading of input data. While the 2-D use a regular array of simple processors that operate in the two semi-systolic manners to produce a fully systolic system. The resulting systolic array accepts stream of input data without any preloading.

This open the way for further study of image and speech processing as well as in other DSP applications that based on Wavelet transform.

REFERNCES

[1] C. S. Burrus, R. A. Gopinath, and H. Guo, “Introduction to Wavelets and Wavelet Transforms”, Prentice hall, 1998.

[2] E. E. Swartzlander, Jr., "Systolic FFT processors", in Systolic Arrays, W. Moore, A. McCabe, and R. Urquhart, Eds. Boston, MA: Adam Hilger, 1987, pp. 133-140.

[3] J. C. Goswami and A. K. Chan, “ Fundamentals of Wavelets: Theory Algorithms, and Applications”, John Wiley & Sons Inc., 1999.

[4] J. O'Brien, J. Mather, an B. Holland, "A 200 MIPS single-chip 1K FFT processor," in IEEE Inst. Solid-State Circuits Conf. Rec., 1989, pp. 166-167.

[5] M. H. Lee, "High speed multidimentional systolic arrays for discrete Fourier transform", IEEE Trans. Circuits Syst. II, vol. 39, pp. 876-879, 1992.

[6] M. B. Martin, “Applications of Multiwavelets to Image Compression”, M.Sc. thesis, Virginia Polytechnic Institute and State University, Virginia, June, 1999.

[7] S. Y. Kung, VLSI Array Processors. Englewood Cliffs, NJ: Prentice-Hall, 1988.

[8] V. Strela, “Multiwavelets: Theory and Applications” Ph.D thesis, Massachusetts Institute of Technology, 1996.

Number 2 Volume 13 June 2007 Journal of Engineering

CONFINEMENT AND EXPANSION MODELS FOR NONLINEAR ANALYSIS OF REINFORCED CONCRETE MEMBERS

Dr. Khalid S. Mahmoud
Prof.
Baghdad University

Dr. Ihsan Al-Shaarbaf
Assistant Prof.
Al-Nahrain University

Dr. Abbas A. Allawi
Lecturer
Baghdad University

ABSTRACT

This research pertains to expand the formulation and applicability of using confinement and expansion due to Poisson’s ratio models for three dimensional non-linear finite element analysis of reinforced concrete members. A plasticity based model that acknowledges the asymmetric response of reinforced concrete under multiaxial stress conditions is used to account for the strength improvement under conditions of triaxial compression. Complex behavior of concrete such as compression softening and tension softening are incorporated to simulate concrete behavior. **DIANA** software is used for finite element analysis with the inclusion of confinement and expansion effects. The concept of material pre-strains is extended to accommodate modeling of the Poison’s ratio effect. The applicability of the suggested confinement and expansion models are verified by comparing the results of Kupfer and Vecchio – Collins tests on shear panels with that obtained from **DIANA** software. These comparisons illustrate the ability of the confinement and expansion models to obtain the response of reinforced concrete members subjected to multiaxial stress conditions.

KEYWORDS

Compressive behavior, Confined concrete model, DIANA software, Expansion model, Finite element.

الخلاصة

في هذا البحث تم صياغة و تطبيق نموذج للحصروالتوسع بسبب نسبة بواسون في التحليل اللا خطي الثلاثي الابعاد باستخدام طريقة العناصر المحددة. جرى استخدام النموذج اللدن تحت تاثير حالة اجهاد متعدد المحاورلبيان مدى تاثير التحسن في مقاومة الخرسانة لاجهادات الانضغاط . كذلك جرى الاخذ بنظر الاعتبار تاثير تطرية الانضغاط وتطرية الانفعال للشد وتاثير الخرسانة ذات المقاومة العالية. تم استعمال برنامج **DIANA** للتحليل مع اخذ تاثير الحصر والتوسع بنظر الاعتبار. ان فكرة الانفعال المسبق تم استخدامها لبيان تاثير التوسع الناتج من نسبة بواسون. لبيان مدى تطبيقية استخدام نموذجي الحصر والتوسع المقترحين فقد جرى مقارنة نتائج فحوصات كوبفروفيشكو – كولنز لبلاطات خرسانية مع تلك المستحصلة من التحليل باستخدام برنامج **DIANA** . المقارنة بينت قابلية نموذجي الحصروالتوسع المقترحين على عكس تصرف الاعضاء الخرسانية المسلحة المعرضة الى حالات اجهاد متعدد المحاور بصورة جيدة.

INTRODUCTION

In concrete constitutive modeling, a number of different approaches have been used to calculate the material stiffness matrix. Traditionally, constitutive models for concrete have concentrated on reproducing the experimental observed nonlinear response of reinforced concrete specimens. Many constitutive models for multiaxial stress states are based on modifications to the uniaxial stress –

strain response. Concrete strength and stiffness are sensitive to multiaxial stress conditions. Ultimate strength and ductility are known to be significantly improved in the presence of lateral compressive stress which inhibits the propagation of microcracks (Figure (1)). Some modifications are required to extend the cracked concrete theory from two to three dimensions while a model is needed for material subjected to triaxial compressive stresses. To describe the response of reinforced concrete, models are required for strength degradation due to cracking, strength enhancement because of confinement and expansion due to effect of Poisson's ratio, pre and post-peak stress-strain response in tension and compression.

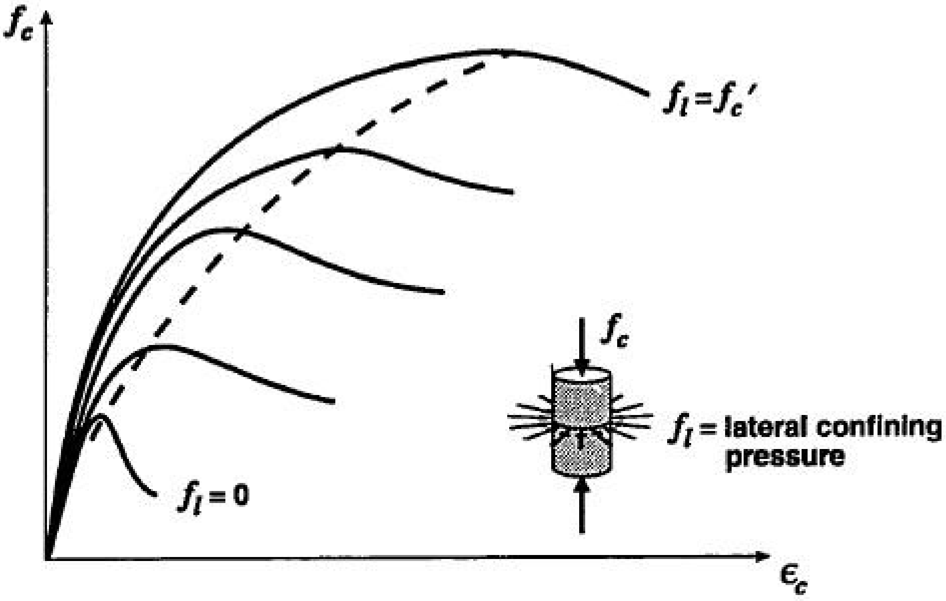

Fig (1): Effect of confinement on strength and ductility of concrete [Chen 1982].

STRESS - STRAIN CURVES FOR COMPRESSIVE RESPONSE

The constitutive equations for multiaxial stress state are based on modifications to the concrete uniaxial stress – strain curve. The Hognestad parabola describes the stress – strain response of a normal strength cylinder loaded in uniaxial compression. The parabolic relationship to determine the compressive stress f_{c3} corresponding to the compressive principal strain ε_{c3} (Vecchio and Collins 1982) is:

$$f_{c3}=\begin{cases} -f_p\left[2\left(\dfrac{\varepsilon_{c3}}{\varepsilon_p}\right)-\left(\dfrac{\varepsilon_{c3}}{\varepsilon_p}\right)^2\right] & ,0>\varepsilon_{c3}>\varepsilon_p \\ -f_p\left[1-\left(\dfrac{\varepsilon_{c3}-\varepsilon_p}{2\,\varepsilon_0-\varepsilon_p}\right)^2\right] & ,\varepsilon_p>\varepsilon_{c3}>2\varepsilon_o \end{cases} \tag{1}$$

where f_p and ε_p are the peak stress and the strain at peak stress, respectively. The strain at peak stress is calculated as $2\,f_c'/E_c$ where E_c is the initial slope to the parabola. For the case of uniaxial compression, the peak stress will be the cylinder strength f_c' which occurs at the strain ε_o

The uniaxial stress – strain response of high strength concrete is more linear in the ascending branch and the descending branch drops more sharply as shown in Figure (2). Therefore, the Hoghnestad parabola does not provide a good representation of the response of high strength concrete. Also, in low strength concrete ($f_c' < 20$ MPa), the Hognestad parabola tends to underestimate stresses at intermediate levels (Vecchio and Collins 1993). Thus, various alternatives were considered. It was found that the Thorenfeldt et al. (1987) model resulted in a good correlation for the full range of concrete strength represented in the database. The Thorenfeldt base curve later was calibrated by Collins and Porasz (1989) and as follows:

$$f_{c3} = f_p \cdot \frac{\varepsilon_{c3}}{\varepsilon_p} \cdot \frac{n}{n-1+\left(\varepsilon_{c3} / \varepsilon_p\right)^{nk}} \tag{2}$$

where n is given by:

$$n = 0.8 + \frac{f_c'}{17} \tag{3}$$

and k equals 1 for ascending branch, and

$$k = 0.67 + \frac{f_c'}{62} \tag{4}$$

for the descending branch (where f_c' is in MPa). For this curve, the strain at peak stress under uniaxial compression is estimated as:

$$\varepsilon_0 = \frac{n}{n-1} \cdot \frac{f_c'}{E_c} \tag{5}$$

The effect of the cylinder strength on the shape of this curve is shown in Figure (2).

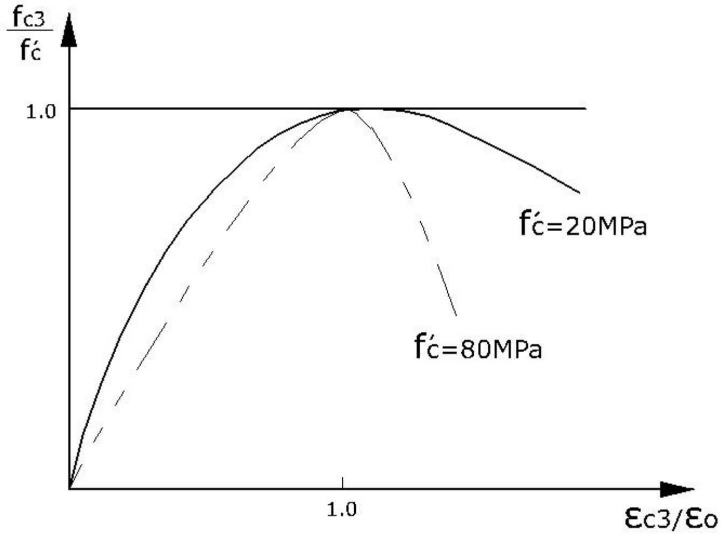

Fig (2): Effect of f_c' on the shape of curve given by Eq. (2) (Collins and Porasz 1989).

CONFINED CONCRETE MODEL

Lateral confining stresses increase the strength, stiffness and strain at peak stress of concrete cylinders. The strength enhancement is modeled by modifying the peak stress of the base curve. The failure surface proposed by Hsieh et al. (1979) is:

$$2.0108 \frac{\sqrt{J_2}}{f_c'^2} + 0.9714 \frac{\sqrt{J_2}}{f_c'} + 9.1412 \frac{f_{c1}}{f_c'} + 0.2312 \frac{I_1}{f_c'} - 1 = 0 \tag{6}$$

is used to find the stresses required in the major compressive direction to cause failure, f_{c3f} , in the presence of the stresses f_{c1} and f_{c2}. The invariants J_2 and I_1 are defined in terms of the stress f_{ci} in concrete according to:

$$J_2 = \frac{1}{6}\left(\left(f_{c1} - f_{c2}\right)^2 + \left(f_{c2} - f_{c3}\right)^2 + \left(f_{c3} - f_{c1}\right)^2\right) \tag{7}$$

$$I_1 = f_{c1} + f_{c2} + f_{c3} \tag{8}$$

and f_{c1} is the tensile principal stress in concrete.
The multipliers in this equation are curve fitting factors chosen to represent the results of a number of tests (Chen 1982). The stress f_{c3f} is used as the peak stress of the base curve and a peak stress factor , K_{σ} is defined as:

$$K_{\sigma} = \frac{f_{c3f}}{f_c'} \tag{9}$$

while experimental evidence suggests the same factor can be applied to find the peak stress and the corresponding peak strain in cracked concrete, different factors must be applied to f_c' and ε_o for confined concrete. The peak strain increases much more rapidly than the peak stress as confining pressure is increased. To relate the peak stress factor and the strain at peak stress factor, K_{ε} , a two part expression is implemented as shown in Figure (3). For low peak stress ratios ($K_{\sigma} < 3$), a fit to the data of Kupfer et al. (1969) is used.

$$K_{\varepsilon} = 0.2036\ K_{\sigma}^{4} - 2.819\ K_{\sigma}^{3} + 13.313 K_{\sigma}^{2} - 24.42\ K_{\sigma} + 13.718\sqrt{K_{\sigma}} + 1 \tag{10}$$

And for peak stress ratios, the expression is:

$$K_{\varepsilon} = 5\ K_{\sigma} - 4 \tag{11}$$

The coordinates of the apex of the base curve become

$$f_p = K_{\sigma} \cdot f_c' \tag{12}$$

$$\varepsilon_p = -\varepsilon_0 \left[K_{\sigma} \left(1 - \frac{f_{c3}}{f_{c3f}} \right) + K_{\varepsilon} \left(\frac{f_{c3}}{f_{c3f}} \right) \right] \tag{13}$$

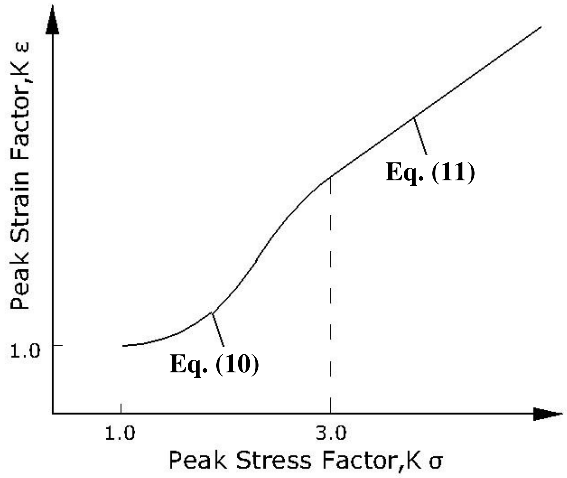

Fig (3): Peak stress and corresponding peak strain in confined concrete.

The ratio f_{c3} / f_{c3f} is a measure of the degree of nonlinearity. When this value is low, the strain at peak stress is close to $K_{\sigma}\ \varepsilon_o$. At ultimate strength level, the strain at peak stress becomes closer to $K_{\varepsilon}\ \varepsilon_o$. The modified stress – strain curve is then used to determine all three concrete stresses from the corresponding principal strains. Increased ductility is evident when concrete is confined. To simulate the descending branch given in Figure (4) of the stress – strain curve of confined concrete, a liberal modification was made to modify Kent – Park model (Scott et. al. 1982). The descending branch is given by:

$$f_{c3} = -f_p\left[\ 1 + Z_m\left(\varepsilon_{c3} - \varepsilon_p\right)\ \right] \quad \leq \quad -0.2 f_p \tag{14}$$

where

$$Z_m = \frac{0.5}{\dfrac{3+0.29 f_c'}{145\, f_c' - 1000} \cdot \left(\dfrac{\varepsilon_0}{-0.002} \right) + \left(\dfrac{-I_1 + f_{ci}}{170} \right)^{0.9} + \varepsilon_p} \tag{15}$$

I_1 is the first stress invariants, f_{ci} is the current stress in the principal direction under consideration, and ε_o and ε_p are negative quantities. This equation is in S.I. units.

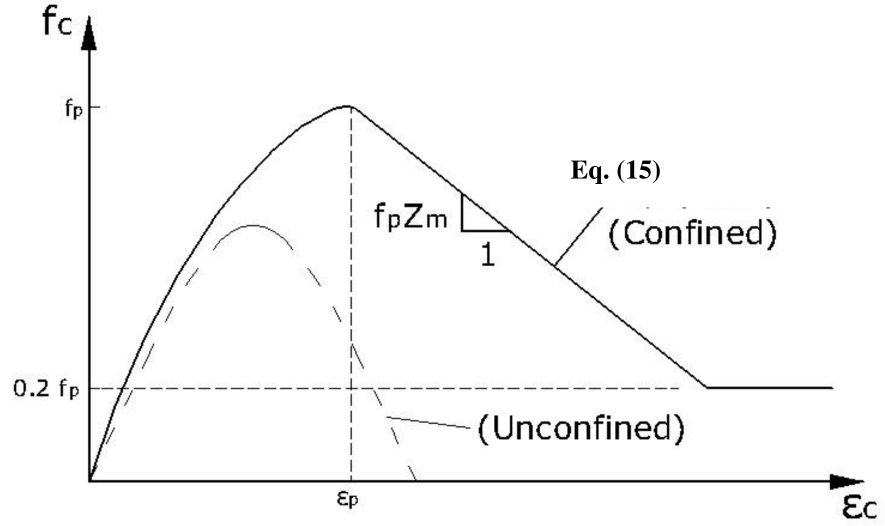

Fig (4): Compressive stress-strain model for confined concrete.

Lateral expansion increases rapidly near the peak stress as shown in Figure (5). At compressive stresses close to failure, the Poisson's ratio can exceed 0.5 (i.e., volume increasing). This behavior is modeled by a fit to the Kupfer et al. (1969) as follows:

$$\nu_{ij} = \begin{cases} \nu_0 & ; \; 0 > \varepsilon_{cj} > \dfrac{\varepsilon_p}{2} \\ \nu_0 \left[1 + 1.5 \left(\dfrac{2\varepsilon_{cj}}{\varepsilon_p} - 1 \right)^2 \right] \le 0.5 \; ; & \dfrac{\varepsilon_p}{2} > \varepsilon_{cj} \end{cases} \tag{16}$$

where υ_o ratio is the initial Poisson's ratio. This relationship implies that only three Poisson's ratios are independent since:

$$\left. \begin{aligned} \nu_{21} &= \nu_{31} \\ \nu_{12} &= \nu_{32} \\ \nu_{13} &= \nu_{23} \end{aligned} \right\} \tag{17}$$

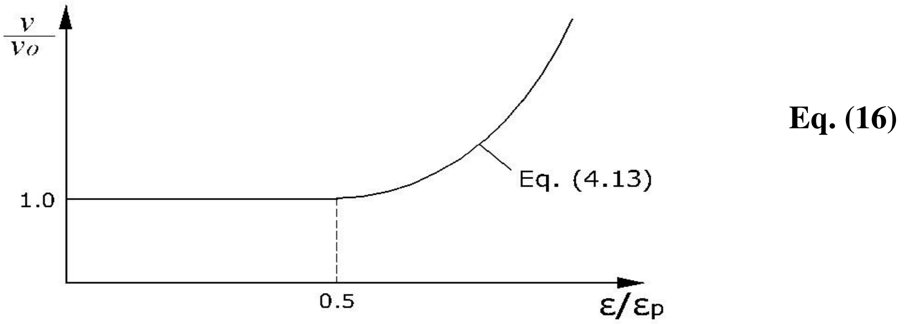

Fig (5): Increase in Poisson's ratio close to peak stress.

For uncracked concrete in tension, the initial Poisson's ratio is used. Upon cracking in the tensile principal direction, expansion normal to this direction is set to zero only. (i.e., $\upsilon_{21} = \upsilon_{31} = 0$, but all other Poisson's ratio are nonzero). If the intermediate principal direction also cracks, υ_{12} and υ_{32} are set equal to zero. All Poisson's ratios are zero if three orthogonal tensile failures occur (i.e., cracked concrete case).

In the current work, concrete cracking is based on the smeared model approach with plasticity model. It is simulated by an elastic-plastic work hardening response (based on Thorenfeldt base curve) followed by a perfectly plastic plateau which is terminated at the onset of crushing.

EXPANSION EFFECT

The Poisson effect of a material determines the lateral displacement of a specimen subjected to a uniaxial tensile or compressive loading. If these displacements are constrained, a passive lateral confinement will act on the specimen. This effect is considered important in a three-dimensional modeling of reinforced concrete structures. This effect is modeled through a pre-strain concept in which the lateral expansion effects are accounted for with an additional external loading on the structure with 2-dimensional nature (Vecchio 1992). Cracked concrete treated using the smeared crack approach is inherently modeled as an orthotropic material. In confined concrete, the adoption of an orthotropic model allows for the consideration of anisotropic behavior close ultimate. The three dimensional orthotropic material stiffness matrix can be written in the principal directions (Weaver and Johnston 1984) as:

$$[D_c]' = \frac{1}{\phi}\begin{bmatrix} E_1(1-\nu_{32}\nu_{23}) & E_1(\nu_{12}+\nu_{13}\nu_{32}) & E_1(\nu_{13}+\nu_{12}\nu_{23}) & 0 & 0 & 0 \\ E_2(\nu_{21}+\nu_{31}\nu_{23}) & E_2(1-\nu_{31}\nu_{13}) & E_2(\nu_{23}+\nu_{21}\nu_{13}) & 0 & 0 & 0 \\ E_3(\nu_{31}+\nu_{21}\nu_{32}) & E_3(\nu_{32}+\nu_{12}\nu_{31}) & E_3(\nu_{23}+\nu_{21}\nu_{13}) & 0 & 0 & 0 \\ 0 & 0 & 0 & \phi G_{12} & 0 & 0 \\ 0 & 0 & 0 & 0 & \phi G_{23} & 0 \\ 0 & 0 & 0 & 0 & 0 & \phi G_{31} \end{bmatrix} \tag{18}$$

where E_i is the modulus of elasticity in the i-direction and the Poisson's ratio v_{ij} is the component of strain in the i-direction due to a stress in the j-direction and

$$\phi = 1-\nu_{32}\nu_{23}-\nu_{21}\nu_{12}-\nu_{31}\nu_{13}-\nu_{21}\nu_{32}\nu_{13}-\nu_{31}\nu_{12}\nu_{23} \tag{19}$$

The three shear moduli are given by:

$$G_{12} = \frac{E_1 E_2}{E_1(1+\nu_{12})+E_2(1+\nu_{21})} \tag{20}$$

$$G_{23} = \frac{E_2 E_3}{E_2(1+\nu_{23})+E_3(1+\nu_{32})} \tag{21}$$

$$G_{13} = \frac{E_1 E_3}{E_1(1+\nu_{13})+E_3(1+\nu_{31})} \tag{22}$$

To maintain symmetry in the stiffness matrix, the following three conditions must be satisfied:

$$E_1\nu_{12} = E_2\nu_{21} \tag{23}$$

$$E_2\nu_{23} = E_3\nu_{32} \tag{24}$$

$$E_1\nu_{13} = E_3\nu_{31} \tag{25}$$

In cracked concrete, most orthotropic material descriptions (i.e., smeared crack models) have assumed that the Poisson's ratio effect is negligible. All of diagonal terms in Eq. (18) become zero since the six Poisson's ratios are neglected, i.e., $v_{ij} = 0$. This assumption is relatively good for many cases, but for the case in which the tensile strains in cracked concrete are relatively small, the lateral expansion of concrete arising from Poisson's ratio effect can be predicted in this situation. Also, in triaxial compressive stress conditions the Poisson's ratio effect cannot be neglected.

This concept is also applied to the nonlinear material model implemented in **DIANA** software. Provisions were included to model pre-strains arising from strain offset effects such as pre-stressing of reinforcement, shrinkage or expansion of concrete and thermal expansion of either concrete or reinforcement. For concrete, a pre-strain vector is $\left\{\varepsilon_c^{\,o}\right\}$ defined relative to the global x, y, and z system as:

$$\left\{\varepsilon_c^{\,o}\right\}=\left\{\varepsilon_{cx}^{\,o}\ \ \varepsilon_{cy}^{\,o}\ \ \varepsilon_{cz}^{\,o}\ \ \gamma_{cx}^{\,o}\ \ \gamma_{cy}^{\,o}\ \ \gamma_{cz}^{\,o}\right\}^T \tag{26}$$

accounting for all nonstress related straining. A similar vector developed for the reinforcement pre-strains. An equivalent force approach was then used to incorporate the pre-strain effects. From the known pre-strains, free nodal displacements $\{r_c\}$ and $\{r_s\}$ were calculated for the concrete and steel, respectively:

$$\{r_c\}=\int\left\{\varepsilon_c^{\,o}\right\}\,dV \tag{27}$$

$$\{r_s\}=\int\left\{\varepsilon_c^{\,o}\right\}\,dV \tag{28}$$

The equivalent nodal loads due to the pre-strains, $\left\{F^*\right\}$ can be calculated as:

$$\left\{F^*\right\}=[k_c]\{r_c\}+\sum_{i=1}^{n}[k_s]_i\ \{r_s\}_i \tag{29}$$

where $[k_c]$ and $[k_s]_i$ are the element stiffness matrices evaluated separately for the concrete and each reinforcement component. These equivalent nodal forces due to the pre-strains are then added to the externally applied nodal forces to determine the total nodal forces. The total nodal load vector is updated on each iteration since the equivalent nodal forces depend on the component stiffness. This algorithm will be modified here to include the expansion effect due to Poisson's ratio effect. The expansion strains in the principal directions are written as:

$$\left\{\varepsilon_{cp}^{\,o}\right\}=\left\{\varepsilon_{c1}^{\,o}\ \varepsilon_{c2}^{\,o}\ \varepsilon_{c3}^{\,o}\right\}^T \tag{30}$$

where

$$\varepsilon_{c1}^{\,o}=-\nu_{12}\,\frac{f_{c2}}{E_{c2}}-\frac{\nu_{13}\ f_{c3}}{E_{c3}} \tag{31}$$

$$\varepsilon_{c2}^{\,o}=-\nu_{21}\,\frac{f_{c1}}{E_{c1}}-\frac{\nu_{23}\ f_{c3}}{E_{c3}} \tag{32}$$

$$\varepsilon_{c3}^{\,o}=-\nu_{31}\,\frac{f_{c1}}{E_{c1}}-\frac{\nu_{32}\ f_{c2}}{E_{c2}} \tag{33}$$

The expansion strains are then transformed to the global x, y, and z axes according to:

$$\left\{\varepsilon_c^{\,o}\right\}=[T]\left\{\varepsilon_{cp}^{\,o}\right\} \tag{34}$$

where [T] is the transformation matrix that defines the orientation of the principal axes. Equivalent nodal loads are calculated as outlined in Eq. (29) to include all straining arising from expansion in the right hand side of Eq. (35).

$$[K]\{r\}=\{F\} \tag{35}$$

All of the expansion strains are modeled through the pre-strain concept so the material stiffness matrix then includes diagonal terms only.

$$[D_c]' = \begin{bmatrix} E_{c1} & 0 & 0 & 0 & 0 & 0 \\ 0 & E_{c2} & 0 & 0 & 0 & 0 \\ 0 & 0 & E_{c3} & 0 & 0 & 0 \\ 0 & 0 & 0 & G_{c12} & 0 & 0 \\ 0 & 0 & 0 & 0 & G_{c23} & 0 \\ 0 & 0 & 0 & 0 & 0 & G_{c13} \end{bmatrix} \tag{36}$$

where E_{c1}, E_{c2} and E_{c3} are the tangent modulus.

$$E_{c1} = \frac{f_{c1}}{\varepsilon_1} \tag{37}$$

$$E_{c2} = \frac{f_{c2}}{\varepsilon_2} \tag{38}$$

$$E_{c3} = \frac{f_{c3}}{\varepsilon_3} \tag{39}$$

and the shear modulus are given by:

$$G_{c12} = \frac{E_{c1}\ E_{c2}}{E_{c1} + E_{c2}} \tag{40}$$

$$G_{c23} = \frac{E_{c2}\ E_{c3}}{E_{c2} + E_{c3}} \tag{41}$$

$$G_{c13} = \frac{E_{c1}\ E_{c3}}{E_{c1} + E_{c3}} \tag{42}$$

The principal strains used in Eqs. (37 – 39) are that part of strains occurred due to direct stress. That is, any nonstress-related strains are first subtracted from the total strains before calculating the principal values. The pre-strains approach is valid for both uncracked and cracked concrete. An iterative procedure is required for finite element analysis based on this approach.

CRACKED CONCRETE MODEL

Cracked reinforced concrete is treated as an orthotropic nonlinear material based on a smeared rotating crack model. In cracked concrete, large strains perpendicular to the principal compressive direction reduce the concrete compressive strength. Thus, the compressive stress f_{c3} is a function of εc1 in addition to ε_{c3}. The compression softening factor, λ, is given by:

$$\lambda = \frac{1}{0.85 - 0.27\left(\dfrac{\varepsilon_{c1}}{\varepsilon_{c3}}\right)} \quad \leq \quad 1.0 \tag{43}$$

where ε_{c1} is the tensile principal strain.

The above compression softening relationship was derived by (Vecchio and Collins 1982) from tests on reinforced concrete panels of normal strength concrete. Also, high strength concrete is thought to exhibit a more pronounced compression softening effect due to smoother fracture planes. The compression softening factor was updated (Vecchio and Collins 1993) based on statistical evaluations of data, the strength and strain softening model shown in Figure (6) is referred as Model A and takes the form:

$$\lambda = \frac{1}{1 + K_s \cdot K_f} \quad \leq \quad 1.0 \tag{44}$$

where

$$K_s = 0.35\left(\frac{-\varepsilon_{c1}}{\varepsilon_{c3}} - 0.28\right)^{0.8} \quad \geq 1.0 \tag{45}$$

$$K_f = 0.1825\sqrt{f_c'} \tag{46}$$

and f_c' is expressed in MPa. The K_s factor accounts for the effect of the transverse straining and K_f represents the influence of the concrete cylinder strength. The peak stress and strain of the base curve are modified to account for the effect.

$$f_p = \lambda \,.\, f_c' \tag{47}$$

$$\varepsilon_p = \lambda \,.\, \varepsilon_o \tag{48}$$

After that, only slightly weaker correlation was obtained by using a strength only softening model as a function of $\varepsilon_{c1.}$ The optimal form attained, referred to as model B (Vecchio and Collins 1993) which is adopted in this research and illustrated in Figures (7) and (8), is:

$$\lambda = \frac{1}{1 + K_c} \quad \leq 1.0 \tag{49}$$

where

$$K_c = 0.27\left(\frac{\varepsilon_{c1}}{\varepsilon_0} - 0.37\right) \tag{50}$$

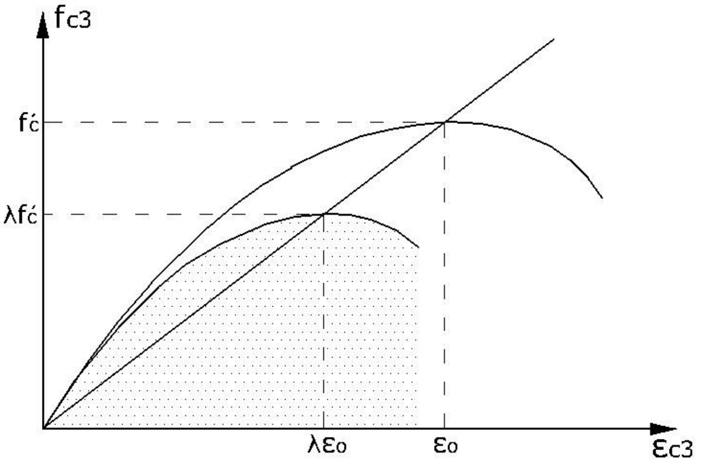

Fig (6): Model A for compression softening (Vecchio and Collins 1993).

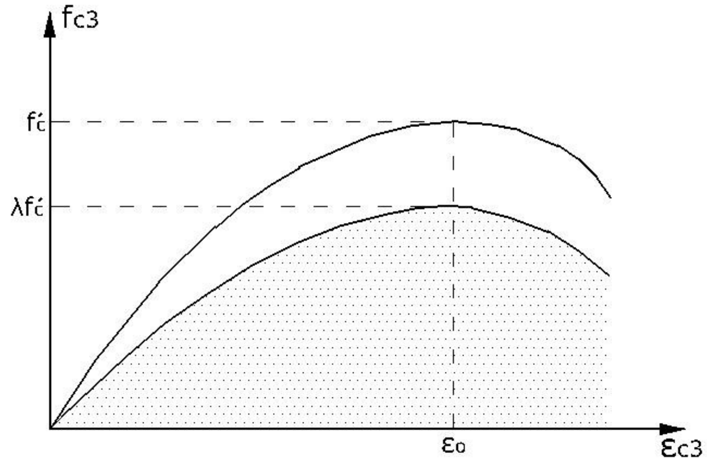

Fig (7): Model B for compression softening (Vecchio and Collins 1993).

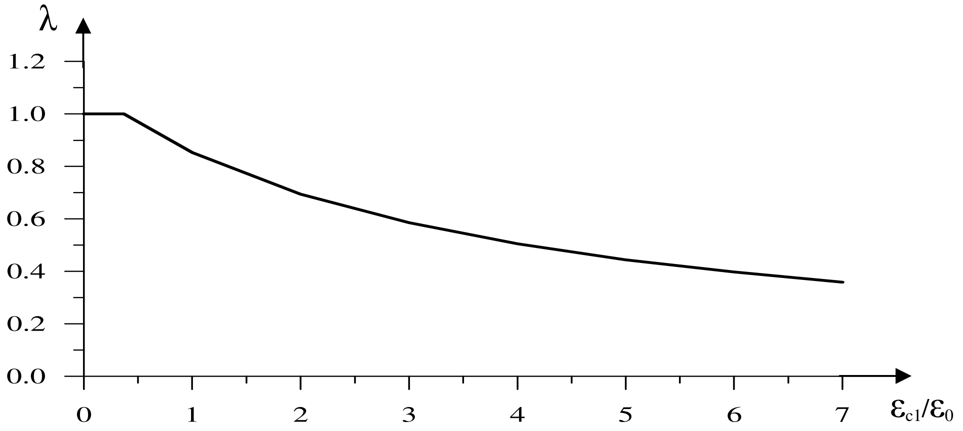

Fig (8): Model B for compression softening due to lateral cracking , Eq. (49) (Vecchio and Collins 1993).

In tension, a strain softening model is used by adopting the behavior which is based on a bilinear stress-strain relationship (Hillerborg et al. 1976) and as shown in Figure (9).

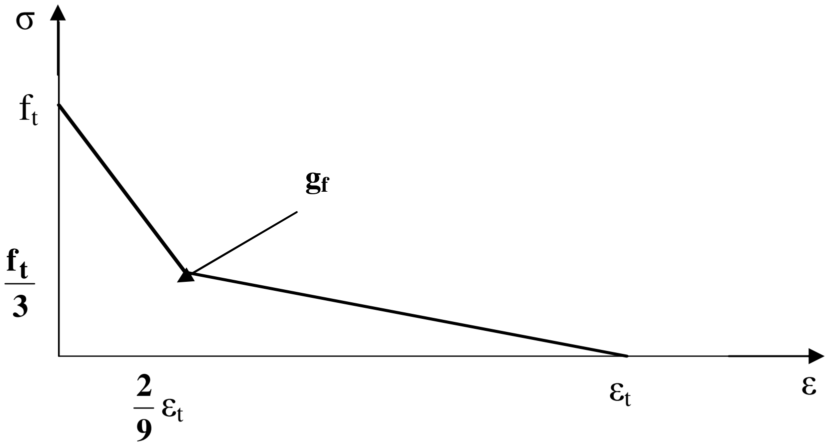

Fig (9): Hillerborg et al strain softening model (Hillerborg et al. 1976)

The shear stiffness at a cracked sampling point becomes progressively smaller as the crack widens. So the shear modulus is reduced to *β G.* Before cracking, the factor *β* is set equal to 1.0. When the crack is sufficiently opened, a constant value is assigned to *β,* to account for the dowel action as shown in Figure (10). The following relations are used to account for the shear retention effect (Al-Shaarbaf 1990).

$$\beta = 1.0 \quad \text{for } \varepsilon_n \le \varepsilon_{cr}$$

$$\beta = \frac{(\gamma_2 - \gamma_3)}{(\gamma_1 - 1.0)} \cdot \left(\gamma_1 - \frac{\varepsilon_n}{\varepsilon_{cr}} \right) + \gamma_3 \quad \text{for } \varepsilon_{cr} \le \varepsilon_n \le \gamma_1\, \varepsilon_{cr} \qquad (51)$$

$$\beta = \gamma_3 \quad \text{for } \varepsilon_n > \gamma_1\, \varepsilon_{cr}$$

where $\gamma 1$, γ_2 and γ_3 are the shear retention parameters. γ_1 represents the rate of decay of shear stiffness as the crack widens, γ_2 represents the sudden loss in the shear stiffness at the onest of cracking, and γ_3 represents the residual shear stiffness due to the dowel action.

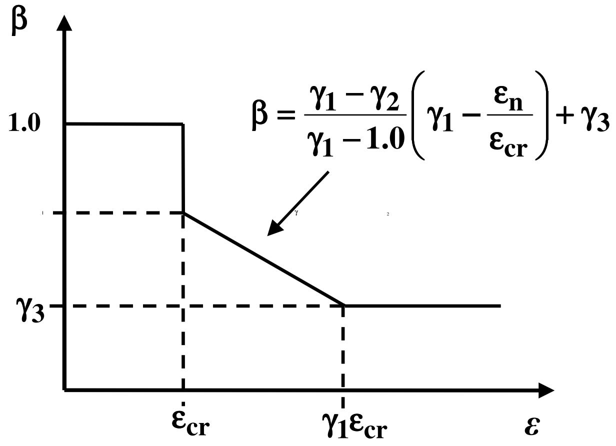

Fig (10): Shear retention model for concrete (Al-Shaarbaf 1990).

MODELING OF REINFORCEMENT

Modeling of reinforcing steel in connection with the finite element analysis of reinforced concrete members is much simpler than the modeling of concrete. The steel bars are long and relatively slender, and therefore, they can be assumed to transmit axial force only. In the current work, the embedded reinforcement model with an elastic-linear work hardening model is adopted to simulate the uniaxial stress-strain behavior of reinforcing steel bars, Figure (11).

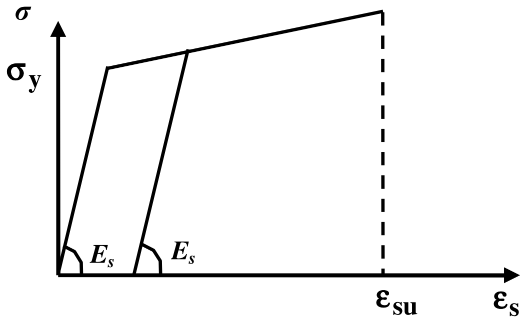

Fig (11): Stress-strain relationship of reinforcing steel bars (Al-Shaarbaf 1990).

FORMULATION OF FINITE ELEMENT ANALYSIS

In the present study, the computer software, **DIANA V9.0** (Witte and Kikstra, 2002), has been adopted to carry out the numerical analysis. The main objective of the study is to analyze some experimental cases to verify the use of both the confining and expansion models and as follows:

A - CONCRETE IDEALIZATION

The 20-node hexahedral brick element is used in the current study to model the concrete. Each node of this element has three translation degrees of freedom u, v and w in the x, y and z directions respectively as shown in Figure (12) (Al-Shaarbaf 1990). The element employs the standard shape functions to define the displacement field (Dawe 1984). The displacements of the brick element are given by:

$$\begin{aligned} u(\xi,\eta,\zeta) &= \sum_{i=1}^{20} Ni(\xi,\eta,\zeta).u_i \\ v(\xi,\eta,\zeta) &= \sum_{i=1}^{20} Ni(\xi,\eta,\zeta).v_i \\ w(\xi,\eta,\zeta) &= \sum_{i=1}^{20} Ni(\xi,\eta,\zeta).w_i \end{aligned} \tag{52}$$

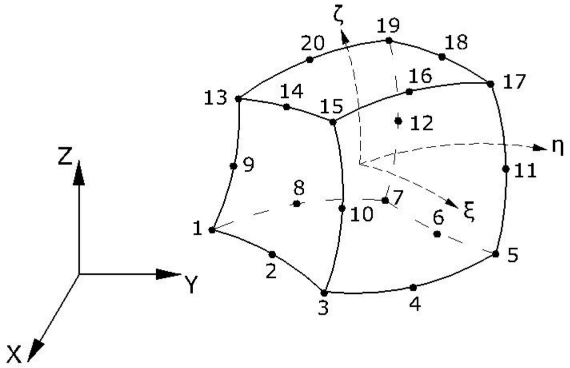

Fig (12): 20-Nodded isoparametric brick element

B - REINFORCING BAR IDEALIZATION

The reinforcing bars are idealized as axial members embedded within the brick elements (Zeinkiwecz 1977). Reinforcing bars are assumed to be capable of transmitting axial force only. The stiffness matrix of steel bars is added to that of the concrete to obtain the global stiffness matrix of the brick element. The shape functions of the brick element can be used to represent the displacements of the embedded bar (Al-Shaarbaf 1990). For example,

$$\begin{aligned} u &= \sum_{i=1}^{20} Ni(\xi).u_i \\ v &= \sum_{i=1}^{20} Ni(\xi).v_i \\ w &= \sum_{i=1}^{20} Ni(\xi).w_i \end{aligned} \tag{53}$$

where a bar is considered lying parallel to the local coordinate axis ξ with $\eta = \eta_c$ and $\zeta = \zeta_c$ (constant), Figure (13).

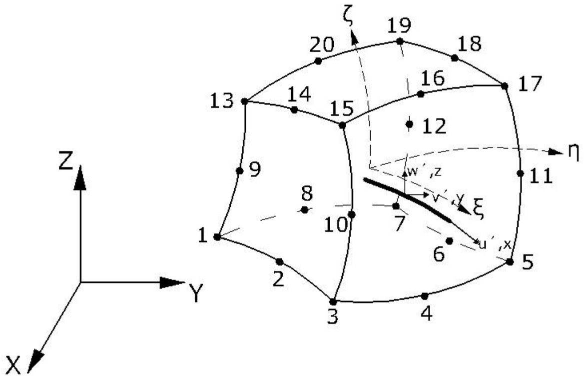

Fig (13): Representation of embedded reinforcement.

C- General Nonlinear Solution Procedure

The incremental-iterative method is the most common technique used for solving nonlinear structural equations. Loading on the studied specimens is induced by means of a prescribed displacement at the point load. The numerical integration has been conducted by using the 27 points Gaussian rule (3x3x3).

VERIFICATION WITH EXPERIMENTAL RESULTS

A – Confined Concrete Model

The data collected by Kupfer, Hilsdorf and Rusch (Kupfer et. al 1969) from a series of plain concrete specimens tested under different combinations of in plane biaxial loading were selected to establish the ability of proposed model for confined concrete under multiaxial compressive stresses. The 200 mm square and 50 mm thick specimens subjected to biaxial compression were selected. The plain concrete had cylinder strength of 18.7 MPa. Further concrete properties are shown in Table (1). Analysis was carried out using **DIANA** for lateral confining stress equal to zero (i.e., uniaxial compression), $\sigma_3 / 2$ and σ_3 (i.e., equal biaxial compression). The ratio of lateral to axial stress, σ_2 / σ_3 was held constant throughout the test. The out of plane stress σ_1 was zero in all three tests. Also another analysis was made but without including the effect of confinement. For biaxial compression, the volumetric strain (i.e., $\Delta V/V = .\varepsilon_1 + \varepsilon_2 + \varepsilon_3$) for various stress ratios (f_{c3}/f_c) are shown in Figure (14). The response, including the peak stress and strain at peak stress, was well duplicated in all cases. Also, the expansion was realistically reflected even near ultimate. It was noted that confined concrete model was capable of adequately obtaining the strength and deformation response under multiaxial stresses of the plain concrete.

B – Expansion Model

Two of Vecchio – Collins shear panels (Vecchio 1982) were selected to show the improvement in modeling that can realize when the Poisson's ratio effect is included in the cracked concrete theory. The normal strength panels, PV23 and PV25, were 890mm square by 70mm thick and symmetrically reinforced with two layers of wire mesh of 50mm grid. A clear cover of 6 mm was provided. They were equally reinforced in the longitudinal and transverse directions ($\rho_x = \rho_y = 1.875\%$, see Table (1)) and were loaded in shear and equal biaxial compression. No reinforcement yielded in either specimen before failure by crushing of the concrete. The improvement is evident in Figures (15) and (16) which shows the results of analyses using **DIANA** with and without the expansion model. It was noted that the effect of expansion on the load deformation response is to increase the strength and to increase the stiffness near ultimate. Little influence is apparent at low and intermediate stress levels.

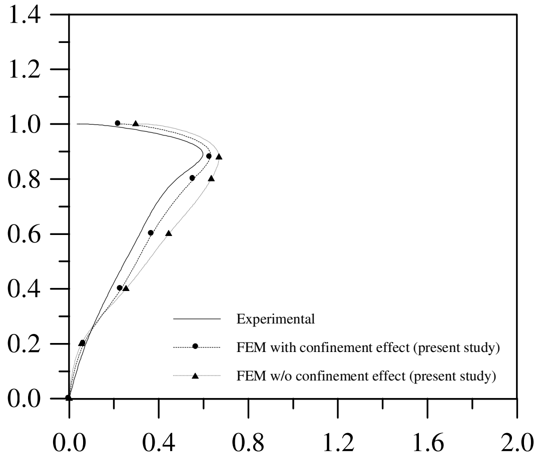

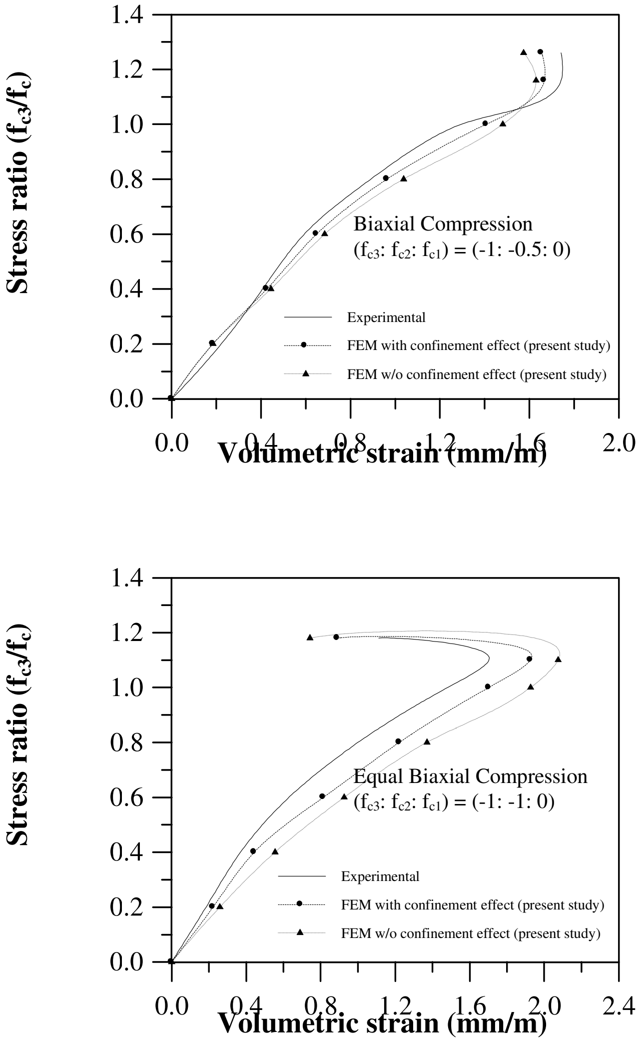

Fig (14): Volumetric response of the Kupfer et al. analysis

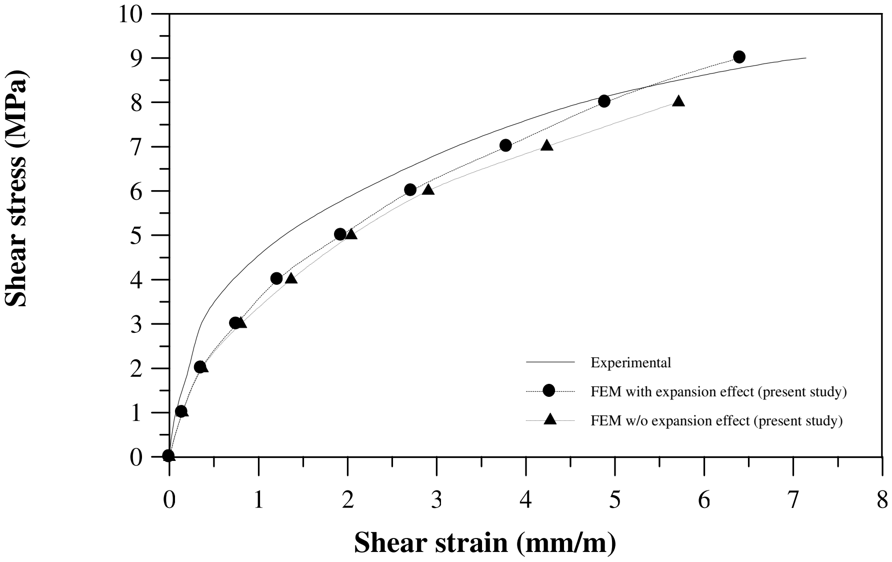

Fig (15): Influence of expansion Effect for Panel (PV23) (Vecchio 1982).

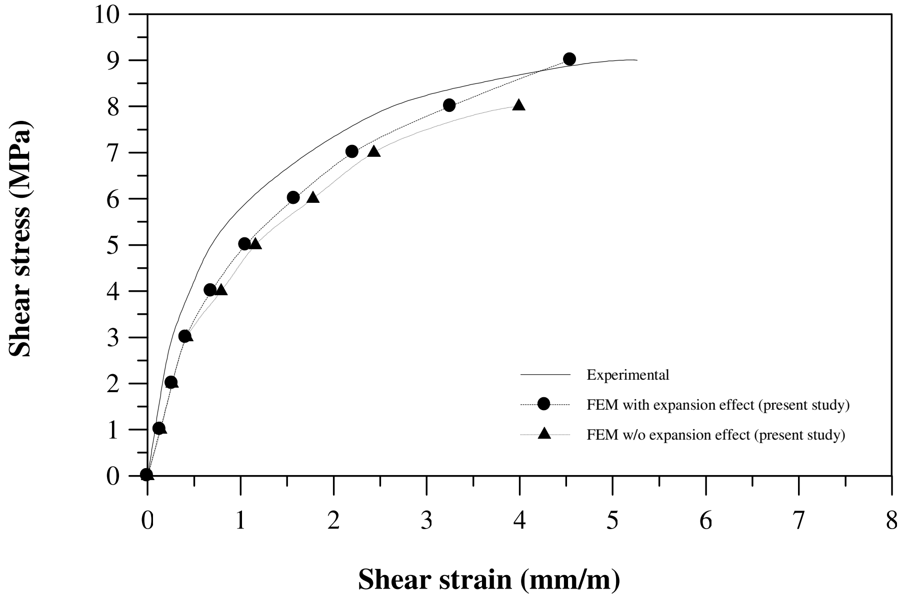

Fig (16): Influence of expansion Effect for Panel (PV25) (Vecchio 1982).

Table (1): Specimens properties

Specimen	f'_c ,MPa	f_t,MPa	ε_o	v_o	ρ_x , %	f_{yx},MPa	ρ_y , %	f_{yy},MPa
Kupfer et al.	18.7	1.46	0.002	0.15	-	-	-	-
PV23	20.5	1.5	0.002	0.3	1.785	518	1.785	518
PV25	19.2	1.45	0.002	0.3	1.785	466	1.785	466

CONCLUSIONS

Based on the analytical work, the following conclusions are made:

1- The proposed confined concrete model proved capable of providing good estimates of strength and deformations for concrete elements subjected to multiaxial compressive stresses. Applications of the model to finite element analyses were successful when behavior was sought on a “macroscopic” level.

2- The consideration of the Poisson’s ratio effect can have a significant effect and has improved the accuracy near ultimate strength.

3- The consideration of the Poisson’s ratio effect can have a significant effect when the tensile principal strain is relatively small.

4- The pre-strain approach handled the asymmetry of the material stiffness matrix in a numerical stable manner when including the effect of Expansion due to Poisson’s ratio.

5- Both confinement and expansion effect can model the response of concrete members subjected to different load conditions.

REFERENCES

Al-Shaarbaf, I..(1990). "*A Non-Linear Three-Dimensional Finite Element Analysis.*" Ph.D. Thesis, University of Bradford.

Chen, W.F. (1982). "*Plasticity in Reinforced Concrete.*" McGraw-Hill, New York, USA.

Collins, M.P. , and Porsaz, A. (1989). "*Shear Strength for High Strength Concrete* ", Bull. No. 193 "*Design Aspects of High Strength Concrete.*" Committee Euro-International du Beton (CEB), pp. 75-83.

Dawe, D.J. (1984)."*Matrix and Finite Element Displacement Analysis of Structures.*" Clarendon Press, Oxford.

Hillerborg, A., Mondeer, M., and Petersson, P.E. (1976)." *Analysis of Crack Formation and Growth in Concrete by Means of Fracture Mechanics and Finite Elements.*" Cement and Concrete Research, V. 6, No. 6, 1976, pp. 773-782.

Hsieh, S.S., Ting, E.C., and Chen, W.F. (1979)." An Elastic *Fracture Model of Concrete.*" Proc. 3rd Engineering Division Spec. Conference , ASCE, Austin , Texas, pp. 137-440.

Kupfer, H. , Hilsdorf, K.H,. and Rusch, H.(1969). "*Behavior of Concrete Under Biaxial Stresses.*" Journal of the American Concrete Institute, V. 66, No. 8, pp. 656-666.

Scott, B.D., Park, R. and Priestley, M.J.N. (1982). "*Stress-Strain Behavior of Concrete Confined by Overlapping Hoops at Low and High Strain Rates.*" Journal of the American Concrete Institute, V. 79, No. 1, pp. 13-27.

Thorenfeldt, E. , Tomaszewicz, A. , and Jensen, J.J. (1987)." *Mechanical Properties of High Strength Concrete and Application in Design.*" Proc. Symposium Utilization of High Strength Concrete. Stavanger, Norway, Tapir Trondheim.

Vecchio, F.J., and Collins, M.P. (1982). " *The Response of Reinforced Concrete to in-Plane Shear and Normal Stresses.*" Publication No. 82-03, Dept. of Civil Engineering, University of Toronto, Canada.

Vecchio, F. J. (1992). "*Finite Element Modeling of Concrete Expansion and Confinement.*" Journal of Structural Division, ASCE, Vol. 118, No.9-10, pp. 2390-2406.

Vecchio, F.J., and Collins, M.P. (1993). " *Compressive Response of Cracked Concrete.*" Journal of Structural Engineering , ASCE , V. 119, No.12 , 1993, pp. 3590-3610.

Weaver, W., J., and Johnston, P. R. (1984). "*Finite Elements for Structural Analysis.*" Prentic-Hall, Englwood Cliffs, N. J.

Witte, F.C. D., and Kikstra, W.P. (2002). "**DIANA** *Finite Element Analysis – User's Manual, Release 9.0.*" TNO Building and Construction Research, The Netherlands.

Zeinkiweicz, O.C. (1977). "*The Finite Element Method.*" Third Edition, McGraw-Hill, London, 1977.

NOTATIONS

$[D_c]'$	Concrete material stiffness matrix in principal direction
E_c	Modulus of elasticity of concrete (initial tangent modulus)
E_{c1}	Concrete tangent modulus in tensile principal strain direction
E_{c2}	Concrete tangent modulus in intermediate principal strain direction
E_{c3}	Concrete tangent modulus in compressive principal strain direction
E_s	Modulus of elasticity of reinforcing bars
f_c	Compressive principal stress in concrete
f_c'	Compressive strength of concrete cylinder
f_{c1}	Tensile principal stress in concrete
f_{c2}	Intermediate principal stress in concrete
f_{c3}	Compressive principal stress in concrete
f_{c3f}	Required f_{c3} to cause failure in presence of on f_{c1} and f_{c2}
f_p	Peak stress
f_t	Modulus of rupture
$\{F\}$	Structure nodal force matrix
$\{F^*\}$	Equivalent nodal loads due to prestrain
G	Shear modulus
G_{12}	Tangent shear modulus of concrete relative to 1,2 axes
G_{23}	Tangent shear modulus of concrete relative to 2,3 axes
G_{13}	Tangent shear modulus of concrete relative to 1,3 axes
g_f	Area under tensile stress-crack strain curve
I_2	Second invariant of stress vector
J_2	Second invariant of deviatoric stress tensor
K_c	Coefficient reflecting influence of transverse tensile straining (Model B)
K_f	Coefficient reflecting influence of nominal strength of concrete
K_s	Coefficient reflecting influence of transverse tensile straining (Model A)
K_σ	Peak stress factor
K_ε	Strain at peak stress factor
$[K]$	Structure stiffness matrix
$[k_c]$	Element stiffness matrix evaluated for concrete component
$[ks]_i$	Element stiffness matrix evaluated for i-direction reinforcement
n	Curve fitting factor
$\{r\}$	Structure nodal displacement matrix
$\{r_c\}$	Free nodal displacement due to concrete prestrain
$\{r_s\}$	Free nodal displacement due to steel prestrain
u,v,w	Displacement coordinates in x,y and z Cartesian coordinates
x,y,z	Cartesian coordinates
$[T]$	Transformation matrix
Z_m	Slope factor for post-peak compressive curve
β	Shear retension factor
$\gamma_1, \gamma_2, \gamma_3$	Shear retension parameters
$\Delta V/V$	Volumetric strain = $.\varepsilon_1+\varepsilon_2+\varepsilon_3$
ε_c	Compressive principal strain in concrete
ε_{cr}	Cracking strain
ε_{c1}	Largest principal tensile strain in concrete
ε_{c2}	Intermediate principal strain in concrete
ε_{c3}	Compressive principal strain in concrete
ε_{c1}^{o}	Concrete expansion strain in 1-direction

ε_{c2}^{o}	Concrete expansion strain in 2-direction
ε_{c3}^{o}	Concrete expansion strain in 3-direction
$\{\varepsilon_{c}^{o}\}$	Concrete pre-strain relative to global axis
$\{\varepsilon_{cp}^{o}\}$	Expansion strain in principal direction
ε_o	Strain in concrete cylinder at peak stress f_c' (a negative value)
ε_p	Strain at peak stress (a negative value)
ε_s	Strain in steel reinforcement
ε_{su}	Ultimate strain for steel reinforcement
$\{\varepsilon_{s}^{o}\}$	Smeared reinforcement pre-strain relative to global axis
ε_t	Tensile fracture strain
ε_1	Tensile principal strain
ε_2	Intermediate principal strain
ε_3	Compressive principal strain
λ	Concrete compression softening factor
ν	Poisson's ratio of linear isotropic material
σy	Yield stress of reinforcing bars
ν_{ij}	Component of strain in i-direction due to a stress in the j-direction
ν_o	Initial Poisson's ratio
γ_{xy}	Shear strain relative to x,y axes
γ_{yz}	Shear strain relative to y,z axes
γ_{zx}	Shear strain relative to z,x axes

Number 2 Volume 13 June 2007 Journal of Engineering

ANALYTICAL AND NUMERICAL STRESS ANALYSIS OF THICK CYLINDER SUBJECTED TO INTERNAL PRESSURE

Assist. Prof. Dr. Adnan N. Jamel
University of Baghdad / College of Eng.
Mechanical Eng. Dept.

Assist. Lecturer: Oday. I. Abdullah
University of Baghdad / College of Eng.
Nuclear Eng. Dept.

ABSTRACT

The present work is an attempt to investigate the vibrations characteristics and effect of static stresses and deformation in partially pressurized thick cylindrical shells, such as the gun barrels. The method used cover analytical investigation developed to determine static stresses and deformation along the thick cylindrical shell using LAME'S equation. The numerical investigation is developed using the finite element method with axisymmetric element (Plane 42) four nodes to determine the static response and solid element (Solid 45) eight nodes for vibration analysis by using the ANSYS package. The obtained results show a good agreement with the other investigators. It's found that the natural frequency of the selected models almost equal (150. Hz) and these results indicate that the frequency of powder gasses pressure more than (150 Hz) to be far away from resonance phenomena.

الخلاصة

أن العمل الحالي هو محاولة لمعرفة الخصائص الاهتزازية و تأثير الاجهادات و التشوهات الاستاتيكية في الاسطوانات سميكة الجدران كما هو الحال في سبطانة المدفع. وتشمل الطرق المستخدمة, التقنيات التحليلية و العددية, طور الحل التحليلي لإيجاد الاجهادات و التشوهات الاستاتيكية على طول النماذج المستخدمة باستعمال معادلة لامي (LAME'S EQUATION), تم انجاز الحل العددي باستخدام طريقة العناصر المحددة و اختيار العنصر المسطح (Plane 42) ذو الأربع عقدة لإيجاد الاستجابة الاستاتيكية, و العنصر الصلب (Solid 45) ذو ثمانية عقد لحساب الاهتزازات الحرة و باستخدام برنامج حاسبة (ANSYS). بينت النتائج التي تم الحصول عليها تطابقا جيدا مع نتائج الباحثين الآخرين. لقد وجد بأن التردد الطبيعي للنماذج المستخدمة (150 Hz) تقريبا وتبين هذه النتيجة بان تردد ضغط الغازات يجب أن يكون اكبر من (150 Hz) لتكون بعيدة عن ظاهرة الرنين.

KEY WORDS
Thick Cylinder, Barrels, FEM, Static Stresses, ANSYS Package, Vibration.

INTRODUCTION

The gun barrel loaded by the pressure of powder gasses has a dynamic characteristics deformations and stresses which do not depend on the value of the pressure of powder gasses only but also on the velocity of loading. This means that they depend on the jumps of pressure from the loaded points to unloaded points and on the barrel wall stiffness. The solution of barrel strength as a dynamic problem is a very complex problem and can be solved by a new progressive mathematical solution like finite element computations.

The static and dynamic behavior of the gun barrel are obtained by considering the barrel as a perfectly asymmetrical, and for the actual problem, the following assumptions are taken into consideration **(Mahmood, 1995).**

1. The barrels are two types.
a- Thin-walled pressure vessels.
b- Thick-walled pressure vessels.
2. Material of barrel wall is homogenous and isotropic.
3. Barrel is loaded by uniformly distributed pressure which is the pressure of powder gasses affecting the barrel as continuously uniformly distributed pressure on the whole barrel length.

There is a great amount of work has been down towards the investigation of the circular cylindrical shells under static load. The static stresses and deformation for a thick hollow cylinder under the affect of partially pressure are studied and reported in **(Mahmood, et al, 1990)**. The study of the static stresses and deformations a long the inner surface of (152 mm) gun-barrel are reported in **(Mahmood, 1995)** in which the effect of variation of powder gas pressure and driving band pressure a long the axial length of gun barrel were considered. The free vibration of the thick circular cylindrical shells and rings are discussed in **(Singal and Williams, 1992)**. The well knows energy method which is bases on the three-dimensional theory of elasticity was used in the derivation of the frequency equation of the shell. This yields resonant frequencies for all the circumferential modes of vibration including the breathing and beam-type modes. A semi analytical finite element was employed in **(Ganesan and Sivadas, 1994)** for the investigation of vibration behavior of cantilever homogeneous isotropic circular cylindrical shells with variable thickness, the thickness varies in the axial direction; the mass of the shell is made constant for particular length to radius ratio.

The dynamic behavior of steel cylindrical shell panels subjected to air-blast loading has been investigated in **(Redekop, 1990),** a combined theoretical and numerical solutions where obtained, results where computed for cases of rectangular and square panels having hinged and immovable boundary condition, a comparison of the study was presented for several panel rise cases, and conclusions are drowning. The work done in **(Weingarten and Fisher, 1982)** concerned the transient response of a homogeneous, hollow, conical frustum loaded by an ax symmetric time dependent lateral pressure, mode shapes and eigenvalues calculated in the free vibration analysis were used in a modal solution for the transfer displacement, stress resultant, stress couple, resultant and meridian stress of the forced vibration problem. Numerical results were presented for fully clamped frustum subjected to an instantaneous impulsive loading. A solution was presented in **(Wiliam, 1972)** for a semi-infinity cylinder shell subject to dynamic loading at one and using the method characteristics, explicit results were obtained for the propagation of discontinuities, these results were combined with a simple numerical reduce to obtain the solution in all region.

ANALYTICAL SOLUTION:

The problem of determining the tangential stress (σ_t) and the radial stress (σ_r) at any point of a thick walled cylinder in terms of the applied pressures and the dimensions was solved by the French electrician Gabriel Lame in (1833). The cylinder shown in **Fig. 1** has radii (a) and (b) subjected to both a uniformly distributed internal pressure of (P_i) and an external pressure of (P_o).

Select a thin shell of radius (r), the thickness (dr) and the length unity. The tangential stress in this shell is (σ_t), the radial stress on the inner surface is (σ_r) and that on the outer surface is $(\sigma_r + d\sigma_r)$, where $(d\sigma_r)$ is the increment in (σ_r) due to the variation of pressure across the cylinder wall. The radial stresses are assumed (in correctly) to be tensile, so a negative result for (σ_r) will denote compression. This shell may be treated as a thin cylinder, hence, for equilibrium, a vertical summation of forces must equal zero **(Nasman, 2005)**, **Fig. 2** shows a half-section of a typical shell:

$$(\sigma_r + d\sigma_r).2(r + dr) - \sigma_r\ (2r) - 2\sigma_t\, dr = 0 \tag{1}$$

The final equation obtained from solving Eq. (1) give the following general expression for (σ_r) and (σ_t) at any point **(Nasman, 2005):**

$$\sigma_r = \frac{a^2 P_i - b^2 P_o}{b^2 - a^2} - \frac{a^2 b^2 (P_i - P_o)}{(b^2 - a^2) r^2},\ \sigma_t = \frac{a^2 P_i - b^2 P_o}{b^2 - a^2} + \frac{a^2 b^2 (P_i - P_o)}{(b^2 - a^2) r^2} \tag{2}$$

Under the effect of internal pressure, the deformation of the cylinder walls takes place that results in stresses in the cylinder metal **(Nasman, 2005)**. Every wall element limited by adjacent radial and concentric circular sections is subjected to circular and axial extension and to radial compression as shown in the **Fig. 3**.

The wall deformation at r=a:

$$\Delta r_i = \frac{a}{E}\left(P.\frac{b^2 + a^2}{b^2 - a^2} + \upsilon \right) \tag{3}$$

Similarly at r=b;

$$\Delta r_o = \frac{b}{E}\left(P\frac{2a^2}{b^2 - a^2} \right) \tag{4}$$

THE FINITE ELEMENT SOLUTION:

The finite element method can be applied for any kind of problem including the investigated problem because it is a powerful method and it's almost easy to be implemented by the computer, therefore many packages may be found which deal with this kind of problem. One of these packages is the ANSYS which is a powerful package and can deal with the static and dynamic problems with a merely simple input data in files stored in files and from these data the results are obtained.

For the static analysis the element Plane 42 is used. This element used for 2-D modeling of solid structures. The element can be used either as a plane element (plane stress or plane strain) or as an axisymmetric element. The element is defined by four nodes having two degrees of freedom at each node: translations in the nodal X and Y directions as shown in **Fig. (4)**.

But for the free vibration analysis the Solid 45 element is used. This element used for the three-dimensional modeling of solid structures. The element is defined by eight nodes having three degrees of freedom at each node: translations in the X, Y and Z directions as shown in **Fig. (5)**.

Static Analysis

The system equations formed for static analysis include the system stiffness matrix and the system load vector. The equations may be written in matrix relations as follows **(Batha, 1976):**

$$[K]\{U\} = \{F\} \tag{5}$$

Eq. (5) solved by Gauss iteration method.

Normal Modes Analysis

The system equation for normal mode analysis includes the system stiffness and mass matrices may be written in matrix notation as follows **(Batha, 1976):**

$$[M]\{\ddot{U}\}+[K]\{U\}=0 \tag{6}$$

$$U_i=\Phi_i\sin(\omega_i t+\theta_i) \qquad i=1,2........DOF \tag{7}$$

In this harmonic expression, Φ_i is a vector of nodal amplitudes (mode shape) for the ith mode of vibration. The symbol ω_i represents the angular frequency of mode i, and θ_i denotes the phase angle. By differentiating **Eq. (7)** twice with respect to time:

$$\ddot{U}_i=-\omega_i^2\Phi_i\sin(\omega_i t+\theta_i) \tag{8}$$

Substitution of **Eq. (8)** and **Eq. (7)** into **Eq. (6)** allows cancellation of the term sin (ωi t+θi), which leaves,

$$([K]-\omega_i^2[M])\Phi_i=0 \tag{9}$$

Eq. (9) has the form of the algebraic eigenvalue problem. **Eq. (9)** can be solved by subspace iteration method.

Verification Test for Static Analysis:

The following example is given to show applicability of the used program ANSYS to solve the cylindrical shells subjected to pressure loading,

$R_i=a=37.5mm, R_o=b=62.5mm, P=60\frac{MN}{mm^2}, L=651mm$

The output result are compared with numerical solution given by **(Cook, 1981)** are show in **Table. 1**. A good agreement is obtained which proves the applicability of ANSYS to deal with the static analysis of thick cylindrical shells.

Verification Test for Normal Mode Analysis The following example is given to show the applicability of the used program ANSYS to solve the cylindrical shells:

$R_i=a=76mm, R_o=b=114.3mm, L=250.4mm, \rho=7860\frac{Kg}{m^3}, E=207Gpas, \upsilon=0.28$

The values of the first three natural frequencies for the cylindrical shell were compared with numerical results given by **(Cook, 1981)** are show in **Table. 2**. A good agreement is obtained which proves the applicability of ANSYS to deal with the vibration of thick cylindrical shells.

GUN BARREL GEOMETRY

The geometry of the studied gun barrel is shown in **Fig. 6** where (t) is the thickness of the barrel and the chosen thickness is between (3-8 mm) (the internal diameter (caliber) of (60.7 mm), external diameter of (69.14 mm) and its length equal to (651 mm))(. The gun barrel is fixed from one end to the base and the other side is free where the projectile is fed and fired. The internal surface of the gun barrel is coated with chrome to decrease the friction and erosion between the projectile and the surface of the gun barrel.

The pressure-length curve and pressure-time curve are shown in **Figs.7 and 8** respectively after the ignition starts (**Mahmood, 1995**), the pressure starts to increase until it reach (5.6 M Pa) which is able to carry the projectile and start moves, then the pressure keep on increasing until its reach the maximum value (56 M Pa) after (2.23 ms) when the projectile is (80 mm) away from the base of the barrier. Then the pressure began to decrease until the projectile leave the barrier after (6.33 ms).

Model No.	**1**	**2**	**3**
Thickness (mm)	3	4.2	8

RESULTS

Static Results:

Model-1

Figs. (9, 10, 11 and 12) show the static radial deflection and, the radial, tangential and equivalent static stress distribution along the cylinder at different time steps.

Model-2

Figs. (13, 14, 15 and 16) show the static radial deflection and, the radial, tangential and equivalent static stress distribution along the cylinder at different time steps.

Model-3

Figs. (17, 18, 19 and 20) show the static radial deflection and, the radial, tangential and equivalent static stress distribution along the cylinder at different time steps.

Vibration Analysis:

Fig. 21 shows the optimum mesh size for the first model. The first three natural frequencies for the first, second and third models are shown in **Table. 3.** **Figs. (22, 23 and 24)** show the first three modes shape of the first, second and third models respectively.

DISCUSSION:

The static deformations, stresses, natural frequencies and mode shapes are computed for thick cylinder (three models). It has been found that the maximum static radial deflections are (0.105mm), (0.074mm) and (0.042mm) for model (1), model (2) and model (3) respectively, and for the same models the maximum equivalent stresses along the cylinder are (640 N/mm^2), (460 N/mm^2) and (245 N/mm^2) respectively. From the static results, it can be observed the increases in of the cylinder thickness leads to decreases in the stresses and deformations and that due to the higher increases in the structural stiffness. It was observed that the equivalent static stresses induced at the cylinder wall for different time steps some positions the stresses reach a maximum values at a certain time.

Also it can be noted that when the thickness increases the natural frequency increases too. The percentage increases in the fundamental natural frequency when thickness variation from (3 mm to 8 mm) is found (7 %).

CONCLUSIONS

From this analysis can be concluded:-

1. It can be noted, the stresses and radial deformations in the first model larger than the second and third models.
2. The natural frequency decreases when the thickness of the cylindrical shell decreases because reduction in structural stiffness.
3. The maximum effect of the equivalent stresses occurs between (80 and 100 mm).
4. Were obtained a good agreement between the present numerical and the present analytical results.

Table. 1 Values of tangential stress and radial stress for cylindrical shell subjected to pressure loading.

Solution Type	$\sigma_r\ (N/mm^2)$	$\sigma_t (N/mm^2)$
FEM (Cook, 1981)(	-19	86.5
ANSYS (present)	-18.35	89.1
Error (%)	3.4	3

Table. 2 Values of the first three natural frequencies for the cylindrical shell.

Solution Type	**First Mode (Hz)**	**Second Mode(HZ)**	**Third Mode(HZ)**
FEM (Cook, 1981)(	1898.1	1873.52	2988.19
ANSYS (present)	1898.1	1898.2	3013.8
Error with Exact (%)	1.0	1.3	0.85

Table.3 The first three natural frequencies of thick cylinders models.

	First Mode (Hz)	**Second Mode(HZ)**	**Third Mode(HZ)**
Model-1	150.00	150.02	864.97
Model-2	152.90	152.94	879.52
Model-3	162.40	162.45	926.34

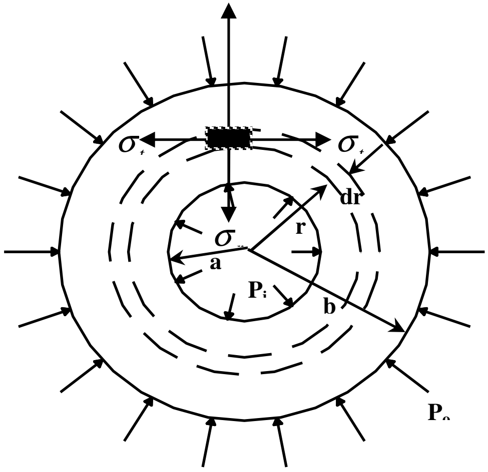

Fig. 1 Thick-walled cylinder subjected to uniform internal pressure (P_i) and external pressure (P_o).

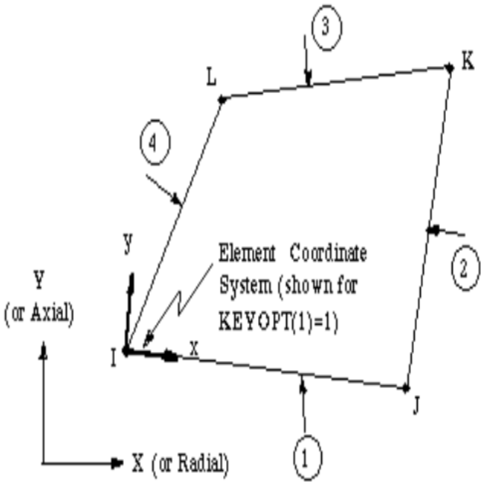

Fig. 4 Plane 42 structure solid element.

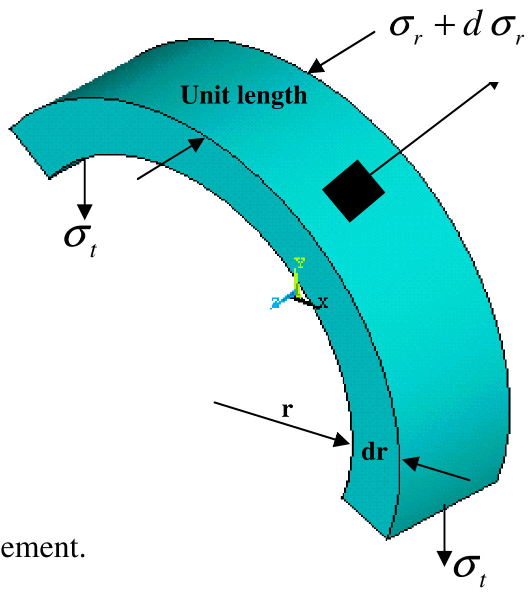

Fig. 2 Stress on half-shell cylinder.

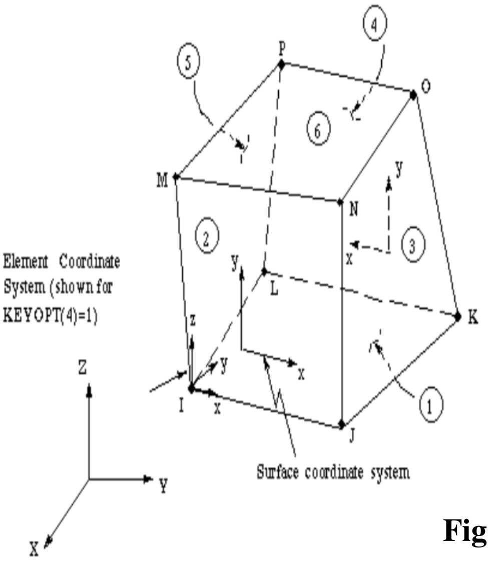

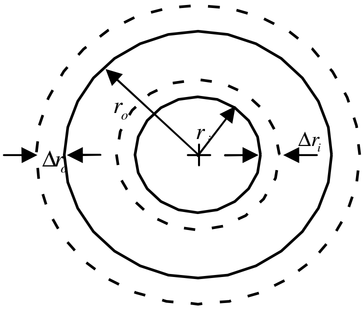

Fig. 3 Cylinder wall deformation.

Fig. 5 Solid 45 structure solid element.

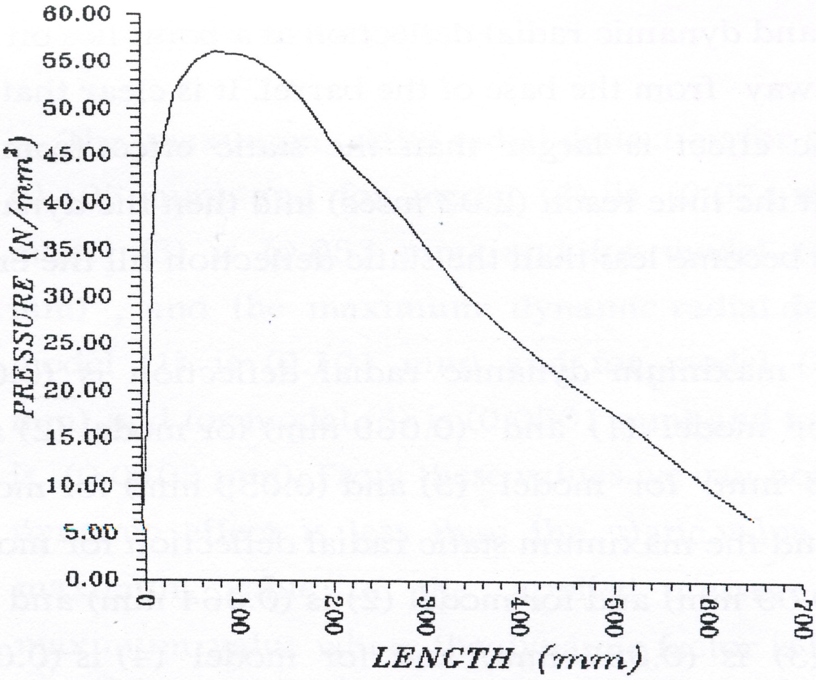

Fig. 7 Pressure Length Curve.

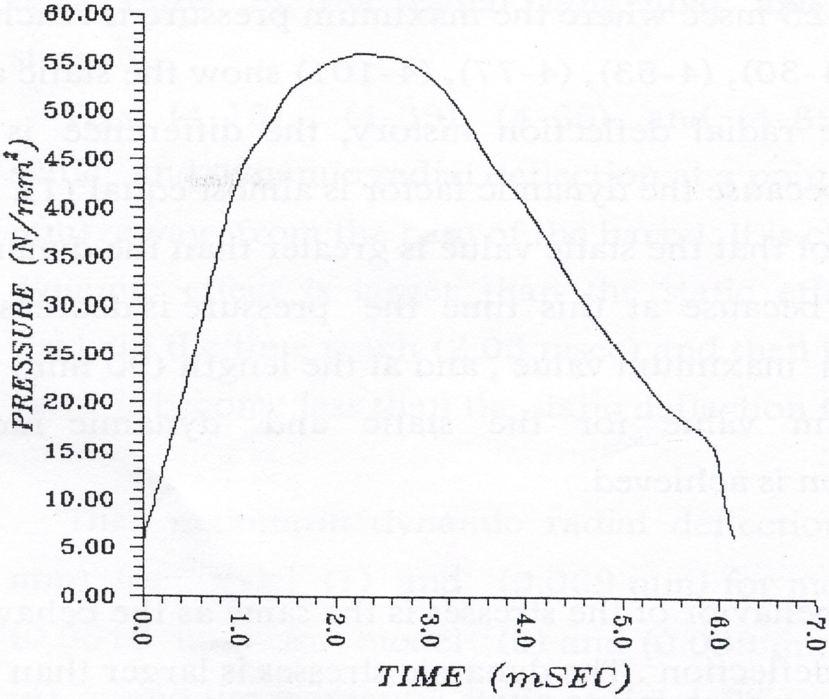

Fig. 8 Pressure Time Curve.

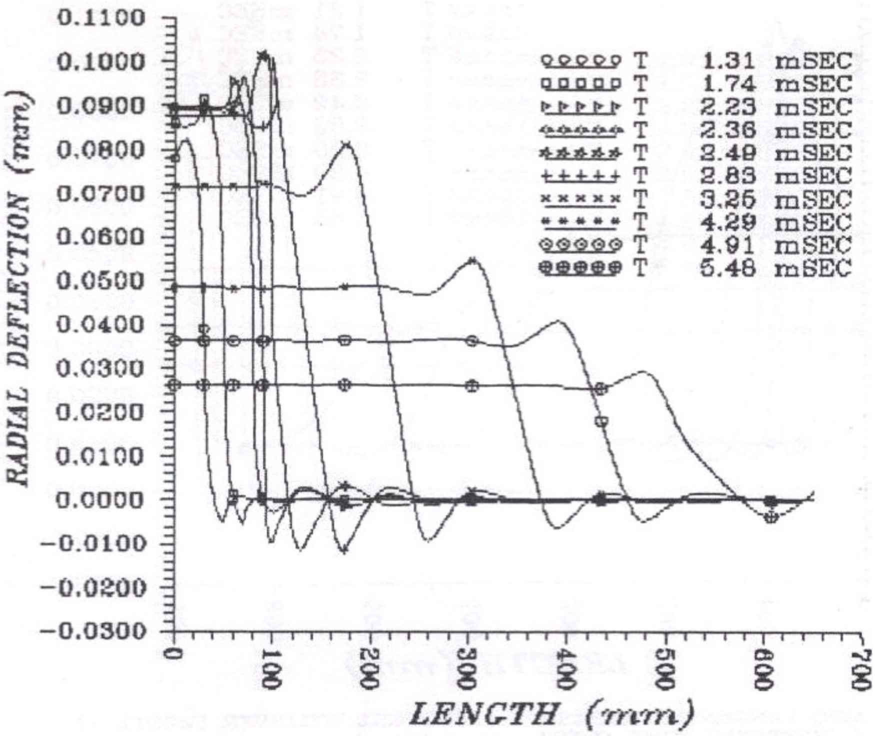

Fig.9 Static Radial Deformation along the Cylinder (Model-1) at Different Time Steps.

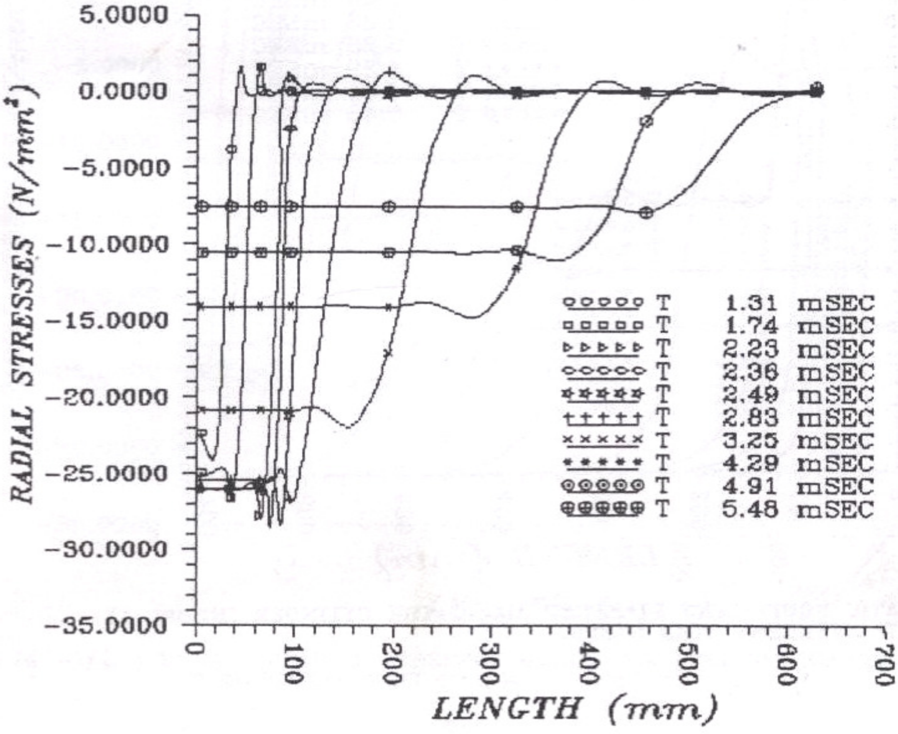

Fig. 10 Static Radial Stresses Along the Cylinder (Model-1) at Different Time Steps.

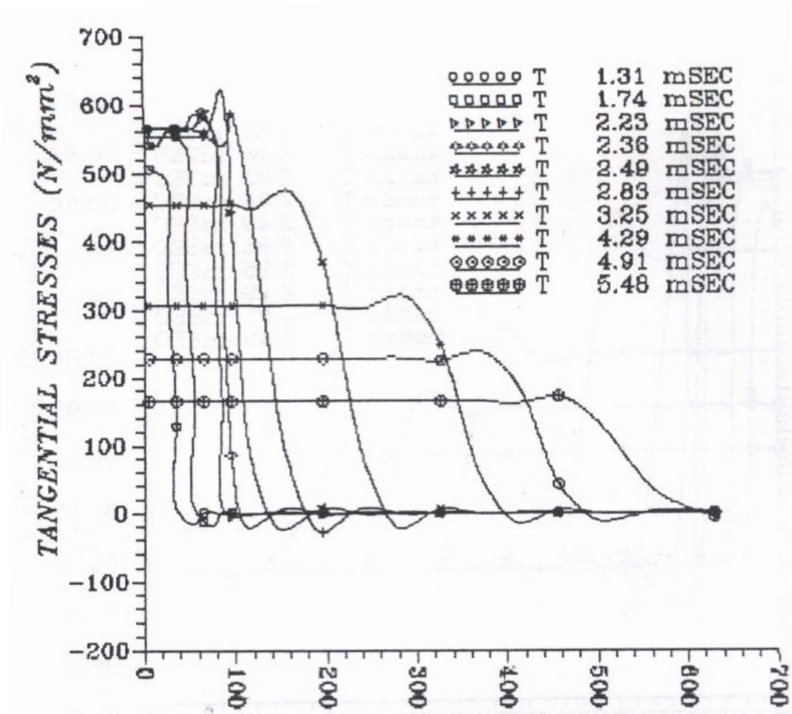

Fig. 11 Static Tangential Stresses Along the Cylinder (Model-1) at Different Time Steps.

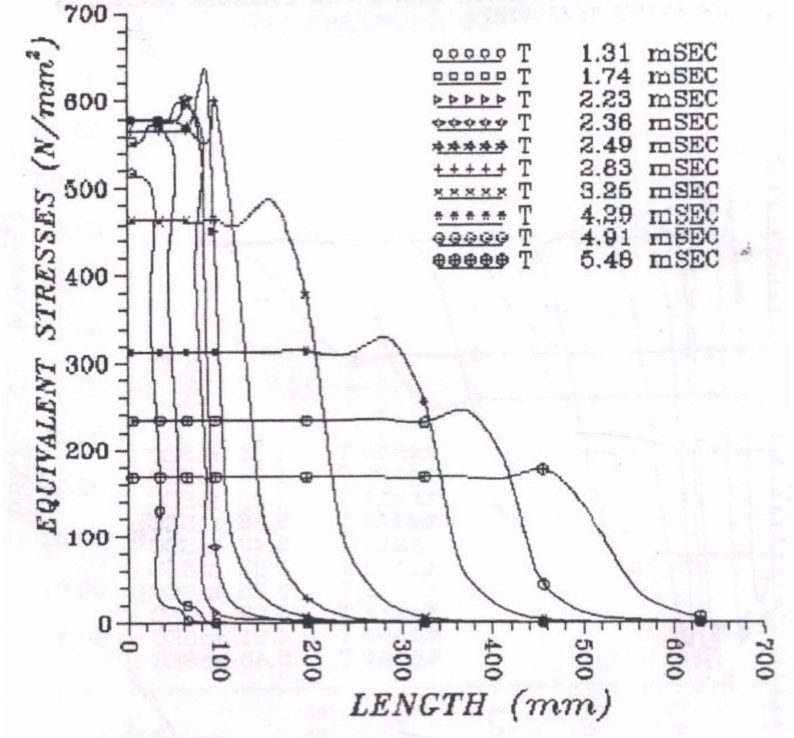

Fig. 12 Static Equivalent Stresses Along the Cylinder (Model-1) at Different Time Steps.

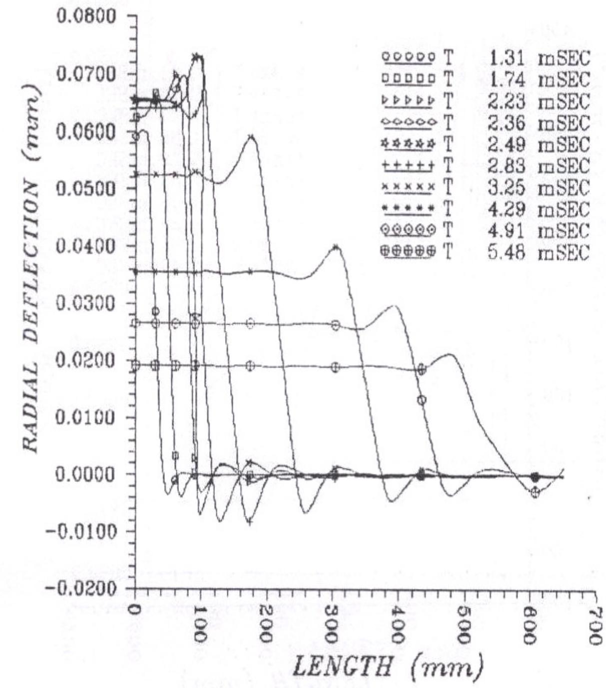

Fig. 13 Static Radial Deformation along the Cylinder

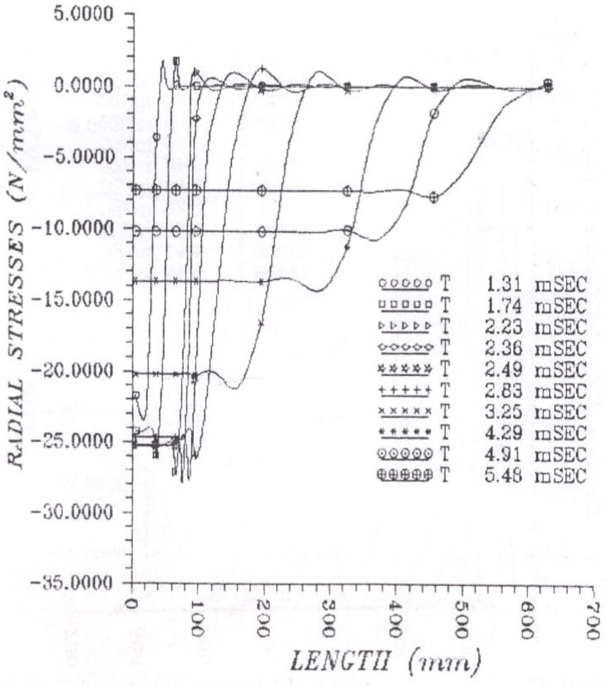

Fig. 14 Static Radial Stresses Along the Cylinder

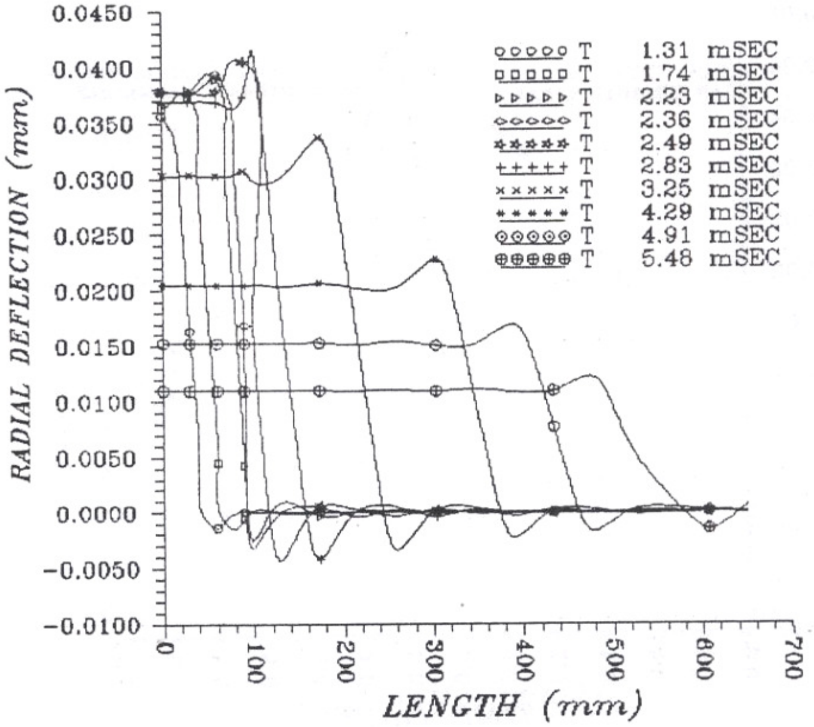

Fig. 17 Static Radial Deformation along the Cylinder (Model-3) at Different

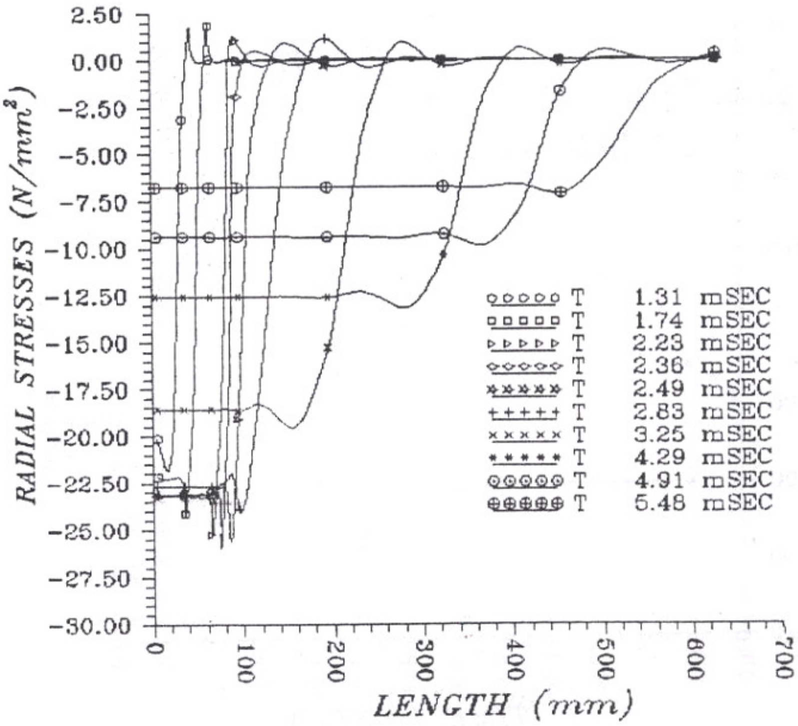

Fig. 18 Static Radial Stresses Along the Cylinder (Model-3) at Different

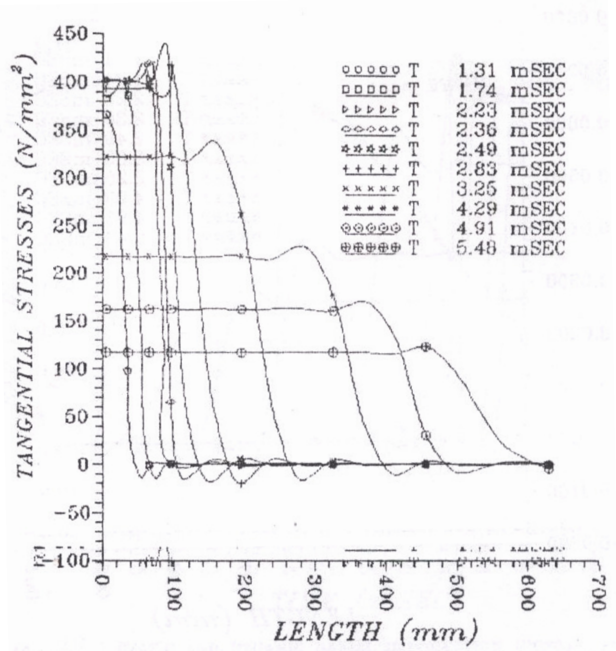
TANGENTIAL STRESSES (N/mm²)
450
400
350
300
250
200
150
100
50
0
-50
-100
0
100
200
300
400
500
600
700
LENGTH (mm)
T 1.31 mSEC
T 1.74 mSEC
T 2.23 mSEC
T 2.36 mSEC
T 2.49 mSEC
T 2.83 mSEC
T 3.25 mSEC
T 4.29 mSEC
T 4.91 mSEC
T 5.48 mSEC

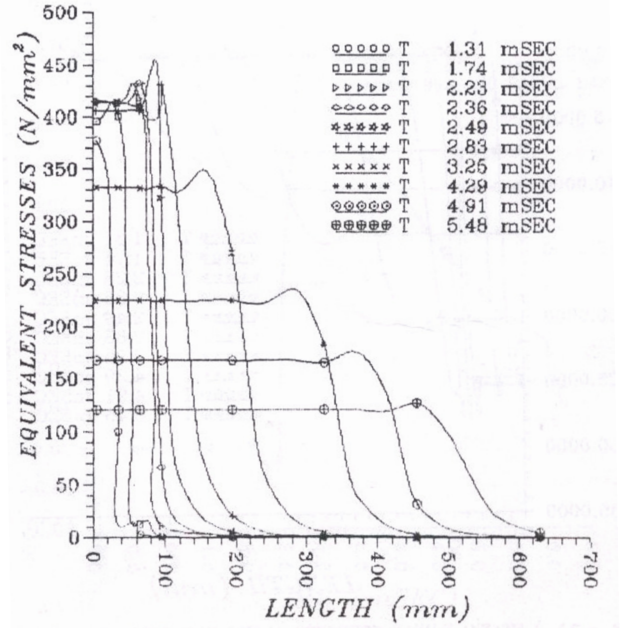
EQUIVALENT STRESSES (N/mm²)
500
450
400
350
300
250
200
150
100
50
0
0
100
200
300
400
500
600
700
LENGTH (mm)
T 1.31 mSEC
T 1.74 mSEC
T 2.23 mSEC
T 2.36 mSEC
T 2.49 mSEC
T 2.83 mSEC
T 3.25 mSEC
T 4.29 mSEC
T 4.91 mSEC
T 5.48 mSEC

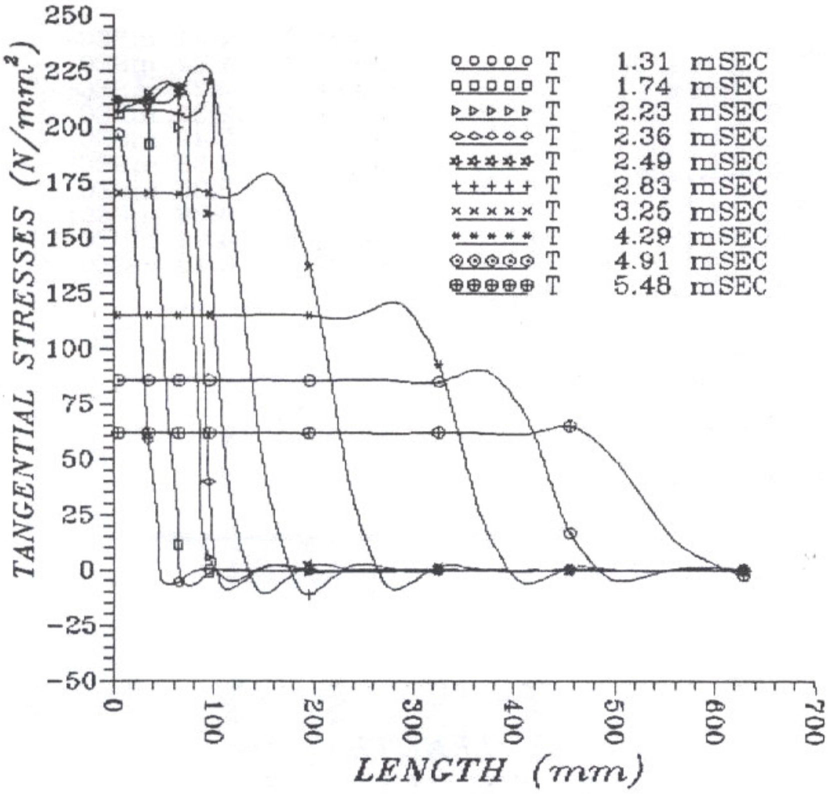

Fig. 19 Static Tangential Stresses Along the Cylinder (Model-3) at Different Time

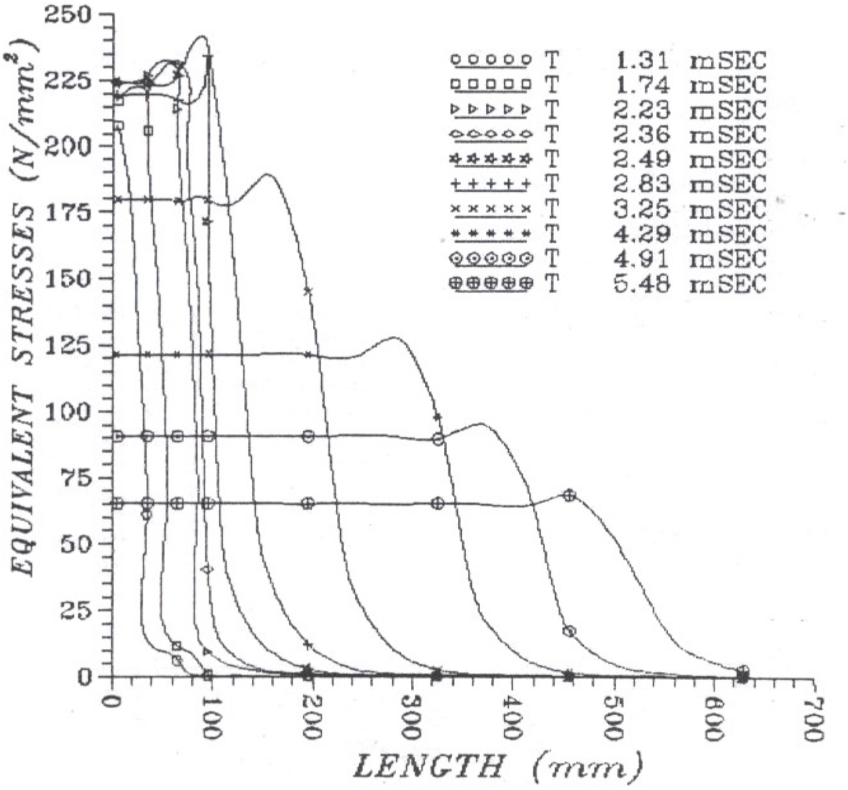

Fig. 20 Static Equivalent Stresses Along the Cylinder (Model-3) at Different Time Steps

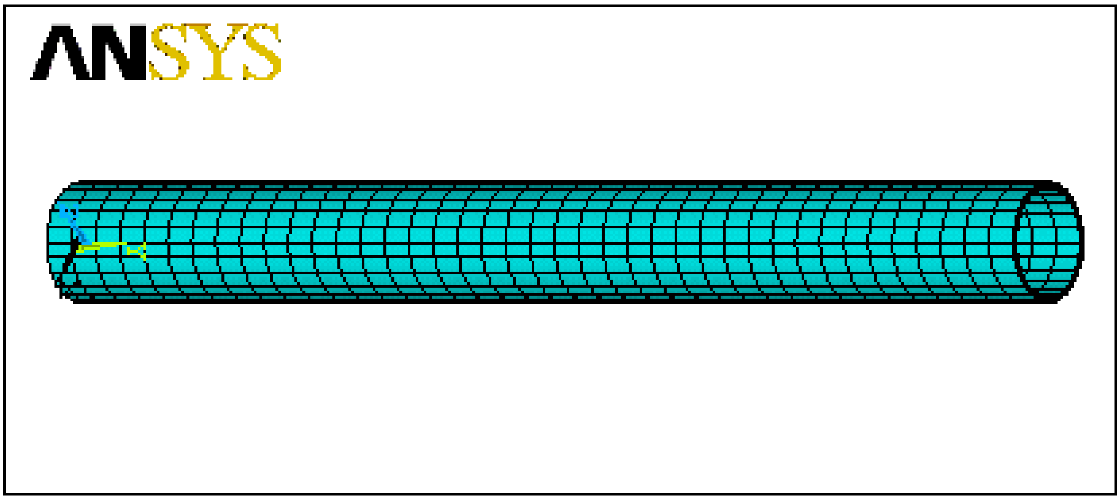

Fig. 21 Suitable mesh size for thick cylinder (Model-1).

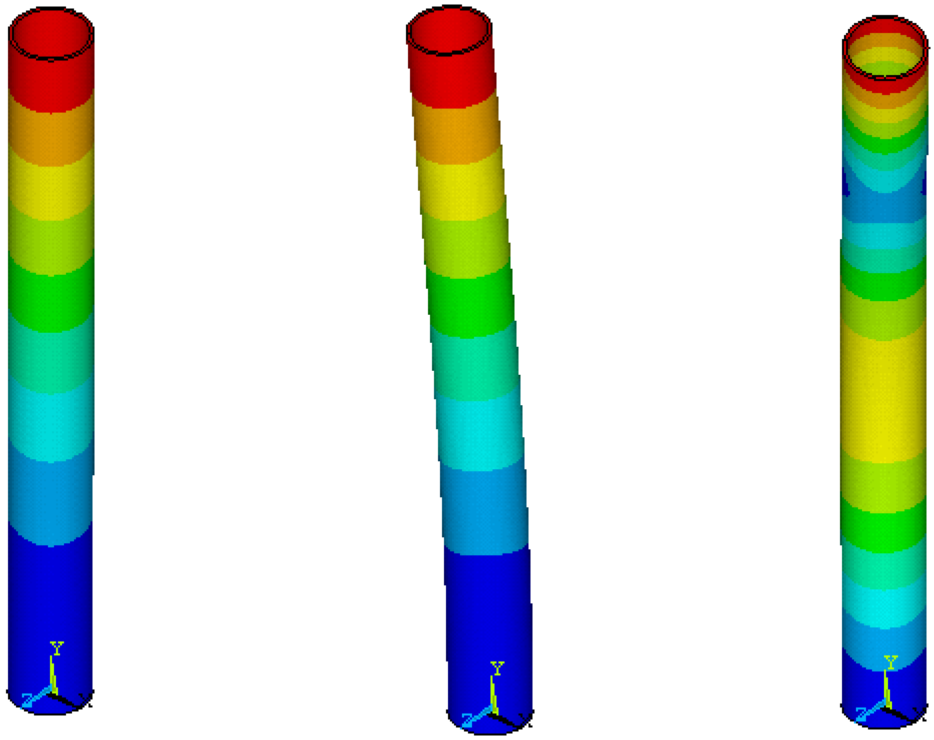

First mode shape

Second mode shape

Third mode shape

Fig 22 The first three mode shapes for the (Model-1).

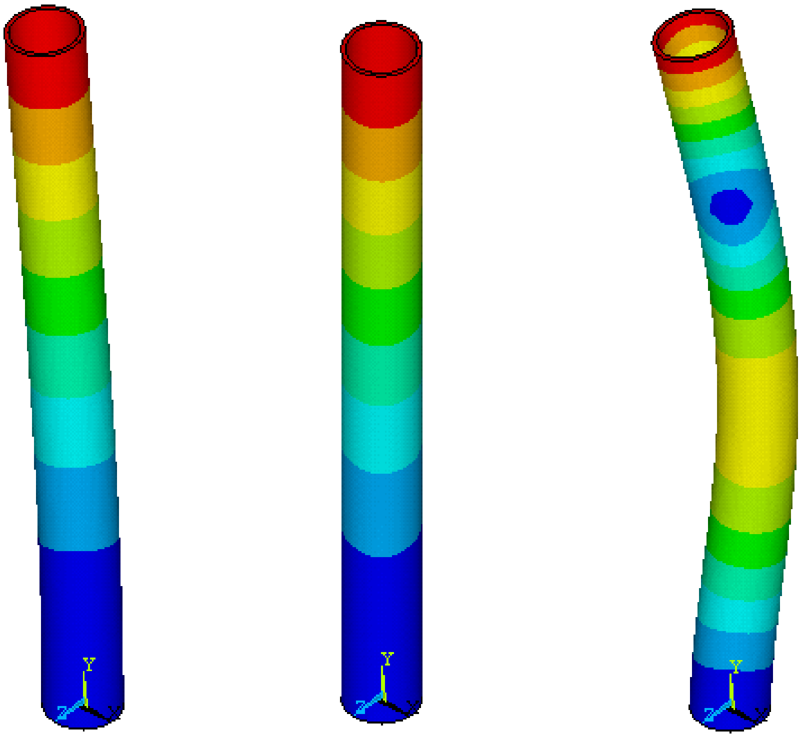

First mode shape

Second mode shape

Third mode shape

Fig 23 The first three mode shapes for the (Model-2).

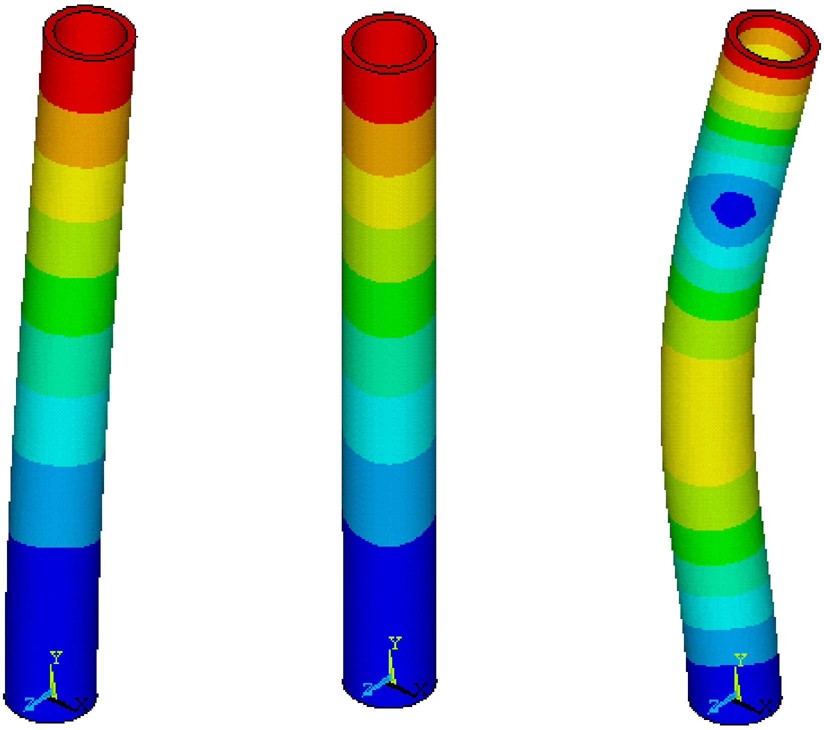

First mode shape

Second mode shape

Third mode shape

Fig 24 The first three mode shapes for the (Model-3).

REFERENCES

Batha. K. J, Wilson. E. L, "Numerical method in finite element analysis", Prentice-Hall, Englewood Cliffs, 1976.

Cook. R. D, "Concept and applications of finite element analysis", 2nd, John Willey and sons, NewYork, 1981.

Ganesan. N and Sivadas. K. R, "Free vibration of cantilever circular cylindrical shells with variable thickness", Computers and structures, Vol. 34, No. 4, 1994.

Nasman G. D, "Pressure Vessels Design and Practical", Prentice-Hall, Englewood Cliffs, 2005.

Mahmood. M. H, "Locally loaded cylindrical shells and application to gun barrels", Ph. D, desseration, Bno 1995.

Mahmood. M. H, N. Jweeg. M. J and Rajab. M. Y, "An investigation of partially pressurized thick cylindrical shells. Modeling, simulation and control", ASME press, Vol. 6, P. 9-20, 1990.

Redekop, D. ;Azar, "Response cylindrical shells panel to air-blast loading", ASME, Vol. 18, No. 13, 1990.

Singal. R. K and Williams. K, " A theoretical and experimental study of vibration of thick circular cylindrical shells and rings", J. of vibration, Acaustics, stress and reliability in design, Vol. 110/573, 1992.

Weingarten. L. I and Fisher. H. D, "Transient axisymmetric response of a conical shells frustum", J. of sound and vibration, Vol. 25, No. 3, 1982.

Wiliam. R Spiliers, "Wave propagation in a thin cylindrical shell", J. of applied mechanics, Vol. 4, P-346, 1972.

NOMENCLATURE:

a	Internal radius of thick cylinder (mm).
b	External radius of thick cylinder (mm).
L	Length of thick cylinder (mm).
r	Radius of thick cylinder (mm).
P_i	Distributed internal pressure (M Pa).
P_o	Distributed external pressure (M Pa).
(σ_t)	Tangential stress at any point of a thick walled cylinder N / mm^2.
(σ_r)	Radial stress at any point of a thick walled cylinder N / mm^2.
υ	Poisson's ratio.
E	Young's modulus.
Δr_i	Internal wall cylinder deformation (mm).
Δr_o	External wall cylinder deformation (mm).
$[K]$	Stiffness matrix.
$\{F\}$	Force load vector.
$\{U\}$	Displacement vector.
$\{U^{\bullet}\}$	Velocity vector.
$\{U^{\bullet\bullet}\}$	Acceleration vector.
$[M]$	Mass matrix.
Φ_i	Vector of nodal amplitudes (mode shape) for the ith mode of vibration.
ω_i	The angular frequency of mode I (rad /sec).
ρ	Density, Kg / m^3.

NATURAL CONVECTION HEAT TRANSFER IN A VERTICAL CONCENTRIC ANNULUS

Dr. Akeel A. Mohammed
Mech. Engr. Dept.
University of Technology
Baghdad-Iraq

ABSRACT

Experiments were carried out to study the local and average heat transfer by natural convection in a vertical concentric cylindrical annulus. The experimental setup consists of an annulus has a radius ratio of 0.555 and inner cylinder with a heated length 1.2m subjected to the constant heat flux while the outer cylinder is subjected to the ambient temperature. The investigation covers heat flux range from 58.2 W/m^2 to 274.31 W/m^2. Results show an increase in the natural convection as heat flux increases leads to an improve in the heat transfer process. An empirical equation of average Nusselt number as a function of Raylieh number was deduced .

الخلاصة

أجريت تجارب عملية لدراسة انتقال الحرارة الموقعي و المعدل بالحمل الحر بتجويف حلقي بين أسطوانتين متحدتي المركز بالوضع العمودي، نسبة نصف القطر لهما تعادل 0.555 و بطول 1.2 متر . سخنت الأسطوانة الداخلية تحت فيض حراري ثابت، بينما عرّضت الأسطوانة الخارجية إلى درجة حرارة الجو. تغطي الدراسة مدى للفيض الحراري يتراوح من $58.2\ W/m^2$ إلى $274.31\ W/m^2$. بيّنت النتائج زيادة معدلات الحمل الحر بزيادة الفيض الحراري مما يؤدي إلى تحسين معامل انتقال الحرارة.

KEY WORDS

Heat Transfer, Natural Convection, Concentric Annulus

INTRODUCTION

The problem of natural convection heat transfer across a horizontal and vertical cylindrical annulus has received considerable attention in view of its fundamental importance germane to numerous engineering applications. As a result, extensive experimental and theoretical works dealing with the flow and associated heat transfer characteristics of natural convection in such configuration have been reported in the literature. Comprehensive reviews on natural convection in concentric and eccentric annuli are available **(Kueehn 1976 &1978, Van de Sande 1979, and Yao 1980)** and there is no need to repeat them. However, all of the previous studies are concerned with the horizontal annulus; little attention has been paid to annuli with a vertical position. **(Van de Sande and Hamer 1979)** have obtained empirical correlations for natural convection heat transfer in concentric and eccentric annuli of constant heat flux. **(Glakape et al. 1986)** presented a numerical solution for air in concentric and eccentric configurations with specified constant heat flux at the boundaries. **(Akeel 2005)** has presented an experimental and theoretical study for mixed convection heat transfer through concentric annuli. The lack of experimental data concerning the problem of natural convection in the vertical concentric annulus, and the practical importance of this problem in the industry applications, motivated the present work.

EXPERIMENTAL APPARATUS

The test section is shown diagrammatically in **Fig.1** and consists of 4 mm wall thickness, 50 mm outside diameter and 1.2 m long aluminum cylinder (K) located centrally in 5 mm thickness , 90 mm inside diameter and 1.2 m long aluminum cylinder (I), by fitting it at the test section inlet with the 20 mm inside diameter , 50 mm outside diameter and 15 mm long Teflon tube (N) and at the test section exit with the teflon piece (M). A ring (P) is used to hold and support the aluminum cylinder (K) with the teflon piece (N) centrally inside the settling chamber by adjustable screws (Q). The teflon was chosen because of its low thermal conductivity in order to reduce the heat loss from the aluminum cylinder ends. A well design Teflon bell mouth (H) is fitted at the annulus outer aluminum cylinder (I) and bolted inside the settling chamber (D). The inlet air temperature was measured by one thermocouple (J) located in the settling chamber (D) while the outlet bulk air temperature was measured by three thermocouples (Z) located in the test section exit . The local bulk air temperature was calculated by using a straight line interpolation between the measured inlet and outlet bulk air temperature.

The inner cylinder was heated electrically using an electrical heater which consists of a nickel-chrome wire , wound as a coil spirals around solid teflon tube and is covered by a 2 mm thickness asbestos layer , and the space between the asbestos and the inner cylinder wall is fitted with a fine grade sand to avoid heat convection in it and to smooth out any irregularities in the heat flux. The hole apparatus is designed with a view to obtain a good concentricity of the core cylinder and the containing cylinder. The temperature of the outside surface of the inner cylinder was measured by seventeen asbestos sheath alumel-chromel (type K) thermocouples , arranged along the cylinder , the measuring heads of the thermocouples were made by fusing together the ends of two wires.

The thermocouples were fixed by drilling holes of 1.5 mm diameter in the cylinder wall and the ends of the holes chamfered by a 3 mm slug to locate the measuring junctions which were then fixed by a high temperature application Defcon adhesive . The excess adhesive was removed and the cylinder outer surface was cleaned carefully by fine grinding paper. All the thermocouples wires and heater terminals were taken out the test section through both teflon pieces (N,M) .

On the other hand , ten thermocouples (type K) were used to measure the inner surface temperature of the annulus outer cylinder (I). Thermocouples positions at the outer surface were located and then a 2 mm deep pits were drilled in which the thermocouples were fixed by Defcon adhesive. All thermocouples were used with leads , the thermocouple with lead and without lead were calibrated against the melting point of ice made from distilled water and the boiling points of several pure chemical substances. To determine the heat loss from the test section ends, two thermocouples were fixed in each teflon piece. The distance between these thermocouple was 12 mm. Knowing the thermal conductivity of the teflon , the ends condition could thus be calculated.

EXPERIMENTAL PROCEDURE

To carry out an experiment the following procedure was followed:

1- The electrical heater was switched on and the heater input power then adjusted to give the required heat flux.

2- The apparatus was left at least three hours to establish steady state condition. The thermocouples readings were measured every half an hour by means of the digital electronic multimeter until the reading became constant , a final reading was recorded. The input power to the heater could be increased to cover another run in a shorter period of time and to obtain steady state conditions for next heat flux.

3- During each test run , the following readings were recorded:

   a- The readings of the thermocouples in °C.

   b- The heater current in amperes.

   c- The heater voltage in volts.

DATA ANALYSIS

Simplified steps were used to analyze the heat transfer process by natural convection from the inner cylinder which was subjected to a uniform heat flux while the outer cylinder was subjected to the ambient temperature. The total input power supplied to the inner cylinder can be calculated:

$$Q_t = V'' \times I \qquad (1)$$

The convection and radiation heat transferred from the inner cylinder is :

$$Q_{cr} = Q_t - Q_{cond} \qquad (2)$$

where Q_{cond} is the conduction heat loss which was found experimentally equal to 5 % of the input power. The convection and radiation heat flux can be represented by:

$$q_{cr} = Q_{cr}/A \qquad (3)$$

where:

$A = 2\pi\, r_1\, L$

The convection heat flux , which is used to calculate the local heat transfer coefficient is obtained after deduce the radiation heat flux from q_{cr} value. The local radiation heat flux can be calculated as follows:

$$q_r = F_{1-2}\, \varepsilon\, \sigma \left[\left((t_s)_z + 273 \right)^4 - \left(\overline{(t_{s2})}_z + 273 \right)^4 \right] \qquad (4)$$

where:

F_{1-2}= view factor between inner and outer cylinder ≈1

$(t_s)_Z$ = local temperature of inner cylinder.

$\overline{(t_{s2})}_z$ = average temperature of outer cylinder.

ε = emissivity of the polished aluminum surface=0.09.

Hence the convection heat flux at any position is:

$$q = q_{cr} - q_r \tag{5}$$

The local heat transfer coefficient can be obtained as:

$$h_z = \frac{q}{(t_s)_z - (t_b)_z} \tag{6}$$

$(t_b)_z$ = Local bulk air temperature.

All the air properties were evaluated at the mean film air temperature (Keys 1966):

$$(t_f)_z = \frac{(t_s)_z + (t_b)_z}{2} \tag{7}$$

t_f = Local mean film air temperature.

The local Nusselt number (Nu_z) then can be determine as:

$$Nu_z = \frac{h_z \quad D_h}{\kappa} \tag{8}$$

The average values of Nusselt number Nu_m can be calculated based on calculation of average inner surface temperature and average bulk air temperature as follows:

$$\bar{t}_s = \frac{1}{L} \int_{z=0}^{z=L} (t_s)_z \quad dz \tag{9}$$

$$\overline{t_b} = \frac{1}{L}\int_{z=0}^{z=L} (t_b)_z \quad dz \qquad (10)$$

$$\overline{t_f} = \frac{\overline{t_z} + \overline{t_b}}{2} \qquad (11)$$

$$Nu_m = \frac{q \quad D_h}{k(\overline{t_z} - \overline{t_b})} \qquad (12)$$

The average values of the other parameters can be calculated as:

$$Gr_m = \frac{g \quad \beta \quad D_h^3 \quad (\overline{t_z} - \overline{t_b})}{\nu^2} \qquad (13)$$

$$Pr_m = \frac{\mu \quad C_p}{k} \qquad (14)$$

$Ra_m = Gr_m \, . \, Pr_m$ (15)

where:

$$\beta = 1/(273 + \overline{t_f})$$

All the air physical properties ρ, μ, ν, and k were evaluated at the average mean film temperature ($\bar{t}_f$).

EXPERIMENTAL RESULTS

The variation of the inner cylinder surface temperature for different heat flux is shown in **Fig.2** . It is obvious that the surface temperature increases at the stage of entrance and attains a maximum point after which the surface temperature begins to decrease at high heat flux ($q \geq 181$ W/m^2) and be almost constant for small heat flux ($q \leq 152$ W/m^2). The rate of surface temperature rises at early stage is directly proportional to the wall heat flux because of the faster increasing of the thermal boundary layer as heat flux increase (i.e., increasing of buoyancy effect).

Fig.3 & 4 show the effect of heat flux on the local and average Nusselt number along the inner cylinder. It is clear that the results of higher heat flux for local and average Nusselt number are higher than that of lower heat flux. **Fig.3** shows also sharp decrease for the local Nusselt number values at the entrance of the annulus because the boundary layer thickness is zero and the natural convection is poor in this region, then increase downstream because of increasing of natural convection. The values of the mean Nusselt number are plotted in **Fig.5** in the form of log(Nu_m) against log(Ra) for the range of Ra from 0.68611×10^5 to 1.728559×10^5. All the points as can be seen are represented by linearization of the following equation.

$$Nu_m=2.31812\ Ra^{0.083188} \qquad (16)$$

CONCLUSIONS

1. The extent of the local mixing increases as the heat flux increases.
2. The heat transfer process improves as heat flux increase.
3. The effect of buoyancy is small at the annulus entrance and increase down stream.

REFERNCES

Akeel Abdullah Mohammed An Investigation into laminar combined convection heat transfer through concentric annuli. Ph. D. Thesis, University of Technology, Mech. Eng. Dept., 2005.

Glakape, E. K., Watkins C. B. , Jr., and Cannon, J. N. Constant heat flux solutions for natural convection between concentric and eccentric horizontal cylinders. Numerical Heat Transfer, 1986, 10, 279-295

Kueehn, T. H. and Goldstein, R. J. An experimental and theoretical study of natural convection in the annulus between horizontal concentric clinders. J. Fluid Mech., 1976, 74, 695-719

Kueehn, T. H. and Goldstein, R. J. An experimental study of natural convection heat transfer in concentric and eccentric horizontal cylindrical annuli, ASME J. Heat Transfer, 1978, 100, 635-640

Rao, Y. F., Miki,K. , Fukuda, K. , and Katata, Y. Flow pattern of natural convection in horizontal cylindrical annuli. Int. J. Heat Mass Transfer, 1985, 28, 705-714

Van de Sande, E. and Hamer, B. J. G. Steady and transient natural convection in enclosures between horizontal circular cylinders (constant heat flux). Int. J. Heat Mass Transfer, 1979, 22, 361-370

Yao, L. S. Analysis of heat transfer in slightly eccentric annuli. ASME J. Heat Transfer, 1980, 102, 270-284

NOMENCLUTURE

A: inner cylinder surface area; m^2

D_h: hydraulic diameter=$2(r_2-r_1)$: m

I: current; Amp

κ : thermal conductivity; $W/m^2.°C$

L: annulus length; m

(Nu_m): mean Nusselt number

Q: convection heat loss; W

Q_t: total heat given; W

Q_{cr}: convection- radiation heat loss; W

q_r: radiation heat flux; $W/m^2.°C$

q: convection heat flux; $W/m^2.°C$

r_1: outer radius of inner cylinder; m

r_2: inner radius of outer cylinder; m

V”: voltage; volt

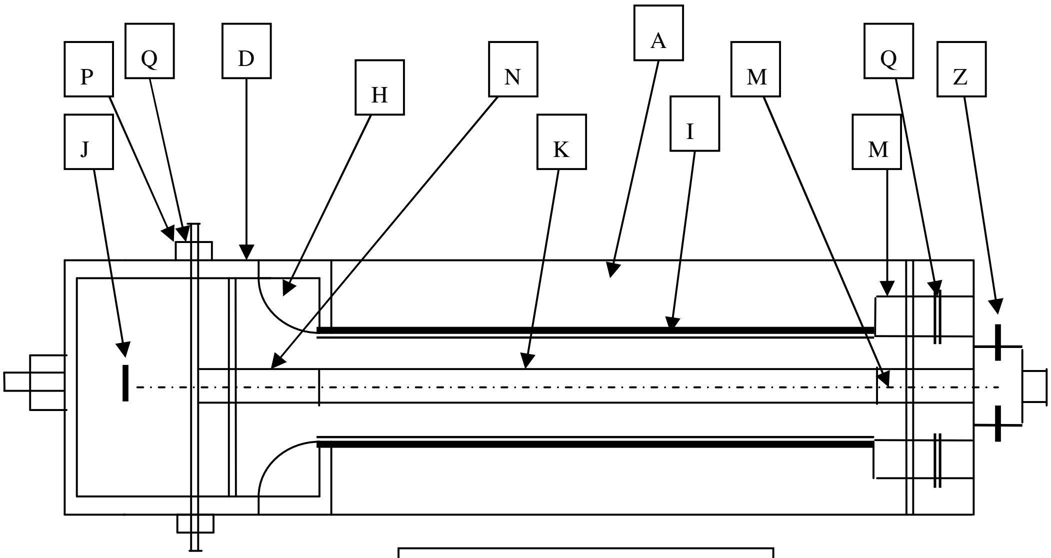

A WOODEN BOARD
D SETTLING CHAMPER
H BELL MOUTH
I OUTER CYLINDER
K INNER CYLINDER
J THERMOCOUPLE
M,N TEFLON
P RING
Z THERMOCOUPLE
Q SCREW

Fig. 1: Diagram of Experimental Apparatus.

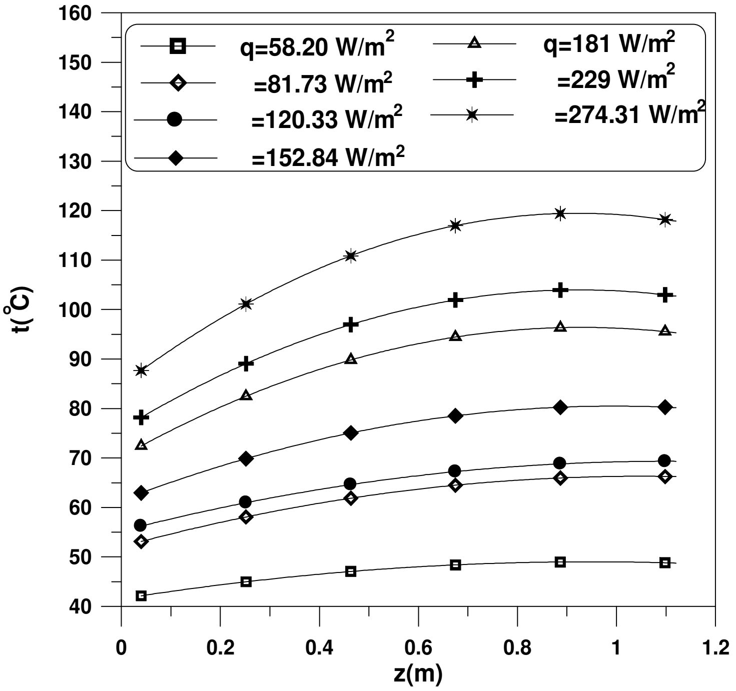

Fig.2: Variation of the Surface Temperature with the Axial Distance

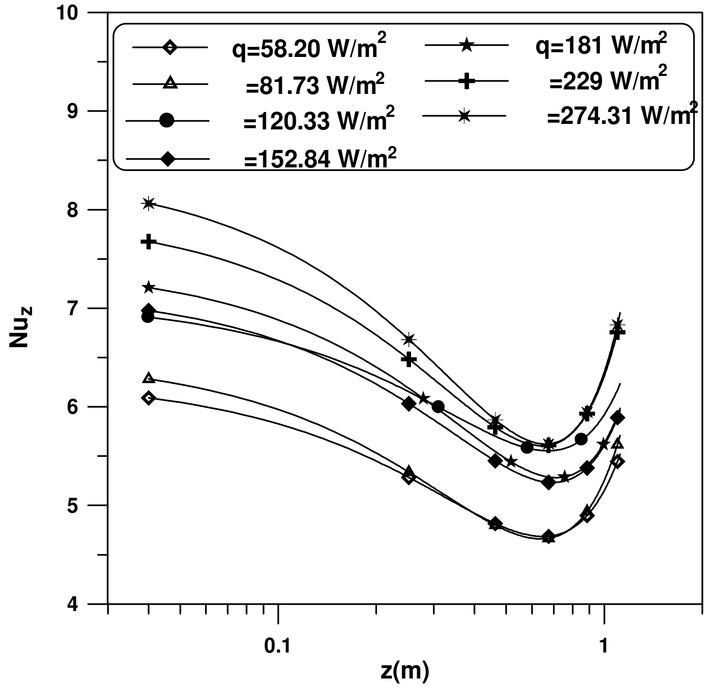

Fig.3: Local Nusselt Number Versus Axial Distance.

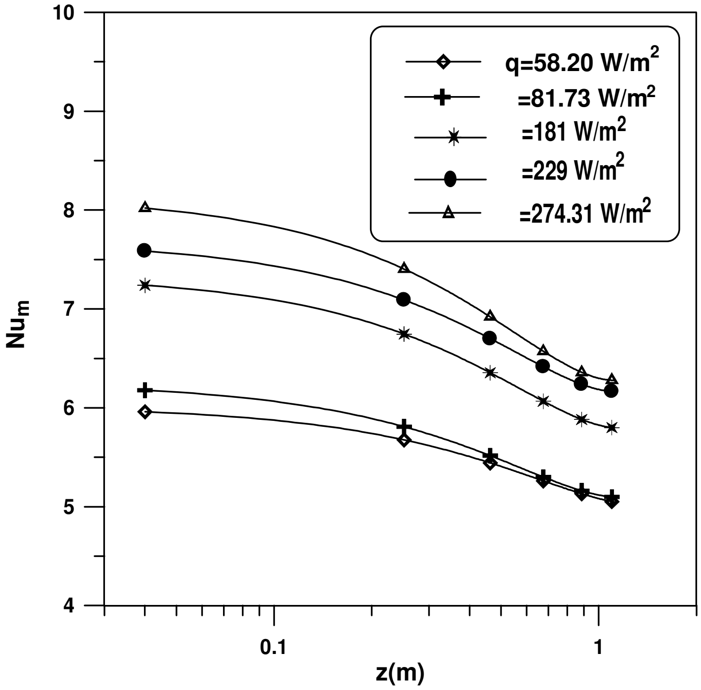

Fig.4: Average Nusselt Number Versus Axial Distance.

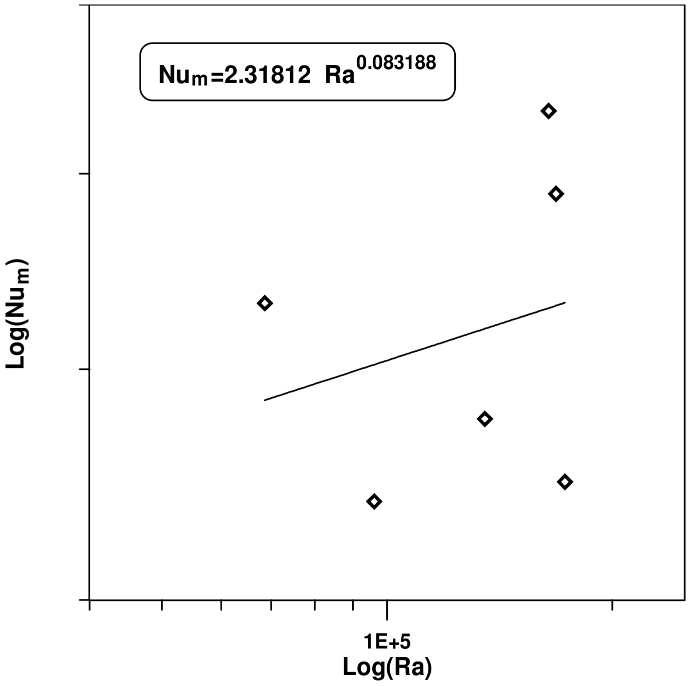

Fig.5: Logarithm Average Nusselt Number Versus log(Ra).

NUMERICAL SIMULATION OF TWO DIMENSIONAL TRANSIENT NATURAL CONVECTION HEAT TRANSFER FROM ISOTHERMAL HORIZONTAL CYLINDRICAL ANNULI

Ayad K. Hassan
University of Technology
Baghdad-Iraq

Jasim M. A. Al-lateef
University of Diyala
Baghdad-Iraq

ABSTRACT

Numerical solutions are presented for the transient natural convection heat transfer problem in horizontal isothermal cylindrical annuli, enclosed in heated inner and cooled outer cylinders. Solutions for laminar case were obtained within Grashof number based on the inner diameter which varied from $1x10^2$ to $1x10^5$ in air. Both vorticity and energy equations were solved using alternating direction implicit (ADI) method and stream function equation by successive over relaxation (SOR) method. The structure of fluid flow such as a velocity vector and temperature distribution as well as Nusselt number were obtained and the effect of diameter ratio on them is examined. In addition, the Grashof number was changed with the influence of variation Prandtle number and diameter ratio. Our numerical calculation are summarized by Nussult number vs. Grashof number curves with diameter ratios and prandtl as a parameter, which serves as a guide to natural convection heat transfer calculated from annulus. Good agreement with previous data were obtained.

الخلاصة

يقَدَّم هذا البحث حَلّ عددي لمسالةِ انتقال الحرارةِ العابرةِ بالحمل ِ الطبيعي في العمود الحلقي الإسطواني ثابت درجة الحرارةِ بوضع الأفقي، حيث تكونَ الاسطوانة الداخليةِ مسخنِة وَ الإسطوانة َ الخارجية مبردة. تم حل المسالة لحالةِ الجريان الطباقي ولرقم كراشوف مستندة على القطرِ الداخلي يتراوح بين $1x10^2$ الى $1x10^5$ للهواء ِ.معادلة الدوامية ومعادلة الطاقةِ حلتا بإستعمال بطريقة الإتّجاهَ الضمنيَ المتناوبُ ومعادلة الانسياب بطريقة فوق التراخي المتعاقبة.تم الحصول علىّ تركيبَ جريان المائع كمتجه السرعةِ وتوزيعِ درجةِ حرارة بالإضافة إلى رقم نسلت، تم اختبار تأثيرِ نسبةِ القطرِ عليها .بالإضافة الى دراسة تأثيرِ إختلافِ رقم كراشوف مع إختلافِ رقم برانتل و نسبة القطرَ عليهاَ .تم اجمال الحسابات العددية بواسطة منحنيات رقم نسلت مع رقم كراشوف و نسبة القطرَ ورقم برانتل .التي يمكن الاستفادة منها كدليل لحسابات انتقال الحرارة بالحمل الطبيعي من الشكل الحلقي.تم الحصول على توافق جيد بين النتائج الحالية وبياناتِ البحوث السابقةِ.

KEYWORD

Natural Convection, Numerical Simulation, Isothermal , Cylindrical Annuli

INTRODUCTION

IN RECENT years, natural convection heat transfer in a cylindrical annulus has attracted much attention with relation to thermal storages systems, solar collectors, spent nuclear air fuel cooling, nuclear reactors, aircraft fuselages insulation, cooling of electrical equipments. The horizontal convection isothermal cylinders were used pressurized gas underground electric transsimition cables **(Pederson et.al. 1971)**. In this paper, we present a brief review of selected experimental papers and concerned theoretical studied. **(Liu et.al. 1961**) measured the overall heat transfer and radial temperature profiles of air , water and silicone fluid. Qualitative flow descriptions were given for each fluid-Photographs of flow patterns in air using smoke were presented by **(Bishop and Caley 1966)** and **(Bishop et.al 1968)**. Different flow regimes depending on the Grashof number and diameter ratio were delineated by **(Powe et.al. 1969)**. The first determination of local heat transfer coefficients in annular geometry with air was made by **(Eckert and Soehngen 1970)** using Mach-Zender interferometer The first numerical solution of natural convection between horizontal convection cylinders was obtained by **(Crawford and Lemlich 1962)** using Gauss-Seidel iteration approach for Prandtl number of 0.7 and for diameter ratio of 2, 8 and 57. **(Abbot 1964)** obtains a solution for diameter ratio close unity using matrix inversion techniques. **(Mack and Bishop 1968)** employed a power series expansion valid in the range diameter ratios from 1.15 to 4.15. However, as pointed out by **(Hodnett 1973)**, if the diameter ratio becomes too large; there is a region in the annulus where convection effects are as important as conduction effects. Such a problem has been attacked by **(Hodnett 1973)** using a perturbation method. **(Powe et. al. 1971)** examined the transition from steady to unsteady flow for air with Prandtl around 0.7 by determining the critical Rayleigh number at which an eddy forms and turns in the opposite direction of the main cells. **(Kuehn and Goldstein 1978)** performed experimental and theoretical–numerical studies for air and water at Rayleigh numbers from $2.1\text{x}10^4$ to $9.8\text{x}10^5$ at diameter ratio of 2.6. **(Charrier-Mojtabi et al 1979)** presented numerical solutions at a Prandtl number of 0.7 and 0.02 with various diameter ratios and Rayleigh numbers. **(Tsui and Tremblay 1983)** carried out theoretical-numerical study at Grashof number from $7\text{x}10^2$ to $9\text{x}10^4$ and Prandtl number of 0.7 with diameter ratio of 1.2, 1.5 and 2. A numerical investigation has been performed by Hand and Back (1999), to examine the interaction between radiation and steady laminar natural convection in cylindrical annuli filled with a dry gas. Radiation was found to play an important role in determining thermo-fluid dynamics behavior in natural convection induced by hot inner cylinder under large temperature difference. All references cited except references **(Charrier-Mojtabi et.al.1979)** and **(Tsui and Trembaly 1983)**are confined to the steady-state analysis. Even **(Charrier-Mojtabi et al 1979)** gives the steady- state results only, and **(Tsui and Tremblay 1983)** presents the transition-state results with Prandtl around 0.7 only.

The purpose of this paper is to present the transient-state results with the effect of variation of Prandtl number and diameter ratio, which are new to the author's knowledge.

MATHEMATICAL FORMULATION

The physical model and the coordinate system in the present analysis are shown in **Fig.1**. A fluid layer is enclosed between two concentric cylinders with radii r_i and r_o. Temperatures at the heated inner cylinder surface and the cooled outer one, designated by T_h and T_c , respectively, are to be constant. Flow and temperature fields are assumed to have a symmetric nature with respect to vertical plane ($\theta=0^o$ and 180^o) and the region of computation is limited between $\theta=0^o$ and 180^o.

The physical system consists of a Newtonian fluid air, in an annulus bounded by two isothermal surfaces. To formulate the problem it is assumed that: (a) the fluid motion and temperature distribution are two-dimensional (2-D), (b) the fluid is viscous and incompressible, (c) frictional heating is negligible, (d) the difference in temperature between the two isothermal boundaries is small compared with $1/\beta$, (c) the fluid properties are constant except for the density variation with temperature. Thus, within the Boussinesq approximation, four governing equations (two momentum, one energy and continuity) in polar coordinate are as follows **(Torrance 1985)** and **(Chun-Yen 1979):**

$$\frac{1}{r}\frac{\partial}{\partial r}(ru)+\frac{1}{r}\frac{\partial v}{\partial \theta}=0 \tag{1}$$

$$\frac{\partial u}{\partial t}+u\frac{\partial u}{\partial r}+\frac{v}{r}\frac{\partial u}{\partial \theta}=g\beta(T-T_c)\cos\theta-\frac{1}{\rho}\frac{dp}{dr}+\upsilon(\nabla^2 u-\frac{u}{r^2}-\frac{2}{r^2}\frac{\partial v}{\partial \theta}) \tag{2}$$

$$\frac{\partial v}{\partial t}+u\frac{\partial v}{\partial r}+\frac{v}{r}\frac{\partial v}{\partial \theta})=g\beta(T-T_c)\sin\theta-\frac{1}{\rho}\frac{1}{r}\frac{dp}{dr}+\upsilon(\nabla^2 v-\frac{v}{r^2}+\frac{2}{r^2}\frac{\partial u}{\partial \theta}) \tag{3}$$

$$\frac{\partial T}{\partial t}+u\frac{\partial T}{\partial r}+\frac{v}{r}\frac{\partial T}{\partial \theta}=\alpha(\nabla^2 T) \tag{4}$$

where all constants, variables and operators are dimensional.

The coordinates are *r*, measured from the center of the system, and *θ*, measured counterclockwise from the downward vertical line. The radial velocity *u* is positive radially outwards, and the tangential (angular) velocity *v* positive in the counterclockwise direction for $0^o \leq \theta \leq \pi$.

The vector potential Ψ and vorticity vector Ω are introduced (Torrance 1985)

$$V=\nabla x\Psi \tag{5}$$

$$\Omega=\nabla xV \tag{6}$$

where Ψ and Ω satisfy the following solenoid condition

$$\nabla.\Psi=0 \tag{7}$$

$$\nabla.\Omega=0 \tag{8}$$

The vector potential satisfies the equation of continuity, **eq. (1)**, automatically. Then, the relation between Ψ and Ω is presented in the following dimensionless form

$$\Omega=-\nabla^2\Psi \tag{9}$$

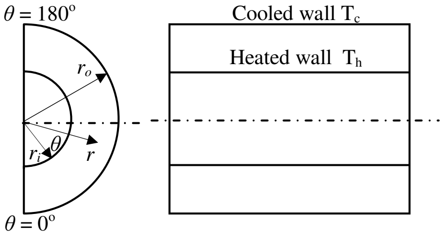

Fig.1. Natural Convection in Air Filled Annulus Bounded by Two Isothermal Walls

Taking the curl of **eqs.(2)and(3)** to eliminate the pressure term, the vorticity transport equation is obtained in the dimensionless form

$$\frac{\partial\Omega}{\partial\tau}+U\frac{\partial\Omega}{\partial R}+\frac{V}{R}\frac{\partial\Omega}{\partial\theta}=Gr\left(\cos\theta\frac{1}{R}\frac{\partial(R\Theta)}{\partial R}-\sin\theta\frac{1}{R}\frac{\partial\Theta}{\partial\theta}\right)+\nabla^2\Omega \qquad (10)$$

In the same manner, the dimensionless form of the energy equation is written as

$$\frac{\partial\Theta}{\partial\tau}+U\frac{\partial\Theta}{\partial R}+\frac{V}{R}\frac{\partial\Theta}{\partial\theta}=\frac{1}{\mathrm{Pr}}\nabla^2\Theta \qquad (11)$$

$$\text{also,}\,U=\frac{1}{R}\frac{\partial\Psi}{\partial\theta},\; V=-\frac{\partial\Psi}{\partial R} \qquad (12)$$

where all constants, variables and operators are dimensionless.

In the **eqs. (9-12)**, the following dimensionless variables and parameters are used

$$R=\frac{r}{r_i},\;\theta=\theta\;U=\frac{ur_i}{\upsilon},\;V=\frac{vr_i}{\upsilon},\;\tau=\frac{t\upsilon}{r_i^2},\;\Theta=\frac{T-T_c}{T_h-T_c},\;Gr=\frac{g\beta(T_h-T_c)r_i^3}{\upsilon^2},$$

$$\nabla^2=r_i^2\nabla^2 \qquad (13)$$

Eqs. (10) and **(11)** are coupled through the buoyancy force. Furthermore, both the vorticity **eq (10)** and energy **eq. (11)** are non-linear due to the convective terms. It is to be noted that both the vorticity **eq. (10)** and energy **eq. (11)** are of the parabolic type and the stream function **eq. (9)** is of the elliptic type. **Eq. (9)** is coupled with **eqs. (10)** and **(11)** through **eq. (12)** which relates the stream function to the velocities. Our problem is to seek Θ(r,θ,t), Ω(r,θ,t) and ψ(r,θ,t) which satisfy three partial differential **eqs. (9), (10) and (11)** as well as the following initial and boundary conditions. To begin with, the fluid in the annulus is stationary with a uniform temperature:

$$\Omega=\Psi=T=0\,\text{every where at }\tau=0 \qquad (14)$$

The boundary conditions are

$$\Psi=\frac{1}{R}\frac{\partial\Psi}{\partial\theta}=\frac{\partial\Psi}{\partial R}=0\text{ on both walls,i.e. }R=R_i\text{ and }R=R_o, \qquad (15)$$

$\theta = 1$ at $R = 1$, (16-a)

$\theta=0$ at $R =$ (16-b)

Eqs (5) and (9-11) are the final form of governing equations, which were transformed into the finite difference equations and solved numerically **(Chun-Yen 1979)**. The relaxation factors chosen (1.7) for the stream function, and the number of nodal points in the grid was 41, 21 for the *R-θ* respectively.

NUMERICAL SOLUTION

In the field of heat transfer, several numerical methods have been developed to deal with complicated physical problems. The finite difference method is one of the most widely used numerical methods for decades. The present work is concerned with numerical simulation of two dimensional transient natural convection flow, by means of alternating direction implicit (ADI) method for vorticity and energy equation, and by successive over relaxation (SOR) method for stream function equations. The time increment **(Tsui and Trembaly1983)** is

$$\Delta\tau = \frac{2}{2\left(\frac{1}{(\Delta r)^2}+\frac{1}{(\Delta\theta)^2}\right)+\frac{U}{\Delta r}+\frac{V}{\Delta\theta}} \qquad (17)$$

The convergence criteria for Nusselt number is

$$\frac{Nu^{n+1}-Nu^{n}}{Nu^{n+1}} \le \varepsilon \qquad (18)$$

The way for checking the convergence is to compare the mean Nusselt numbers at the inner and outer radius. These are usually within $\varepsilon = 10^{-4}$ at convergence. This convergence criteria is employed in this paper.

In order to gain confidence in our numerical results, we tried to compare ours with previously published resultsre **(Charrier-Mojtabi et.al.1979)** and **(Tsui and Trembaly1983)**. **Fig.2-a**, which depicts streamlines and isotherms for Gr=10 000, Pr=0.7 and a=2, resemble results presented by **(Tsui and Tremblay 1983)** at Gr =10000, Pr=0.7, and a=2.0. **Fig.2-b** which shows streamlines and isotherms for Gr =38800, Pr=0.71 and a=2, is similar to one given by **(Charrier-Mojtabi et al. 1979)** at Ra = 3x10^4, Pr = 0.7 and a = 2.0. We see good agreement in results at diameter ratio of 2.0 and some deviation occurs in results with diameter ratio of 1.5.

After obtaining confidence in our results see Table1, we processed to compute the mean transient Nusselt numbers at inner and outer radius for our calculations, which cover the Grashof number 10^2 to 10^5 including physical realistic cases and **(Tsui and Trembaly 1983).**

Table 1. Mean Nusselt number resultsfor a=2.0, Pr=0.7

a	Gr_{Ri}	$\overline{Nu}$ (Tsui and Trembaly 1983).	$\overline{Nu}$ (Present study)
2.0	10 000	1.64	1.658
	38 800	2.4	2.42
	88 000	3.08	2.99

Local Nuselt numbers at the inner and outer radius Nu_i and Nu_o are defined as follows:

$$Nu_i = -\ln a\left[R\frac{\partial\Theta}{\partial R}\right]_{r=R_i} \qquad (19a)$$

$$Nu_o = -\ln a\left[R\frac{\partial\Theta}{\partial R}\right]_{r=Ro} \qquad (19b)$$

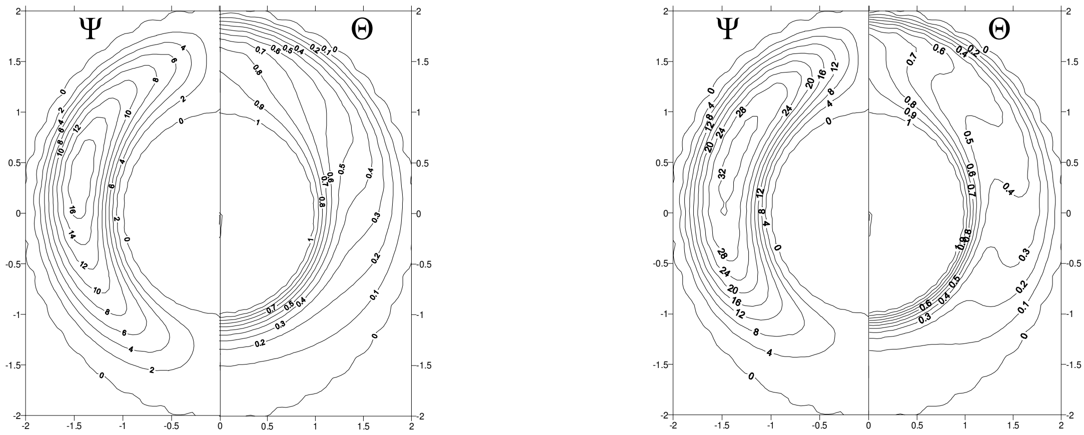

a) Gr=10 000 (Tsui and Trembaly 1983).

b) Gr=38 800 (Charrier-Mojtabi et.al.1979)

Fig.2: Streamlines and isotherms, diameter ratio=2.0, Pr = 0.7,(Tsui and Trembaly 1983).

The mean Nusselt numbers $\overline{Nu_i}$ and $\overline{Nu_o}$ are the angular average of their local values over the cylinder inner and outer surface and can be carried out using numerical integration by Trapezoidal rule **(Gerald 1970)**, through **eq. (19c).**

$$\overline{Nu} = \frac{1}{A}\int_{A} Nu.dA \qquad (19c)$$

Both mean transient $\overline{Nu_i}$ and $\overline{Nu_o}$, vs. dimensionless time, τ, are plotted in **Fig.3**, which included physical realistic cases **(Tsui and Trembaly 1983).** As τ increases, both $\overline{Nu_i}$ and $\overline{Nu_o}$ approach to their steady- state values and should be equal based on a simple energy balance. In fact, due to the numerical techniques involved, the values actually obtained differ somewhat. Generally, we can note that the dimensionless time increases with increases diameter ratio and decreases with increased Grashof number.

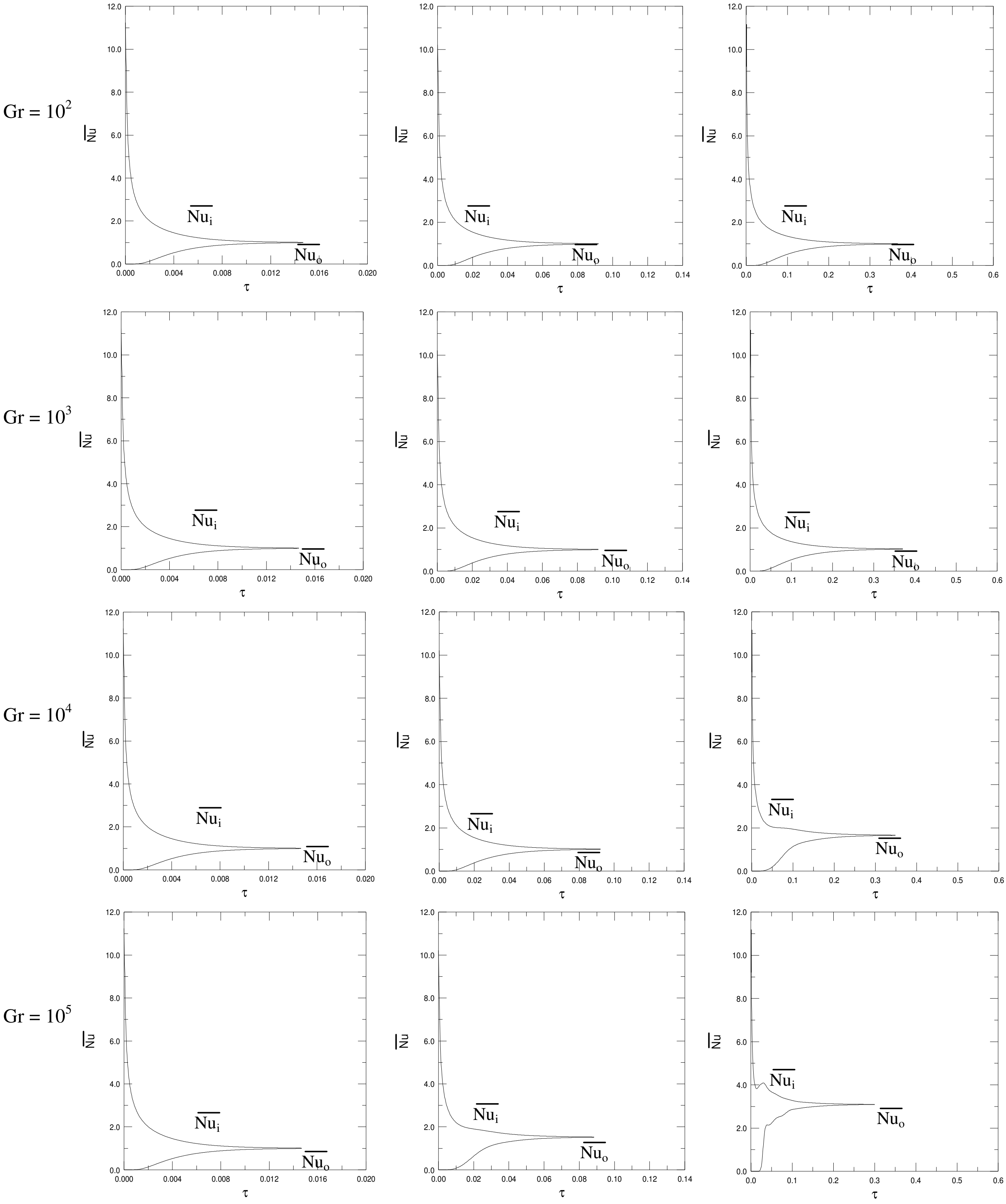

a)a=1.2 b)a=1.5 c)a=2.0

Fig.3. Mean Nusselt number vs. dimensionless time, Pr=0.7

The effect of Prandtl number on results was determined by varying Prandtl number at values 0.7, 5.0, and 10.0 respectively, corresponding to the same values of Grashof numbers and diameter ratios. Looking at the effect of variation in Prandtl number that when the diameter ratio changes from 1.2 to 2.0, It seen that, at a diameter ratio a=1.2, there is no significantly change in the convection heat transfer, i.e., $\overline{Nu}$ even Gr=1x10^{5}

The maximum non-dimensional transition time increases with increases Prandtl number and high convection occur, see **Fig.4** The values of mean Nusselt number of higher Prandtl number are higher than those for air.

The convection heat transfer increases very rapidly when the diameter ratio increases further from 1.5 to 2.0 and especially at high Grashof number. A review of **Fig.3** and **4** show both $\overline{Nu_i}$ and $\overline{Nu_o}$ approach unity as time increase.

The maximum non-dimensional transition time from transient- state to steady- state is increased with increase Grashof number that less than unity and excesses unity at high Prandtl number and diameter ratio.

Local Nusselt number is generally smaller and more uniform at lower Prandtl number as, including an approach to conduction. The numerical data obtained in the present study are correlated to one-fourth power law see **Fig.5**.

The win OS cpu 1.7G and software (Grafer 4.0 and surfer 7.0)to plot graphs in present study.

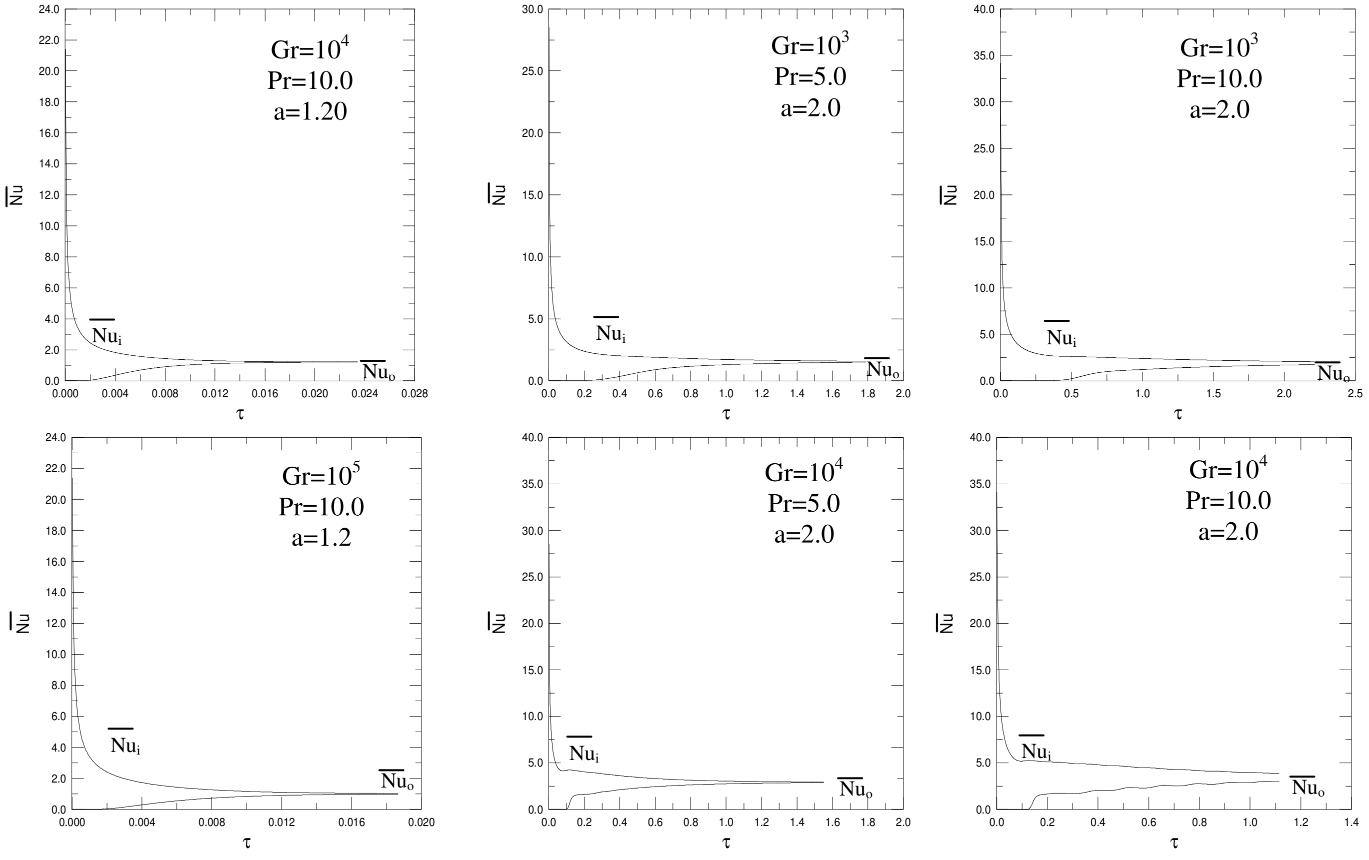

Fig.4. Dimensionless Time τ at different Prandtl Numbers

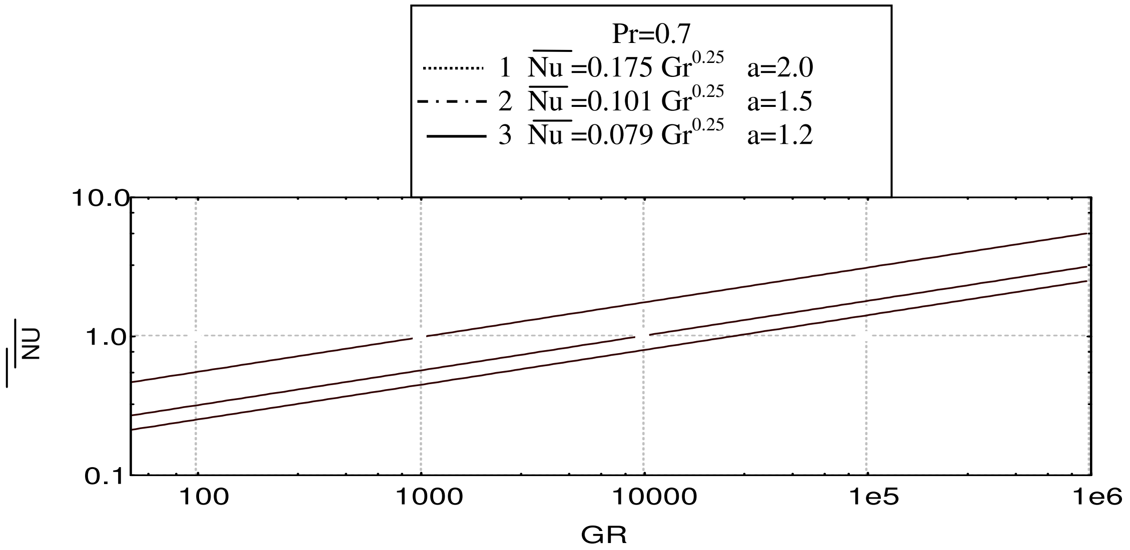
Pr=0.7
1 $\overline{Nu}$ =0.175 $Gr^{0.25}$ a=2.0
2 $\overline{Nu}$ =0.101 $Gr^{0.25}$ a=1.5
3 $\overline{Nu}$ =0.079 $Gr^{0.25}$ a=1.2
10.0
1.0
0.1
$\overline{NU}$
100
1000
10000
1e5
1e6
GR

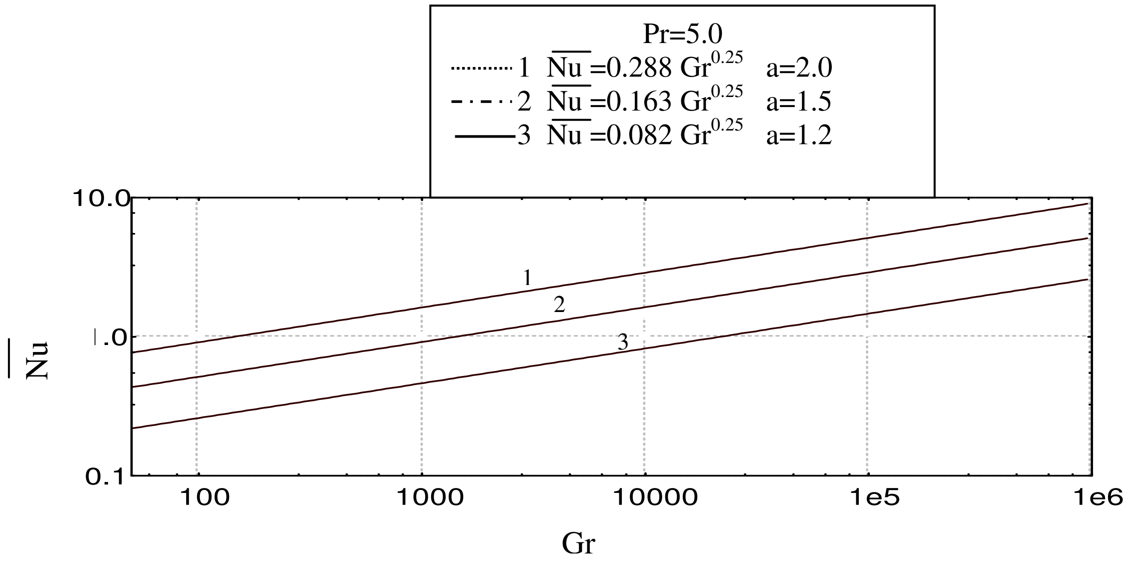
Pr=5.0
1 $\overline{Nu}$ =0.288 $Gr^{0.25}$ a=2.0
2 $\overline{Nu}$ =0.163 $Gr^{0.25}$ a=1.5
3 $\overline{Nu}$ =0.082 $Gr^{0.25}$ a=1.2
10.0
1.0
0.1
1
2
3
$\overline{Nu}$
100
1000
10000
1e5
1e6
Gr

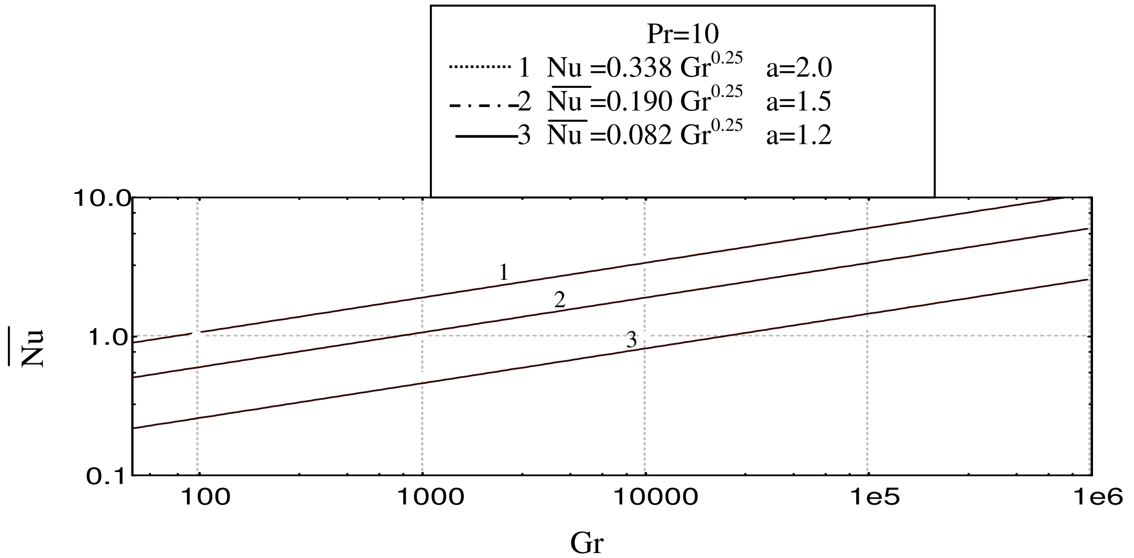
Pr=10
1 Nu =0.338 $Gr^{0.25}$ a=2.0
2 $\overline{Nu}$ =0.190 $Gr^{0.25}$ a=1.5
3 $\overline{Nu}$ =0.082 $Gr^{0.25}$ a=1.2
10.0
1.0
0.1
1
2
3
$\overline{Nu}$
100
1000
10000
1e5
1e6
Gr

Fig.5 Correlation of mean Nusselt number as a function of Grashof number for different Prandtl number

RESULTS AND DISCUSSION

Our range of interest covers Grashof numbers from approximately $1x10^2$ to $1x10^5$ and diameter ratio from 1.2, 1.5 and 2.0. Three steady state mean Nusselt number, $\overline{Nu}$ vs. Grashof number, Gr, curves are shown in **Fig.5** with diameter ratio, a, as a parameter. It is seen that, at a diameter ratio a=1.2, there is no or little convective heat transfer even $Gr=1x10^5$ which has been substantiated by Kuehn and Goldstein's calculation **(Kuehn and Goldstein 1978).**

Also, it is clear that the maximum increment in the amount of convection heat transfer with larger Prandtl number ($Gr=10^5$) by 31% and 25% at a=1.5, 2.0 respectively compared with corresponding values at low Prandtle number.

Looking at the variation of $\overline{Nu}$ vs. a at fixed Gr it follows that when the diameter ratio, a, changes from 1.2 to 1.5, the mean Nusselt number increases very rapidly. When the diameter ratio increases further from 1.5 to 2.0, there is a substantial enhancement of the convective heat transfer .However; the rate of increase of $\overline{Nu}$ vs. a slow down (with increase a than 2.0). After (a) it reaches 2, the rate of increase of convective heat transfer flattens out. This is demonstrated **(Kuehn and Goldstein 1976).**

], which despite a collection of experimental data from previous authors. From an engineer viewpoint, there is no advantage to increase the diameter ratio beyond two as far as natural convection is concerned.

The flow and heat transfer results can be divided in to several regimes (**Kuehn and Goldstein 1978**).Near Grashof number of 10^2 the maximum stream function or center of rotation is near 90^o. The flow in the top and bottom portions of the annulus is symmetric about the 90^o position. The velocity profiles at any one position are similar, with the magnitudes directly proportional to the Grashof number. The velocities too small to affect the temperature distribution, which remains essentially as in pure conduction, see **Fig.6**.

This makes the convection terms in **eqs. (10) and (11)** vanish. Therefore, **eqs. (10) and (11)** can be approximated by

$$\nabla^2\Omega = Gr\left(\sin\theta\frac{1}{R}\frac{\partial\Theta}{\partial\theta} - \cos\theta\frac{\partial\Theta}{\partial R}\right) \qquad (19)$$

$$\nabla^2\Theta = 0 \qquad (20)$$

A transition region exists for Grashof numbers between 10^2 and 10^4. The flow remains in essentially the same pattern but becomes strong enough to influence the temperature field. As the Grashof number increases, the center of rotation moves upwards.

The isotherms begin to resemble eccentric circles near a Grashof of 10^3, as can be seen in **Fig. 6** at different diameter ratio. This has been called the 'pseudo-conductive regime' **(Grigull and Hauf 1966),** since the overall heat transfer remains essentially that of conduction.

With further increase in Grashof number and increasing diameter ratio, the temperature distribution becomes distorted, resulting in an increase in mean Nusselt number. From a plot of streamlines and isotherms at Grashof number of 10^4, the radial temperature inversion appears indicating the separation of the inner and outer cylinder thermal boundary layers which obvious clearly at the top portion of a=2.0. The cross indicates the location of maximum value of the stream function, which would be the center of rotation. This maximum is located near the 70° position. Local heat transfer flux values are becoming further distorted from those of conduction. Essentially heat is being convected from the lower portion of inner cylinder to the outer cylinder. The vorticity in the central core is almost constant, including a region approaching solid-body rotation; see **Fig.6**-c at high Grashof number.

In addition, steady laminar boundary layer regime exists between Grashof number of 10^4 and 10^5. Streamlines and isotherms in this region are shown in **Fig.5.** Boundary layer exists on both cylinders although the lower portion of the annulus is practically stagnating.

As the Grashof number increases further, the flow above the inner cylinder will become turbulent. This will create a turbulent boundary layer on the outer cylinder while the inner boundary layer remains laminar **(Lis1966)**. Eventually, the inner boundary layer will also become turbulent.

The effect of diameter ratio on the results was determined by vary R_o/R_{in} from 1.2 to 2.0 for the whole range of our numerical calculations. The flow pattern don't change significantly at lower Grashof numbers although the center of rotation moves towards the top with increasing diameter ratio (a), but separation is clear at high Grashof numbers. The maximum Nusselt number occur near a=2.0 at Gr=10^5 but occurs at smallest value at larger a. However, the mean Nusselt number increased as the outer cylinder is made large at constant Grashof number. As the outer cylinder becomes large relative to the inner diameter, the mean temperature in the annulus decreased. This indicates that the thermal resistance around the inner cylinder is becoming the dominant factor in the mean Nusselt number. As the outer cylinder become infinitely large, the only thermal resistance is around the inner cylinder with the temperature in the gap equal to that of the outer cylinder. At large diameter ratio, the total heat flow will be essentially that from a single horizontal cylinder in an infinite medium.

Fluids with larger Prandtle number will remain steady until larger Grashof number is attained. This is observed **(Liu et.al. 1980)** and **(Charrier-Mojtabi 1979)** and confirmed by the present numerical results. **Fig.6** shows streamlines and isotherms at different Grashof number and diameter ratio with Prandtl around 0.7.

The maximum stream function is about 15° from the top with lower portion of annulus particularly stagnant. The vorticity approaching to zero in the central portion of the annulus, indicating the beginning of stationary core region. The center of rotation moved near the top as the Prandtl number increased.

Also, with further increase in Grashof number and increasing diameter ratio, the temperature distribution becomes distorted, resulting in an increase in mean Nusselt number. From a plot of streamlines and isotherms at Grashof number of 10^4, the radial temperature inversion appears indicating the separation of the inner and outer cylinder thermal boundary layers which is obvious clearl at the top portion of a=2.0. As the Grashof number increased further, the flow above the inner cylinder will become turbulent. This will create a turbulent boundary layer on the outer cylinder while the inner boundary layer remains laminar **(Lis 1966).**

Eventually, the inner boundary layer will also become turbulent. An oscillating laminar flow regime begins near Grashof number of 10^5.

At low Prandtl number, the velocity profile at any one position is similar with the magnitude directly proportional to the Grashof number. The velocities are too small at low Grashof number and increases with increased Garshof number and Prandtle number causing the separation of inner and outer cylinder thermal boundary layer.

The velocity profile in the outer cylinder boundary layer in the top half of the annulus ($30^0 \le \theta \le 90^o$) are independent of angular position. As the fluid moves down past the 90° position the outer boundary layer weakens, and disappears entirely near the bottom, see **Fig.7**, at high Grashof number. The velocities at the bottom of the annulus are very low compared to the velocities at the middle and top regions **(Kuehn and Goldstein 1978).**

On the basis of the good agreement between numerical results of the present study and experimental and numerical results of previous work. It seems possible to determine heat transfer parameters free convection in enclosures using either method. The experiments have the advantage of being applicable to unsteady flow and turbulence, where the numerical computation becomes unstable. However, the numerical analysis gives more information, including the velocity vector, which is difficult to obtain experimentally. The error in numerical results arise from the constant property assumption, the finite number of grid of nodes and the convergence level of the solution though not perfect owing to the consideration mentioned above is quite good lending validity to results with previous work.

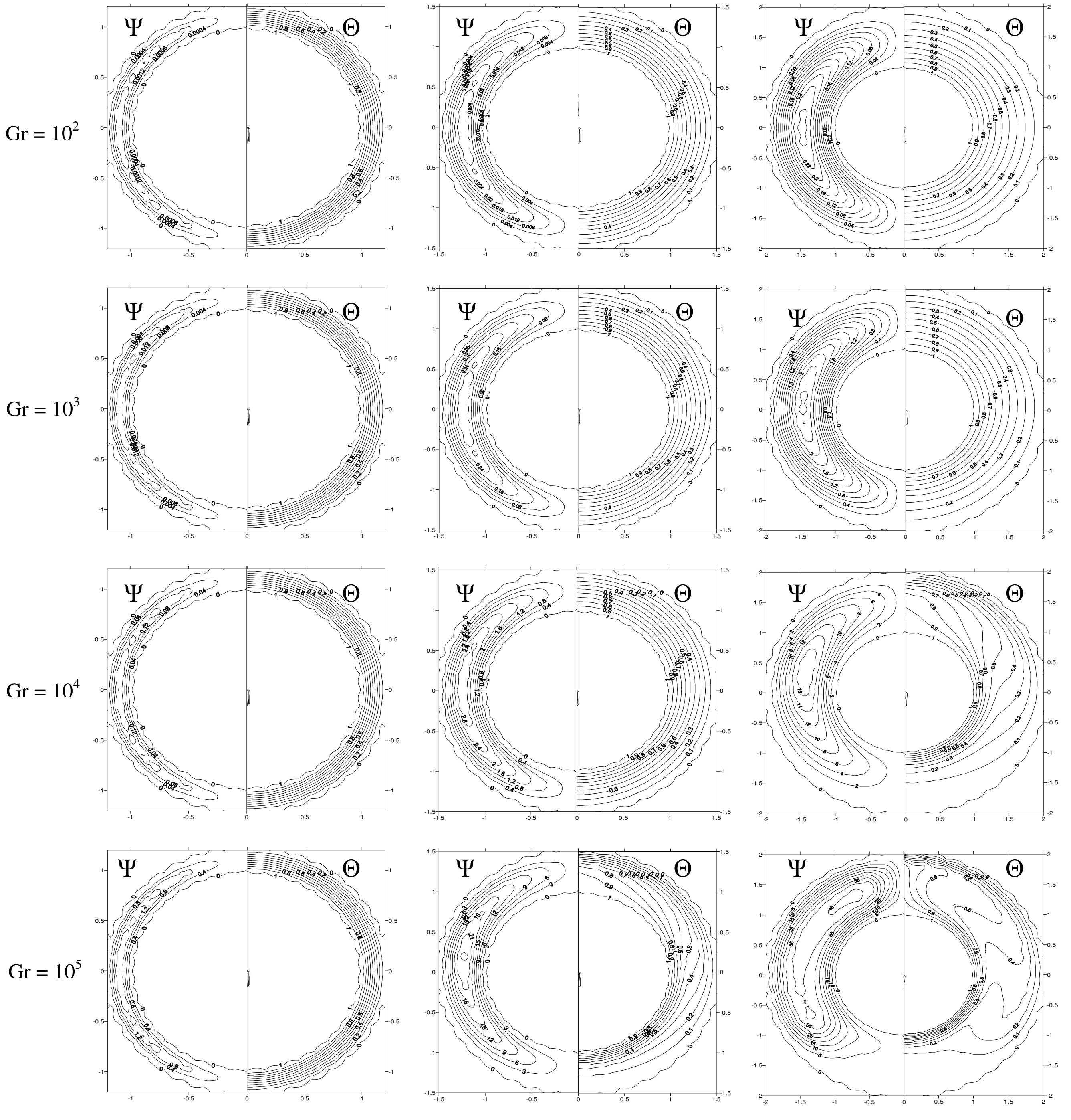

a=1.2 a =1.5 a =2.0

Fig.6 Streamlines and Isotherms at Different Grashof Number, Pr=0.7

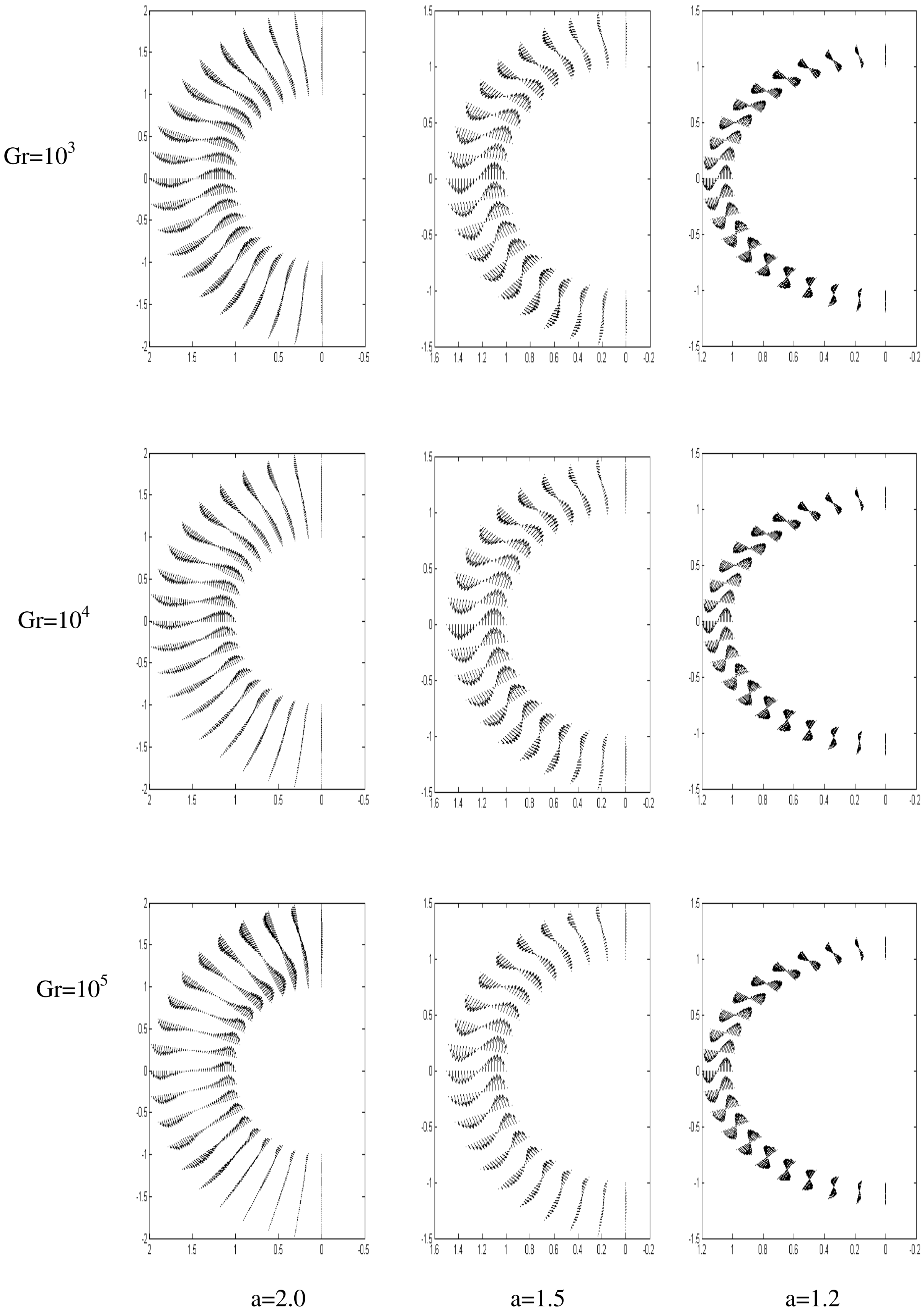

Fig.7 Velocity vector for natural convection in an annulus at Pr=0.7

SUMMARY

The numerical study of natural convection heat transfer and fluid flow between horizontal isothermal concentric cylinders has been presented. Quantities obtained numerically include temperature distribution, local and average Nusselt numbers. The numerical solutions confirm velocity distribution and extend results to lower Grashof numbers.. Numerical solutions covered the range of Grashof numbers from pure conduction to steady laminar boundary layer flow for R=1.2, 1.5, and 2.0. The flow was steady for all Grashof numbers investigated. The influence of diameter ratio and Prandtl number was determined. Good agreements with available previous published resultes.

REFERENCES

Abbott M. R. (1964).", A numerical method for solving the equations of natural convection in a narrow concentric cylindrical annulus with a horizontal axis", Q. JI Mech. Appl. Math, pp 471-481, 1964.

Bishop, E. H. and Carely, C. T. (1966,)."Photographics studies of natural convection between concentric cylinders, Proc Heat Transfer Fluid Mech. Inst. Pp63-78, 1966.
Bishop, E. H., Carley, C. T. and Powe, R. E. (,1968). " Natural convection oscllatoryoscillatory flow in cylindercalcylindrical annuli".,Int. J. Heat Mass Transfer,11,pp. 1741-1752,1968..

Charrier-Mojtabi M.C, A.Mojtabi A.and J.P Caltagirone J.P(1979,). "Numerical solution of a flow due to natural convection in hoporizontal cylindrical annulus", J.Heat Transfer 101,171-173(1979).

Chun-Yen .Chow, Jone Wilely and sons, (1979)."An Introduction to computational fluid mechanics". McGraw-Hill, 2nd Edition, 1979.

Crawford, L. and R . Lemlich R, (1962)."Natural convection in horizontal concentric cylindrical annuli"., IEC Fundamental (4), pp 260-264, 1962.

Eckert, E. R. G. and Soehngen, E. E. , (19)."Studied on heat transfer in laminar free convection with the Zehnder-Mach interferometer". Wright. Patterson AFB Tech. Rep., no. 5747, ATI44580.

Gerald C. F, (1970). "Applied numerical analysis" , Addison-Wesley publishing company, 1970.

Grigull, U. and Hauf. W., (1966). "Natural convection in horizontal cylindrical annuli", 3rd Int. Heat Transfer Conf., Chicago, pp. 182-195, 1966.

Han C. Y. and S. W. Baek S. W., (1999)."Natural convection phenomena affected by radiation in concentric and eccentric horizontal cylindrical annuli, Numerical Heat Transfer, Part A, 36: pp 473-488, 1999.

Hodnett P. F., (1973). "Natural convection between horizontal heated concentric circle cylinders", Z. Angew. Math Phys. 24, pp 507-516, 1973..

Kuehn T. H. and R.J. Goldstein R.J. (1976). ", Correlationg equations for natural convection heat transfer between horizontal circular cylinders". Int. J. Heat Transfer 19, 1127-1134(1976).

Kuehn T.H. and R. J. Goldstein R. J (1978)., "An experimental and theoretical study of natural convection in the annulus between horizontal concentric cylinders"., J.Fluid Mech.4, 695-719(1978).

Lis, J. (1966). "Experimental investigation of natural convection heat transfer in simple and obstructed horizontal annuli, ". 2nd Int. Heat Transfer Conf., Chicago, pp. 196-204, 1966.

Liu, C. Y., Mueller, W. K. ad Landis, F,(1961).," Natural convection heat transfer in simple and obstructed horizontal annuli", Int. Developments in Heat Transfer, A.S.M.E. pp976-984.,1961.

Liu, C. Y., Mueller, W. K. and Lands, F.(1962). ", Natural convection heat transfer in long horizontal cylinder annuli"., Int Development in Heat Transfer, A.S.M.E., pp. 976-984.

Mack L. R. and E. H. Bishop E. H.(1968), "Natural convection between horizontal concentric cylindrical for low Rayleigh numbers" , Q. JI Mech, Appl. Math, pp 223-241, 1968.

Pederson, B. O., Doepken, H. C. and Bolin, P. C., (1971). "Development of a compressed-gas insulated transmission line". I. E. E. E. Winter Poer MKetting, paper 71 TP 193-PWR, 1971.

Pow, R. E., Carley, C. T. and Bishop, E. H., (1969). "Free convection flow patterns in cylindrical annuli, " J. Heat Transfer, 91, pp. 310-314, 1969.

Powe R. E., C. T. Carley C. T.(1971) and S. L., "A numerical solution for natural convection in cylindrical annuli"., J. Heat Transfer 93, pp 210-220, 1971.

Torrance K.E.(1985), "Numerical method Heat Transfer, Handbook of Heat Transfer Fundamentals"., McGraw-Hill, 2nd Edition.

Tsui Y.T. and B. Trembaly B.(1983), "On Transient Natural Convection Heat Transfer in the Annulus between Convective, Horizontal Cylinders with Isothermal Surfaces", Int.J. Heat and Mass Transfer, Vol.27, No.1, pp.103-111, 1983.

NOMENCLATURE

Δr	mesh interval in r-direction
$\Delta\theta$	mesh interval in θ-direction
a	diameter ratio, radius ratio, r_o/r_i
c_p	specific heat at constant pressure
g	gravitational acceleration
Gr	Grashof number, $g\,\beta\,(T_h-T_c)\,r_i^3\,/\upsilon^2$
k	thermal conductivity
Nu	local Nusselt number
Pr	Prandtl number, υ/α
r	radial distance
R	dimensionless radial coordinate, r/r_i
Ra	Rayleigh number, $Ra= Gr.Pr$
T	temperature
U	dimensionless radial velocity, $ur_i/\,\upsilon$
u	radial velocity
V	dimensionless tangential velocity, $vr_i/\,\upsilon$
v	tangential velocity

GREEK SYMBOLS

ψ	dimensionless stream function
τ	dimensionless time, $t\upsilon/\,r_i^2$
ρ	fluid density
α	thermal diffusivity, $(\,k/\rho\,c_p)$
β	thermal expansion coefficient of fluid
Θ	dimensionless temperature, $(T-T_c\,)/(T_h-T_c)$
υ	kinematics viscosity
Ω	dimensionless vorticity

SUBSCRIPTS

h,c	hot and cold, respectively
i,o	inner and outer, respectively

SUPERSCRIPTS

—	mean

EVALUATION OF TEMPERATURE DISTRIBUTION AND FLUID FLOW IN FUSION WELDING PROCESSES

Ass. Prof. Dr. Ihsan Y. Hussain
Mech. Engr. Dep.
College of Engr.
University of Baghdad
Baghdad – Iraq

Salah Sabeeh Abed - AlKareem
Al-Tahreer Institute
Ministry of Labor and Social Affairs
Baghdad – Iraq

ABSTRACT

A theoretical study of heat transfer and fluid flow phenomena in welding process has been carried out in the present work. The study involved the numerical solution of the transient Navier-Stokes and Energy equations of the weld pool region by using Finite Difference Method. The electromagnetic force field and buoyancy were included in the formulation The stream-vorticity formulation was used in the mathematical model. The numerical solution is capable of calculating the vorticity, stream function, velocity, temperature, and the interface movement of the weld pool in Gas Metal Arc Welding (GMAW). The model can be used to solve the Gas Tungesten Arc Welding (GTAW) problem. A numerical calculations algorithm was developed to carry out the numerical solution. The numerical results showed that the finger penetration phenomena occurs in the Gas Metal Arc weld is adequately explained through the application of the model. It is found that the frequency of spray transfer is a dominant factor in addition to shape of the weld pool geometry. A verification of numerical results was made through a comparison with a previous work, the agreement was good, confirming the capability and reliability of the proposed numerical algorithm in calculating fluid flow and heat transfer in Gas Metal Arc weld pools.

الخلاصة

في هذا البحث ، تمت دراسة انتقال الحرارة وجريان المائع في عمليات اللحام ألانصهاري نظرياً ، تضمنت الدراسة النظرية الحل العددي للمنظومة العابرة (غير المستقرة) لمعادلة الزخم والطاقة لمنطقة بركة اللحام (منطقة الطور المنصهر) باستخدام طريقة الفروق المحددة. تضمنت الصياغة قوة المجال الكهرومغناطيسي وقوة الطفو وتم استخدام صياغة الدوامية ودالة الانسياب في النمذجة الرياضية . أمكانية الحل العددي تتضمن حساب الدوامية ، دالة الانسياب ، السرعة ، درجة الحرارة والسطح البيني المتحرك لمنطقة اللحام بطريقة لحام القوس الكهربائي المعدني باستعمال غطاء غازي . هذا النموذج نستطيع استخدامه لحل المسألة بطريقة لحام القوس الكهربائي بقطب التنكستن باستعمال الغاز الواقي . تم التوصل لبرنامج حسابات عددية لتنفيذ الحل العددي . أظهرت النتائج العددية بأن ظاهرة التغلغل الإصبعي التي تحدث في طريقة لحام القوس الكهربائي المعدني باستعمال غطاء غازي وافية بالغرض للتوضيح من خلال التطبيق في النموذج المعمول به . لقد وجدنا بأن مقدار أنتقال الرش الترددي هو العامل السائد بجانب الشكل الهندسي المستخرج لبركة اللحام . تمت مقارنة النتائج العددية التي تم إنجازها مع البحوث السابقة . التوافق بين النتائج جيد ويؤكد أمكانية وموثوقية الخطوات العددية المقترحة في حساب جريان المائع وانتقال الحرارة بطريقة لحام القوس الكهربائي المعدني باستعمال غطاء غازي في بركة اللحام .

KEY WORDS : Heat Transfer, Fluid Flow, Electromagnetic Force, Weld Pool, Numerical Solution

INTRODUCTION

The heat and fluid flow in the weld pool can significantly influence the pool geometry and the temperature gradients. A detailed knowledge of the temperature filed and thermally induced flow in a weld pool is important in understanding the phenomena and in development of improved welding techniques, and numerical simulations offer the possibility of avoiding this difficulty and provide a better quantitative description of the coupled solution behavior. If we consider a molten weld pool resulting from an applied surface temperature or heat flux, the thermal gradients induce buoyancy forces in the weld pool that tend to cause fluid flow. It is of considerable practical interest to understand quantitatively the heat and fluid flow phenomena in weld pool, because both the velocity and temperature distributions of molten metal affect the weld pool geometry, microstructure, and mechanical properties of the weld produced. Inherent to the welding process is the formation of a pool of molten metal directly below the heat source. The shape of this molten pool is influenced by the flow of both heat and metal, with melting occurring ahead of the heat source and solidification behind it. Fluid flow in weld pool can strongly affect the quality of the resultant weld. Variations in the weld characteristics, which are likely to occur from changes in the weld pool fluid flow are weld penetration, undercutting, surface smoothness segregation pattern, gas porosity and solidification structure, **(Gukan and Sundararajan. 2001)**, see **Fig.1**. The problem was investigated in literatures with different approaches, **(Oreper and Szekely.1987)** developed a general mathematical statement to describe the transient weld pool development. In the formulation, axi-symmetric systems are considered and allowance is made for buoyancy, surface tension, and electromagnetic forces. **(Tsao and Wu.1988)** developed a mathematical model to evaluate the effect of the electromagnetic force field, the velocity field and the temperature field in a Gas Metal Arc (GMA) weld pool. **(Tsai and Kou. 1990)** studied the convection flow induced by the electromagnetic force in the weld pool during gas tungsten arc welding. In order to accurately describe the boundary conditions, **(Kim and Na. 1994)** developed a computer simulation of three dimensional heat transfer and fluid flow in Gas Metal Arc (GMA) welding by considering the three driving forces for weld-pool convection. **(Gukan, et. al. 2001)** developed a systematic study of a two dimensional model to analyze the role of convection in the stationary (GTA) welds to analyze the behavior of weld pool convection and its effect on the weld geometry.

The present work represents the beginning of a new research line in Iraq that aims to investigate the thermal and fluid flow phenomena associated with welding process. A computational study of fluid flow and heat transfer phenomena occurred in the weld pool. The simulation covers the molten phase, the two phase and the solid phase region.

MATHEMATICAL MODEL

Fig.2 shows a diagram of a Gas Metal Arc (GMA) liquid pool and the cylindrical coordinate system chosen for analysis. Velocities along the radial and axial directions are expressed as U and V, respectively. A spatially distributed heat flux, q(r), and current flux, j(r), fall on the free surface at (Z = 0), which is the surface of the workpiece, the energy exchange between the spray droplets and molten pool is ΔH.As shown in **Fig.2**, let U=U(r,z) and V=V(r,z) denote the velocity components in the radial r and axial z directions, respectively. The unsteady-state continuity, momentum and energy equation of the incompressible fluid in the molten pool is **(Salah. 2005)** ;

$$\frac{1}{r}\frac{\partial}{\partial r}(rU)+\frac{\partial}{\partial z}(V)=0 \tag{1}$$

$$\rho\left(\frac{\partial U}{\partial t}+U\frac{\partial U}{\partial r}+V\frac{\partial U}{\partial z}\right)=F_r-\frac{1}{\rho}\frac{\partial p}{\partial r}+\mu\left[\frac{\partial}{\partial r}\left(\frac{1}{r}\frac{\partial}{\partial r}(rU)\right)+\frac{\partial^2 U}{\partial z^2}\right] \tag{2}$$

$$\rho\left(\frac{\partial V}{\partial t}+U\frac{\partial V}{\partial r}+V\frac{\partial V}{\partial z}\right)=F_z-\frac{1}{\rho}\frac{\partial p}{\partial z}+\mu\left[\frac{1}{r}\frac{\partial}{\partial r}\left(r\frac{\partial V}{\partial r}\right)+\frac{\partial^2 V}{\partial z^2}\right] \tag{3}$$

$$\left(\frac{\partial T}{\partial t}+U\frac{\partial T}{\partial r}+V\frac{\partial T}{\partial z}\right)=\alpha\left[\frac{\partial^2 T}{\partial^2 r}+\frac{1}{r}\frac{\partial T}{\partial r}+\frac{\partial^2 T}{\partial^2 z}\right]+\Delta H/\rho C_p \tag{4}$$

Using the vorticity transport formulation **(Salah 2005)**, it can be shown that ;

$$\frac{\partial \omega}{\partial t}+\frac{\partial (U\omega)}{\partial r}+\frac{\partial (V\omega)}{\partial z}=\upsilon\left[\frac{\partial}{\partial r}\left(\frac{1}{r}\frac{\partial (r\omega)}{\partial r}\right)+\frac{\partial^2 \omega}{\partial z^2}\right]+g\beta\frac{\partial T}{\partial r}+\nabla\times\left(\bar{j}\times\bar{B}\right) \tag{5}$$

The stream function equation is ;

$$\frac{\partial}{\partial z}\left(\frac{1}{r}\frac{\partial \psi}{\partial z}\right)+\frac{\partial}{\partial r}\left(\frac{1}{r}\frac{\partial \psi}{\partial r}\right)=-\omega=\nabla^2\psi \tag{6}$$

The temperature equation in the conservative form is ;

$$\frac{\partial T}{\partial t}+\frac{1}{r}\frac{\partial (rUT)}{\partial r}+\frac{\partial (VT)}{\partial z}=\alpha\left[\frac{\partial^2 T}{\partial r^2}+\frac{1}{r}\frac{\partial T}{\partial r}+\frac{\partial^2 T}{\partial z^2}+\frac{\Delta H}{\rho C_p}\right] \tag{7}$$

The electromagnetic force term in **equ.(5)** is **(Tsao and Wu 1988)** ;

$$\nabla\times\left(\bar{j}\times\bar{B}\right)=\frac{C_o\mu_o l^2}{2\pi^2 L r^3}\left[1-\exp\left(-\frac{r^2}{2\sigma_j^2}\right)\right]^2\left(1-\frac{z}{L}\right) \tag{8}$$

and the energy exchange (ΔH) is ;

$$\Delta H=(2.28f\, e^{-C_1 r^2}) \tag{9}$$

Initial and Boundary Conditions Representations

The initial conditions used to solve temperature, vorticity and stream function equations are ;
$T_{i,j} = w_{i,j} = \psi_{i,j} = V_{i,j} = 0$ at $t=0$
The boundary conditions used are given in **Fig.3** .

NUMERICAL SOLUTION

The governing equations mentioned above were solved numerically by using the FDM. A grid arrangement was generated with the notation of **Fig.4**. The temperature of each grid point in weldment is compared with the melting temperature T_m. Once the liquid region emerges, the fluid flow and heat transfer in the weld pool and the heat conduction out of the molten pool are calculated.

The nodal equation at i=1 ; $1 \le j \le M$

$$\therefore T'_{1,j}=(a_1+a_2)T_{2,j}+a_3T_{1,j}+a_4T_{1,j-1}+a_5T_{1,j+1}+B(i) \tag{10}$$

The nodal equation at i=1 ; j =1

$$T'_{1,1}=(a_1+a_2)T_{2,1}+a_3T_{1,1}+\left(a_4+a_5\right)T_{1,2}+a_4\frac{2\Delta z}{K}q(i)+B(i) \tag{11}$$

The nodal equation at $2 \le i \le R/\Delta r+1$ (i.e r=R)

$$T'_{i,1}=a_1T_{i-1,1}+a_2T_{i+1,1}+a_3T_{i,1}+\left(a_4+a_5\right)T_{i,2}+a_4\frac{2\Delta z}{K}q(i)+B(i) \tag{12}$$

At i=1 ; j =1

$$\begin{aligned}&T'(i,j)=(1\text{-}4*\mathrm{k}*\mathrm{dt}/(\mathrm{row}*\mathrm{cp}*\mathrm{dr}^2)-2*us*dt/dr-2*vs*dt/dr)*T(i,j)+\\&(2*k*dt/(row*cp*dr^2)+2*us*dt/dr)*T(i+1;j)+\ldots\ldots.\\&(2*\mathrm{k}*\mathrm{dt}/(\mathrm{row}*\mathrm{cp}*dr^2)+2*vs*dt/dr)*T(i,\mathrm{j}+1)+\\&2*\mathrm{a1ph}*\mathrm{q(i)}*\mathrm{dt}/(\mathrm{row}*\mathrm{cp}*\mathrm{dr}^2)+dH(i)*dt/(row*cp)\ ;\ldots\end{aligned}\tag{13}$$

At i=1 ; j =M

$$\begin{aligned}&T'(i,j)=(1\text{-}4*\mathrm{k}*\mathrm{dt}/(\mathrm{row}*\mathrm{cp}*\mathrm{dr}^2)-2*h*dt/(row*cp*dr))*T(i,j)+\\&(2*k*dt/(\mathrm{row}*\mathrm{cp}*\mathrm{dr}^2))*T(i+1,\mathrm{j})+\ldots(2*\mathrm{k}*\mathrm{dt}/(\mathrm{row}*\mathrm{cp}*\mathrm{dr}^2))*T(i,j-1)\\&+(2*h*dt/(\mathrm{row}*\mathrm{cp}*\mathrm{dr}))*\mathrm{Ta}\ ;\ldots.\end{aligned}\tag{14}$$

At i=1 ; JFL < j < M

$$\begin{aligned}&T'(i,j)=(1\text{-}4*\mathrm{k}*\mathrm{dt}/(\mathrm{row}*\mathrm{cp}*\mathrm{dr}^2))*T(i,j)+(2*k*dt/(row*cp*dr^2))*T(i+1,j)+\ldots\\&(k*dt/(row*cp*dr^2))*T(i,j+1)+(k*dt/(row*cp*dr^2))*T(i,j-1)\ ;..\end{aligned}\tag{15}$$

At 1< i < N$_q$; j=1

$$\begin{aligned}&T'(i,j)=(1\text{-}4*\mathrm{k}*\mathrm{dt}/(\mathrm{row}*\mathrm{cp}*\mathrm{dr}^2)-2*us*dt/dr-2*vs*dt/dr)*T(i,j)+\\&(k*dt/(row*cp*dr^2)+us*dt/dr)*T(i+1,j)+(k*dt/(row*cp*dr^2)+\\&us*dt/dr)*T(i-1,j)+\ldots(2*\mathrm{k}*\mathrm{dt}/(\mathrm{row}*\mathrm{cp}*\mathrm{dr}^2)+2*vs*dt/dr)*T(i,j+1)+\\&2*dt*q(i)*a1ph/(row*cp*dr^2)+dH(i)*dt/(row*cp)\ ;\ldots.\end{aligned}\tag{16}$$

At i=N$_q$; j=1

$$\begin{aligned}&T'(i,j)=(1-4*k*dt/(row*cp*dr^2)-2*h*dt/(row*cp*dr)-us*dt/dr)*T(i,j)\\&+(k*dt/(row*cp*dr^2))*T(i+1,j)+(k*dt/(row*cp*dr^2)+us*dt/dr)*T(i-1,j)\\&+\ldots(2*\mathrm{k}*\mathrm{dt}/(\mathrm{row}*\mathrm{cp}*\mathrm{dr}^2))*T(i,j+1)+2*h*dt*Ta/(row*cp*dr)+\\&dH(i)*dt/(row*cp)\ ;\ldots\end{aligned}\tag{17}$$

At i=N ; j=1

$$\begin{aligned}&T'((i,j)=(1\text{-}4*\mathrm{k}*\mathrm{dt}/(\mathrm{row}*\mathrm{cp}*\mathrm{dr}^2)-4*h*dt/(\mathrm{row}*\mathrm{cp}*\mathrm{dr}))*\mathrm{T(i,j)}+\\&(2*\mathrm{k}*\mathrm{dt}/(\mathrm{row}*\mathrm{cp}*\mathrm{dr}^2))*T(i,j+1)+(2*k*dt/(\mathrm{row}*\mathrm{cp}*\mathrm{dr}^2))*T(i-1,j)+\\&(4*h*dt/(\mathrm{row}*\mathrm{cp}*\mathrm{dr}))*\mathrm{Ta}\ ;\ldots..\end{aligned}\tag{18}$$

At N$_q$ < i < N ; j=1

$$\begin{aligned}&T'(i,j)=(1-4*k*dt/(row*cp*dr^2)-2*h*dt/(row*cp*dr))*T(i,j)+\\&(k*dt/(row*cp*dr^2))*T(i+1,j)+(k*dt/(row*cp*dr^2))*T(i-1,j)+\ldots\\&(2*k*dt/(row*cp*dr^2))*T(i,j+1)+(2*h*dt/(row*cp*dr))*Ta\ ;\ldots\end{aligned}\tag{19}$$

At i=N ; j=M

$$T'(i,j)=(1-4*k*dt/(row*cp*dr^2)-4*h*dt/(row*cp*dr))*T(i,j)+$$
$$(2*k*dt/(row*cp*dr^2))*T(i-1,j)+(2*k*dt/(row*cp*dr^2))*T(i,j-1)+$$
$$(4*h*dt/(row*cp*dr))*Ta\;;... \tag{20}$$

At 1< i < N ; j=M

$$T'(i,j)=(1-4*k*dt/(row*cp*dr^2)-2*h*dt/(row*cp*dr))*T(i,j)+$$
$$(k*dt/(row*cp*dr^2))*T(i+1,j)+(k*dt/(row*cp*dr^2))*T(i-1,j)+....$$
$$(2*k*dt/(row*cp*dr^2))*T(i,j-1)+(2*h*dt/(row*cp*dr))*Ta\;;.... \tag{21}$$

At i = N ; 1< j < M

$$T'(i,j)=(1-4*k*dt/(row*cp*dr^2)-2*h*dt/(row*cp*dr))*T(i,j)+$$
$$(2*k*dt/(row*cp*dr^2))*T(i-1,j)+(k*dt/(row*cp*dr^2))*T(i,j+1)+.....$$
$$(k*dt/(row*cp*dr^2))*T(i,j-1)+(2*h*dt/(row*cp*dr))*Ta\;;..... \tag{22}$$

At 1< i < IFL (j) ; 1< i < IFL

$$T'(i,j)=(1-4*k*dt/(row*cp*dr^2))*T(i,j)+(k*dt/(row*cp*dr^2))*T(i+1,j)$$
$$+(k*dt/(row*cp*dr^2))*T(i-1,j)+.....(k*dt/(row*cp*dr^2))*T(i,j+1)+$$
$$(k*dt/(row*cp*dr^2))*T(i,j-1)\;;... \tag{23}$$

The temperature equation in weld pool ;

$$\mathrm{T}'_{i,j}=a\mathrm{T}_{i-1,j}+a_2\mathrm{T}_{i+1,j}+a_3\mathrm{T}_{i,j}+a_4\mathrm{T}_{i,j-1}+a_5\mathrm{T}_{i,j+1}+\mathrm{B} \tag{24}$$

Where ;

$$a_1=\frac{-\Delta t\left(U_b+\left|U_b\right|\right)\ (1-2i)}{4i\Delta r}+\frac{\alpha\Delta t(i-0.5)}{i(\Delta r)^2}$$
$$a_2=\frac{-\Delta t\left(U_f-\left|U_f\right|\right)(1+2i)}{4i\Delta r}+\frac{\alpha\Delta t(i+0.5)}{i(\Delta r)^2}$$
$$a_3=1-\Delta t\left(\frac{\left(U_f+\left|U_f\right|\right)(1+2i)+\left(U_b+\left|U_b\right|\right)(1-2i)}{4i\Delta r}\right)\cdot \tag{25}$$
$$\Delta t\left(\frac{\left(V_f+\left|V_f\right|-V_b+\left|V_b\right|\right)}{2\Delta z}+\frac{2\alpha}{(\Delta z)^2}+\frac{2\alpha}{(\Delta r)^2}\right)$$
$$a_4=\frac{\Delta t\left(V_b+\left|V_b\right|\right)}{2\Delta z}+\frac{\alpha\Delta t}{(\Delta z)^2}$$
$$a_5=\frac{-\Delta t\left(V_f+\left|V_f\right|\right)}{2\Delta z}+\frac{\alpha\Delta t}{(\Delta z)^2}$$
$$B=\Delta t(2.28\,fe^{-C_1(i\Delta r)^2})/\rho C_P$$

The electromagnetic force field in the vorticity equation ;

$$\nabla\times(\bar{J}\times\bar{B})=\frac{C_o\mu_o I^2}{2\pi^2 L(i\Delta r)^3}\left[1-\exp\left(-\frac{(i\Delta r)^2}{2\sigma_j^2}\right)\right]^2\left(1-\frac{j\Delta z}{L}\right) \tag{26}$$

$$\omega'_{i,j}=b_1\omega_{i-1,j}+b_2\omega_{i+1,j}+b_3\omega_{i,j}+b_4\omega_{i,j-1}+b_5\omega_{i,j+1}+C \tag{27}$$

$$b_1=\frac{\Delta t\left(U_b+|U_b|\right)}{2\Delta r}+\frac{\Delta t\upsilon(i-0.5)}{i(\Delta r)^2}$$

$$b_2=\frac{-\Delta t\left(U_f-|U_f|\right)}{2\Delta r}+\frac{\Delta t\upsilon(i+0.5)}{i(\Delta r)^2}$$

$$b_3=1-\Delta t\left(\frac{\left(U_f+|U_f|-U_b+|U_b|\right)}{2\Delta r}+\frac{\left(V_f+|V_f|-V_b+|V_b|\right)}{2\Delta z}\right)$$

$$-\Delta t\left(+\frac{2\upsilon}{(\Delta z)^2}+\frac{2\upsilon}{(\Delta r)^2}+\frac{\upsilon}{(i\Delta r)^2}\right) \tag{28}$$

$$b_4=\frac{\Delta t\left(V_b+|V_b|\right)}{2\Delta z}+\frac{\Delta t\upsilon}{(\Delta z)^2}$$

$$b_5=\frac{-\Delta t\left(V_f+|V_f|\right)}{2\Delta z}+\frac{\Delta t\upsilon}{(\Delta z)^2}$$

$$C=\frac{\Delta tg\beta\left(T'_{i+1,j}-T'_{i-1,j}\right)}{2\Delta r}+\frac{\Delta tC_o\mu_o l^2}{2\pi^2 L(i\Delta r^3)}\left[1-\exp\left(-\frac{(i\Delta r\ )^2}{2\sigma_j^2}\right)\right]^2\left(1-\frac{j\Delta z}{L}\right)$$

The temperature equation at the centerline as ;

$$\frac{T_{0,j}-T_{0,j}}{\Delta t}+\frac{2T_{1,j}\left(Uf_0-|Uf_0|\right)+2T_{0,j}\left(Uf_0+|Uf_0|\right)}{\Delta r}+$$

$$\frac{\left(Vf_0-|Vf_0|\right)T_{0,j+1}+\left(Vf_0-|Vf_0|-Vb_0+|Vb_0|\right)T_{0,j}}{2\Delta z}-\frac{\left(Vb_0+|Vb_0|\right)T_{0,j-1}}{2\Delta z}=$$

$$\alpha\left[\frac{4\left(T_{1,j}-T_{0,j}\right)}{(\Delta r)^2}+\frac{T_{0,j+1}-2T_{0,j}+T_{0,j-1}}{(\Delta z)^2}\right]+\frac{\Delta H}{\rho C_p} \tag{29}$$

Where ;

$$
\begin{aligned}
C_1 &= \frac{4\alpha\Delta t}{(\Delta r)^2} - \frac{2\Delta t\left(Uf_0 - |Uf_0|\right)}{\Delta r} \\
C_2 &= 1 - \Delta t\left[\frac{2\left(Uf_0 - |Uf_0|\right)}{\Delta r} + \frac{\left(Vf_0 + |Vf_0| - Vb_0 + |Vb_0|\right)}{2\Delta z} + \frac{4\alpha}{(\Delta r)^2} + \frac{2\alpha}{(\Delta z)^2}\right] \\
C_3 &= \frac{-\Delta t\left(Vf_0 - |Vf_0|\right)}{2\Delta z} + \frac{\alpha\Delta t}{(\Delta z)^2} \\
C_4 &= \frac{\Delta t\left(Vb_0 + |Vb_0|\right)}{2\Delta z} + \frac{\alpha\Delta t}{(\Delta z)^2} \\
C_5 &= \frac{\Delta t\Delta H}{\rho C_p}
\end{aligned}
\qquad (30)
$$

The vorticity equation at centerline ;

$$
\omega'_{0,j} = D_1\omega_{1,j} + D_2\omega_{0,j} + D_3\omega_{0,j+1} + D_4\omega_{0,j-1} + D_5 \qquad (31)
$$

Where ;

$$
\begin{aligned}
D_1 &= \frac{-\Delta t\left(Uf_0 - |Uf_0|\right)}{2\Delta r} - \frac{\Delta t\left(Ub_0 + |Ub_0|\right)}{2\Delta r} \\
D_2 &= 1 - \frac{\Delta t\left(Uf_0 + |Uf_0| - Ub_0 + |Ub_0|\right)}{2\Delta r} - \frac{\Delta t\left(Vf_0 + |Vf_0| - Vb_0 + |Vb_0|\right)}{2\Delta z} - \frac{2\nu\Delta t}{(\Delta r)^2} - \frac{2\nu\Delta t}{(\Delta z)^2} \\
D_3 &= \frac{-\Delta t\left(Vf_0 - |Vf_0|\right)}{2\,\Delta z} + \frac{\nu\Delta t}{(\Delta z)^2} \\
D_4 &= \frac{-\Delta t\left(Vb_0 - |Vb_0|\right)}{2\,\Delta z} + \frac{\nu\Delta t}{(\Delta z)^2} \\
D_5 &= \frac{\Delta t C_0 \mu_0 I^2}{2\pi^2 L (i\Delta r)^3}\left[1 - \exp\frac{-(i\Delta r)^2}{2\sigma_j^2}\right]^2\left(1 - \frac{i\Delta z}{L}\right)
\end{aligned}
\qquad (32)
$$

The stream function for the next iteration (m+1) ;

$$
\begin{aligned}
\psi^{(m+1)}_{i,j} = (1-\Omega)\,\psi^{(m)}_{i,j} + \frac{\Omega}{4}\Bigg[\, & i\,(\Delta r)^3 \omega' i,j + \left(\psi^{(m)}_{i+1,j}\left(1 - \frac{1}{i}\right) + \psi^{(m+1)}_{i-1,j}\left(1 + \frac{1}{i}\right)\right) \\
& + \left(\psi^{(m)}_{i,j+1} + \psi^{(m+1)}_{i,j-1}\right)\ \Bigg]
\end{aligned}
\qquad (33)
$$

From **(Petrovic and Stuper. 1996)** ;

$$
\gamma = \left[\frac{\cos\dfrac{\pi}{(N_r - 1)} + \left(\dfrac{\Delta r}{\Delta z}\right)^2 \cos\dfrac{\pi}{(N_z - 1)}}{1 + \left(\dfrac{\Delta r}{\Delta z}\right)^2}\right]^2 \qquad (34)
$$

$$\Omega_{OPT} = \frac{2-2\sqrt{1-\gamma}}{\gamma} \tag{35}$$

The radial and vertical velocities ;

$$U_{i,j} = \frac{\left(\Psi_{i,j+1} - \Psi_{i,j-1}\right)}{i\Delta r\Delta z} \tag{36}$$

$$V_{i,j} = -\frac{\left(\Psi_{i+1,j} - \Psi_{i-1,j}\right)}{i(\Delta r)^2} \tag{37}$$

Calculation of the Vertical Velocity at Centerline from **(Chow.1979)** ;

$$V_{0,j} = \frac{-2\Psi_{1,j}}{i(\Delta r)^2} \tag{38}$$

RESULTS AND DISCUSSIONS

Fig.5 shows the computed isotherms and convection patterns in the pool of the weld to account for convection and temperature distribution in moving weld pools driven by buoyancy and electromagnetic forces at times (0.1, 0.3, 0.5 and 0.75 seconds). As time passes, the molten pool increases for MIG welding process. The deep penetration is observed in the figure. The liquidus temperature is 1440°C and the solidus 1000°C. **Fig.6** shows the computed stream function in the case of combined buoyancy and electromagnetically driven flow of the weld pool at times (0.1, 0.3, 0.5 and 0.75 seconds), respectively. As time passes, the molten pool increases. **Fig.7** shows a strong counterclockwise circulation pattern, with very high velocities, which is dominated by the combined effect of the buoyancy and electromagnetically driven flow components. The weld pool shape, involving deep penetration, is consistent with the circulation pattern, (0.1, 0.3, 0.5 and 0.75 seconds), and the large the weld pool. It is this transfer of additional heat from the metal droplets (ΔH) in the GMA process which plays a very important role in the formation of the finger penetration in the GMA welds. This phenomenon is not present in the GTAW process. **Figs.8 and 9** show the interface between the molten pool and the solid region at different times (0.1, 0.5, 0.75 and 1 seconds) respectively during MIG and TIG welding processes. A comparison between the calculated numerical results of the present work and the results of TSAO and Wu (1988) will be made for verification. Some results were selected in order to check the model. Figures (8) and (9) of the present work may be compared with **Figs 10 and 11** of **(TSAO and Wu 1988)** for GMA and TIG results. The comparison show good qualitative and quantitative agreement.

CONCLUSIONS

A numerical study of heat transfer and fluid flow phenomena in welding process has been carried out in the present work. The weld pool size in GMA welding increases at a faster rate at small times (0.1 – 0.3 Sec.) and the stream function at times 0.1 sec and 0.3 sec appear increasing in the (r) and (z) directions. Two circulation loops in the weld pool appears one near the free surface and the other in the bulk weld pool, the maximum velocity which occurs at the free surface. And the flow at the free surface is radially outward from the (z) axis to the pool boundary.

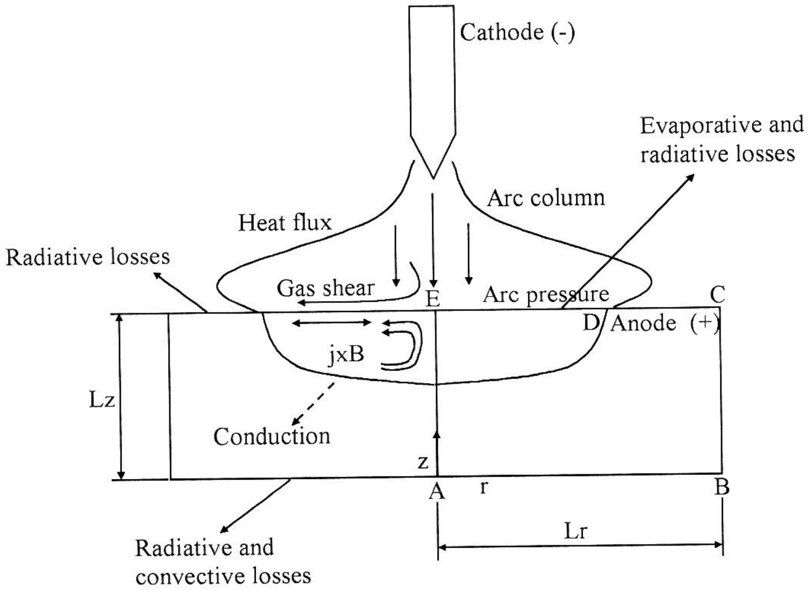

Fig. (1): Schematic Representation of Gas Tungsten arc Weld Phenomena (Gukan and Sundararajan 2001).

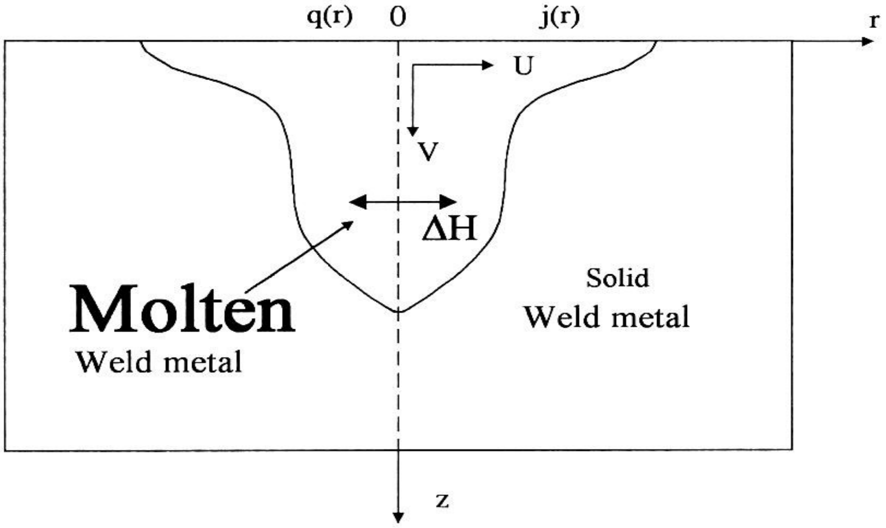

Fig. (2): Sketch the weldment of GMAW

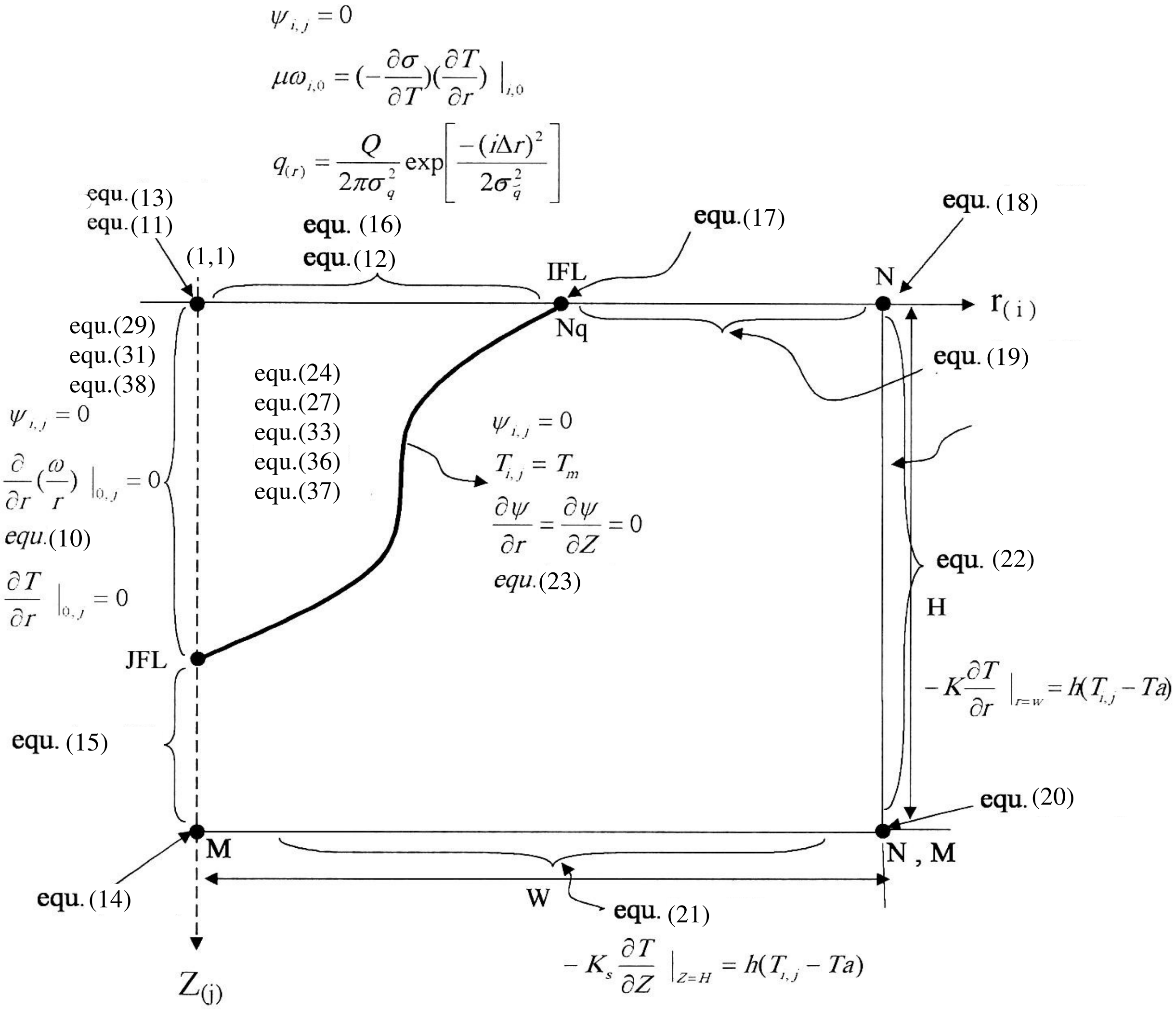

Fig.(3): Nodes Equations of the Numerical grid arrangement of weldment using temperature distribution , pool temperature distribution and boundary conditions used in calculations

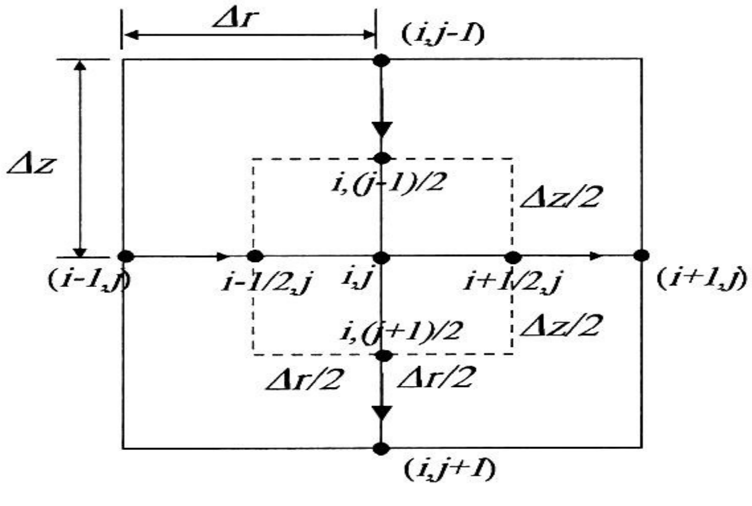

Fig. (4) The Nodal Points Used in Numerical Solution

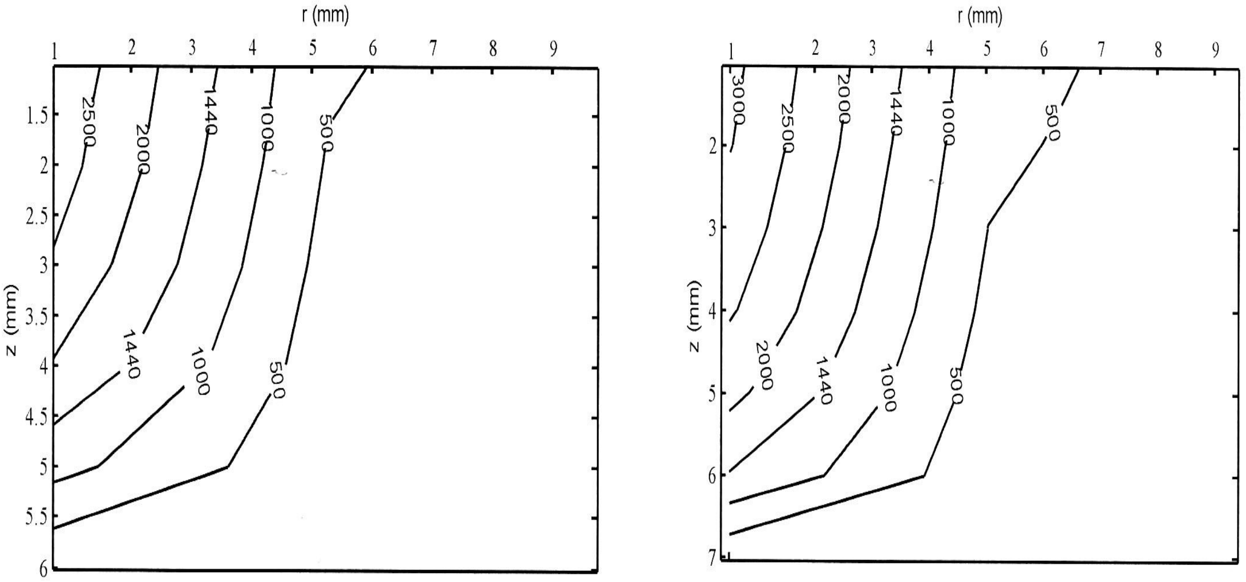

a. 0.1 sec

c. 0.5 sec

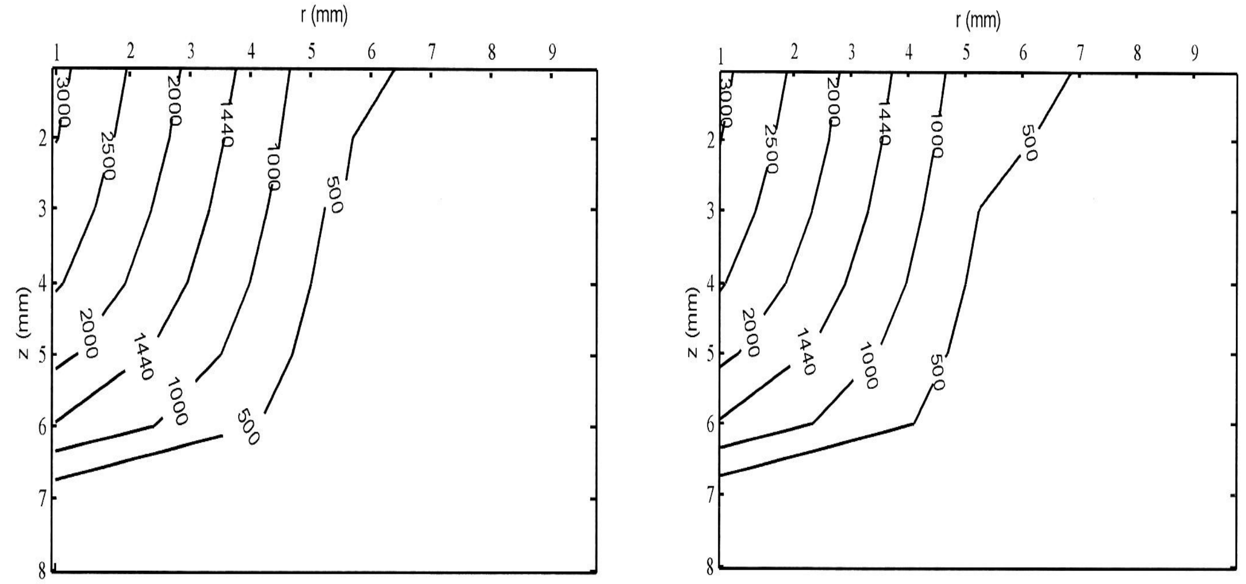

b. 0.3 sec

d. 0.7 sec

Fig. (5): Calculated Temperature Distribution at Different Times in GMA Weld Pool.

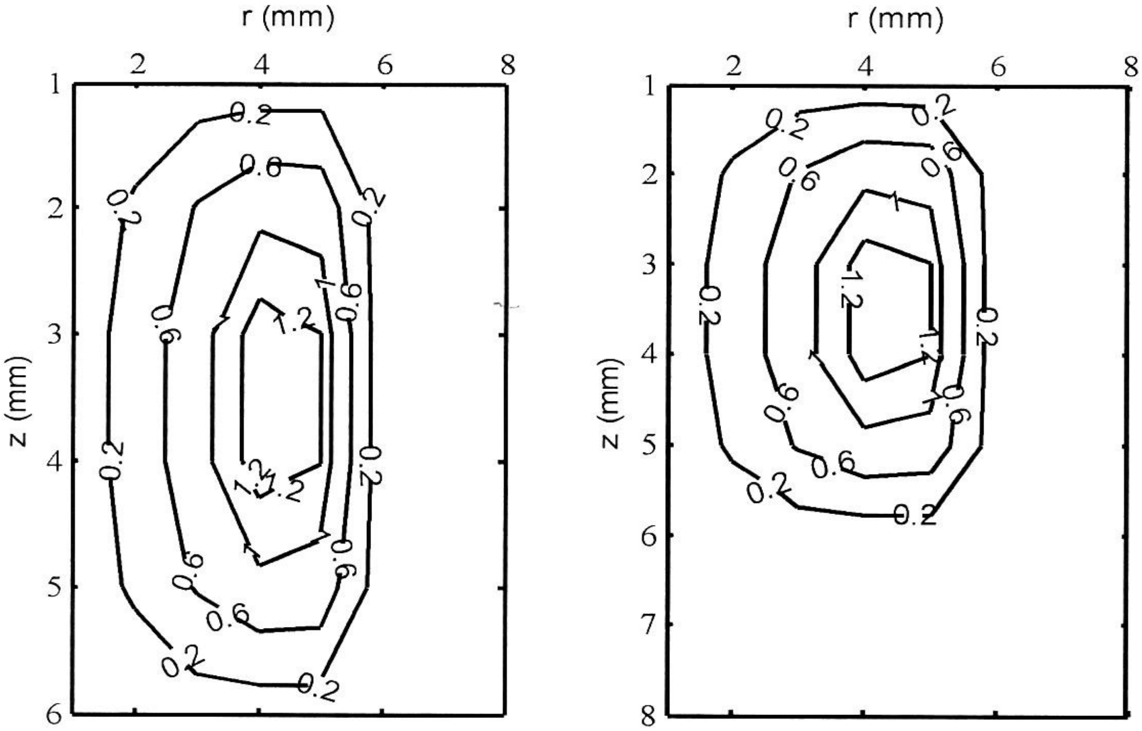

a. 0.1 sec b. 0.3 sec

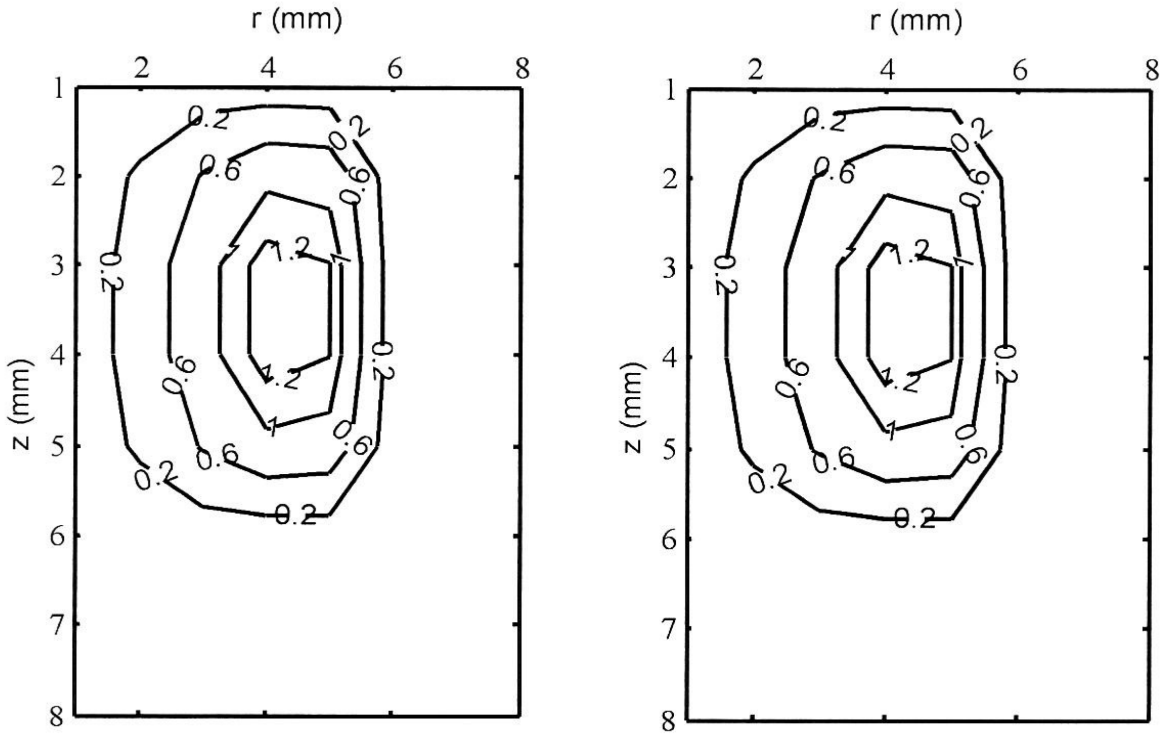

c. 0.5 sec d. 0.75 sec

Fig.(6): Calculated Stream Function Contours in GMA Weld Pool at Different Times.

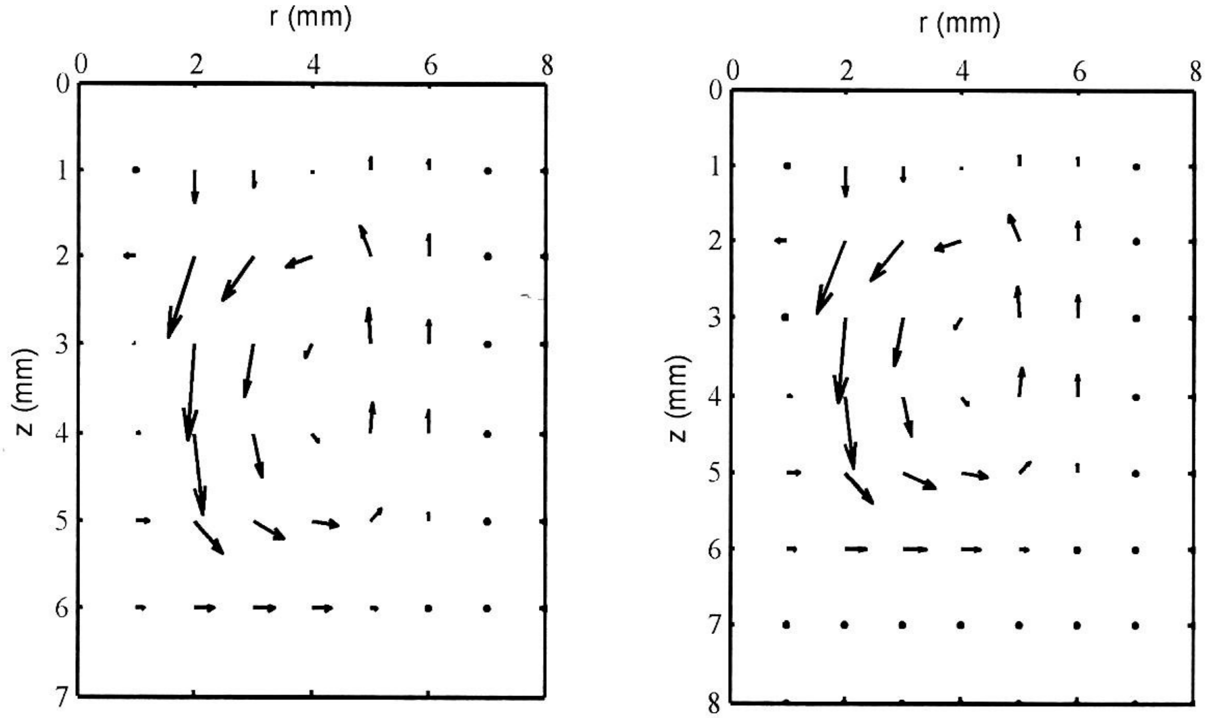

a. 0.1 sec b. 0.3 sec

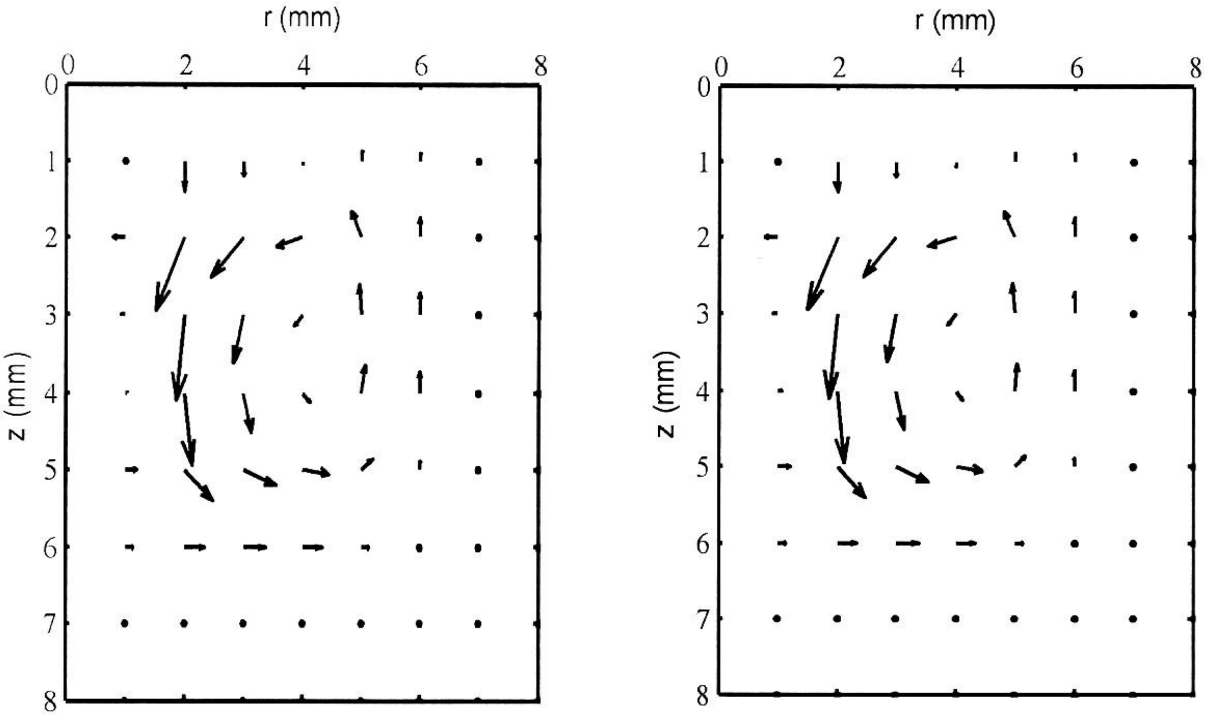

c. 0.5 sec d. 0.75 sec

Fig.(7): Calculated Velocity Distribution in GMA Weld Pool at Different Times.

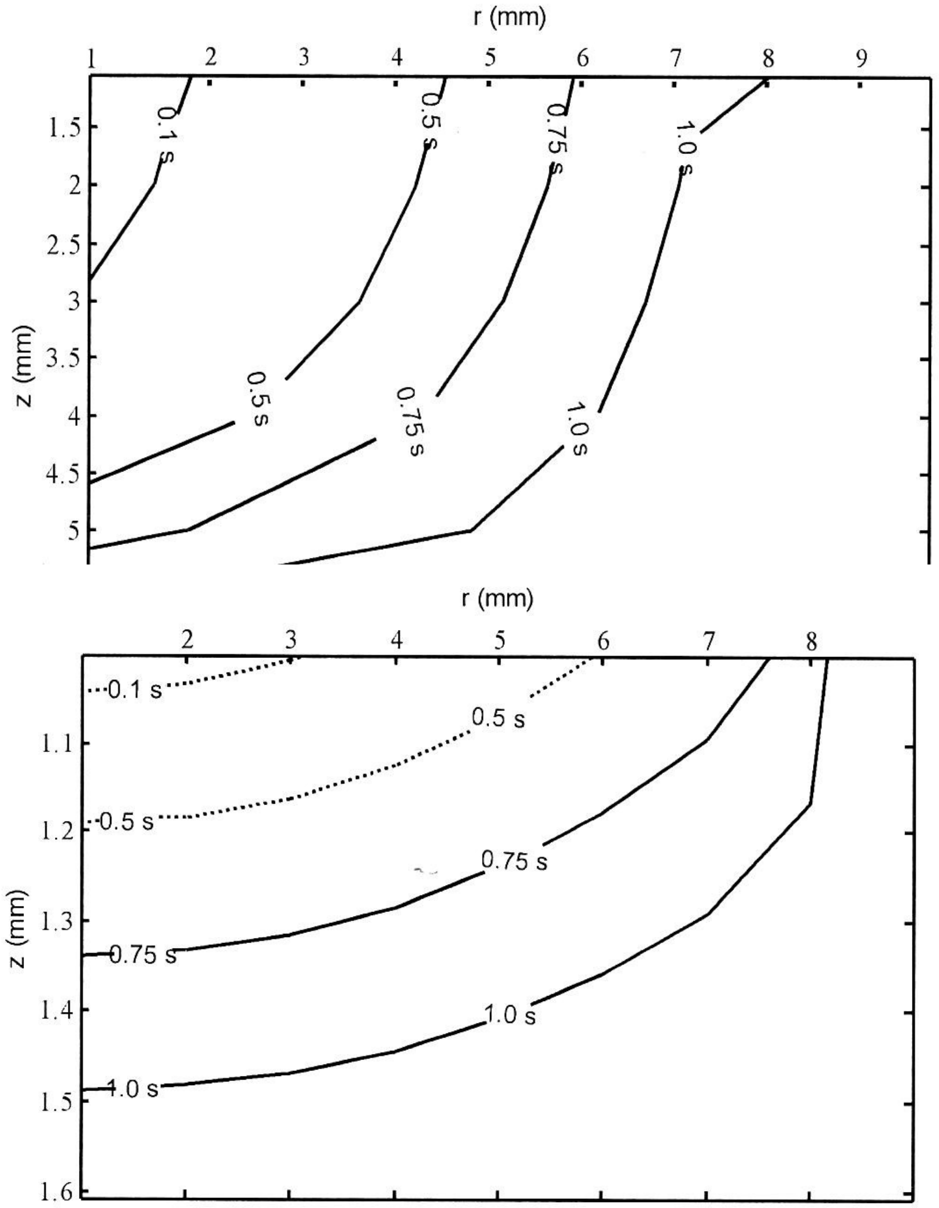

Fig.(9): Calculated Liquid – Solid interface of TIG Welding
With Same Heat Input at Different Times.

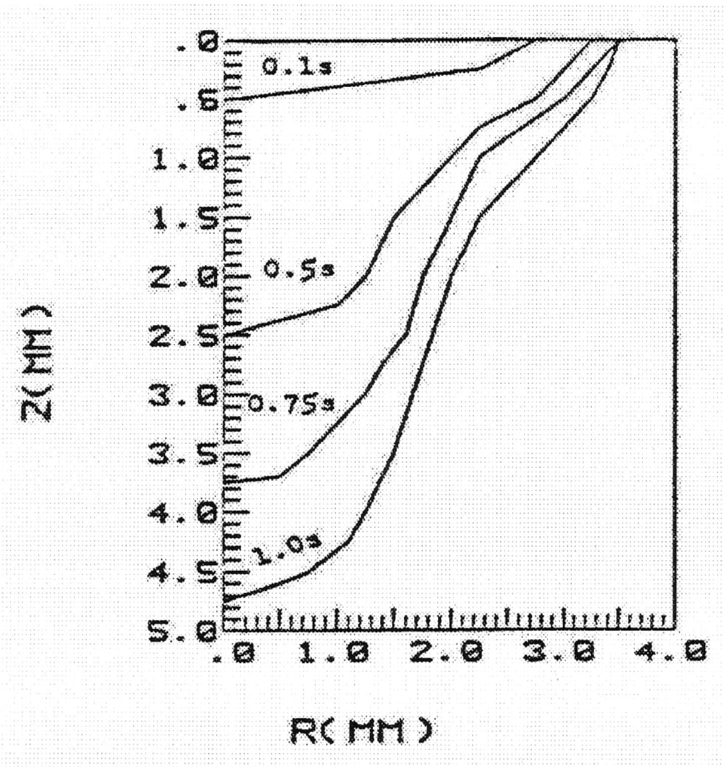

Fig.(10): Liquid – Solid Interface of GMA Welding Ref.(Tsao and Wu 1988)

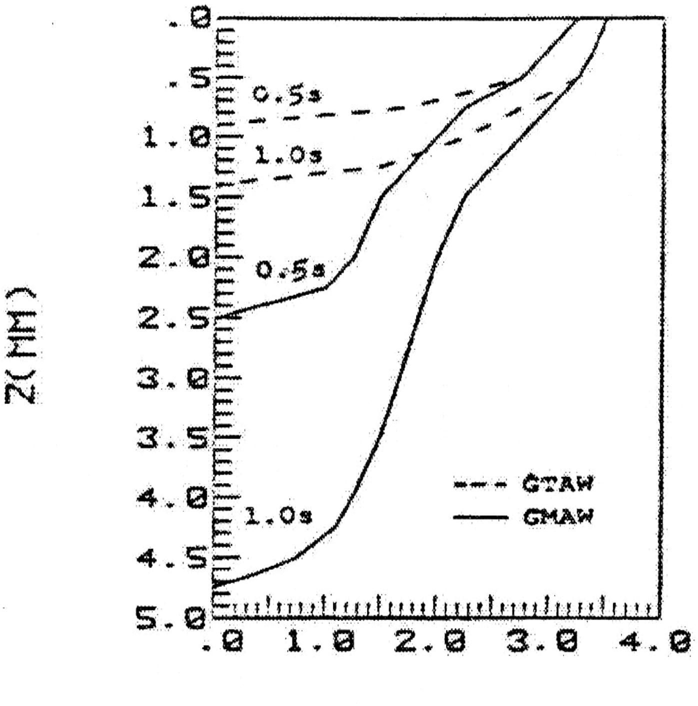

Fig.(11): Comparison of GMA and TIG weld Pool Boundaries with the Same Heat Input Ref.(Tsao and Wu 1988)

REFERENCES

Chow, C. Y., “An Introduction to Fluid Mechanics”, Wiley, New York, 1979.

Gukan, R., Guha, B. and Sundararajan, T., “Finite Element Modeling of Fluid Flow on Weld Pentration of Stationary Gas-Tungsten-Arc Weld Pool”, Department of Mechanical Engineering – IIT Madras. Chemmai-600 036 , 2001, p.p. 279-285.

Kim, J. W. and Na, S. J., “A Study on The Three-Dimensional Analysis of Heat and Fluid Flow in Gas Metal Arc Welding Using Boundary-Fitted Coordinates”, Journal of Engineering for Industry, Vol. 116, February 1994, p.p. 78-85.

Oreper, G. M. and Szekely, J., “A Comprehensive Representation of Transient Weld Pool Development in Spot Welding Operations”, Metallurgical Transactions A, Vol. 18A, July 1987, p.p. 1325.

Petrovic, Z. and Stupper, S., “Computational Fluid Dynamics One”, Mechanical Engineering Falculty, Belgrade, 1996.

Salah S. Abed-Alkreem , " Evaluation of Temperature Distribution and Fluid Flow in Fusion Welding Processes ", P.H.D Thesis, The College of Engineering , Mechanical Engineering Dept. ,University of Baghdad, March 2005.

Torrance, K. E., “Numerical Method in Heat Transfer”, Handbook of Heat Transfer Fundamentals, McGraw-Hill, second edition, 1985.

Tsai, M. C. and Kou, S., “Electromagnetic Force Induced Convection in Weld Pools With A Free Surface”, Welding Journal, Vol. 69, No. 6, June 1990, p.p. 241S-246S.

Tsao, K. C. and Wu, C. S., “Fluid Flow and Heat Transfer in GMA Weld Pools”, Welding Journal, March 1988, p.p. 70S-75S.

NOMENCLATURE

Latin Symbols

Symbol	Definition	Unit
Co	Length scale factor if scale uses in mm=10^6	—
g	Acceleration of gravity	mm/sec^2
h	Convection heat transfer coefficient	J/mm^2. sec.°C
H	Length of plate	mm
i	Finite difference index in the r-direction	—
I	Welding current	Ampere
IFL	Index of fusion limit in r-direction.	—
j	Finite difference index in the z-direction	—
j(r)	Welding current distribution at the plane (z=0)	Amp/mm^2
JFL	Index of fusion limit in z-direction.	—
K_L	Thermal conductivity of liquid metal	W/mm.°C
K_s	Thermal conductivity of solid metal	W/mm.°C
L	Thickness of work piece	mm
M	Number of grid in z-direction	—

N	Number of grid in r-direction	—
N_r	Number of grid in r-direction of weld pool	—
N_z	Number of grid in z-direction of weld pool	—
$q(r)$	Heat flux on the plane at z=0	J/mm^2
Q	Heat input per unit time	W
r	Cylindrical coordinates.	mm
T	Temperature in x-y coordinates, also temperature of weldment.	°C
T_a	Ambient temperature	°C
T_i	Initial temperature	°C
T_m	Melting temperature	°C
T_s	Solid temperature	°C
U	Velocity in radial direction (r)	mm/sec
U_b	Average back velocity in r-direction	mm/sec
$U_{b\,0}$	Average back velocity at center line	mm/sec
U_f	Average front velocity in r-direction	mm/sec
$U_{f\,0}$	Average front velocity at center line	mm/sec
V	Velocity in axial direction (z)	mm/sec
V	Voltage duty	Volts
V_b	Average back velocity in z-direction	mm/sec
$V_{b\,0}$	Average back velocity at center line	mm/sec
V_f	Average front velocity in z-direction	mm/sec
$V_{f\,0}$	Average front velocity at center line	mm/sec
W	Width of plate also width of workpiece.	mm
z	Cylindrical coordinate	mm

GREEK SYMBOLS

Symbol	Definition	Unit
α_L	Thermal diffusivity of molten metal	mm^2/sec
α_S	Thermal diffusivity of solid metal	mm^2/sec
β	Coefficient of thermal expansion (exposivity)	1/k
ΔH	Heat transferred into weld pool by molten filler droplets	w/mm^{-3}
Δr	Step size in r-direction	mm
Δz	Step size in z-direction	mm
η	Heat input efficiency	—
μ	Dynamic viscosity	kg/mm.sec
μ_0	Magnetic permeability of free space	H/mm
υ	Kinematic viscosity	mm^2/sec
ρ_1	Density of welding wire	Kg/mm^3
ρ_2	Density of filler droplet	Kg/mm^3
σ	Surface tension	N/mm
σ_j	Current distribution parameter	Amp/mm^2
σ_q	Heat flux distribution parameter	w/mm^2
ψ	Stream function	M^3/sec
Ω	Successive over relaxation parameter	—
Ω_{OPT}	Optimum successive over relaxation parameter	—
ω	Vorticity	1/sec
f	Spray transfer frequency	HZ

تحليل الأنساق

PATTERNS' ANALYSIS

PROF. SABA JEBBAR NI'MA/ DEPARTMENT OF ARCH./ BAGHDAD UNIVERSITY
ASSIS. PROF. SAHIR AL-QEISI/ DEPARTMENT OF ARCH./ BAGHDAD UNIVERSITY
PH.D. STUDENT: Dr. HASSAN 3A. AL-GUESBI/ BABYLON UNIVERSITY

الخلاصة

من الممكن الاستدلال على بعض الحقائق ذهنياً رغم تغيّرها المستمر. **فتعقّب هذا التغيّر** وإدراكه يضمن للإنسان نوعاً من الاطمئنان من مخاوفه، والثقة بنفسه، والتفوّق على ماحوله. وتقدم أشكال بعض الأنساق **المستدامة** *(Sustained Patterns)* الدليل الموضوعي الموثوق على نجاح وتفوّق العديد من النتاجات الاحيائية والطبيعية والبشرية... التي صمدت وثبُتت حتى وصلت إلينا. ويعزو البحث سر نجاح مثل هذه الأنساق الى أنماطٍ كامنةٍ فيها قد لا تكون واضحة للعيان أو مخفية ضمن ما يبدو من عشوائية وتعقيد **(وهذا ما تطرحه** نظرية الفوضى *(Chaos Theory)*، **وإحدى تطبيقاتها العمليّة المتمثلة** بالهندسة الكسرية أو الجزئية *(Fractal Geometry)* اللاإقليدية**). ولكن يمكن الاستدلال عليها عن طريق حساب ما يُعرَف** بالبعد الكسري أو الجزئي *(Fractal Dimension/ D)* اللاإقليدي باعتباره مؤشراً حساساً لنمط التغيّر.

عمد البحث الى تحليل وتقييس النسق الشكلي لنموذج احيائي ناجح ومتزن ومستدام بشكل موثوق (بستان زيتون) لإيجاد نمط رقمي ضمنه عن طريق إحتساب بعده الكسري أو الجزئي اللاإقليدي. حيث يرى البحث **ان للأنظمة الناجحة ميول متشابهة للارتباط والاتصال** *(Connection)* **من جهة، والتراص** *(Compactness)* **من جهة أخرى، لتكشف هذه الأنظمة عن نفسها على هيئة أنساق عند وصولها الى حد أو حافة أو حالة من الاتزان والتنظيم الذاتي** *(Self-Organized Criticality)*. **ثم تبنى البحث** أسلوب التحليل المقارن *(Comparative Analysis)* **عند دراسته لنسق نظام حضري ببعدين** *(2-Dim.)* **واقع وقائم (المخطط الأفقي لمدينة بغداد) اعتماداً على نسق بستان الزيتون.**

ABSTRACT

It is possible to infer some facts by capturing them directly or trying to trace their evolutions and changes mentally. This will guarantee human beings a sort of self-confidence, control and power. Some *sustained patterns* of natural, biological and human artifacts provide trusty physical and objective proofs on their success and survive.

The research claims that the secret beyond the success of these patterns lies in ambiguous or hidden or invisible orders within the seeming randomness and complexity. Successful systems reflect distinguishable order when they reach a critical threshold of stability and self-organizing between their trends to connect and to compact. Then, patterns can reveal themselves and express their similar structural and morphological changes. In the same manner, guiding other systems to reach such edges and thresholds may ensure having successful patterns, solving serious problems and leading the way ahead correctly.

The research depends on a new mathematical tool from the *Fractal Geometry* to reveal and measure the hidden orders in these patterns by calculating the repetitions of form's changes. This tool could be defined as a *Fractal Dimension (D)*, which is considered to be a sensitive index or parameter of the system's behaviors.

Also, the research adopts the comparative analysis method of analyze and measure the form of a trusty successful, natural and sustained pattern of a fruit trees orchard, trying to find a numerical order by calculating its fractal dimension. The obtained fractal dimension represents a referential base in analyzing some patterns of urban systems (e.g. Baghdad's two dimensional image), a reliable index and parameter to detect the system's behaviors and trends to connect or to compact.

Comparing the pattern of an existing urban fabric for the city of Baghdad with the orchard's pattern refers to an obvious defect in the inner structure and morphology of the capital. Baghdad tends to connect rather than to compact in a pathological way. The research ends with the need for urgent and careful interference to tune the parameters of connectivity and compactivity equally by suitable and practical suggestions and recommendations.

<u>KEY WORDS</u>

نظرية الفوضى *(Chaos Theory)*، الهندسة الكسرية أو الجزئية *(Fractal Geometry)* اللاإقليدية، تعقّب التغيّرات *(Tracing the changes)*، النسق *(Pattern)*)، الارتباطية أو الاتصالية *(Connectivity)*، التراص *(Compactivity)*، البعد الكسري أو الجزئي اللاإقليدي *(Fractal Dimension)*.

مقدمة منطقية

يبحث الإنسان دوماً عن قيم كونية يؤمن بها، وعن نواميس عليا يركن إليها، لها من صفات الثبات والديمومة، أو على الأقل من التغييرات المحسوبة، ضمن تقديراته وتنبؤاته، ما يسد حاجته، ويشبع رغبته، ويسوّغ سلوكه، ويطمئن مخاوفه في مواجهته لما حوله. فالحقيقة تتغيّر باستمرار بين إمكان ووجود، فلا وجود بلا إمكان، ولا يمكن الاستدلال على الإمكان بلا وجود، حيث يمكن تصوّر ما يمكن وما لايمكن التحقق منه، ولا يمكن، بالمقابل أيضاً، التحقق من كل ما يمكن تصوّره أو لا يمكن تصوّره أصلاً. **وتوفّر لنا الأنساق المستدامة شواهد حية مازالت صامدة يمكن تعقّب التغيّرات عبرها *(Tracing the changes)* طلباً لإطراداتٍ متكررة (متشابهات في جملة متغيّرات، أو متغيّرات في جملة متشابهات) في سعينا الحثيث خلف الحقيقة.** كما ويمكن أن تقدّم لنا عمارة الأنظمة الحضرية ما نحتاجه من دليل ملموس على ذلك.

وتتأصل في عقل الإنسان **أربعة جواهر عقلية بديهية قبلية** يستدل بها على كل حقيقة مابين: **العلية *(Causality)*، الماهية أو الحركة الجوهرية *(Essence)*، الكيفية أو عدم التناقض وتناقض الأضداد *(Thesis,***

Antithesis and Synthesis) **والوجودية أو التطور والتكامل** ***(Evolution and Integration)***. فالعلية تعزو كل حادثة الى سبب، وكل معلول الى علة، وان العلة (السبب) تؤدي الى المعلول نفسه (النتيجة). وتتسم هذه العلاقة بالانسجام الكلي والغائية والترابط والتلازم المستمر، فهناك علة لما قبل وغاية لما بعد (الحيدري، لا ضرر ولا ضرار، ص: 25-29). وتتناول الماهية أو الحركة الجوهرية مبدأ الحركة أو الحياة في الفلسفة، وتعني خروج الشيء من الإمكان (القوة) الى الوجود (الفعل). كما وتشير الى التغيّر الذي يحصل في ذات الشيء (دي بور، تأريخ الفلسفة في الإسلام، ص: 65-70). وتشير الكيفية الى إستحالة أن تضم الأشياء نقائضها داخلها، وإستحالة حصول التناقض بين الأجزاء (الصدر، الفتاوى الواضحة، ص: 12-25). أما الوجودية أو التطور والتكامل، سواء أكان على هيئة تدفقات تغيّرية كمية أم قفزات تحولية كيفية، فيشير الى نزعات ذاتية للنمو والاندثار، للتوسع والانكماش، للارتباط والاتصال (*Jencks, The architecture of Jumping Universe, p: 164-170*).

المقياس الرباعي الفلسفي العام

في سعيه الحثيث طلباً للحقيقة، شكّل البحث من الرباعية المنطقية أعلاه مقياساً فلسفياً عاماً ومشتركاً. ويشير المخطط (1)، أدناه، الى هذا المقياس الرباعي الفلسفي العام:

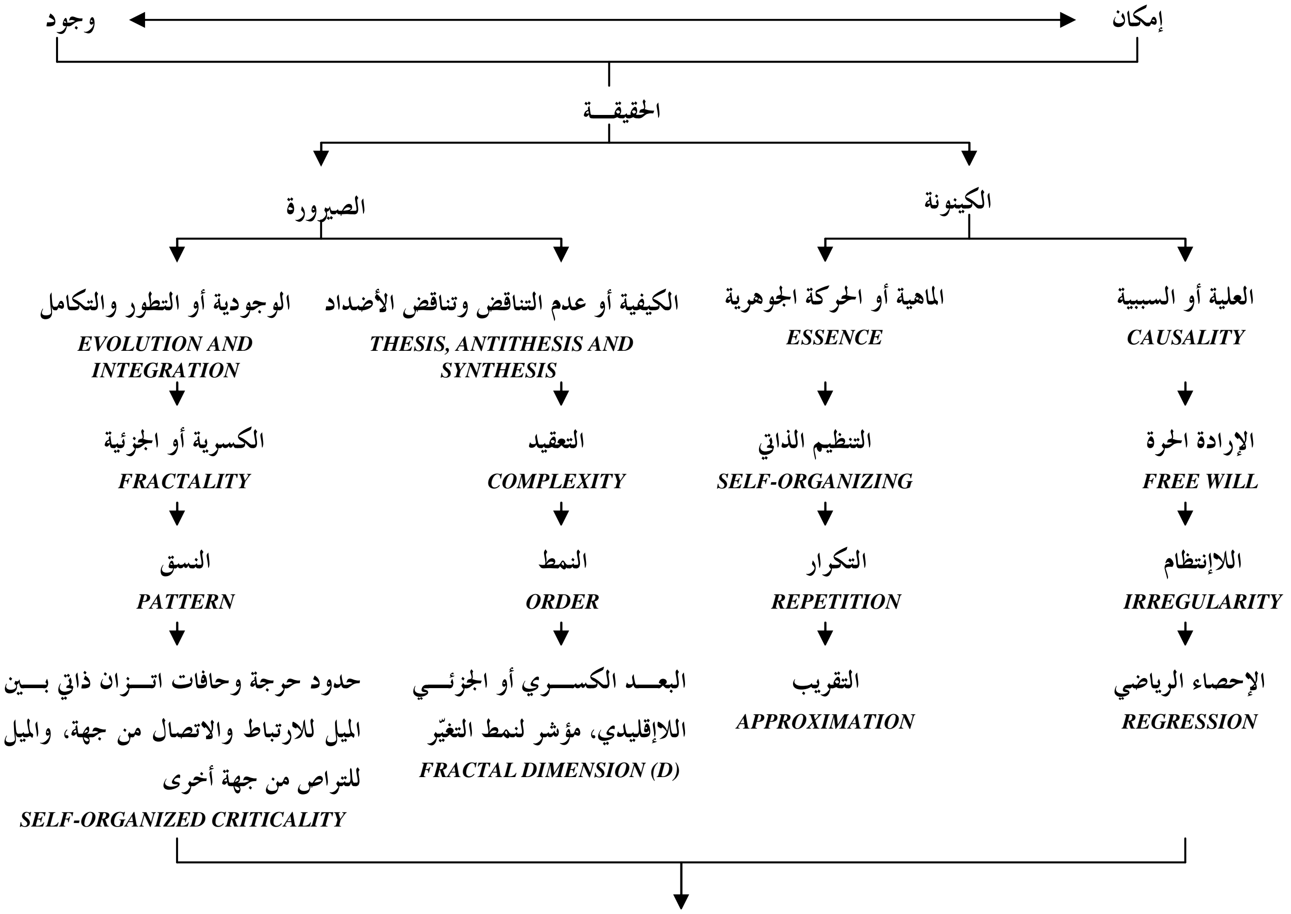

محاولة تقييس التغيّر في الأنماط الكامنة خلف الأنساق (تكرارات التغيّر في أشكالها) إعتماداً على حساب البعد الكسري أو الجزئي اللاإقليدي.

مخطط رقم (1): مقياسنا الرباعي الفلسفي العام.

حيث ينتج عند إخضاع نظرية الفوضى *(Chaos Theory)* لهذا المقياس رباعية أخرى تتضمن (الإرادة الحرة *(Free Will)*، التنظيم الذاتي *(Self-Organizing)*، التعقيد *(Complexity)* والكسرية أو الجزئية *(Fractality)*) مقابل (العلية، الماهية، الكيفية، الوجودية) على التوالي. فالإرادة الحرة تعني "الاختيار والانتقاء الذاتي ضمن مجموعة خيارات محددة سلفاً، ولا يمكن أن تكون مطلقة مهما توسعت خياراته وزادت" (*Davies, The Cosmic Blueprint, p: 73*). ويحدث التنظيم الذاتي تلقائياً عن طريق إعادة الهيكلة والتدوير للبحث عن ترتيب وإنتظام فيما يبدو من عشوائية (*Gleick, Chaos: Making a New Science, p: 32*). ويحاول التعقيد إحتواء التغيّر، حيث يتجه العلم الحديث الى الاعتقاد بوحدة كيان المادة، أي ان المحتوى الداخلي للمادة واحد، وليست الأشكال المتنوعة التي تتخذها إلا حالات متبادلة على محتوى واحد ثابت. ولا وجود لنقائض مستقلة عن بعضها البعض داخل المحتوى الواحد، أو لصراعات داخلية بين هذه النقائض (الحيدري، لا ضرر ولا ضرار، ص: 60). وتعكس الكسرية أو الجزئية صفة لأشكال طبيعية أو احيائية غير منتظمة، وعلاقات لا تقليدية، وهياكل كسرية (غير صحيحة)، وأنساق قد تبدو مبتورة وغير كاملة (*Wahl, Exploring Fractals on the Macintosh, p: 2*).

وتتناول الهندسة الكسرية أو الجزئية *(Fractal Geometry)* اللاإقليدية، باعتبارها تطبيق عملي لنظرية الفوضى، رباعيةً أخرى تقابل رباعيتنا الفلسفية السابقة عند إخضاعها لمقياسنا الرباعي العام. وتتضمن هذه الرباعية (اللاإنتظام *(Irregularity)*، التكرار *(Repetition)*، النمط *(Order)* والنسق *(Pattern)*) على التوالي أيضاً. فاللاإنتظام يعكس مبدأ العلية وصراع الإرادات. "**إن للفراغ بنية، ولهذه البنية نفوذ وسطوة على الأشكال جميعاً**" (السمهوري، إشكالية خصوصية بنية النسيج العمراني في المدينة العربية الإسلامية: درجات النظام والعفوية، ص:5). ويشير التكرار الى قابلية ذاتية معقولة للأنظمة المتزنة لامتصاص التدخّلات دون فقدان الاتزان الموجود. أما إذا كان التدخل كبير ويفوق طاقة النظام، فإن النظام قد ينهار ويحل محله نظام آخر بنتائج مختلفة تماماً (أكبر، عمارة الأرض في الإسلام، ص: 355). كما ويحاول النمط تقييس التغيّر، بحسب فتروفيوس، وقد يكون ذلك عن طريق التقريب الكمي (*Moughtin, Urbanism in Britain, p: 31*). ويوثق النسق نتاجَ وروحَ عصرٍ مضى بشكلٍ موضوعي. ويمكن أن تعكس التقاليد *(Traditions)* أنساقاً متوارثة، فهي تتضمن إيحاء قوي بمعنى المحاكاة في محاولة لتطبيق وتقليد ماهو موروث من أنساق إجتماعية وعمرانية وبيئية متميزة (الهذلول، المدينة العربية الإسلامية، ص: 3-4). بينما تعكس الأعراف *(Norms)* سلسلة متتالية من القيود تتيح حرية أكبر للإرادة والتصرف ضمنها (أكبر، عمارة الأرض في الإسلام، ص:432-433).

الارتباطية أو الاتصالية *(CONNECTIVITY)*، والتراص *(COMPACTIVITY)* في الأنظمة الحية:

يرى البحث **ان الارتباطية أو الاتصالية تعبّر عن ميل أو نزعة ذلك النظام للهجوم والامتداد والتوسّع والنمو عند وصوله الى حد أو حافة حرجة *(Critical Threshold)* من الاكتظاظ والتراص، والعكس صحيح.** وتقاس هذه النزعة أو الميل بحساب أعداد جميع الارتباطات أو الاتصالات *(Number of connections/ N)* المحتملة والمباشرة بين كل أجزاء ومكوّنات ذلك النظام. أما **التراص** فهو إحدى آليّات الدفاع والاختزال والمقاومة التي تُبديها جميع الأنظمة الحية. ويمكن تقييسها بحساب أطوال جميع الارتباطات أو الاتصالات *(Lengths of connections/ L)* الممكنة دون تكرار. ومن المعروف أن الأنظمة جميعها تسعى الى تقليل عدد الارتباطات أو الاتصالات بين أجزائها الى أدنى حد ممكن لزيادة تراصّها، وحفاظاً على ما يُصرف ويُستهلك من طاقاتها *(Energies)*، مقابل سعيها الحثيث الى الارتباط والاتصال المستمر.

ويبدو أن للأنظمة، بشكلٍ عام، ميول خارجية وداخلية مشتركة. إذْ تسعى للتوسّع والانتشار والامتداد والاتصال والارتباط الخارجي طلباً لمزيد من المعلومات مقابل ميل ونزعة داخلية للدفاع والتراص وإعادة الهيكلة والتنظيم الذاتي حفاظاً على طاقاتها. فهي تحاول زيادة عدد ارتباطاتها أو اتصالاتها *(Number of Connections/ (N) as an index of Connectivity)* الى أقصى حد ممكن، وتقليل أطوال هذه الارتباطات *(Lengths of these Connections/ (L) as an index of Compactivity)* الى أدنى حد ممكن، وصولاً الى حالة من الاستقرار والاتزان.

النسق *(PATTERN)*، توثيق موضوعي للحياة:

النسق *(Pattern)* هو حلٌّ مُكْتَشَف لمشكلةٍ ما، تم إختباره مراراً عبر (المكان– الزمان) وتحت ظروفٍ مختلفة وثَبُتَ نجاحه، فهو لم يُخْتَرَعْ أو يُبْتَكَر. وقد يكون شفرة أو أحجية بحاجة الى حل. وتمثل الأنساق إنتظاماتٍ وأنماطاً *(Orders)* متناقلةً أو متوارثةً للسلوك ناجمةً عن تسجيل وتوثيق الحوادث المتكررةِ الحدوث تحت مختلف الظروف *(Salingaros, The Laws of architecture from Physicist's Perspective, p: 5)*. إن الأنظمة الناجحة، باعتقادنا، تعكس نمطاً مميّزاً لحظة وصولها الى حالة من الاتزان والتنظيم الذاتي، تستطيع عندها أنساقها الشكلية اللامنتظمة، والتي تبدو بأنها عشوائية لأول وهلة، أن تكشف سرّها وتعبّر عن حقيقة ما يجري داخلها من تغييرات بنيوية ومورفولوجية متشابهة. وبمحاولة الرجوع أو الوصول بأي نظام آخر الى مثل هذه الحدود أو الحافات الحرجة *(Steady states or critical edges)*، عن طريق اختزاله أو دفعه أو حتى توجيهه، نستطيع أن نضمن له الحصول على أشكالِ أنساقٍ ناجحة، وتقديم حلول لمشكلاتٍ قائمة وتوصيات لمراحلٍ قادمة، تقود ذلك النظام نحو بر الأمان والنجاح.

ويعزو البحث نجاح أي نظام ديناميكي حي في طبيعة أنساقه لحظة وصوله الى حد أو حافة حرجة يتزن فيها النظام، ويتشابه عندها ميله للارتباط والاتصال من جهة، وميله للتراص من جهة أخرى. فالأنساق الناجحة تضم هياكل ذات أشكال كسرية تتغيّر بأنماط متشابهة من حيث بعدها الكسري أو الجزئي *(Fractal*

***(Dimension/ D* اللاإقليدي، وهذه الأبعاد تميل للاقتراب من $(D \approx 1)$. ان البعد الكسري أو الجزئي اللاإقليدي هو مؤشّر حساس لحالة النظام وسلوكه وميوله نحو الإرتباطية أو الاتصالية *(Connectivity)* أو حتى التراص *(Compactivity)*.**

منهجية البحث:

تبنى البحث أسلوب التحليل المقارن *(Comparative analysis)* بالاعتماد على تحليل وتقييس النسق الشكلي لنموذج أحيائي ناجح ومتزن ومستدام بشكلٍ موثوق (بستان الزيتون)، لإيجاد نمط رقمي ما ضمنه عن طريق إحتساب بُعده الكسري أو الجزئي اللاإقليدي. واعتمد البحث أيضاً على هذا البُعد كمقياس يمكن الرجوع إليه عند تحليل أنساق بعض الأنظمة القائمة، ومنها الأنظمة الحضرية (كمدينة بغداد مثلاً)، للاستدلال على حالة ذلك النظام وسلوكياته وميوله سواء للارتباط والاتصال أو للتراص.

سر البستان:

يستعرض البحث أدناه نموذجاً ومثالاً مهماً عن نسق سلوكي طبيعي لعلاقة وثيقة بين أشجار الزيتون المزروعة في بستان، وحشرات التربة الضارّة التي تحاول التطفّل على هذه الأشجار. فتحت نفس العنوان (سر البستان/ *The Mystery of Orchard*)، كتب برنت وال *(Bernt Wahl)* في الصفحة (5) من كتابه *(Exploring Fractals on the Macintosh)*، قائلاً "قامت مجموعة من الرهبان الفرنسيين في القرن الخامس عشر بتجريب زراعة بستان لهم بغية الحصول على أكبر عدد من أشجار الزيتون فيه. فاستغلّوا في البداية كل مساحة البستان بزراعة الأشجار في صفوف وبمسافات متساوية. وعلى الرغم من أن ذلك قد ساعدهم على زراعة أكبر عدد ممكن من الأشجار، إلا إن ذلك قد ساعد بالمقابل حشرات التربة الفتّاكة والضارة على الإنتقال من شجرة الى أخرى ومن صف الى آخر بسهولةٍ ويسر. وبالتالي تم غزو وتدمير البستان بالكامل. فحاول الرهبان حل هذه المشكلة بمباعدة الأشجار بعضها عن بعض على حساب تقليل عددها ثم نتاجها. والسؤال هو: كيف يمكن للرهبان أن يتوصّلوا الى أحسن نسق للأشجار يضمن أحسن إستخدام لمساحة البستان وأكثر عدد أشجار مقابل تقليل تأثير حشرات التربة الضارة الى الحد الأدنى. وللدهشة، فقد كان الجواب في **التوصّل تجريبياً الى نسق *(Pattern)* ذو شكل كسري أو جزئي، ظلَّ غامضاً وغير قابل للوصف الدقيق أو القياس**" (*Wahl, Exploring Fractals on the Macintosh, p: 13*). أنظر الشكل (1) أدناه.

وعند التمعّن بهذا النسق طويلاً، فإننا قد نعجز عن إيجاد ما يمكن أن نميّزه فيه من مباديء وقواعد ومعايير هندسية تقليدية معروفة للجميع كالتناسب أو التناظر أو التدرّج أو التناغم...الخ. وسوف يستفيد البحث من بعض طروحات الهندسة اللاإقليدية *(Fractal Geometry)* الجديدة في البحث وبمنظار مختلف تماماً عن خاصيةٍ جديدةٍ ضمن هذا النسق، قد لا تبدو واضحة للعيان من أولِ وهلة، وأقل ما يُذكر لوصفها هو ما اصطلحنا عليه سابقاً بالكسرية أو الجزئية *(Fractality)*. فشكل هذا النسق غير منتظم *(Irregular)* حتى عند

تغيير المقياس، وحدوده الخارجية وتقطيعاته وتفصيلاته الداخلية متكسّرة ومتشرشبة بلا إنتظام. فهل يُعْقَل أن يتضمّن هذا النسق معياراً ثابتاً (يمكن تقييسه) يتميّز به عن غيره؟ وهل أن اصطفاف أشجار الزيتون بهذا النسق يتضمن نمطاً كامناً لا يتغيّر؟

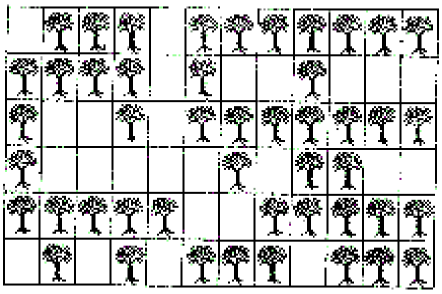

شكل رقم (1): سر البستان يكمن في أنساق زراعته.

(المصدر: 12، صفحة: 5)

لنبدأ العمل أولاً بالاستعاضة عن الأشجار بدوائر وترقيمها تباعاً، كما موضّح في الشكل (2) أدناه:

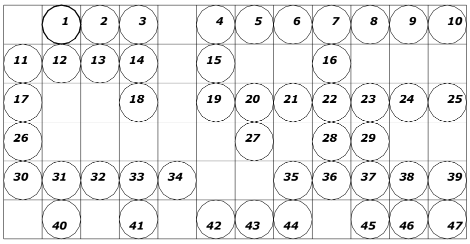

شكل رقم (2): نموذج لترقيم الأشجار تباعاً في بستان الزيتون.

(المصدر: الباحث)

وعلى أساس أن البستان يمتاز بنظام أحيائي متكامل ومتّزن ساعده على الديمومة والاستمرار، يرتبط كل جزء فيه بالكل في وحدةٍ واحدة، فإن كل شجرة زيتون تتصل وترتبط *(connect)* بجميع أشجار الزيتون دون استثناء، مع ملاحظة عدم تكرار أي اتصال أو ارتباط لأكثر من مرة، اعتماداً على مركز الدائرة الافتراضية كتعبير عن الأشجار عند التمثيل بالرسم، أنظر الشكل رقم (3) أدناه.

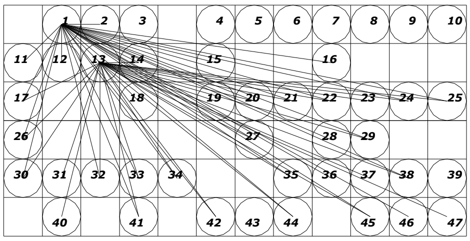

شكل رقم (3): توضيح لفكرة ارتباط كل جزء من أجزاء النظام (بستان الزيتون) ببقية أجزائه، أما بشكل مباشر أو بشكلٍ غير مباشر، حيث لا يجوز تكرار الارتباط لأكثر من مرة واحدة.

(المصدر: الباحث)

إن ارتباطية ***(Connectivity)*** الشجرة رقـــم*(1)*، على سبيل المثال، يكون مباشراً مع الأشجار بالأرقام

(2,11,12,13,14,15,16,17,20,21,22,24,25,26,27,28,29,30,32,33,34,35,36,39,41,42,44,45,46)، بينما يكون غير مباشراً مع الأشجار بالأرقام *(3,4,5,6,7,8,9,10,18,19,23,31,37,38,40,43,47)*. فإذا حسبنا عدد الارتباطات أو الاتصالات المباشرة *(Number of connections/ N)* لشجرة رقم *(1)* كان *(29)* ارتباطاً، أي أن *(N=29)*. أما الارتباطات غير المباشرة فيتم احتسابها ضمن حساب عدد ارتباطات بقية الأجزاء. فمثلاً الارتباط بين شجرة رقم *(1)* وشجرة رقم *(18)* يكون غير مباشر، ويتم عن طريق شجرة رقم *(13)* ... وهكذا، والاتصال بين شجرة رقم *(13)* وشجرة رقم *(18)* سيكون مباشراً ويُحْسَب ضمن ارتباطات شجرة رقم *(13)* والتي سيكون عدد ارتباطاتها *(N=27)*، وكما موضح في الشكل رقم (3). ويُشار الى عدد الارتباطات أو الاتصالات المباشرة *(Number of connections/ N)* بالارتباطية أو الاتصالية *(Connectivity)*، والتي تعبّر عن ميل أو نزعة أي نظام للامتداد والانتشار والتوسّع والنمو عند وصوله الى حد أو حافة حرجة *(Critical Threshold)* من الاكتظاظ والتنظيم الذاتي والتراص *(Compactivity)*، والعكس صحيح. أما التراص *(Compactivity)* فهو إحدى آليات الدفاع أو الإصلاح أو التنظيم الذاتي، ويمكن أن يُعَبَّر عنه بطول الارتباطات أو الاتصالات الكلية المباشرة *(Lengths of connections/ L)*.

ويمكن في حالة البستان أن نحسب وبسهولة جميع إحتمالات أطوال الارتباطات أو الاتصالات *(L)*. فترتيب واصطفاف الأشجار بهذا النسق *(Pattern)* يتيح لنا الحساب وبشكلٍ دقيق. فكما هو واضح من شكل النسق، فإن الارتباطية بين شجرة رقم *(1)* وشجرة رقم *(2)* تساوي وحدة طول واحدة، أي *(L=1)*، وبين شجرة رقم *(1)* وشجرة رقم *(11)* أو شجرة رقم *(13)* تساوي $(L=\sqrt{2})$، بتطبيق قاعدة فيثاغورس، وبين شجرة رقم *(1)* وشجرة رقم *(14)* أو شجرة رقم *(17)* تساوي $(L=\sqrt{5})$، وبين شجرة رقم *(1)* وشجرة رقم *(30)* أو شجرة رقم *(32)* تساوي $(L=\sqrt{17})$... وهكذا. وينتج عن إجراء كامل حسابات (عدد الارتباطات بين أشجار الزيتون *(N)*، وأطوال هذه الارتباطات *(L)*)، الجدول رقم (1) أدناه:

جدول رقم (1): الحسابات التفصيلية لعدد الارتباطات أو الاتصالات *(N)*، وأطوالها *(L)*، في البستان.

Assumed Location No. of each tree	No. of Connections (N)	Lengths of Connections (L)
1	29	165.811
2	30	160.268
3	27	135.232
4	28	123.114
5	26	110.09
6	31	146.852
7	31	155.002
8	28	150.217
9	29	163.392
10	27	180.561
11	28	195.507
12	26	149.723
13	27	137.485
14	26	122.847
15	24	95.642
16	25	112.031
17	20	134.115
18	20	90.134

	19	*20*	*75.855*
	20	*19*	*72.008*
	21	*18*	*68.233*
	22	*19*	*80.105*
	23	*18*	*83.646*
	24	*18*	*86.562*
	25	*18*	*104.47*
	26	*18*	*112.001*
	27	*18*	*63.086*
	28	*17*	*64.69*
	29	*14*	*63.795*
	30	*9*	*53.675*
	31	*9*	*46.458*
	32	*9*	*40.212*
	33	*9*	*34.757*
	34	*9*	*32.487*
	35	*9*	*25.294*
	36	*9*	*26.723*
	37	*9*	*29.171*
	38	*9*	*33.212*
	39	*8*	*37.872*
	40	*1*	*2*
	41	*1*	*2*
	42	*1*	*1*
	43	*1*	*1*
	44	*1*	*2*
	45	*1*	*1*
	46	*1*	*1*
	47	*0*	*0*
TOTAL	*47*	*775*	*3772.335*

وعند تمثيل عمليات الارتباط والاتصال كلها لأجزاء النظام جميعها (أشجار الزيتون جميعها)، ينتج لدينا الشكل رقم (4) أدناه:

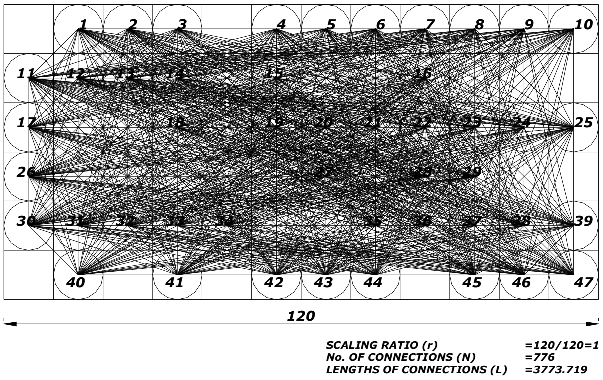

شكل رقم (4): تمثيل إفتراضي لعمليات الارتباط والاتصال كلها بين أشجار بستان الزيتون جميعها.

(المصدر: الباحث)

ويبدو عند النظر للشكل الناتج، ولأول وهلة، الى إن نسقه *(Pattern)* هو في غاية التعقيد. ولا يمكن لنا الجزم بأي حال من الأحوال بوجود نمط *(Order)* كامن ضمنه. وللتحقق من فرضيات البحث، نقــوم بتغييــر المقياس *(Scaling ratio/ r)* طولياً في إثني عشر مستوياً إبتداءً مــن $(r=\frac{1}{12})$ ثــم $(r=\frac{2}{12})$ و $(r=\frac{3}{12})$... وانتهاءً بالمستوي $(r=\frac{12}{12}=1)$. ونحسب التراكمات في عدد الارتباطات أو الاتصالات *(N)*، وأطوالها *(L)* لكل

مستوي. فمثلاً، يضم المستوي $(r=\frac{1}{12})$ الأشجار بالأرقام *(10,25,39,47)*، بينما يضم المستوي $(r=\frac{2}{12})$ أشجار المستوي السابق مضافاً لها الأشجار *(9,24,38,46)*. ثم نحسب أعداد الارتباطات أو الاتصالات الكلية *(N)*، وأطوالها *(L)* لكل مستوي، حيث أن *(N=54, L=322.903)* في المستوي $(r=\frac{1}{12})$، وأن *(N=111, L=607.069)* في المستوي $(r=\frac{2}{12})$ ...وهكذا. أنظر الشكلين (5)، (6) اللذين يعكسان أشكالاً ذات هياكل كسرية متشرشبة ومتعرّجة ومتكسّرة يصعب معها الوقوف بصرياً على ما يميّزها.

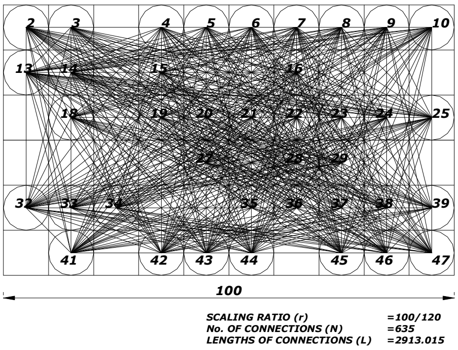

شكل رقم (5): حساب عدد الارتباطات أو الاتصالات *(N)*، وأطوالها الكلية *(L)* لنسق البستان عندما $(r=\frac{10}{12})$.

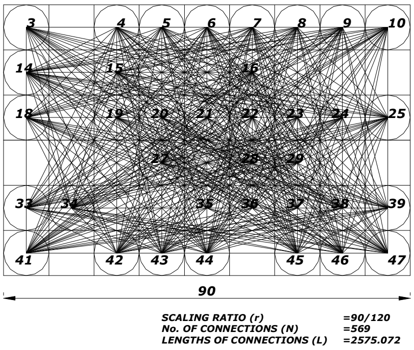

شكل رقم (6): حساب عدد الارتباطات أو الاتصالات *(N)*، وأطوالها الكلية *(L)* لنسق البستان عندما $(r=\frac{9}{12})$.

كما ويوضح الجدول رقم (2) أدناه الحسابات الكلية التفصيلية لعدد الارتباطات أو الاتصالات *(N)*، وأطوالها *(L)* التراكمية لجميع مستويات تغيير المقياس *(r)* الاثني عشر. وبالمقابل يُظْهِر الجدول رقم (3) القيم اللوغاريتمية لهذه الحسابات.

جدول رقم (2): الحسابات الكلية التفصيلية لعدد الارتباطات *(N)* وأطوالها *(L)* بشكلٍ متراكم عبر اثني عشر مستوياً من مستويات تغيير المقياس *(r)* في بستان الزيتون.

	1	2	3	4	5	6	7	8	9	10	11	12

Scaling Ratio (r)	12/12=1	11/12	10/12	9/12	8/12	7/12	6/12	5/12	4/12	3/12	2/12	1/12
No. of Connections (N)	776	701	635	569	486	477	404	340	282	181	111	54
Lengths of Connections (L)	3773.719	3278.421	2913.015	2575.072	2190.11	2157.623	1862.012	1615.828	1373.449	934.898	607.069	322.903

جدول رقم (3): القيم اللوغاريتمية الكاملة لعدد الارتباطات *(N)* وأطوالها *(L)* بشكلٍ متراكم عبر اثني عشر مستوياً من مستويات تغيير المقياس *(r)* مع حساب البعد الكسري أو الجزئي اللاإقليدي في بستان الزيتون.

	1	2	3	4	5	6	7	8	9	10	11	12	Fractal Dimension (D)
Log (r)	0	-0.03778	-0.07918	-0.12493	-0.17609	-0.23408	-0.30102	-0.38021	-0.47712	-0.60205	-0.77815	-1.07918	
Log (N)	2.88986	2.84571	2.80277	2.75511	2.68663	2.67851	2.60638	2.53147	2.45024	2.25767	2.04532	1.73239	**1.067**
Log (L)	3.57676	3.51566	3.46434	3.41078	3.34046	3.33397	3.26998	3.20839	3.13781	3.97076	2.78323	2.50907	**0.963**

وعند تمثيل العلاقة اللوغاريتمية بين *(log(r))* مع *(log(N))* من جهة، ثم *(log(r))* مع *(log(L))* من جهةٍ أخرى على الإحداثيات الديكارتية، نخلص الى الشكلين (7)، (8) على التوالي:

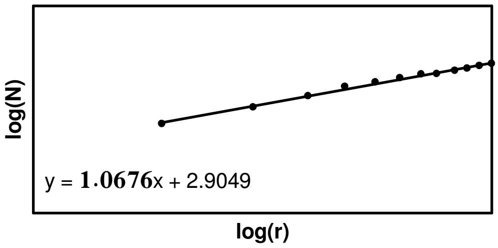

شكل رقم (7): العلاقة بين القيم اللوغاريتمية لتغيير المقياس *(log(r))* والقيم اللوغاريتمية لتغيير عدد الارتباطات أو الاتصالات *(log(N))* في بستان الزيتون تكون خطيّة.

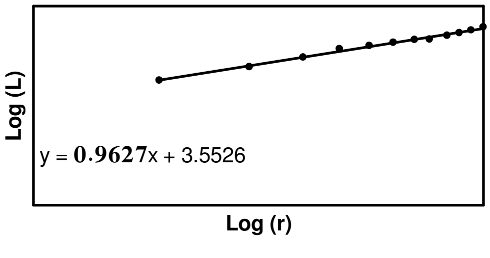

شكل رقم (8): العلاقة بين القيم اللوغاريتمية لتغيير المقياس *(log(r))* والقيم اللوغاريتمية لتغيير

أطوال الارتباطات أو الاتصالات *((log(L)* في بستان الزيتون تكون خطّيّة أيضاً.

وكما هو واضح من التمثيل الديكارتي، فإن العلاقة بين القيم اللوغاريتمية لتغيير المقياس *((log(r)*، والقيم اللوغاريتمية لتغيير عدد الارتباطات أو الاتصالات *((log(N)* من جهة، وأطوالها *((log(L)* من جهة أخرى، هي علاقة خطية (طردية) بنمطٍ متشابه (حيث أن الميل *(Slope)* في الحالة الأولى يساوي ($Slope \approx 1.067$) وفي الحالة الثانية ($Slope \approx 0.963$)) والميل هنا يمثّل البعد الكسري أو الجزئي اللاإقليدي *(Fractal Dimension/ D)*. **وهذا يؤيّد ما ذهبنا إليه من أن (الأنساق الناجحة تضم هياكل ذات أشكال كسرية تتغيّر بأنماط متشابهة من حيث بُعدها الكسري أو الجزئي اللاإقليدي عند تغيير مقياسها).**

ومما سبق يتضح أن ميل هذا النظام الاحيائي الناجح (بستان الزيتون) نحو الارتباط والاتصال يعادل ميله للتراص. أي أنه قد وصل الى حد حرج وحالة من الاتزان مابين قدرته على النمو والهجوم والتوسّع والامتداد، ومابين قابليته على التماسك والتراص والتنظيم الداخلي، يعكسها البعد الكسري.

تحليل نسق النظام الحضري لمدينة بغداد:

تمتاز العاصمة بغداد، حالها حال معظم المدن العراقية بميلٍ ونزعةٍ للامتداد والتوسّع الأفقي. وقد يعكس هذا عدة مؤشرات منها تشريعية، وأخرى تخطيطية أو اجتماعية أو اقتصادية أو مناخية... وقد ساهم ذلك في دعم اختيارها للتطبيق العملي *(as a case study)* في هذا البحث، والاعتماد على مخططها الأفقي بالذات للتطبيق، على الرغم من أن ذلك قد ذُكِرَ كإحدى المحددات البحثية.

وقد تم الاعتماد بالأساس على صورة جوية مأخوذة عن طريق الأقمار الصناعية *(Satellite)* لواقع حال مدينة بغداد للعام (2004). وتم استخدام تكنيك يدوي من تطبيق برنامج الأوتوكاد *(Auto-CAD)* لرسم مدينة بغداد (نسخها) بالمشي فوق جميع أجزاء وتفاصيل صورتها الأصلية يدوياً بالاستفادة من قابلية هذا البرنامج على تغيير المقياس وحساب المتغيّرات بسهولةٍ ومرونةٍ عالية اعتماداً على التقريب بصرياً *(Visual approximation)*. أنظر الشكلين (9)، (10).

شكل رقم (9): صورة بالأقمار الصناعية لواقع حال مدينة بغداد (2004) م.

شكل رقم (10): تحويل صورة بغداد الجوية الى مخطط أفقي تفصيلي باستخدام الأوتوكاد *(Auto-CAD)*، وبالأبعاد نفسها تقريباً.

واعتماداً على طريقة حساب الخلايا أو الوحدات أو المربعات*(The Cell-Counting Method)*، نختار شبكة *(Grid)* مناسبة لتغطية المخطط الأفقي كله لمدينة بغداد *(10×10 units)*، أنظر الشكل رقم (11).

شكل رقم (11): تغطية مخطط مدينة بغداد الأفقي بشبكة من المربعات *(10×10 units)* لتسهيل عملية العد والحساب التقريبي.

إن تقليل أبعاد الشبكة أصغر فأصغر يُزيد من دقة القيم والبيانات المستحصلة، ويزيد من صعوبة الحسابات بالمقابل. لذا تم اختيار هذه الأبعاد *(10×10 units)* تقريباً للفكرة، وتسهيلاً للمهمة. حيث يتم بعدها تحويل هذا المخطط الشبكي الى نموذج مرقّم بشكلٍ متتالي (باتباع خطوات العمل ومراحله نفسها على بستان الزيتون سابقاً) اعتماداً على التقريب بصرياً في حساب وتثبيت المربعات (المشغول نصفها أو أكثر بمساحات مظللة (مبنيّة) ضمن مخطط مدينة بغداد الكلي)، ليُختَزَل المخطط الشبكي الى نموذج مرقّم بالأبعاد *(8×8 units)*، وكما موضّح في الشكل (12) أدناه:

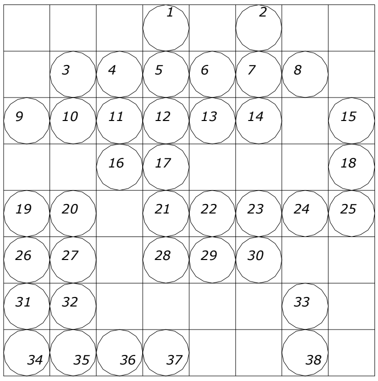

شكل رقم (12): نموذج لترقيم المربّعات المشغولة بالبناء تباعاً في مخطط بغداد الأفقي.

(المصدر: الباحث)

ثم نبدأ بِعَدِّ وحساب عدد الارتباطات أو الاتصالات *(Number of connections/ N)*، وأطوالها *(Lengths of connections/ L)* لكل مربّع مشغول بنائياً ضمن وحدات أو أجزاء النظام ككل. لينتج عن القيام بكافة الحسابات التفصيلية الجدول رقم (4):

جدول رقم (4): الحسابات التفصيلية لعدد الارتباطات أو الاتصالات *(N)* بين أجزاء النظام، وأطوالها *(L)* في مخطط مدينة بغداد الأفقي.

Assumed Location No. of each part	*No. of Connections (N)*	*Lengths of Connections (L)*
1	23	95.108936
2	25	120.32109
3	20	80.78994
4	25	96.32088
5	21	57.77892
6	21	75.23209
7	23	91.46485
8	20	83.75320
9	18	80.46066
10	17	68.16164
11	19	68.92173
12	19	71.27665
13	19	68.7522
14	19	75.99183
15	18	93.29037
16	17	52.77669
17	16	52.20484
18	14	70.66625
19	10	31.51071
20	12	37.31795
21	11	27.85598
22	12	35.56487
23	12	40.09242
24	10	37.21045
25	11	53.80046
26	7	21.66315
27	8	22.19896
28	9	23.83622
29	9	26.49206
30	8	29.16368
31	6	14.89532
32	6	16.16351
33	5	19.46716
34	1	1
35	1	1

	36	1	1
	37	1	3
	38	0	0
TOTAL	38	494	1846.505666

وعند تمثيل جميع عمليات الارتباط والاتصال لجميع أجزاء النظام، نحصل على الشكل (13).

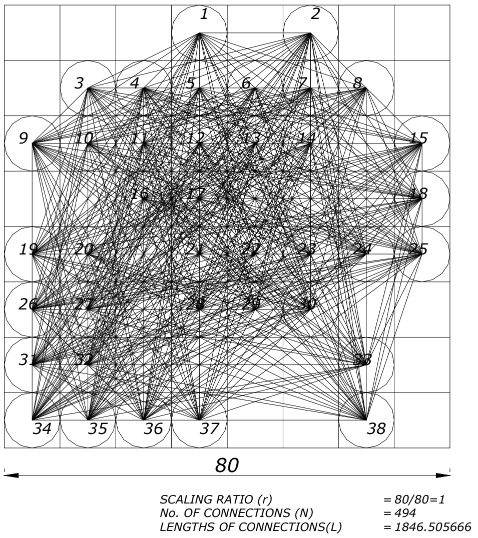

شكل رقم (13): تمثيل إفتراضي لكل عمليات الارتباط والاتصال بين جميع وحدات المخطط الأفقي لبغداد.

ولنتحقق الآن من فروضنا اعتماداً على أسلوب التحليل المُقارن *(Comparative Analysis)* بالنظام الاحيائي الناجح والمتّزن لبستان الزيتون. ونستطيع الحصول هنا على ثمانية مستويات من تغيير المقياس *(r)* طولياً، تبدأ من ($r=\frac{1}{8}$) ثم ($r=\frac{2}{8}$)...، وتنتهي بالمستوي ($r=\frac{8}{8}=1$). ثم نحسب أعداد الارتباطات أو الاتصالات *(N)*، وأطوالها *(L)*، المتراكمة في مستوي. حيث يضم المستوي ($r=\frac{1}{8}$)، على سبيل المثال، الخلايا أو الوحدات بالأرقام *(15,18,25)*، ويضم المستوي ($r=\frac{2}{8}$) الأرقام *(8,24,33,38,15,18,25)*، ... وهكذا. وعند حساب عدد الارتباطات أو الاتصالات *(N)*، وأطوالها *(L)* في كل مستوي من مستويات تغيير المقياس الثمانية، نجد أن *(N=45, L=232.16468)* في المستوي الأول ($r=\frac{1}{8}$)، وأن *(N=81, L=380.292)* في المستوي الثاني ($r=\frac{2}{8}$)، ... وهكذا. أنظر الأشكال (14)، (15) التي تعكس أشكالاً ذات هياكل كسرية متشظية تفتقر لوجود أي نمط ضمنها عند النظر إليها لأول وهلة.

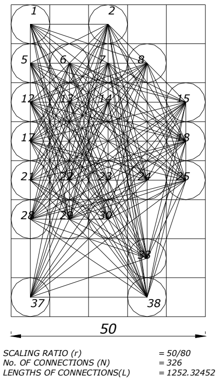

شكل رقم (14): حساب عدد الارتباطات أو الاتصالات *(N)*، وأطوالها *(L)* لنموذج مدينة بغداد في المستوي الخامس ($r = 50/80$) من تغيير المقياس.

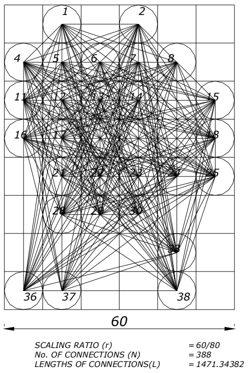

شكل رقم (15): حساب عدد الارتباطات أو الاتصالات *(N)*، وأطوالها *(L)* لنموذج مدينة بغداد في المستوي السادس ($r = 60/80$) من تغيير المقياس.

ويوضّح الجدول رقم (5) أدناه الحسابات الكلية التفصيلية بهذا الخصوص، بينما يُظهِر الجدول رقم (6) القيم اللوغاريتمية لهذه الحسابات.

جدول رقم (5): الحسابات الكلية التفصيلية لعدد الارتباطات *(N)*، وأطوالها *(L)* بشكلٍ متراكم عبر ثمانية مستويات من تغيير مقياس *(r)* نموذج مدينة بغداد.

	1	2	3	4	5	6	7	8
Scaling Ratio (r)	1/8	2/8	3/8	4/8	5/8	6/8	7/8	8/8
No. of Connections (N)	43	78	165	226	326	388	452	494
Lengths of Connections (L)	217.75708	358.18789	715.22176	921.26298	1252.32452	1471.34382	1696.97582	1846.50566

جدول رقم (6): القيم اللوغاريتمية الكاملة لعدد الارتباطات *(N)*، وأطوالها *(L)* بشكلٍ متراكم عبر ثمانية مستويات من تغيير مقياس *(r)* نموذج مدينة بغداد.

	1	2	3	4	5	6	7	8	**Fractal Dimension (D)**
Log (r)	-0.903089	-0.602059	-0.425596	-0.301029	-0.204119	-0.124938	-0.05799	0	
Log (N)	1.633346	1.89209	2.21748	2.3541	2.513217	2.58883	2.655138	2.69372	**1.2471**
Log (L)	2.33797	2.55411	2.85444	2.96438	3.097716	3.167714	3.22967	3.26635	**1.0901**

ويمكن الاعتماد على التمثيل الديكارتي أو التحليلات الإحصائية *(regression)* للقيم اللوغاريتمية للمتغيّرات لإيجاد العلاقة فيما بينها. فالتمثيل الديكارتي للعلاقة بين القيم اللوغاريتمية لتغيير المقياس *(log(r))* في ثمانية مستويات مقابل القيم اللوغاريتمية لتغيّر عدد الارتباطات أو الاتصالات *(log(N))* مرة، ومقابل القيم اللوغاريتمية لتغيّر أطوال هذه الارتباطات أو الاتصالات *(log(L))* مرةً أخرى، تنتج عنه علاقة خطية طردية أيضاً بأنماطٍ مختلفة ذات ميلٍ أو انحدار *(slope)* متباين. فإذا ما كان الميل أو الانحدار *(slope)* في التمثيل على الإحداثيات الديكارتية يمثّل طريقة أخرى للتعبير عن البعد الكسري أو الجزئي اللاإقليدي *(Fractal Dimension/ D)*، فإن الميل أو البعد الكسري لعلاقة *(log(r))* مع *(log(N))* يساوي $(D_N \approx 1.2471)$، أما لعلاقة *(log(r))* مع *(log(L))* فيساوي $(D_L \approx 1.0901)$.

وتشير هذه النتائج ضمناً، إذا ما قورنت بنتائج بستان الزيتون، الى أن شكل هذه الهياكل الكسرية على الرغم من تشظّيها وشرشبتها لا يمكن أن يؤلّف نسقاً *(Pattern)* ناجحاً ومتّزناً. أما نمط *(Order)* أو ميل أو نزعة النظام نحو التوسع والامتداد والنمو أفقياً فهو ملحوظ بشكلٍ ملفت للنظر (حيث أن: $(D_N = 1.2471)$)، ولكنه يختلف عن نمط أو ميل أو نزعة نفس النظام (مدينة بغداد) للدفاع والتراص والتنظيم الذاتي (حيث أن: $(D_L = 1.0901)$). إذ ان مؤشر نمط الارتباط أو الاتصال (D_N) يستقر الى مستوى غير طبيعي، مقارنةً بحاله في الأنساق الناجحة والذي يقترب فيها من $(D_N \approx 1)$. وهذا يعني تشخيصاً لحالةٍ مَرَضيّةٍ (غير صحية) في توسّع وامتداد مدينة بغداد أفقياً وبشكلٍ غير مدروس. بمعنى أن المؤثرات الخارجية من تشريعات وقوانين وقيود طبيعية أو اجتماعية أو اقتصادية أو ملكيّة شخصية... لم تَحِد أو تمنع المدينة من التوسّع والامتداد الأفقي.

لذا يجب تقليل مؤشر نمط الارتباط أو الاتصال (D_N) الى مستويات مقبولة يقترب فيها من $(D_N \approx 1)$، ويتساوى فيها مع مؤشر نمط التراص (D_L)، أي أن $(D_N \approx D_L \approx 1)$. ومن البديهي أن تتبادر للذهن في هذه

الحالة عدة خيارات ومقترحات لتحقيق ذلك، منها تشريعية تخص الملكية وأحكام البناء، وأخرى تنفيذية تتعلّق برفع التجاوزات والبناء العشوائي، وأخرى تخطيطية تقود وتوجّه عمليّات استغلال الأرض واستعمالاتها، وغيرها اقتصادية تتعلّق بأسعار الأراضي والعقارات... ولكن علاج المشكلة ليس بهذه البساطة. إذ ان إحتمالات إعادة هيكلة وترتيب أجزاء وخلايا النظام (بلا حذف أو إضافة) لغرض ضبط البُعد الكسري أو الجزئي اللاإقليدي (بوصفه مؤشراً لنمط التغيّر في عدد الأجزاء (N) أو أطوالها (L) عند تغيير المقياس (r)) تكون محدودة عادةً. فأي تغيير، على سبيل المثال، في أي جزء أو خلية أو وحدة (رغم صعوبة ذلك) يتضمّن تغييراً في أعداد الارتباطات أو الاتصالات بينها (N) من جهة، يقابله تغيير مختلف، وقد يصعب حسابه، في أطوالها (L) من جهة أخرى. وهنا جاءت الحاجة ملحّة للقيام بالكثير من العمليّات الحسابية المعقّدة والمتكررة وبشكلٍ يفوق قدرة الإنسان الاعتيادية لضبط هذه التوليفة بشكلٍ متناغم ومتشابه مع تلك التي تم حسابها لنسق البستان الناجح والمتّزن. فتم اللجوء الى تقنيّات الحاسوب المتطوّرة للاستفادة منها في هذا المجال.

وعلى الرغم من كل ذلك، فإن الصعوبة مازالت قائمة في الوصول الى نسقٍ (حتى ولو بشكلٍ إفتراضي) ناجح ومتّزن وذو أنماط وميول متشابهة نحو الارتباط والاتصال من جهة، ونحو التراص من جهةٍ أخرى. ومن الصعوبة أيضاً التحكّم بمقياس هذه الأنماط (عن طريق البعد الكسري أو الجزئي اللاإقليدي) صعوداً ونزولاً. ويتطلب الأمر محاولاتٍ عدة للتوليف والترهيم والتقريب. كما وإن المحافظة على هذا النسق من دون تغيير أو ضمن تغييرات محسوبة ومقبولة يُعَدّ أمراً في غاية الصعوبة، كون أن الأنظمة الحية خصوصاً ومنها الأنظمة الحضرية هي في حالة تغيُّر وتبدُّل وتطوُّر مستمر. فهل يمكن لهذه الأنساق الناجحة أن تتكرر لاحقاً في ظرفٍ آخر ومكان وزمان مختلف وبشكلٍ مغاير؟ وهل أن تكرارها سيكون بنفس أشكال الهياكل الكسرية ولكن بأبعادٍ مضاعفة؟

وبرأينا، فإن حساب البعد الكسري أو الجزئي اللاإقليدي (بوصفه مقياساً لنمط الارتباط أو التراص هنا في هذا البحث) يوفّر لنا حدوداً وقيوداً في عالمٍ فوضويٍّ معقد، متسارع التغيّر. وبالمقابل يترك لنا المجال واسعاً لاختيار أنساقٍ متنوعةٍ بحريّةٍ أكبر. وهذه الحرية هي بحد ذاتها ليست مطلقة، بل تخضع لحساباتٍ أخرى وقيودٍ جديدة. وكما أسلفنا، فإن الحرية لا تُدرك إلا بالقيد، والعكس صحيح.

إن حرية إرادة الإنسان (الرهبان) تلي إرادة السماء ولكنها ليست مطلقة. فلو كانت مطلقة لتمكّن هؤلاء الرهبان من زراعة كل البستان بـ (72) شجرة زيتون (بأقل مساحة من الأرض، وبأقل مسافات بينية ممكنة)، أو حتى أن يزرعوا دوماً ما يختارونه من أرضٍ بالكامل من دون تبذير. فكان في خلق حشرات التربة، مثلاً، ما يشير الى إرادة السماء المطلقة، ويُمْسِك بحرية إرادة الإنسان ويمنعها من الانفلات بإتجاه الاعتقاد والظن بمطلقية حرية إرادته عندما يزرع كلَّ ما يختاره على وفقَ ما يراه، وما يُقيّد حرية أشجار الزيتون من أن تعتاش كيفما تشاء على التربة بلا رادعٍ ولا ضابط. وجاء خلْق الأشجار نفسها وطريقة إصطفافها وترتيبها بموجب واقعها الفيزيائي الوجودي على وفق مسافات بينية ونسبٍ محددة قيداً مؤطّراً لحرية الإنسان لا يستطيع

تجاهله أو تجنّبه إذا ما أراد أن يحقق مُبتغاه، ولغزاً دفاعياً محيّراً لحشرات التربة.

ويلجأ الإنسان عادةً بإرادته الحرة التي يتفوّق بها على ما سواه من المخلوقات لاتخاذ زمام المبادرة باستمرار لصنع أنظمة وعوالم خاصة به. ويحاول دوماً أن يسيطر على سلوكيات هذه الأنظمة، وأن يسخّرها لمصلحته. ومن أجل ذلك، فقد اجتهد الإنسان طويلاً (عبر قرون عديدة) حتى استطاع أن يحصل على نسقٍ ناجح ومتّزن لزراعةِ بستانٍ بأشجار الزيتون. ومع ذلك فمازالت هناك محددات لا حصر لها ولا سلطان له عليها تحكمه وتحدّ من إرادته (كأقصى عدد كلي ممكن من الأشجار مثلاُ، أو كأبعاد البستان نفسه أو شكله، أو حتى مورفولوجيته وطريقة اصطفاف وترتيب الأشجار فيه...). وهذا لا ينفي وجود إحتمالات أخرى ممكنة لأنساقٍ مختلفة وفق محددات جديدة لحريته، من أعدادِ أشجارٍ وأبعادٍ وأشكالٍ مغايرة. فإذا ما استهدف أحدها (كأن يكون مبتغاه الحصول على أكبر عدد ممكن من الأشجار في أقل مساحة ممكنة)، فإنه لن يستطيع أن يتنبّأ أو أن يجزِم بالبقية كشكل البستان الجديد أو أبعاده أو حتى مورفولوجيته...

والشيء نفسه يُقال فيما يخص حالتنا الدراسية حول نظام حضري واقعي قائم(وهو مخطط مدينة بغداد الأفقي). **فقياس نمط الارتباط أو الاتصال فيه** $(D_N \approx 1.2471)$ **لا يشابه قياس نمط التراص** $(D_L \approx 1.0901)$ **من جانب، وقيمته أكبر من** *(1)* **من جانبٍ آخر. وهذا يشير الى خلل واضح في مورفولوجية وبناء هيكل النسيج الحضري للمدينة.** ونحتاج لتقليله وضبطه مع الأخير ليكون مساوياً لـ $(D_N \approx D_L \approx 1)$، أن نتحكّم بعدد الخلايا أو الوحدات المبنية (أجزاء النظام)، وبطريقةِ توزيعها واصطفافها وأعداد الارتباطات أو الاتصالات *(N)* فيما بينها وأطوالها *(L)* أيضاً. وبما أن النظام الحضري هو نظام ديناميكي معقّد ويتغيّر باستمرار لا يمكن اختزاله بنسقٍ ثابت أو اختصاره الى مجرد أنماطٍ متشابهة دوماً. لذا جاءت الحلول جزئية وآنيّة وصعبة التطبيق وغير محسوبة النتائج.

ويكمن الحل الأمثل، باعتقادنا، بالتأني عند التدخّل في علاج مشكلات النسيج الحضري الحرجة، والاستمرار بمراقبة مؤشر نمط الارتباط أو التراص (متمثلاً بالبعد الكسري أو الجزئي اللاإقليدي) عند اتخاذ أي قرار مستقبلي في أي مستوى من مستويات التخطيط والتصميم حفاظاً على أنماطٍ مرغوبة، أو تجنّباً لأنماطٍ أخرى غير مقبولة، أو تحقيقاً لأنماطٍ مسبقةِ الحساب. ولا بد هنا من الاستعانة بتقنيّات الحاسوب لتحليل نسق مدينة بغداد وتحويله الى مخطط شبكي بدقة أكبر (عدم الاكتفاء بالأبعاد *(8×8 units)* عند التحليل، بل يمكن الوصول بالدقة الى مستوى وحدة الجيرة *(Neighborhood)* أو حتى الى تفاصيل الوحدة السكنية الواحدة أو المبنى المنفرد). وعندئذٍ يمكن متابعة ومراقبة مقياس البعد الكسري أو الجزئي بدقة أكبر وموثوقية أعلى، وبشكلٍ مستمر ومتواصل لغرض توجيهه بالاتجاه الصحيح مستقبلاً ليتساوى فيه ما بين الميل للارتباط والنزعة نحو التراص، ويقترب مقداره من $(D \approx 1)$. وقد يتطلب تحقيق مثل هذا الأمر الكثير من التنسيق والجهد والوقت.

الاستنتاجات والتوصيات:

أشارت النتائج الى أن ميل بستان الزيتون (كنظام احيائي ناجح ومتزن تم توارثه عبر عصور) نحو الارتباط والاتصال يعادل ميله للتراص. أي أنه قد وصل الى حد حرج وحالة من الاتزان مابين قدرته على النمو والهجوم والتوسع والانتشار والامتداد من جهة، ومابين قابليته على التماسك والتراص والتنظيم الداخلي من جهة أخرى. ويعكس هذه الحالة البعد الكسري أو الجزئي اللاإقليدي الذي تم احتسابه. كما وان قيمة هذه الأبعاد الكسرية أو الجزئية متساوية وتقترب قيمتها من $(D \approx 1)$.

أما بخصوص تحليل النسيج الحضري الأفقي *(2-dim.)* لمدينة بغداد ومقارنته بنسق نظام بستان الزيتون، فقد شخّص البحث حالة مرضية (غير صحية) في التركيب الداخلي والمورفولوجي لهذا النسيج. فالمدينة في مخططها الأفقي تميل للتوسع والامتداد والارتباط أفقياً أكثر من ميلها للتراص. وخلص البحث الى صعوبة علاج مرض أي نسيج حضري بالتدخّل الفجائي الكبير في أنساقه لغرض تعديل وضبط مؤشّري الارتباط أو الاتصال (D_N)، والتراص (D_L). إذْ لا يمكن التغاضي عن القرارات الفردية الصغيرة والمتراكمة، أو عن محددات ومعيقات لمثل هذا النوع من التدخّل سواء أكانت طبيعية أم اقتصادية أم اجتماعية أم دينية... لذا وجب التدخّل بعنايةٍ فائقة عند الحاجة أو على وفق ستراتيجية محسوبة بدقةٍ بالغة (كأن يُراد سحب نمو المدينة وتوجيهه بإتجاه معين).

ويوصي البحث بالحيلولة دون تهرؤ وتمزّق النسيج الحضري عن طريق مراقبة مؤشر أنماط التغيّر (البعد الكسري أو الجزئي اللاإقليدي كمؤشر لنمط الارتباط والاتصال، أو كمؤشر لنمط التراص) وضبطه بشكلٍ متوازن، كما أسلفنا، يضمن توجيه نمو وتغيّر النظام الحضري بشكلٍ صحيح. ولا يجوز اختزال أو اختصار هذه الأنظمة الى مجرد عيّنة مختبرية تخضع للتجريب والترهيم، بل يجب التعامل معها على انها كائن حي بعلاقة تبادلية، مع السماح للأنساق أن تكتمل دون بترها أو قطعها *(Anti-patterns)*، بفرض قيود قسرية غير مدروسة، أو بعدم المبالاة بإطلاق الحريات عشوائياً.

المصادر:

1. أكبر، جميل عبد القادر؛ *عمارة الأرض في الإسلام*؛ دار القبلة للثقافة الإسلامية؛ جدة؛ (1992).
2. الحيدري، كمال؛ *لا ضرر ولا ضرار*؛ مركز بقية الله الأعظم؛ بيروت؛ (2000)م.
3. دي بور، ت.ج.؛ *تاريخ الفلسفة في الإسلام*؛ ترجمة: محمد عبد الهادي؛ القاهرة؛ مطبعة لجنة التأليف والترجمة والنشر؛ (1971)م.
4. السمهوري، وائل؛ *إشكالية خصوصية بنية النسيج العمراني في المدينة العربية الإسلامية: درجات النظام والعفوية*؛ مجلة جامعة دمشق للعلوم والهندسة؛ المجلّد (14)؛ العدد (2)؛ (1998).
5. الصدر، محمد باقر؛ *الفتاوى الواضحة*؛ مركز الأبحاث والدراسات التخصصية؛ بيروت؛ لبنان؛ (1981)م.

6. الهذلول، صالح بن علي؛ *المدينة العربية الإسلامية: أثر التشريع في تكوين البيئة العمرانية*؛ فهرسة مكتبة الملك فهد الوطنية؛ المملكة العربية السعودية؛ (1994).

7. Davies P.; *The Cosmic Blueprint*; University of Huston; USA; (1988).
8. Gleick J.; *Chaos: Making a New Science*; William Heinemann LTD; Great Britain; (1988).
9. Jencks, C.; *The Architecture of the Jumping Universe*; Academy Editions; Great Britain; (1995).
10. Moughtin J.C. "Urbanism in Britain"; *Town Planning Review Journal*; TPR. 63 (1), (1992).
11. Salingaros N.; The Laws of Architecture from a Physicist's Perspective"; *Physics Essay*; Vol.8; No.4; (1995).
12. Wahl B.; *Exploring Fractals on the Macintosh*; Addison-Wesley Publishing Company; USA; (1998).

Number 2 Volume 13 June 2007 Journal of Engineering

ANALYSIS OF CORNER BEAM-COLUMN JUNCTION WITH INCLUSION OF THE EFFECT OF CONSTRUCTION JOINTS

Prof. Dr. Husain M. Husain
University of Tikrit

Dina M. Hamza
M.Sc. Graduate
University of Baghdad

ABSTRUCT

This paper describes a comparison between beam-column junctions with and without construction joint, also, a parametric study deals with construction joint is presented by taking various conditions of the junction. These include the various positions of the construction joint, the axial load on the column, strength of concrete in the second cast and the amount of dowels crossing the joint. By developing a computer program which was originally written by Dr. Ihsan Al-Shaarbaf (1990), (P3DNFEA, program of three dimensional nonlinear finite element analysis), to consider the effect of construction joint depending on the fact that the shear force can be transmitted across the shear plane either by interlocking of the aggregate particles protruding from each face or by dowel action of the reinforcement crossing the cracks by using Fronteddu's and Millard's models, respectively. It is concluded that the construction joints existed in the beam-column junctions result in a significant reduction in the in-plane shear stiffness and it would affect only on the rotation and shear strains of the joint.

الخلاصة

هذا البحث تضمن مقارنة بين مفاصل الجسور والاعمدة الخرسانية بوجود المفاصل الانشائية وبعدم وجودها كذلك اجريت دراسة واسعة تضمنت كل مايتعلق بالعوامل المؤثرة بالمفصل الانشائي. هذه العوامل تتضمن المواقع المختلفة للمفصل الانشائي، الحمل المحوري للعمود، المقاومة الانضغاطية للخرسانة ضمن الصبة الثانية ومقدار الحديد المار من خلال المفصل. من خلال تطوير برنامج الحاسوب المكتوب اصلا من قبل الدكتور احسان الشعرباف (P3DNFEA وهو برنامج لتحليل المسائل ثلاثية الابعاد تحليلا لاخطيا بطريقة العناصر المحددة)، لادخال تاثير المفصل الانشائي اعتمادا على حقيقة انتقال قوة القص خلال السطح القصي اما عن طريق تداخل حبيبات الركام البارزة من كل وجه او عن طريق تاثير التوتيد للحديد المار من خلال ذلك السطح وذلك باستخدام مويلات فرونتيدو وميلارد بالتتابع. وبعد تطوير البرنامج واجراء التحليل تم الاستنتاج بان المفصل الانشائي الموجود ضمن مفاصل الجسور والاعمدة الخرسانية يؤدي الى تناقص ملحوض في الصلابة القصية وهو يؤثر فقط على دوران المفصل وعلى الانفعالات القصية فيه.

KEYWORDS

Beam-column junction, Reinforced concrete, Finite elements, Construction joints

كلمات دالة: مفصل العتب-العمود، خرسانة مسلحة، عناصر محددة، مفاصل انشائية

INTRODUCTION

The junctions studied are made of two pours, this results in a cold joint. The existence of a cold joint means that the specimens simulate construction practice. In addition to the overall behaviour of the beam-column junction during each stage of loading, it is important to note the mode of failure in this region. Five different modes of failure are possible in the beam-column connection, these include the following:

1) Hinging of the beams at the connection, Fig.(1.a).
2) Hinging of the column, Fig.(1.b).
3)Loss of the concrete cover over the reinforcement in the beam-column core,Fig.(1.c).
4)The loss of anchorage of the reinforcement, Fig.(1.d).
5)The consequences of failure of the connection in shear, Fig.(1.e).

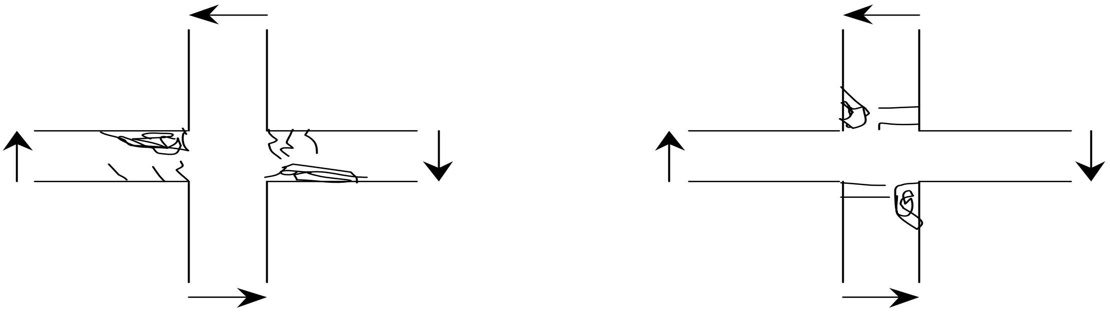

Beam Hinging
(a)

Column Hinging
(b)

Column Crushing
(c)

Reinforcing Bar
Anchorage
(d)

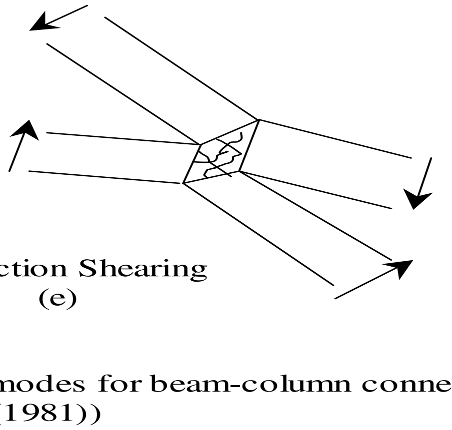

Connection Shearing
(e)

Fig.(1) Failure modes for beam-column connection
(Meinheit et al.(1981))

MATERIAL MODELLING

In addition to the original three-dimensional computational model of P3DNFEA, the models used in the present study and incorporated in the present developed program are as follows:

1) Theoretical Aggregate Interlock Models
2) Theoretical Dowel Action Models

ORIGINAL THREE-DIMENSIONAL COMPUTATIONAL MODEL

The 3-D computational model of original computer program, P3DNFEA is now described.

The behaviour of concrete is simulated by using 20-noded brick elements. An elasto-plastic work hardening model followed by a perfectly plastic response, which is terminated at the onset of crushing is adopted for concrete in compression. The plasticity model was illustrated in terms of the following constituents:

1) The yield criterion of two stress invariants (Cervenka (1985)).
2) An isotropic hardening rule is used (Cervenka (1985)).
3) An associated flow rule (Owen and Hinton (1980)).
4)The crushing rule.

In tension, a smeared crack model with fixed orthogonal cracks is used (Rashid (1968)). The reinforcing bars are idealized as axial members embedded within the brick elements, the elastic-perfectly plastic relation which ignores the strain-hardening region is used.

THEORETICAL AGGREGATE INTERLOCK MODELS

Several models have been proposed to explain or predict the aggregate interlock behaviour. The two-phase model by Walraven and Reinhardt (1981) is an example of a physical model. That type of model gives a better understanding of the mechanism involved at the crack interface. The Yoshikawa et al. (1989) model is an example of an empirical model, in which a free slippage occurs in the initial shear load on the cracked planes, which are not in close contact, and further application of the shear stress makes the cracks stiffer due to firm contact (aggregate interlock). Finally, the shear stress levels off approaching the ultimate shear strength. The Tassios and Vintzeleou (1987) model is another example of empirical model. It covers two types of interfaces, the rough interface and the smooth interface, for normal stresses ranging up to 2 MPa, in this model, the frictional resistance is roughly equal to the tensile strength of concrete, taking into account the tensile strength reduction due to a transverse compressive stress as follows:

$$\tau_u = (0.3 (10+9 (\sigma_c/f_t) - (\sigma_c/f_t)^2)^{0.5}) f_t \qquad (1)$$

Fronteddu et al. (1998) utilized their experimental results from displacement controlled shear tests on concrete lift joint specimens with different surface preparations, to propose an empirical interface constitutive model based on the concept of basic friction coefficient (μb) and roughness friction coefficient (μi):

$$\mu = \frac{\lambda_d \mu_b + \chi_i \mu_i}{1 - \lambda_d \chi_i \mu_b \mu_i} \qquad (2)$$

where $\mu_b = 0.950 - 0.220\ \sigma_n$ for $\sigma_n \leq 0.5$ Mpa

$\mu_b = 0.865 - 0.050\ \sigma_n$ for $0.5 \leq \sigma_n \leq 2.0$ Mpa

μ_i is defined by the equations in Table (1). Two correction factors were introduced: (1) λ_d, the dynamic reduction factor equal to 1.00 for static loading, and 0.85 for dynamic loading; and (2) χ_i, the interface roughness factor equal to 1.00 for cracked homogeneous concrete, 0.8 for water blasted joints, 0.15 for untreated joints, and 0.00 for flat independent concrete surfaces.

Based on the experimental results presented by Fronteddu et al. (1998), a bilinear relationship between shearing stress and slip, Fig. (2), is adopted, which is multiplied by the effective thickness of the Gaussian point of interface element to convert it to a relationship between shearing stress and strain. From Eqs.(1-2) a good prediction of aggregate interlock stiffness can be obtained.

Table (1) Concrete interface model roughness coefficient (Fronteddu et al. (1998))

Interface type	σ_n (Mpa)	Peak μ_{ib}
Homogeneous	$\sigma_n \leq 0.4$ $0.4 \leq \sigma_n \leq 1.5$ $1.5 \leq \sigma_n \leq 2$	$0.90 - 1.367\ \sigma_n$ $0.40 - 0.1167\ \sigma_n$ $0.30 - 0.050\ \sigma_n$
Water- blasted	$\sigma_n \leq 0.275$ $0.275 \leq \sigma_n \leq 1.2$ $1.2 \leq \sigma_n \leq 2$	$0.875 - 1.75\ \sigma_n$ $0.44 - 0.185\ \sigma_n$ $0.25 - 0.0375\ \sigma_n$
Untreated	$\sigma_n \leq 1.0$ $1.0 \leq \sigma_n \leq 2.0$	$0.15 - 0.15\ \sigma_n$ $0.05 - 0.005\ \sigma_n$

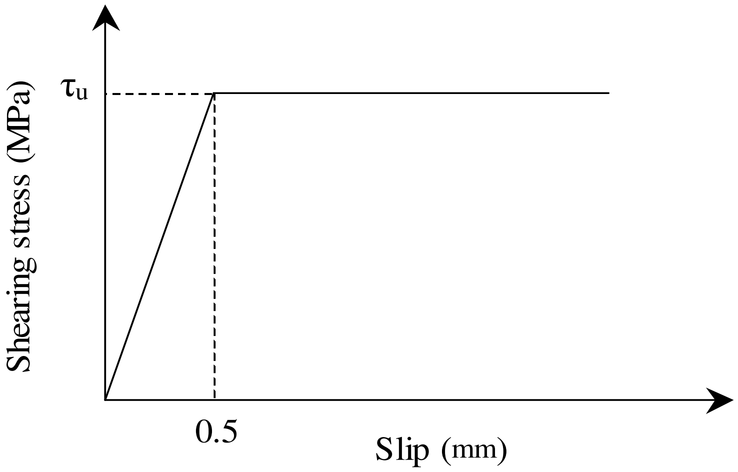

Fig. (2) Adopted shearing stress-slip relationship

THEORETICAL DOWEL ACTION MODELS

Shearing forces can be transmitted across a crack in the reinforced concrete by the reinforcement crossing the crack. If the reinforcement is normal to the plane of cracking, dowel action (shearing and flexure of the bars) will contribute to the overall shear stiffness.

It has been suggested (Paulay et al. (1974)) that there are three mechanisms of shear transfer through the dowel action in cracked reinforced concrete, i.e. direct shear, kinking and flexure of the bars. If the concrete supporting each bar were considered to be rigid, the first two mechanisms would predominate. However, it has been recognized (Mills (1975)) that significant deformation of the concrete does occur, so that flexure of the dowel bar within the concrete is a principal action. This has been modelled (Millard (1984)) by considering the dowel bar as a beam on elastic foundation. This model is adopted, according to this model the dowel force, F_d is given by:

$$F_d = 0.166\,\Delta_t\,Gf^{0.75}\,\Phi^{1.75}\,E_s^{0.25} \qquad (3)$$

where the constant term is dimensionless

Gf: foundation modulus for concrete, A typical value for 35 MPa concrete has been found to be 750 N/mm^3 (ACI Committee 325). For the high strength mix, it has been assumed that Gf α $f_{cu}^{0.5}$.

Φ: diameter of the bar.

E_s: elastic modulus of steel.

Δ_t: slip or relative displacement across the crack.

Only the initial dowel stiffness can be predicted using this equation.

The nonlinear shear stiffness of the dowel action may be attributed to one or both of the following two causes.

1) Crushing or splitting of the concrete supporting the bar.

2) Plastic yielding of the reinforcement.

A good prediction of the ultimate shearing force in a bar with an axial stress of αf_y is given by:

$$F_{du} = 1.3\ \Phi^2 f_{cu}^{\ 0.5} (f_y (1- \alpha^2))^{0.5} \qquad (4)$$

where Fdu is the ultimate dowel force.

An exponential function was used to describe the overall dowel action behaviour. The dowel force, F_d, is as follows:

$$F_d = F_{du} (1\text{-}\exp(-ki\ \Delta_t / F_{du})) \qquad (5)$$

where ki is the initial dowel stiffness given by Eq.(3). By simplifying Eq.(5), the shear stiffness of the dowel action which is used in the present study as a relationship between the shearing stress and shear strain can be found as follows:

$$kd = (ki - \frac{ki^2 \Delta_t}{2F_{du}})\ t / A_c \qquad (6)$$

where t is the effective thickness of the Gaussian point of the interface element (next section), A_c is the contact area.

FINITE ELEMENT IDEALIZATION OF INTERFACE REGION

An isoparametric finite element formulation, which is treated essentially like a solid element, can be used in the present study to represent the behaviour of the interface region (Desai and Zaman (1984)), Fig.(3). Since the element is treated essentially like any other solid element, its incremental stress-strain relationship is expressed as:

$$\{d\sigma\}= [D]_i \{d\ \varepsilon\} \qquad (7)$$

where $[D]_i$ is the constitutive matrix for the interface region. The behaviour of the interface material is assumed to be like the concrete of the softer material properties for all stages of loading except the shear component which represents the shear behaviour specified for the interface region, (G_t, is the shear component represents the combination effects of aggregate interlock and dowel action), the constitutive matrix for the interface element can be written as:

$$[D]_i = \frac{E}{(1+\nu)(1-2\nu)} \begin{bmatrix} 1-\nu & \nu & \nu & 0 & 0 & 0 \\ \nu & 1-\nu & \nu & 0 & 0 & 0 \\ \nu & \nu & 1-\nu & 0 & 0 & 0 \\ 0 & 0 & 0 & G_t & 0 & 0 \\ 0 & 0 & 0 & 0 & G_t & 0 \\ 0 & 0 & 0 & 0 & 0 & G_t \end{bmatrix} \qquad (8)$$

The interface behaviour depends on the properties of the surrounding media. However, it also depends on the thickness of the thin-layer element. If the thickness is too large in comparison with the average contact dimension (B), of the surrounding element, the thin-layer element will behave essentially as a solid element. On the other hand, if it is too small, computational difficulties may arise. Based on the available experimental results, the satisfactory simulation of the interface behaviour can be obtained for (t / B) ratios in the range from (0.01) to (0.1). This conclusion may need modification if the nonlinear behaviour of solids and interfaces were simulated. The 20-noded isoparametric brick element is used.

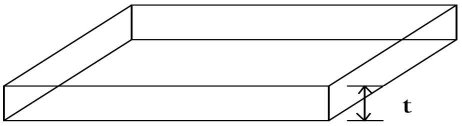

Fig.(3) Thin layer interface element

SARSAM'S SPECIMENS

Nine specimens of beam-column joints (5 exterior, and 4 interior) were tested by Sarsam (1983), the plane exterior ones-EX serie made on the first day. This pour included the specimen up to the level of the top of the joint. The second pour was made on the next day for the top column.

All columns were reinforced with four 16mm longitudinal bars and 8mm closed links at 85mm center to center spacing, giving three joint links. Only specimen EX2 has no links in the joint. All beams were reinforced with two 16mm bars on the tension side and two 12mm bars on the compression side. Beam links were 8mm closed ones spaced at 130mm center to center.

The EX1, EX3 specimens are used in the present study, of dimensions shown in Table(2), Fig.(4). Material properties and additional material parameters of these specimens are shown in Tables (3), (4), respectively. The column was first loaded to a predetermined value of (Nc), prior to any beam loading, the next stage involved loading the beam up to ultimate load. The numerical analysis is done using KT2a method, with a tolerance of 5% on the displacement convergence criterion.

Table (2) Dimensions of Sarsam's specimens

Dimensions/ Specimens	Beam		Column		Lc (mm)	av (mm)	Column Load (kN)
	h (mm)	b (mm)	h (mm)	b (mm)			
Specimen EX1	303	152	205	152	1531	1422	292.6
Specimen EX3	305	152	204	152	1532	661	293.7

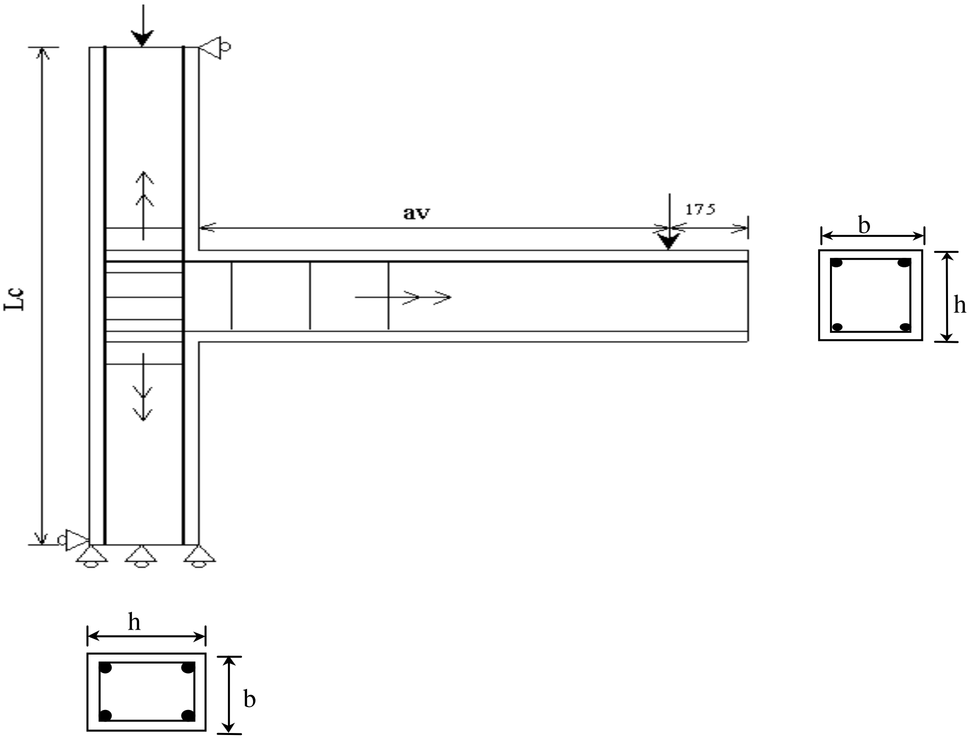

Fig.(4) Experimental corner beam-column joint specimen (Sarsam (1983))

Table (3) Material properties and additional material parameters of Sarsam's specimen EX1

First pour (age=64 days)		
Material properties		Material parameters
Modulus of elasticity , E (MPa)	35500	Tension-stiffening parameters : $\alpha_1=35$, $\alpha_2=0.35$ Shear-retention parameters : $\gamma_1=25, \gamma_2=0.5, \gamma_3=0.1$
Compressive strength, f'_c(MPa)	56.3	
Tensile strength , f_t (MPa)	4.5	
Poisson's ratio , ν	0.2*	
Uniaxial crushing strain	0.00238	

<table>
<tr><th colspan="5">Second pour (age=63 days)</th></tr>
<tr><th colspan="3">Material properties</th><th colspan="2">Material parameters</th></tr>
<tr><td colspan="2">Modulus of elasticity , E (MPa)</td><td>30600</td><td colspan="2" rowspan="5">Tension-stiffening parameters :
α 1=25 , α 2=0.25
Shear-retention parameters :
γ 1=25,γ2=0.5, γ 3=0.1</td></tr>
<tr><td colspan="2">Compressive strength, f'_c (MPa)</td><td>45.8</td></tr>
<tr><td colspan="2">Tensile strength , f_t (MPa)</td><td>3.93</td></tr>
<tr><td colspan="2">Poisson’s ratio , ν</td><td>0.2*</td></tr>
<tr><td colspan="2">Uniaxial crushing strain</td><td>0.003*</td></tr>
<tr><th colspan="5">Steel reinforcement</th></tr>
<tr><td>Longitudinal bar Φ16</td><td rowspan="3">Young’s modulus (MPa)</td><td>208000</td><td rowspan="3">Yield stress (MPa)</td><td>504</td></tr>
<tr><td>Longitudinal bar Φ12</td><td>198000</td><td>507</td></tr>
<tr><td>Stirrup bar Φ8</td><td>197000</td><td>517</td></tr>
</table>

Table (4) Material properties and additional material parameters of Sarsam’s specimen EX3

<table>
<tr><th colspan="5">First pour (age=39 days)</th></tr>
<tr><th colspan="3">Material properties</th><th colspan="2">Material parameters</th></tr>
<tr><td colspan="2">Modulus of elasticity , E (MPa)</td><td>28000</td><td colspan="2" rowspan="5">Tension-stiffening parameters :
α 1=20 , α 2=0.20
Shear-retention parameters :
γ 1=25,γ2=0.5, γ 3=0.1</td></tr>
<tr><td colspan="2">Compressive strength, f'_c(MPa)</td><td>41.3</td></tr>
<tr><td colspan="2">Tensile strength , f_t (MPa)</td><td>3.44</td></tr>
<tr><td colspan="2">Poisson’s ratio , ν</td><td>0.2*</td></tr>
<tr><td colspan="2">Uniaxial crushing strain</td><td>0.00701</td></tr>
<tr><th colspan="5">Second pour (age=38 days)</th></tr>
<tr><th colspan="3">Material properties</th><th colspan="2">Material parameters</th></tr>
<tr><td colspan="2">Modulus of elasticity , E (MPa)</td><td>28200</td><td colspan="2" rowspan="5">Tension-stiffening parameters :
α 1=19 , α 2=0.19
Shear-retention parameters :
γ 1=25,γ2=0.5, γ 3=0.1</td></tr>
<tr><td colspan="2">Compressive strength, f'_c (MPa)</td><td>40.9</td></tr>
<tr><td colspan="2">Tensile strength , f_t (MPa)</td><td>3.56</td></tr>
<tr><td colspan="2">Poisson’s ratio , ν</td><td>0.2*</td></tr>
<tr><td colspan="2">Uniaxial crushing strain</td><td>0.003*</td></tr>
<tr><th colspan="5">Steel reinforcement</th></tr>
<tr><td>Longitudinal bar Φ16</td><td rowspan="3">Young’s modulus (MPa)</td><td>208000</td><td rowspan="3">Yield stress (MPa)</td><td>504</td></tr>
<tr><td>Longitudinal bar Φ12</td><td>198000</td><td>507</td></tr>
<tr><td>Stirrup bar Φ8</td><td>197000</td><td>517</td></tr>
</table>

1) Finite Element Describtion

The concrete of specimens EX1 and EX3 are idealized by using 58 20-noded brick elements (including 1 interface element at the top level of the joint), and 37 20-noded brick elements (including 1 interface element at the top level of the joint), respectively (for half of these specimens), Fig.(5). To simulate the procedure of loading that occurred during the experimental test, the column axial load has been firstly applied in equal increments of 10% of the maximum column load for two specimens. Later, for EX1 two different sizes of increments have been used for beam loading. The beam was loaded initially by increments of 3.75kN up to 75% of the expected collapse load (40kN). Then reduced increments of 1.43kN each were applied until the failure load has been reached. While for EX3 the beam load has been applied in equal increments of 12.5% of the expected collapse load (80 kN). Both the initial and post-cracking stiffness are reasonably predicted for two specimens, Table (3), Table (4).

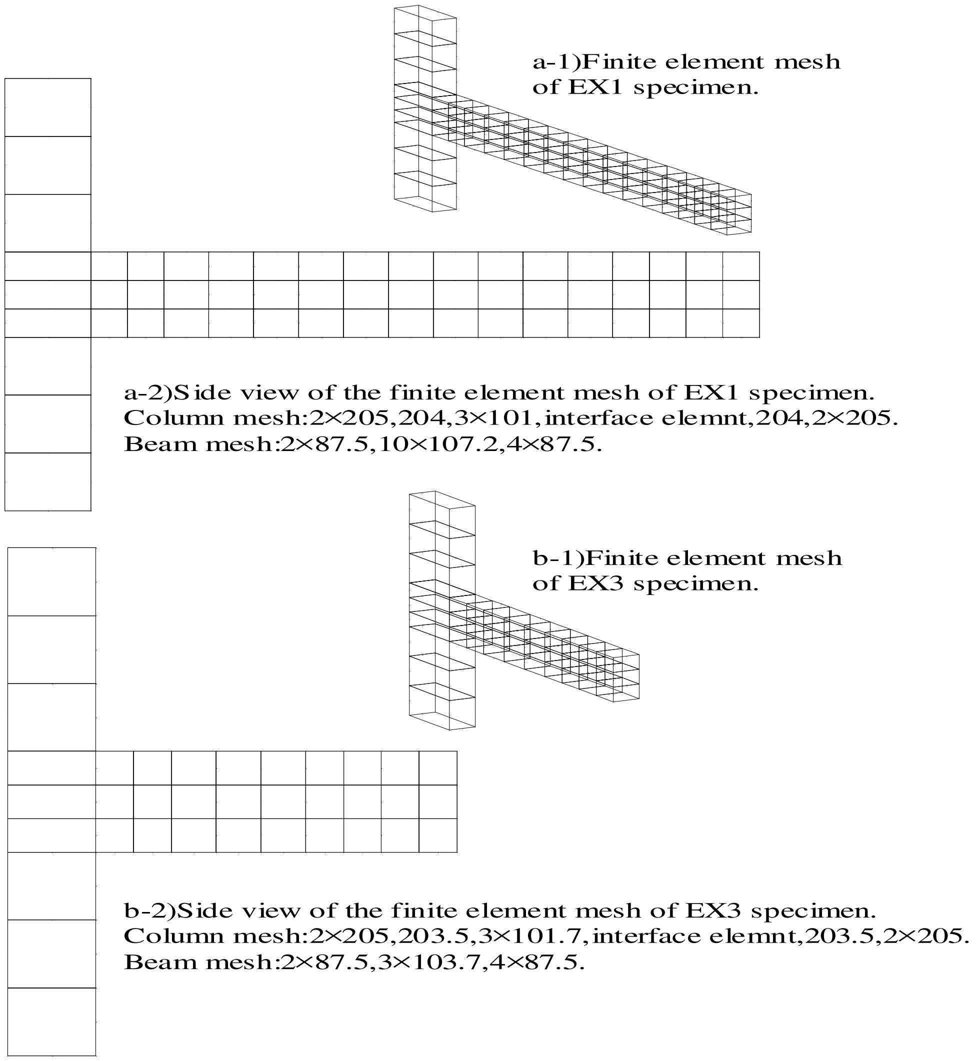

a-1)Finite element mesh of EX1 specimen.

a-2)Side view of the finite element mesh of EX1 specimen.
Column mesh:2×205,204,3×101,interface elemnt,204,2×205.
Beam mesh:2×87.5,10×107.2,4×87.5.

b-1)Finite element mesh of EX3 specimen.

b-2)Side view of the finite element mesh of EX3 specimen.
Column mesh:2×205,203.5,3×101.7,interface elemnt,203.5,2×205.
Beam mesh:2×87.5,3×103.7,4×87.5.

Fig.(5) Finite element discretization of half of EX1,and EX3 specimens.

Analysis of the Specimens

In order to analyze the two specimens, the effect of the thickness of interface element must be examined. For EX1 specimen, numerical tests with values of the thickness (t) equal to 0.014mm, 0.14mm, and 1.4mm have been carried out. The results show that the type of failure of the specimen EX1 is beam hinging in the range of (0.014-0.14)mm for thickness of interface element, Fig.(6). A response stiffer than the experimental results was obtained when the thickness is reduced within the range, and the best fit to the experimental results was obtained at t=0.14mm with effective thickness of Gaussian point of 0.038mm, in which the effect of non-linearities along the loading stages is clear. The failure load of numerical results is 37.5kN while the failure load of experimental results is 36.04kN, so that the error ratio is 3.9%. While for EX3 specimen, numerical tests with values of the thickness (t) equal to 0.0014mm, 0.014mm, and 0.14mm have been carried out. The results show that the type of failure of the specimen EX3 is beam hinging in the range of (0.0014-0.014)mm for thickness of interface element, Fig.(7). A stiffer response was obtained when the thickness is reduced, and the best fit to the experimental results was obtained at t=0.0014mm with effective thickness of Gaussian point of 0.00038mm. The failure load of numerical results is 80kN while the failure load of experimental results is 78.7kN, so that the error ratio is 1.6%. In the present study the value of thickness of the interface element equal to 0.14mm is fixed for EX1 specimen to present a parametric study.

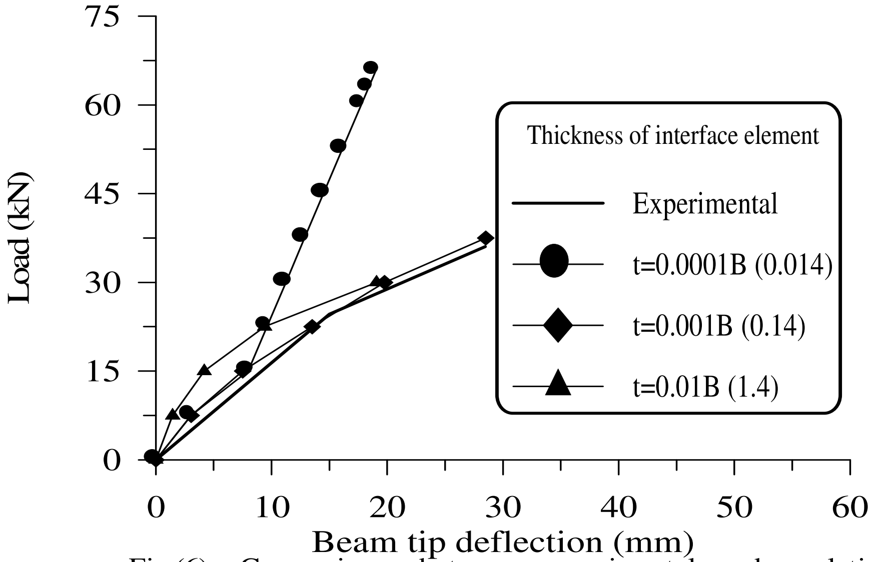

Fig.(6) Comparison between experimental and analytical response of different interface thickness values for EX1

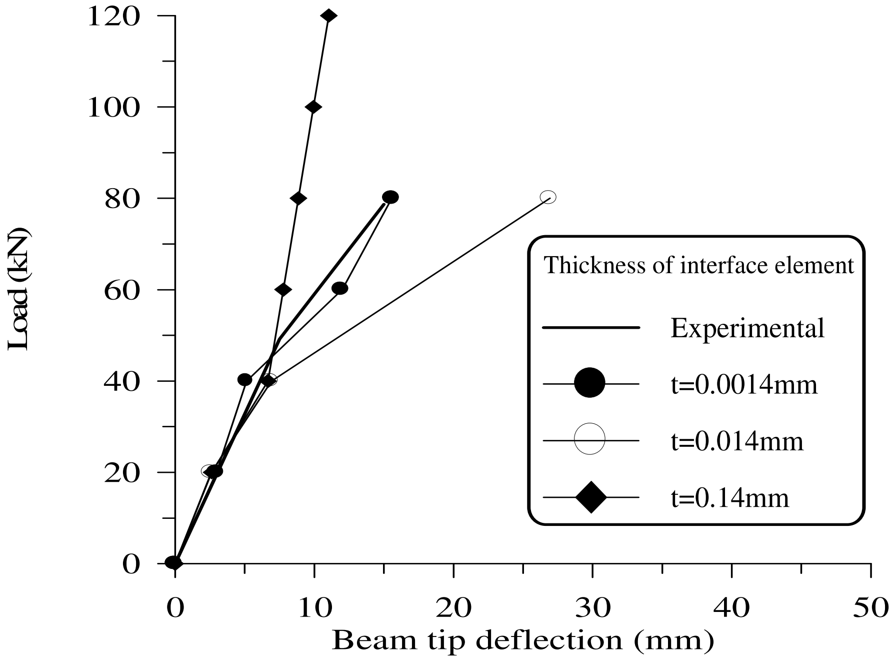

Fig.(7) Comparison between experimental and analytical response of different thickness value for EX3 specimen.

PARAMETRIC STUDY

A parametric study deals with construction joint is presented by taking various conditions of the junction. These include the various positions of the construction joint, the axial load on the column, strength of concrete in the second cast and the amount of dowels crossing the joint as follows:

THE EFFECT OF POSITION OF CONSTRUCTION JOINT

In order to study the effect of the position of construction joint (c.j.), a numerical study on four cases have been carried out, Fig.(8), case (a) without c.j., case (b) with c.j. at the top level of the joint, case (c) with c.j. at the bottom level of the joint, and case (d) with 2 c.j. one at the top level and the other at the bottom level of the joint. These cases were made of three pours (1,2,3) of material properties shown in Table (5). Fig.(9) represents load-tip deflection of these cases. As a result of comparison between curves, a soft response occurred for cases with c.j., the response of case (c) is softer than the response of case (b), and a softer response of all is observed for case (d). It is worth noting that the mode of failure in all cases is beam hinging.

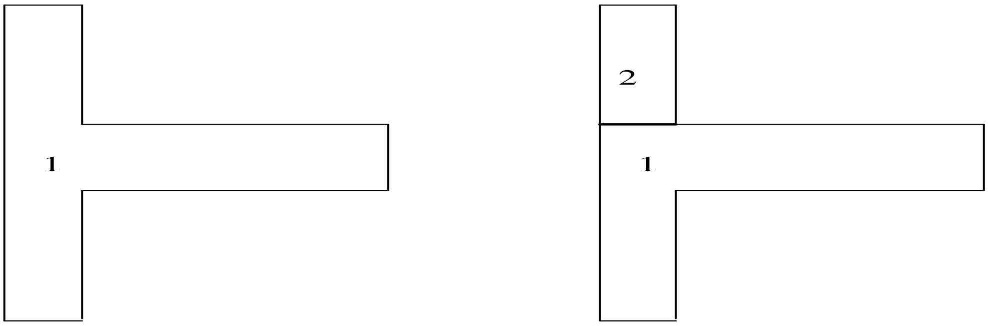

Case (a) Monolithic specimen (without construction joint)

Case (b) Composite specimen (with construction joint at top level of joint)

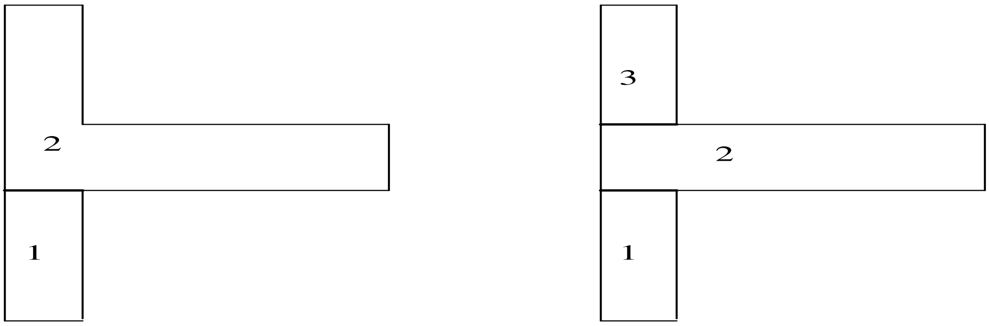

Case (c) Composite specimen (with construction joint at bottom level of joint)

Case (d) Composite specimen (with 2 construction joint at top & bottom levels of joint)

Fig (8) Cases of construction joints of beam-column joint

Table (5) Material properties and additional material parameters of Sarsam's specimen EX1

First pour (1) (age =64 days)		
Material properties		Material parameters
Modulus of elasticity , E (MPa)	35500	Tension-stiffening parameters : α 1=35 , α 2=0.35 Shear-retention parameters: γ 1=25,γ2=0.5, γ 3=0.1
Compressive strength, f'_c(MPa)	56.3	
Tensile strength , f_t (MPa)	4.5	
Poisson's ratio , ν	0.2*	
Uniaxial crushing strain	0.00238	
Second pour (2) (age =63 days)		
Material properties		Material parameters
Modulus of elasticity , E (MPa)	30600	Tension-stiffening parameters : α 1=25 , α 2=0.25 Shear-retention parameters: γ 1=25,γ2=0.5, γ 3=0.1
Compressive strength, f'_c(MPa)	45.8	
Tensile strength , f_t (MPa)	3.93	
Poisson's ratio , ν	0.2*	
Uniaxial crushing strain	0.003*	
Third pour (3) (age =62 days)		
Material properties		Material parameters

Modulus of elasticity , E (MPa)	29200	Tension-stiffening parameters : α 1=25 , α 2=0.25 Shear-retention parameters: γ 1=25,γ2=0.5, γ 3=0.1
Compressive strength, f'_c(MPa)	43.3	
Tensile strength , f_t (MPa)	3.31	
Poisson's ratio , ν	0.2*	
Uniaxial crushing strain	0.003*	

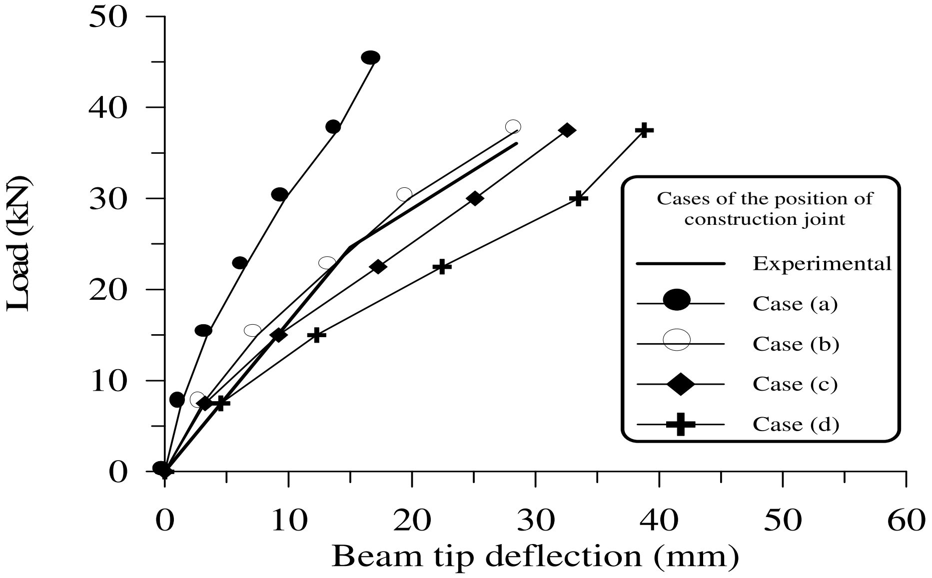

Fig.(9) Load-beam tip deflection for cases of construction joints.

THE EFFECT OF CONSTRUCTION JOINT

There are different contributions to beam tip deflection. The first one is the contribution of joint shear strain, the second involves the contribution of joint rotation, and the third is the contribution of beam flexure. To examine the effect of the construction joint on the behaviour of the specimen, the shear, and normal strains in the joint (at 63.4mm left to the column face), and the normal strains in the beam (at 77.65mm right to the column face) are studied for case b (construction joint at the top level of the joint) and compared with strains of the monolithic specimen (case a) as follows:

From Fig (10), and Fig.(11), the shear and normal strains in the joint for case (b) are greater than the strains for case (a) (monolithic). The amount of increment of strains near the construction joint is larger than the strains in other positions of joint. These results refer to the occurrence of several short diagonal tension cracks along the length of the shear plane (construction joint), and these cracks cause a reduction in shear and in normal stiffness. While the normal strains in beam, Fig.(12), are not much affected by the construction joint. This means that the construction joint affect only on the behaviour of the joint itself.

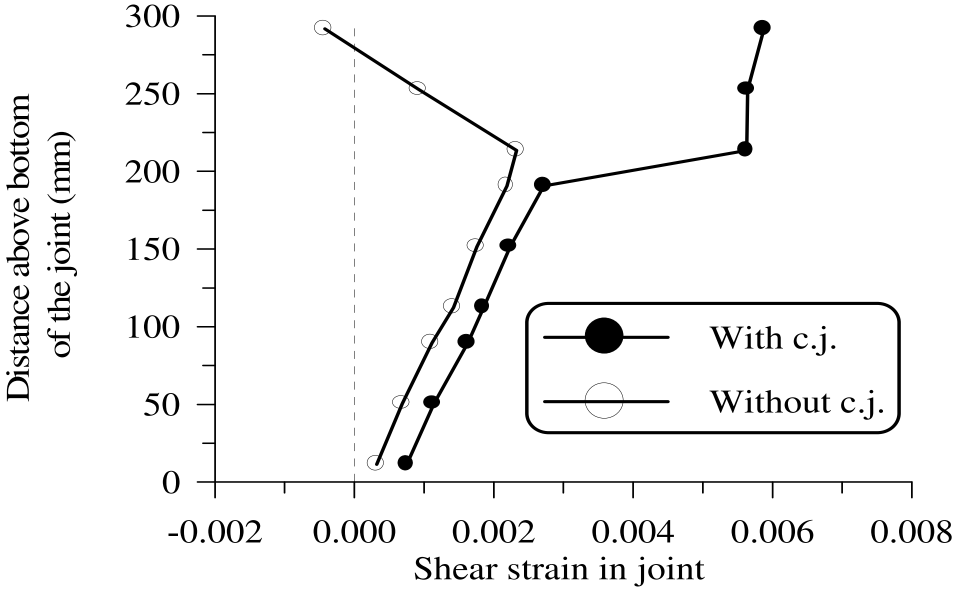

Fig.(10) Shear strains distribution in joint for case a (monolithic) and case b (construction joint at the top level of joint)

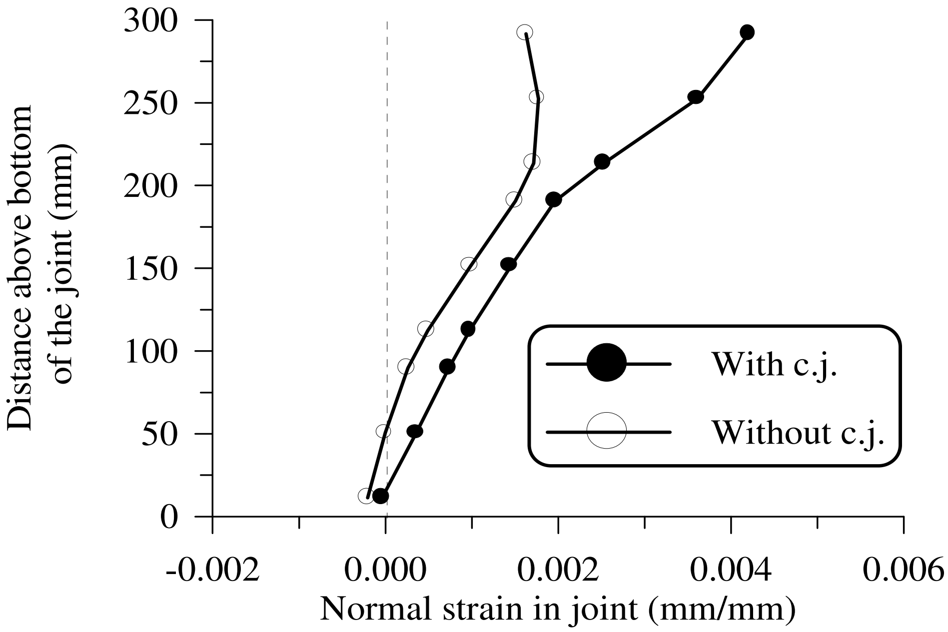

Fig.(11) Normal strains distribution in joint for case a(monolithic) and case b (construction joint at the top level of joint)

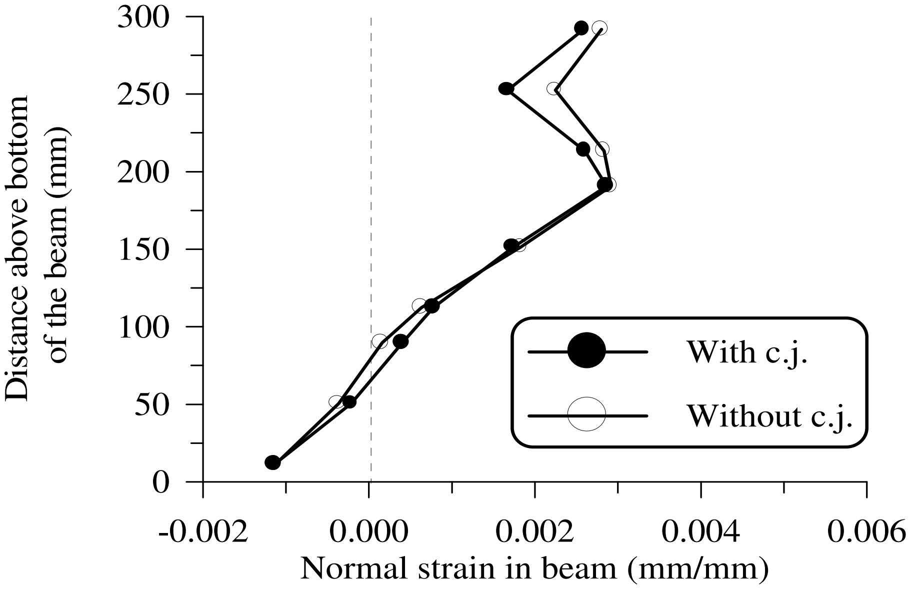

Fig.(12) Normal strains distribution in beam for case a(monolithic) and case b (construction joint at the top level of

The Effect of Column Axial Load

In order to expect the effect of column axial load on the behaviour of construction joint, a numerical study have been carried out, one with experimental column axial load (Nc=292.6kN), and the other without column axial load (Nc=0.0) for case (b) (construction joint at the top level of the joint). It can be observed from Figs.(13) and (14) that the shear and normal strains in the joint for Nc=0.0 are less than the strains for Nc=292.6kN. A possible explanation of this feature may be the following: Higher compressive stresses (at Nc=292.6kN), in spite of the more intimate interlocking they secure, produce a shortening of the protruding asperities and subsequently reduce overriding resistance. This mechanism does not happen at Nc=0.0. On the contrary, due to loss of the confinement for Nc=0.0, the response of the specimen is softer than the response for Nc=292.6kN, Fig.(15) .

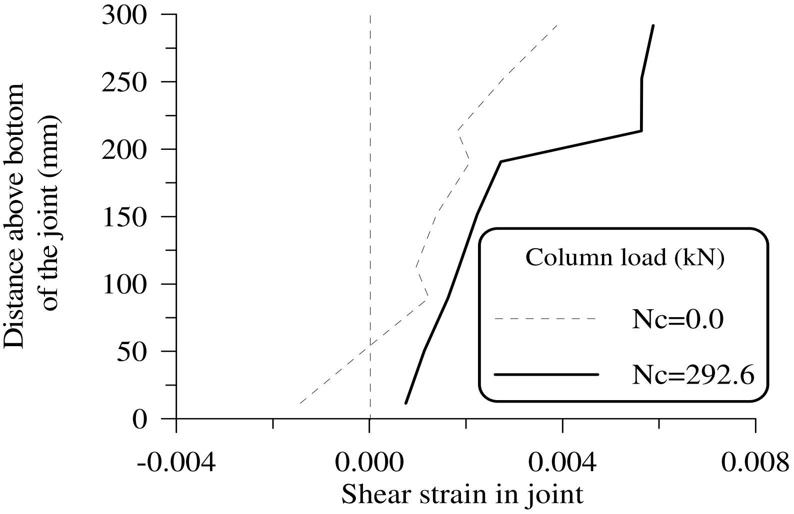

Fig.(13) Shear strains distribution in joint for case b (construction joint at the top level of joint)

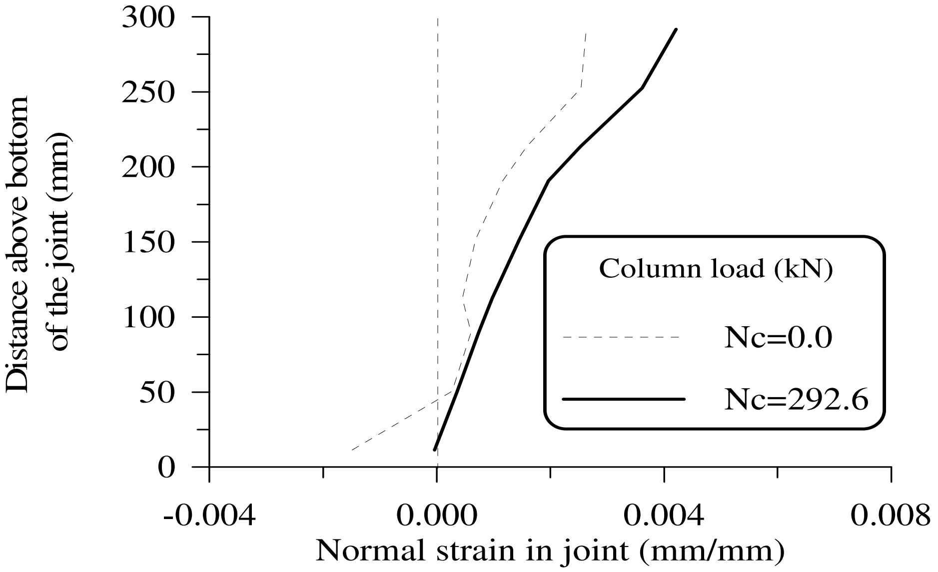

Fig.(14) Normal strains distribution in joint for case b (construction joint at the top level of joint)

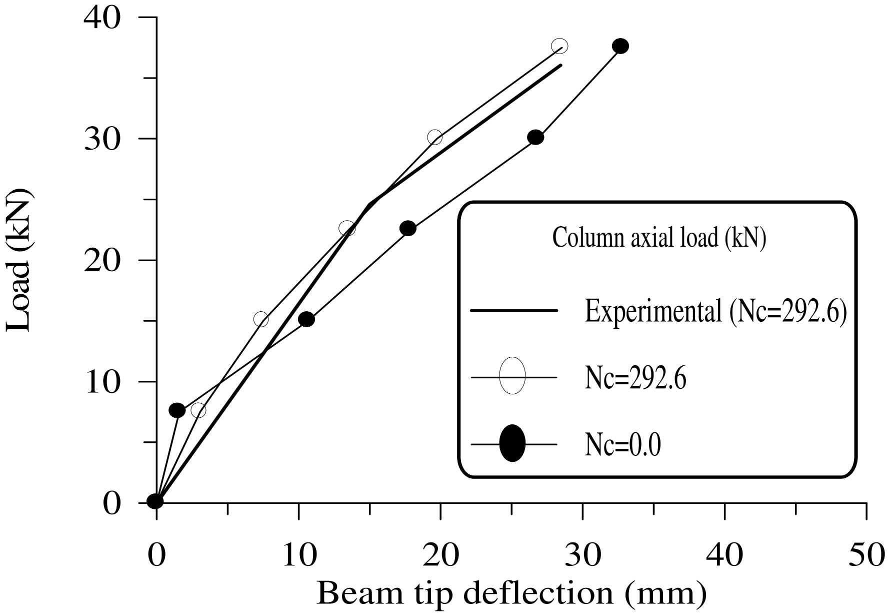

Fig.(15) Load- beam tip deflection for case b (construction joint at the top level of joint)

THE EFFECT OF THE AGE OF CONCRETE

The age of concrete pour has an effect on the compressive strength of the concrete. In order to study the effect this age, three tests have been carried out with f'c values equal to 45.8, 40, 30 MPa, Fig.(16). These values of strengths are for ages approximately equal to 63, 38, 20 days, respectively for the second pour of case (b), including the construction joint. These tests show that the higher concrete compressive strength results in a slight increase in aggregate interlock stiffness of construction joint.

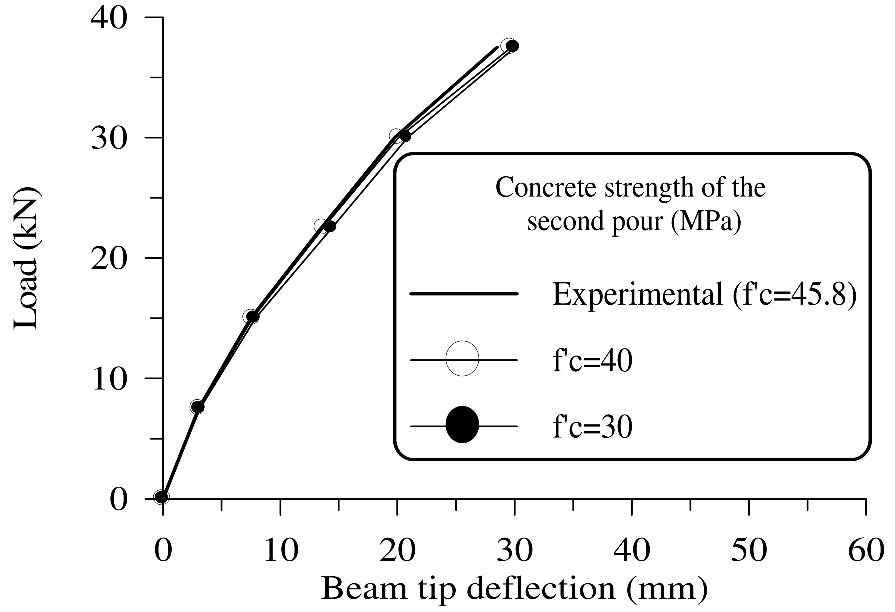

Fig.(16). Effect of compressive strength of concrete on the load-beam tip deflection curve for case b (construction joint at the top level of joint)

The Effect of the Percentage Steel Across the Construction Joint

Three numerical tests have been carried out by using the percentage steel across the construction joint (diameter of the bar) of 0.031 (16mm), 0.033 (18mm), and 0.048 (20mm) for case (b), construction joint at the top level of joint, these tests occurred with original designed specimen. From Fig.(17) that the deflection decrease with the increase in the steel percentage across the construction joint (column reinforcement), the contribution in this result is the decreased strains in joint due to increase in dowel stiffness.

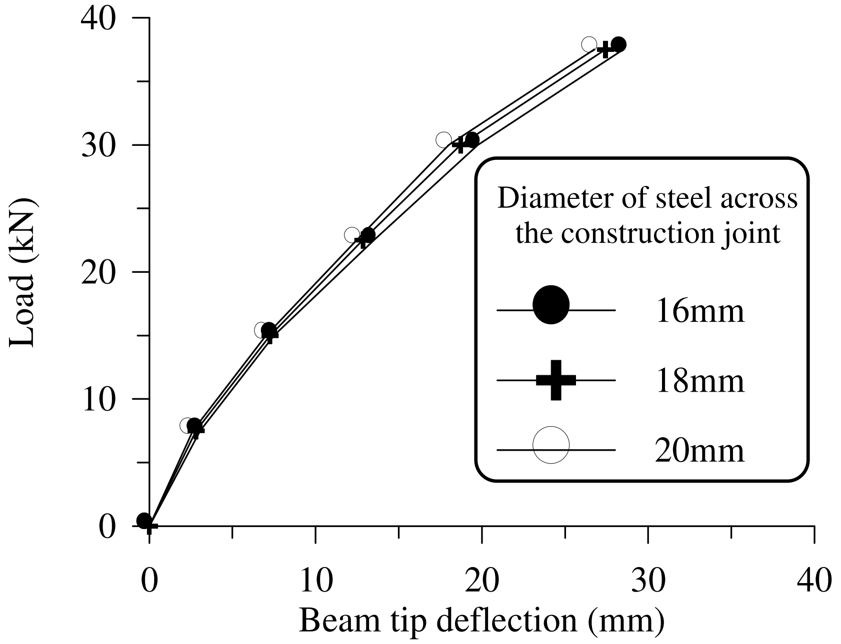

Fig.(17) Effect of diameter of crossed steel on the load-beam tip deflection curve for case b (construction joint at the top level of joint)

CONCLUSIONS

The following conclusions can be drawn from the present study:

1. A good assessment can be obtained for the behaviour of corner beam-column joints by using the developed program of the current study (DPACJ).
2. The performance of the interface element , used in this study to model the shear transfer between two concretes cast in different times, is quite good.
3. A stiff response can be obtained with the decrease in the thickness of the interface element.
4. The response of a specimen can be expected within a certain range of thickness of interface element. This range depend on the finite element mesh, nonlinear behaviour of material, and the combination of stresses.
5. Construction joint is a joint of weakness. Depending on the position of construction joint, the shear and normal strains in joint would increase.
6. The construction joint would affect only on the joint. On the other hand, the mode of failure for all cases of corner beam-column joint in this study is beam hinging, this type of failure conforms with the design requirements.
7. The presence of column axial load would decrease the aggregate interlock stiffness. However, it secures a good confinement for the beam, and so as the result of increase it.
8. The grade of concrete of the second pour, producing a construction joint, does not much affect the behaviour of the corner beam-column joint.
9. The increase of steel percentage across the construction joint would decrease the strains in joint. Consequently, a slightly decrease of deflection occurred.

REFERENCES

ACI Committee 318,(1995).‘‘Building Code Requirements for Reinforced Concrete (ACI 318-95).’’American Concrete Institute, Detroit.

ACI Committee 325, (1956) (Cairman: FINNEY. E.) Structural Design Considerations for Paveement Joints. J. Ame. Con. Inst. Proce., 53(1), July, 1-28, (Cited according to Millard and Johnson (1984)).

Al-Shaarbaf I.(1990).‘‘Nonlinear Three Dimensional Finite Element Analysis Program for Steel and Reinforced Concrete Beam in Torsion.’’ Ph.D. Thesis, University of Bradford.

Cervenka V.(1985).‘‘Constitutive Model for Cracked Reinforced Concrete.’’ACI J.,82(6),877-882,November-December.

Desai C.S., Zaman M.M.,Lightner J.G.,and Siriwardane H.J.(1984).‘‘Thin-Layer Element for Interfaces and Joints.’’J. Nume. Analy. Meth. Geome.,8,19-43.

Fronteddo L.,Léger P.,and Tinawi R.(1998).‘‘Static and Dynamic Behaviour of Concrete Lift Joint Interfaces.’’J. Struct. Engrg.,ASCE,124(12),1418-1430.

Meinheit D.F.,Jirsa J.O., and Members of ASCE(1981).‘‘Shear Strength of Reinforced Concrete Beam-Column Connections.’’ASCE,107(ST11).

Mills G.M.(1975).‘‘A Partial Kinking Criterion for einforced Concrete Slabs.’’ Maga. Conc. Resea.,27(90),13-22.

Millard S.G.,and Johnson R.P.(1984).‘‘Shear Transfer across Cracks in Reinforced oncrete due to Aggregate Interlock and to Dowel Action.’’ Maga. Conc. Resea.,36(126).

Owen D.R.,and Hinton E.(1980).‘‘Finite Element in Plasticity, Theory and Practice. ’’Pineridge Press, Swansea,U.K.

Paulay T.,and Loeber P.J.(1974).‘‘Shear Transfer by Aggregate Interlock. ’’Shear in Reinforced Concrete, Detroit, American Concrete Institute,ACI Special Publication SP 42-1.1,1-15,(Cited according to Millard and Johnson (1984)).

Rashid Y.R.(1968).‘‘Analysis of Prestressed Concrete Pressure Vessels. ’’Nucl. Engng. Desi.,7(4).

Sarsam K.F.(1983).‘‘Strength and Deformation of Structural Concrete Joints. ’’Ph.D. Thesis, University of Manchester.

Tassios T.P.,and Vintzèleou E.N.(1987).‘‘Concrete-to-Concrete Friction. ’’J. Struc. Engrg., ASCE, 114(9), 2133-2136.

Walraven J.C.,and Reinhardt H.W.(1981).‘‘Concrete Mechanics, Part A. Theory and Experiments on the Mechanical Behaviour of Cracks in Plain and Reinforced Concrete Subjected to Shear Loading. ’’Heron.26(1A),1-68, (Cited according to Millard and Johnson (1984)).

NUMERICAL AND EXPERIMENTAL INVESTIGATION OF FLOW FIELD INSIDE ARTERIES AND VEINS

Prof.Dr. Najdat Nashat Abdulla
Asst.Prof. Hussain Yousif Mahmood
Graduate Student Sadiq Elias Abdullah
Department of Mechanical Engineering
University of Baghdad

ABSTRACT

Numerical and experimental investigation of blood flow through stenotic and tapered arteries under pulsation condition are studied. Blood is considered as non-Newtonian fluid. Artery is considered as a rigid wall tapered vessel with different tapering angles (0.5^o, 1^o,1.5^o), as well as, straight vessel for comparison. The governing equations have been written in stream- vorticity method and are transformed into generalized coordinate system. The time marching has been employed to solve the resulting partial differential equations. The experimental work carried out to examine pressure in vessel and pressure drop across the stenosis under pulsation condition. Differential pressure transducer coupled to the data acquision card type PCI-911DG, which is built in computer was used to record pressure data.

The results showed that, as a tapering angle increases (0.5^o, 1^o, 1.5^o) both wall shear stress and pressure drop increasing, also as stenosis increases (50%, 60%, 75%) both wall shear stress and pressure drop increasing. These behaviors are found in literature, pressure drop is used to compare experimental data and numerical results, which indicates agreement. As the distance into taper section increased both wall shear stress and pressure drop are increased, as well as, both wall shear stresses and pressure drop increased with inlet flow rate increased, while decreased with inlet diameter increase.

الخلاصة

تم أجراء دراسة عددية و تجريبية لجريان الدم خلال شريان متضايق و مستدق تحت شرط الجريان النبضي. أعتبر الدم غير نيوتوني وتم أخذ شريان ذو جدار متصلب ومستدق بزوايا مختلفة **(0.5, 1, 1.5)** درجه وتمت مقارنته مع شريان مستقيم. كتبت المعادلات الحاكمة بطريقه داله الانسياب- الدواميه وحولت هذه المعادلات إلى نظام الإحداثيات العمومية 0 كما استخدم طريقه الزحف الزمني لحل المعادلات التفاضلية الجزئية الناتجة. جرى العمل التجريبي لاختبار الضغوط عبر أنبوبه ذات تضبق

تحت شروط الجريان النبضي و الذي تم بواسطة مقياس الضغط التفاضلي (**Transducer**) مرتبط بمعالج بيانات نـــوع **PCI-911DG** مثبت في حاسوب لتسجيل الضغوط.

أظهرت النتائج أنه عند زيادة زاوية الأستدقاق (**0.5 , 1 , 1.5**) درجة تزداد كلا من أجهاد القص على الجدار و هبوط الضغط و كذالك فأنه بزيادة نسبة التضيق (**50% , 60% , 75%**) , فأن أجهاد القص على الجدار يزداد وهذا السلوك وجـــد في البحوث السابقة0 كما تبين أنه بزيادة نسب التضيق يزداد هبوط الضغط وهذا يبين التطابق بين النتائج النظرية و التجريبيـــة 0 وكذالك تزداد كلا من أجهاد القص على الجدار و هبوط الضغط كلما زادت المسافة باتجاه نهاية الاستدقاق, وأظهرت النتائج زيادة كلا من أجهاد القص على الجدار و هبوط الضغط بزيادة التدفق الداخل ,بينما يقلان بزيادة قطر أنبوب الدخول0

INTRODUCTION

Considerable attention was paid to study related circulatory flow in blood vessels toward the beginning of the last century. A large number of theoretical and experimental Investigations relevant to this biomechanical aspect have been carried out in recent years. Hardly need mention that, about three quarter of all death occurring these days are mainly caused by circulatory diseases associated with disturbed flow condition in the blood vessels which lead to the malfunction of the cardiovascular **(Chen 2003).** The presence of stenosis increases flow resistance in arteries which forces the body to raise the blood pressure to maintain the necessary blood supply. Both the high blood pressure and narrowing blood vessel cause high flow velocity, high shear stress and low or negative pressure at the throat of the stenosis .In addition to low shear stress, flow separation and wall compression or even collapse at the distal side of stenosis .This may related to the thrombus formation, atherosclerosis growth and plaque cap rupture which lead directly to stroke and heart attack.

Several studies of fluid dynamics through stenosis have been carried out to evaluate the flow pattern and the shear stress at walls at steady and pulsate flow conditions .Some attempts to study experimentally,**(Walburn and Stein 1981**) measured velocity with Laser Doppler anemometer in plexiglass tube with tapered of 0.5^o, 1.5^o and 2.5^o, measured from centerline to the wall during steady flow. These angles were comparable to the angles of taper observed in abdominal aorta of normal subject 1.5^o. ± 0.2^o "range 0^o to 3^o" as reported. They calculated transition Reynolds number which based on diameter of tube at point of measurement. The results show increasing of transition Reynolds number with increasing angle of tapering, also with increasing distance into tapered section for constant angle of taper. These observations suggested that, tapering of abdominal aorta tends to promote laminar flow.**(Ojha, et al 1989**), used a photochromic tracer method to record pulsatile flow velocity profiles simultaneously at three axial locations along a flow channel. Thereby enabling the time and spatial distribution of the wall shear stress to be studied, as well as visualizing of the flow. In addition, they studied the transition to turbulence triggered by the moderate stenosis. Asymmetric and axisymmetric stenosis models were used. Shape of stenosis were based on clinic observations , percent of area reduction were 45%,65% and 75% for axisymmetric ,while 38% "of total area cross section " for asymmetric stenosis .The work was done for Reynolds number in the ranges of 380-575 and Womersley number of 7.5.

Other numerical studies deal blood as non Newtonian fluid, **(Pontrelli 1999)** investigated steady axisymmetric flow in a constricted rigid tube. A shear- thinning fluid which modeling the deformation dependent viscosity of blood .The governing equation was written in vorticity–stream function and solved numerically by finite difference method. The constriction was described by exponential function. The results demonstrate that, the non-Newtonian character of the blood in some typical regimes modify the flow pattern even beyond the constricted region, reduce the pressure drop and shear stress at the wall across the stenosis**.(Kimmel and Dinnar 1983)** , modeled blood flow through a segment of large arteries between bifurcations as pulsate flow of Newtonian fluid in tapered converging tubes of small angle of converging up to 2 degree .In this study, flow rate considered as a forcing function rather than uniform pressure gradient .Integral method was used in solution of Navier –Stokes equations. The result showed that, change in flow condition due to tapering of blood vessel are significant even for small tapering angle and cannot be ignored. Also as tapering angle increases, peak shear stress at wall also increases, but still below the critical range which lead to damage of endothelial. **(Porenta et al 1985)**, used a finite element method to model pulsating flow in arteries segment including taper, branch, and obstructions. In branch model ,they assumed that the pressure different across location where branch diverter from the main stream was small and can be neglected, while in obstructions model ,they calculate pressure difference across stenosis .The results indicate that, the pressure wave were traveling along artery shows an amplification in distal direction ,and they conclude that each nonlinear term contributes to the effect noticed in the nonlinear case .While the influence of the convective acceleration term in momentum equation was stronger ,also the combined effect of both nonlinearities was larger than the added effect of each individual term .The effect of stenosis on pressure shows that the distal pressure for 50% stenosis only slightly reduced, and distal flows were slightly damped ,while for high stenosis (75% and 90 %) had large effect. Wall shear stress is an important factor in the study of blood flow ,and an accurate predication of the distribution of wall shear stress are particularly useful for understanding the effect of blood on endothelial cells. **(Guo-Tao et al. 2004)** investigated distribution of wall shear stress by simulation of pulsating blood flow through stenotic tapered artery .The incompressible Navire-stokes equations were solved numerically by a finite difference method .The results indicated that, the height of stenosis was more important factor influencing blood flow than wall tapering. Tapering found to have no effect on flow pattern, but only change the value. On the other hand, it becomes bigger value than without tapering; also the peak value of shear stress of tapered artery was bigger than that without taper. In parallel work, **(Hun Jung et al, 2004)** used a finite volume method to solve three dimensional, fully developed flows and blood taken as a non Newtonian fluid which obeys to Carreau-Yasuda. They compared the results with **(Ojha et al 1989)** for case of 45% stenosis trapezoidal profile, and a good agreement was shown .For cosine profile stenosis, a numerical computational was conducted for 50 %and 75% stenosis, and the result showed that, the severity of the stenosis had significant effect on the general flow features such as separation Reynolds number and size of the separation region, while the shape of stenosis had less effect. Also, it showed that, the peak values of wall shear were exerted at the stenosis and negative shear stress were observed in the region where a vortex exists. Summary of the past studies indicated that, the flow of non-Newtonian fluid though constricted taper artery under pulsation condition was not considered .As a conclusion, **(Guo-Tao et al.2004)**, considered Newtonian fluid through constricted taper pipe, but only for small angle 0.5°, while the present study extended to involve 1°, and 1.5°. Also noted that, **(Hun-jug et al. 2004)**, considered flow of non-Newtonian fluid through constricted tube under pulsating condition , but they ignored effect of tapering and restricted the study to small percent of stenosis(25%,33%,50%),which its effect was small on pressure drop across stenosis **(Porenta et al. 1985)**.

The present work will consider the flow of non-Newtonian fluid through constricted artery under pulsation condition for tapering angles up to 1.5° and percent of stenosis up to 75%.Numerical and experimentally investigations of blood flow through constricted taper artery are carried at pulsation condition for vessels with 50%, 60% and 75% stenosis. Blood considered as a non-Newtonian fluid obeying the shear thinning model

MATHEMATICAL MODEL AND NUMERICAL CALCULATION

The governing equations of blood flow through stenosis artery at pulsation condition are formulated and stated in polar coordinate. The working fluid is considered as a Non-Newtonian fluid and incompressible.

A schematic of the stenosis tube geometry considered in this study is shown in **Fig. (1),** which consists of two main parts, tube and the stenosis, stenosis geometry is shown in **Fig.(2)**

Let us now consider a cylindrical coordinate system (x,r,θ) having the x-axis coincident with the pipe axis .since we seek an axisymmetric 2D solution ,all variable are assumed independent of θ and the azimuthal component of v vanishes ,equation of motion can be written as follows:

$$\rho(\frac{\partial u}{\partial t}+u\frac{\partial u}{\partial x}+v\frac{\partial u}{\partial r})=-\frac{\partial p}{\partial x}+2\frac{\partial \mu}{\partial x}\frac{\partial u}{\partial x}+\frac{\partial \mu}{\partial r}(\frac{\partial v}{\partial x}+\frac{\partial u}{\partial r})+\mu(\frac{\partial^2 u}{\partial x^2}+\frac{\partial^2 u}{\partial r^2}+\frac{1}{r}\frac{\partial u}{\partial r}) \qquad (1)$$

$$\rho(\frac{\partial v}{\partial t}+u\frac{\partial v}{\partial x}+v\frac{\partial v}{\partial r})=-\frac{\partial p}{\partial r}+\mu(\frac{\partial^2 v}{\partial x^2}+\frac{\partial^2 v}{\partial r^2}+\frac{1}{r}\frac{\partial v}{\partial r}-\frac{v}{r^2})+\frac{\partial \mu}{\partial x}(\frac{\partial v}{\partial x}+\frac{\partial u}{\partial r})+2\frac{\partial \mu}{\partial r}\frac{\partial v}{\partial r} \qquad (2)$$

Where (u ,v) are the components of V in the r and x directions respectively.

Complex rheological behavior of blood is approximated using a shear thinning model, where the apparent viscosity is expressed as a function of the shear rate (**Pontrelli 1999)** and **(Hun Jung et al 2004**).

$$\mu(\dot{\gamma})=\eta_\infty+(\eta_o-\eta_\infty)(\frac{1+\log e(1+\wedge\dot{\gamma})}{1+\wedge\dot{\gamma}}) \qquad (3)$$

Where

η_o and η_∞ are asymptotic viscosities as $\dot{\gamma}\rightarrow 0$ and ∞ respectively

$\wedge$ is a materiel constant with dimension of time representing the degree of shear thinning .

$\dot{\gamma}$ shear rate which represents a scalar measure of the rate of deformation is given by **(Pontrelli 1999**) and **(Hun Jung et al 2004)**

$$\dot{\gamma}^2=\frac{1}{2}\sum_i\sum_j e_{ij}e_{ji} \qquad (4)$$

To non-dimensionalized the governing equations, a set of variables are introduced **(Pontrelli 1999)**

$$x=\frac{x}{R},\ r=\frac{r}{R},\ t=t*f\ ,u=\frac{u}{V},\ v=\frac{v}{V},\ p=\frac{p}{0.5\rho V^2},\ \Lambda=\frac{\Lambda V}{R}\ ,\ \delta=\frac{\eta_0}{\eta_\infty}$$

Where: R= vessel inlet radius and V =average velocity at inlet

eq.(1) can be written in following form

$$\frac{\lambda^2}{Re}(\frac{\partial u}{\partial t}+u\frac{\partial u}{\partial x}+v\frac{\partial u}{\partial r})=-\frac{\partial p}{\partial x}+\frac{1}{Re}[2\frac{\partial \dot{X}}{\partial x}\frac{\partial u}{\partial x}+\frac{\partial \dot{X}}{\partial r}(\frac{\partial v}{\partial x}+\frac{\partial u}{\partial r})+\dot{X}(\frac{\partial^2 u}{\partial x^2}+\frac{\partial^2 u}{\partial r^2}+\frac{1}{r}\frac{\partial u}{\partial r})] \qquad (5)$$

and **eq.(2)** can be written in following form

$$\frac{\lambda^2}{Re}(\frac{\partial v}{\partial t}+u\frac{\partial v}{\partial x}+v\frac{\partial v}{\partial r})=-\frac{\partial p}{\partial r}+\frac{1}{Re}[\dot{X}(\frac{\partial^2 v}{\partial x^2}+\frac{\partial^2 v}{\partial r^2}+\frac{1}{r}\frac{\partial v}{\partial r}-\frac{v}{r^2})+\frac{\partial \dot{X}}{\partial x}(\frac{\partial v}{\partial x}+\frac{\partial u}{\partial r})+2\frac{\partial \dot{X}}{\partial r}\frac{\partial v}{\partial r}] \qquad (6)$$

Where: $\lambda=R\sqrt{\frac{f}{\upsilon}}$ Womersley number , $Re=\frac{\rho uR}{\mu}$ Reynolds number; f= Frequency of pulsation

$\dot{X}$ = Non dimensional viscosity which is given below

$$\dot{X}(\dot{\gamma}) = 1 + (\delta - 1)\left[\frac{1 + \log e(1 + \wedge \dot{\gamma})}{1 + \wedge \dot{\gamma}}\right] \tag{7}$$

Stream – vorticity approach

By cross differentiating and by subtracting the counterparts of **eqs(5**) and **(6)**, we obtain the vorticity –stream function formulation :

$$\frac{\lambda^2}{\mathrm{Re}}\frac{\partial \omega}{\partial t} - \frac{1}{r}\frac{\partial \psi}{\partial x}.\frac{\partial \omega}{\partial r} + \frac{\omega}{r^2}\frac{\partial \psi}{\partial x} + \frac{1}{r}\frac{\partial \psi}{\partial r}.\frac{\partial \omega}{\partial x} = \frac{1}{\mathrm{Re}}[\frac{\partial \dot{X}}{\partial x} * 2\frac{\partial \omega}{\partial x} + \dot{X}(\frac{\partial^2 \omega}{\partial x^2} + \frac{\partial^2 \omega}{\partial r^2} + \frac{1}{r}\frac{\partial \omega}{\partial r} - \frac{\omega}{r^2})$$
$$+ (\frac{\partial^2 \dot{X}}{\partial x^2} - \frac{\partial^2 \dot{X}}{\partial r^2})(\frac{1}{r}\frac{\partial^2 \psi}{\partial r^2} - \frac{1}{r}\frac{\partial^2 \psi}{\partial x^2} - \frac{1}{r^2}\frac{\partial \psi}{\partial r}) + \frac{\partial \dot{X}}{\partial r}(2\frac{\partial \omega}{\partial r} + \frac{\omega}{r}) + 2\frac{\partial^2 \dot{X}}{\partial x \partial r}(\frac{1}{r^2}\frac{\partial \psi}{\partial x} - \frac{2}{r}\frac{\partial^2 \psi}{\partial x \partial r})] \tag{8}$$

and shear rate can be written as follows

$$\dot{\gamma}^2 = \frac{1}{r^2}(\frac{\partial^2 \psi}{\partial r^2} - \frac{\partial^2 \psi}{\partial x^2} - \frac{1}{r}\frac{\partial \psi}{\partial r})^2 + \frac{4}{r^2}[(\frac{\partial^2 \psi}{\partial x \partial r})^2 - \frac{1}{r}(\frac{\partial \psi}{\partial x})(\frac{\partial^2 \psi}{\partial x \partial r}) + \frac{1}{2r^2}(\frac{\partial \psi}{\partial x})^2] \tag{9}$$

Vorticity and stream function are related by poisson equation:

$$\frac{\partial^2 \psi}{\partial x^2} + \frac{\partial^2 \psi}{\partial r^2} - \frac{1}{r}\frac{\partial \psi}{\partial r} = -\omega r \tag{10}$$

Stream – vorticity approach obtained by eliminating the pressure terms from the momentum equations. Since its important to know pressure drop to used to compare numerical results and experimental data, the pressure drop along x- axis derived from momentum equation for steady incompressible, and non – Newtonian fluid **eq.(5**), (**Nallasamy 1986**).pressure drop calculated from following equation:

$$\frac{dp}{dx} = \frac{1}{\mathrm{Re}}[\dot{X}(-\frac{\partial \omega}{\partial r} - \frac{\omega}{r}) + \frac{\partial \dot{X}}{\partial r}(\frac{1}{r}\frac{\partial^2 \psi}{\partial r^2} - \frac{1}{r}\frac{\partial^2 \psi}{\partial x^2} - \frac{1}{r^2}\frac{\partial \psi}{\partial r})] \tag{11}$$

Also, shear stress at wall is important factor which has direct effects on internal layer of vessel, where a high value of shear stress leads to damage in vessel wall, shear stress at wall calculated from equation:

$$\therefore \tau_{wall} = \frac{\omega_{wall}}{\mathrm{Re}} \tag{12}$$

Initial and boundary conditions

To solve vorticity transport equation **eq(8)** and Poisson equation **eq.(10),** it required that, the appropriate expressions for stream function ψ and vorticity ω be specified at the boundary (**Anderson et al 1984**). The specification of these boundary conditions is extremely important since it directly affects the stability and accuracy of the solution. It is important and care must be taken to ensure that the physics of the problem is correctly modeled, on how to treat these geometries or models.

Hence the boundary conditions are summarized as follows:-

1- At tube center line:

Vorticity and stream function sets equal zero, $\psi = 0$, $\omega = 0$

2- At tube wall:

Since no-slip condition at wall, velocity component equal zero, stream function set

$$\psi_{wall} = q/2 \tag{13}$$

Where q is flow rate for real situation **(Taylor et al 1998)**, the flow changes as shown in **Fig.(3).** While vorticity at wall derived form Poisson **eq. (10)**, with $\frac{\partial \psi}{\partial r} = 0$ (no slip condition), for that **eq.(10)** can be written as (**Agrawal and Sengupta 1989**) and **(Cheng et al 1974)**.

$$\omega_{wall} = \frac{1}{R}\left(\frac{\partial^2 \psi}{\partial x^2} + \frac{\partial^2 \psi}{\partial r^2}\right) \tag{14}$$

3- At tube inlet:

Since the flow at inlet uniform, the vorticity value will set equal zero, while stream function at inlet varied form zero at center line to value of **eq. (13)**.

4- At tube exit:

At exit, the variation in vorticity and stream function is negligible

$$\frac{\partial \psi}{\partial x} = \frac{\partial \omega}{\partial x} = 0 \tag{15}$$

5-Initial condition:

Assume no flow, then stream function and vorticity set equal to zero.

Since the stenosis artery is a complex domain, therefore, the governing equations are transformed from polar coordinate to generalized coordinate.

TRANSFORMATIONS OF GOVERNING EQUATIONS

Transformation stream- vorticity equation:-

$$-\omega r J^2 = \psi_{\zeta\zeta}\alpha + \psi_{\eta\eta}\gamma - \psi_{\zeta}\frac{x_\eta J}{r} - \psi_\eta \frac{x_\zeta J}{r} - 2\beta\psi_{\zeta\eta} \tag{16}$$

$$\alpha = x_\eta^2 + r_\eta^2 \;:\; \gamma = x_\zeta^2 + r_\zeta^2 \;:\; \beta = x_\zeta x_\eta + r_\zeta r_\eta \tag{17}$$

Transformation vorticity transport equation:-

$$\frac{\lambda^2}{\text{Re}}\frac{\partial W}{\partial t} + \frac{1}{r}(\psi_\zeta x_\eta - \psi_\eta x_\zeta)(\omega_\zeta r_\eta - \omega_\eta r_\zeta)\, {}^{1}\!/_{J} - \frac{1}{r}[\psi_\zeta r_\eta - \psi_\eta r_\zeta]$$

$$[\omega_\eta x_\zeta - \omega_\zeta x_\eta] * 1/J + \frac{\omega}{r}[\psi_\zeta r_\eta - \psi_\eta r_\zeta)\frac{1}{J} =$$

$$\frac{1}{\text{Re}}[(\dot{X}_\zeta r_\eta - \dot{X}_\eta r_\zeta)(\omega_\zeta r_\eta - \omega_\eta r_\zeta).\frac{2}{J} + \dot{X}(\omega_\eta \frac{x_\zeta .J}{r} - \omega_\zeta \frac{x_\eta .J}{r} + \alpha\omega_{\zeta\zeta} +$$

$$\gamma\omega_{\eta\eta} - 2\beta\omega_{\zeta\eta} - \frac{\omega .J^2}{r^2}) * \frac{1}{J^2} + (\dot{X}_{\zeta\zeta}\alpha_x + \dot{X}_{\eta\eta}\gamma_x + 2\dot{X}_{\zeta\eta}\beta_x)/J^2 * (\frac{1}{r}(\psi_\zeta \frac{r_\eta .J}{r} -$$

$$\psi_\eta \frac{x_\zeta J}{r} + \alpha_r\psi_{\zeta\zeta} + \gamma_r\psi_{\eta\eta} - 2\beta_r\psi_{\zeta\eta})\frac{1}{J^2} + (\dot{X}_\eta \frac{x_\zeta}{J} - \dot{X}_\zeta \frac{x_\eta}{J})(2(\omega_\eta \frac{\dot{x}_\zeta}{J} - \omega_\zeta \frac{x_\eta}{J}) +$$

$$\frac{\omega}{r}) + {}^{2}\!/_{J^2}[\dot{X}_{\zeta\eta}(r_\eta x_\zeta + r_\zeta x_\eta) - \dot{X}_\zeta r_\zeta x_\zeta - \dot{X}_{\eta\eta} x_\eta r_\eta] * [\frac{1}{r^2}(\psi_\zeta \frac{r_\eta}{J} - \psi_\eta r_\zeta / J) -$$

$$\frac{2}{r}(\psi_{\zeta\eta}(r_\eta x_\zeta + r_\zeta r_\eta) - \psi_{\zeta\zeta} x_\zeta r_\zeta - \psi_{\eta\eta} r_\eta x_\eta) * {}^{1}\!/_{J} \;]$$

(18)

Transformation of pressure drop equation:-

$$\frac{dp}{dx} = -\dot{X}\left(\left(\omega_\eta\, x_\zeta - \omega_\eta\, x_\eta\right)/\,J + \frac{\omega}{r}\right)\left(\dot{X}_\eta\, x_\zeta - \dot{X}_\zeta\, x_\eta\right)1/\,J\,*$$

$$\frac{1}{r}[\psi_\zeta \frac{x_\eta.J}{r} - \psi_\eta \frac{x_\zeta.J}{r} + \alpha_r \psi_{\zeta\zeta} + \gamma_r \psi_{\eta\eta} - 2\beta_r \psi_{\zeta\eta}) * \frac{1}{J^2} \tag{19}$$

Transformation of shear rate equation:-

$$\dot{\gamma}^{2} = \frac{1}{r^2}\left[(\alpha_r \psi_{\zeta\zeta} + \gamma_r \psi_{\eta\eta} - 2\beta_r \psi_{\zeta\eta} + \frac{\psi_\zeta x_\eta J}{r} - \frac{\psi_\eta x_\zeta J}{r})\; {}^{1}\!/_{J^2} \;\right]^2$$

$$+\frac{4}{r^2}\left[((\psi_{\zeta\eta}(r_\eta x_\zeta + r_\zeta x_\eta) - \psi_{\zeta\zeta} x_\zeta r_\zeta - \psi_{\eta\eta} x_\eta r_\eta)\; {}^{1}\!/_{J^2})^2 + \frac{1}{2r^2 J^2}(\psi_\zeta r_\eta - \psi_\eta r_\zeta)^2\right.$$

$$\left. + \frac{J}{r}(\psi_\zeta r_\eta - \psi_\eta r_\zeta) * [(\psi_{\zeta\eta}(r_\eta x_\zeta + r_\zeta x_\eta) - \psi_{\zeta\zeta} x_\zeta r_\zeta - \psi_{\eta\eta} x_\eta r_\eta)\; {}^{1}\!/_{J^2}] \right. \tag{20}$$

Transformation of boundary equation:-

$$\omega_{wall} = \frac{\gamma}{r.J^2}(\psi_{\eta\eta}) \tag{21}$$

Grid Generation

The most common partial differential equation uses for grid generation in two dimensional is a Poisson equation in the form **(Fletcher 1987)** and **(Anderson 1984)**.

$$\alpha x_{\zeta\zeta} - 2\beta x_{\zeta\eta} + \gamma x_{\eta\eta} = -[x_\zeta P(\zeta,\eta) + x_\eta Q(\zeta,\eta)]/J^2 \tag{22}$$

$$\alpha r_{\zeta\zeta} - 2\beta r_{\zeta\eta} + \gamma r_{\eta\eta} = -[r_\zeta P(\zeta,\eta) + r_\eta Q(\zeta,\eta)]/J^2 \tag{23}$$

Where

$$\alpha = x_\eta^2 + r_\eta^2, \gamma = x_\zeta^2 + r_\zeta^2, \beta = x_\zeta x_\eta + r_\zeta r_\eta \text{ and } J = x_\zeta r_\eta - x_\eta r_\zeta$$

all grids used in this investigation are generated with $P(\zeta,\eta)=Q(\zeta,\eta)=0$.(**Bramley and Sloan 1987)** and **(Ali 2002)**.The non linear difference equations are solved iteratively using a point SOR method and, at each cycle of iteration, the coefficients α, β and γ are evaluated using previous approximations. **Fig.(4.a)** and **Fig.(4.b)** show the physical and computational domains which are used in the present study.

Time Marching

The basic principle of time marching is to start from an initial guess of the flow pattern, then the method solves the unsteady continuity, momentum equations for the evolution of the flow in time until equilibrium is established. Basically, the flow region is divided in to a grid network so that different terms in the governing equations are defined at each grid point. The flow field is then solved from the governing equations in finite difference form subjected to the imposed boundary conditions. With the flow equations applied to each grid point in turn, the solution becomes closer to the unsteady state solution for each time step (**Iatridis 1987**).

Experimental Work

The rig was designed to simulate the blood flow through constricted artery, which must satisfy number of requirements: pulsation flow, non-Newtonian fluid, taper vessel, stenosis vessel, developing flow and Laminar flow as shown in **Fig.(5).**

Dosing pump type **ALLDOS** Model EN600034 with flow rate 115 L/h, 3 bars, power 0.09Kw, 0.88-0.9 Ampere and 1270 RPM is used, which its operation is based on using diaphragm movement by rode connected eccentric disc, to generate pulsating flow. In order to measure a pressure drop in the test section under pulsation condition, the differential pressure transducer type **FOXPRO** with range of 20 mbar is used. Its operation is based on diaphragm movement and converting the pressure drop to electrical signal**.** Switch flow meter with range of 130L / h which gives indication for the number of pulses in sec and frequency .Flow meter is connected with interface card and accessed to computer. The amount of flow rate was measured by collecting working fluid in container and time was accounted by stop watch. To simulate the fluid dynamic behavior of blood, a solution of 2:3 glycerin-water with density of 1.120 g/cm^3 and viscosity (3.5 - 4) C.P. was used **(Rose et al 1998), (Cebral et al 2002)**.Density and viscosity were measured every day before starting to record data .To simulate the artery Acrylic tube with inlet diameter 16,18 and 20 mm **(Cox et al 1979)** and **(Wellborn and Stein 1981)**,with taper angle for each size (0.5, 1 and 1.5 degree) were used **(Walburn and Stein 1981),(Kimmel and Dinnar 1983)**.The length of test section was 175 mm **(Walburn and Stein 1981)** and 10 mm threaded added in entrance to use in connection with Acrylic block. The taper of inside diameter of tube match taper angle of out side diameter of stenosis to fix the stenosis in first third length of tube. Small tap was used upstream of joins block to prevent bubbles to inter test section.

Stenosis model is made from Acrylic with trapezoidal shape **(Ojha et al 1989)** and **(Varghese and Frankel 2003)** as shown in **Fig.(2).**

Five taps with sizes according to ISO standard 5167 **(Miller 1983)** were drilled in test section and locations of taps are shown in **Fig.(6)** . A copper tube with 4mm out diameter was fixed on taps (1, 2, 4, and 5) by epoxy, as shown in section (A), while bolt (M4) was used for tap (3), which required a special connection, as shown in section (B).

Data acquisition card type PCI-9111 is used, this data acquisition card is based on the 32-bit PCI bus architecture. High performance design and the state-of-the-art technology make this card ideal for data logging and signal analysis application in areas like medicine and process control, (**Aimen 2005**). In order to read the signal from the Pressure Transducer and Swatch flow meter sensor a program is required to record signal. Before writing this program it is necessary to ensure that the MATLAB defines the DAC in its tools.

Results and Discussion

To study the influence of stenosis and taper on blood "Non – Newtonian fluid" flow through artery, the computations were conducted for various stenosis severity (50%, 60% and 75%) and different values of tapering vessel angles (0, 0.5°, 1°, and 1.5°). To perform a careful parameter analysis, the instantaneous streamlines are calculated and shown during cycle of pulsation flow at intervals of 0.1 sec. The non – dimensional Womersley and Reynolds numbers are considered as 7.1 and 50 respectively .The study was carried out under constant flow rate.

Numerical results

As a first step in the analysis, a check for validation program is performed through the comparison of numerical results with results of **(Pontrelli 1999)**, for steady flow, Newtonian and non-Newtonian fluid at a Reynolds number of 10. The stenosis profile used in this comparison is described as exponential function. The stream at wall "maximum stream function" is 50 **(Pontrelli 1999)**. Comparison shown in the **Fig.(7)** and **Fig.(8)** which indicated that ,the present result has higher values than results in **(Pontrelli 1999)**, for both cases Newtonian fluid and Non – Newtonian fluid .The difference in results is due to method of calculation, the used equation in calculation of wall shear stress and input parameter of **(Pontrelli 1999)**.

The numerical study is carried out under pulsation condition, Re. No. = 50 and Womersley No. =7.1.Blood is considered as a non- Newtonian fluid with parameter Λ =50 which represents the degree of shear – thinning and for ratio of asymptotic viscosities at zero and infinity equal to δ = 40 **(Pontrelli 1999)**. The number of grid points along the axis in (ζ, η) is (176, 16), the time step has been selected as small $\Delta T=10^{-7}$ compared to $\Delta T=10^{-6}$ for steady case [Pontrelli 1999] in order to guarantee the convective and diffusive stability condition in all cases [Fletcher 1987,1].Different angles of vessel tapering (0,0.5°,1°,1.5°) with different degree of stenosis (0,50%,60%,75%) are considered. Streamline, wall shear stress and pressure drop results are plotted and studied.

Streamline distributions inside blood vessel at each time step are plotted for different stenosis present and different vessel tapers. The results indicate that, the stream line changes as inlet flow rate change as shown in **Fig.(9)** , the separation region is noted clearly at time step 0.4 sec and grows as time advanced. Also it can be noted that, the separation region upstream of stenosis showed to be started at time step 0.8 sec .The WSS distribution for tapered vessel 1.5°, with 75% stenosis is shown in **Fig.(10).** Due to taper angle, the WSS increases as distance increased into tapered section, the peak value of WSS is shown at stenosis part. While the WSS values at time step 0.4 sec, 0.5 sec, 0.7 sec and 0.8 sec are not increased due to low inlet flow rate at these time steps. At time step 0.7 sec and 0.8 sec negative values of WSS are indicated. The WSS distribution indicated same behavior as seen when stenosis 60% but a lower reduction is observed with negative value of WSS at time step 0.8 sec, also this effect become lower at 50% stenosis. Comparison WSS of distributions at some instantaneous times reveals that, the highest of stenosis has a significant influence on the WSS at the throat, the downstream of throat, and the length of separation region. Since high WSS is not only damage the vessel wall and causes intimal thickening, but also it actives platelets which causes' aggregation, and finally results in the formation of a thrombus, the wall shear stress at throat deserves to be noticed **(Guo-Tao et al 2004)**.

Pressure drops along the axial length of vessel are plotted, which indicated that, the pressure drops at stenosis part and this drop in pressure reduces at distal stenosis. Also, pressure drop changes as the inlet flow rate changes at each time step. Further, the drops change according to the stenosis percent changes. **Fig.(11)** shows pressure drop along the axial length and the pressure drop changes as inlet flow rate changes. A high reduction in pressure is observed at time step 0.2 sec and 0.3 sec for high flow rate. Pressure at distal stenosis was higher than pressure at proximal stenosis due to the back flow at distal stenosis.

Experimental Results

Experimental work was conducted at Re.No.= 580, Womersley No.= 6.3, and frequency= 2.1Hz. The density of the working fluid was taken as 1.120 g/cm^3 and the viscosity in rang of (0.035-0.04) Posie. Test was carried out at an average flow rate of 51 ml/sec and the data recorded at rate of 1280 samples for duration of 51sec.As the stenosis is increased the pressure difference increased. As the stenosis increase the cross sectional area decreases and flow accelerates, consequently, the pressure energy is converted to the kinetic energy. The reduction in pressure can be calculated from Bernoulli's equation and it can be written as follows **(Walburn and Stein 1981)**:

$$\Delta p = 0.5\rho V^2((\frac{D}{d_m})^4 - 1) \tag{24}$$

Where d$_m$ is diameter of center stenosis: D is diameter upstream stenosis
It is clear that, diameter of stenosis had a direct effect on value of pressure drop value, and power index "four" explain the difference in pressure drop for different percent stenosis (50%, 60% and 75%) as shown in **Fig.(12).**This results are in agreement with the results of **(Porenta et al 1985)**, **(Bapat 2005)**, and consistence with the general observation of the effect stenosis of less than 50% have little effect on pressure and flow .This is one of the reason why stenosis are difficult to diagnose at an early stage. The pressure difference in all measurements are non dimensionalzed with $(\frac{1}{2}\rho V^2)$ for all the cases. In taper section, the flow is accelerated and energy is converted from pressure energy to kinetic energy. This reduction in pressure energy can be calculated by substituting the continuity equation into the Bernoulli equation, with some manipulation, yields **(Walburn and Stein 1981)**.

$$\Delta p = 0.5\rho V^2[(\frac{D}{D - 2l\tan\theta})^4 - 1] \tag{25}$$

eq.(25) indicate that, as tapering angle increases the pressure drop increase as shown in **Fig.(13),** also the pressure drop increases as distance of taper section increases.

Comparisons

To check the validity of the numerical technique, several comparisons of numerical results for different cases are performed at time step 0.2 sec, where the discrepancy is clear and this is due to the maximum flow rate. Experimental results for pressure drop are compared with numerical results and with available literature for same cases.

The effect of different percent stenosis on the WSS for 1.5^o taper vessels are shown in **Fig.(14),** which indicates that, as stenosis degree increases WSS increases and the same trend is by **(Hun Jung et al 2004)**.

Pressure drop plots are used for comparison of numerical results with experimental data for the present study to investigate the effects of stenosis percent for different taper vessels .**Fig.(15)** indicates that, the pressure drop increases as degree of stenosis increases in straight vessel and a high pressure difference is found at 75% stenosis compared with 50% and 60% stenosis .This behavior was in agreement with **(Bapat 2005)** as shown in **Fig.(16).**It indicates that, present experimental data has a higher value, this due to constant viscosity and shape of stenosis used by **(Bapat 2005)**, also it is coincident with the conclusion of the survey investigated by **(Young 1979)**.

On the other hand, the effects of tapering angle are investigated with and without stenosis. For case of without stenosis, comparison of experimental data with **(Walburn and Stein 1981)** is preformed as shown in **Fig.(17)** .It is clear that, present data have higher values than **(Walburn and Stein 1981)** data ,this is due to the viscosity (0.0103 Poise) compared with a mixture fluid with viscosity in range (0.035 to 0.040 Poise) in present study. Also as tapering angle increases WSS increases, and this is clearer at the end of the vessel. This is in agreement with **(Kimmel and Dinnar 1983)** as shown in **Fig.(18).**It shows that , the values of WSS in the present study are higher than

(Kimmel and Dinnar 1983) values, because they are assumed Newtonian fluid, different input flow rate and one dimension flow .

In order to compare the numerical results with experimental data in the present study, calculations are preformed with sine wave profile inlet flow rate to confirm the experimental work with Re.No.= 580 and Womersley No.= 6.3 as shown in **Fig.(19).** This indicate that, the numerical results have same behaviors as experimental results, but with higher values

Conclusions

Computational and experimental simulations for blood flow through stenosis artery under pulsation condition were carried out in this study. A shear thinning model was used to express Blood, which is considered as non-Newtonian fluid. Attention was focused on the effect of stenosis on pressure drop and wall shear stress. The following are the main conclusions drawn from the present investigation work ,Both pressure drop and wall shear stress were increased as taper angle of vessel increase (0.5^o, 1^o, 1.5^o), due to increase in kinetic energy, also increased as stenosis increase (50%, 60% and 75%), and a large effect seen for 75% stenosis.

Wall shear stress had negative values where vortex exists, vortex region may be the origin of red cell damage and thrombus formation and the stenosis will progress further, and the high stress is exerted near the stenosis throat of blood vessel due to fast flow and will generate serious physical damages. Tapering of the artery did not change flow patterns, but only changed values, amplified the values of wall shear stress and pressure drop. As the distance into taper section increased both pressure drop and wall shear stress were increased. Both pressure drop and wall shear stress were increased as the distance into taper section increased. For the stenosis percent less than 50% a little effect on pressure and flow was seen. This is a reason for why the stenosis percent are difficult to diagnosis at an early stage.

As a related to the present work, following suggestions can be put forward. Vessel wall will be consider as a distensible, curved artery will be consider, where curved is more reality, and Bifurcation will be consider.

REFERENCES

Agrawal, A.K. and Sengupta S., 1989. "Laminar flow and heat transfer in blocked annuli", J. Numerical Heat Transfer, Part A, Vol.15, PP.489-508.

Aimen, M. A. B., 2005,"Wear monitoring turning processes using vibration and strain measurements", M.Sc.Thesis, University of Baghdad.

Ali, L. Kaeed. 2002,"Numerical study of forced convection over bank of tubes by using body fitted coordinates system "M. Sc .Thesis, University of Technology.

Anderson,D.Jr." Computional Fluid Dynamics: the Basics with Applications" Mc Graw –Hill,Inc.

Anderson, D. A., Pletcher, R.H. and Tannihill, J. C. 1984 "Computational Fluid Mechanics and Heat Transfer",Hemisphere Publishing Corporation.

Bapat , A.2005 " Predicting stenosis in blood vessels " on web. Site

Bramley, J.S., and Sloan, D.M., 1987,"Numerical solution for two –dimensional flow in a branching channel using boundary – fitted coordinates", J. Computers and Fluids, vol. 15, No.3, pp. 297 – 311.

Cebral, J. R., Yim, P. J., Lohner, R., Soto, O., and Choyke, P.L.,2002, " Blood flow modeling in carotid arteries with computational fluid dynamics and MR. Imaging", Academic Rediology , Vol. 9 . No.11, pp. 1286-1299.

Chen, X. May 2003, "A nonlinear viscoelastic Mooney-Rivlin thin wall model for unsteady flow in stenotic arteries", M .Sc .Thesis, Worcester Polytechnic Institute.

Cheng, L.C., Robertson, J.M., and Clark, M.E., 1974,"Calculation of plane pulsatile flow past wall obstacles", J .Computers and Fluids, Vol.2, pp. 363 – 380.

Cox, J.T, Hoften, J. D.A., and Hwang, H.C., 1979,"Investigation of a pulsatile flow field downstream from a model stenosis", J. Biomechanical Engineering, vol. 101, pp. 141–150.

Fletcher, C.A.J., 1987,"ComputationalTechniquesfor Fluid Dynamics 1 ", Springer–Verlag series

Fletcher,C.A.J., 1987,"Computational Techniques for Fluid Dynamics 2 ", Springer – Verlag series.

Guo – Tao liu, Wang, X.J., Ai. B. Q, and Liu, L. G., 2004, "Numerical study of pulsating flow through a tapered artery with stenosis", Chinese J. of Physics, Vol. 42, No. 4 – I.

Hun Jung, Choi, J.W., and Park, C. G., 2004,"Asymmetric flows of non-Newtonian fluids in symmetric stenosed artery", Korea – Australia journal, Vol. 16, No.2, pp. 101-108.

IATRIDIS, M.I., 1987,"A theoretical study of buoyancy driven circulation in a liquid drop ", M.Sc. Thesis, University of Liverpool

Kimmel, E. and Dinnar, V., 1983,"Pulsatile flow in tapered tubes: a model of blood flow with large disturbances", J. Biomechanical Engineering, Vol.105, pp.112–119

Miller, R.W., 1983,"Flow Measurement Engineering Hand Book", Mc Graw – Hill Book Company

Nallasamy, M.1986,"Numerical solution of the separating flow due to an obstruction" J. Computers &Fluids, Vol.14, No. 1, PP.59-68

Ojha, m., Cobbold, C., Johnston, K. W., and Hummel, R.L., 1989."Pulsatile flow through constricted tubes: An experimental investigation using photo chromic tracer methods",J. Fluid Mech., Vol.203 , pp.173-197.

Pontrelli, G., 1999,"Blood flow through an axisymmetric stenosis", Instituto per le applicazioni Del Calcolo–CNR. Viale Del Policlinico,137, 00161 Roma, Italy.

Porenta, G., Young, D.F., and Rogge,T.R., 1985," A finite – element model blood flow in arteries including taper, branches, and obstructions", J. Biomechanical Engineering

Rose, M.L.J., February 1998,"Development of a muscle powered blood pump: fluid mechanic considerations", Ph .D. Thesis University of Glasgow, Department of Cardiac Surgery, Faculty of Medicine.

Taylor, C. A., Hughes, T. J. R., and Zarins, C.K., 1998, "Finite element modeling of three – dimensional pulsatile flow in the abdominal aorta: Relevance to atherosclerosis" Annals of Biomedical Engineering. Vol. 26, pp. 975 – 987.

Varghese, S.S., and Frankel, S. H., 2003,"Numerical modeling of pulsatile turbulent flow in stenotic vessels ',J. of Biomechanical Engineering , Vol. 125 , pp. 445 – 460 .

Walburn, F. J., and Stein, P.D., 1981, "Effect of vessel tapering on the transition to turbulent flow: Implications in the cardiovascular system", J. Biomechanical Engineering, Vol. 103, pp.116 - 120.

Young, D.F., 1979,"Fluid mechanics of arterial stenosis", J. Biomechanical Engineering, Vol.101,pp. 157 – 175.

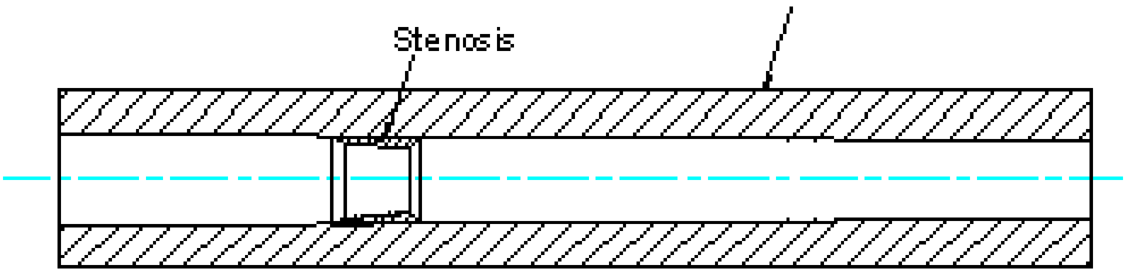

Fig. (1): Schematic of geometry

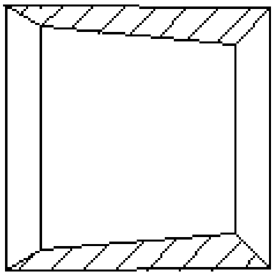

Fig. (2): Geometry of stenosis

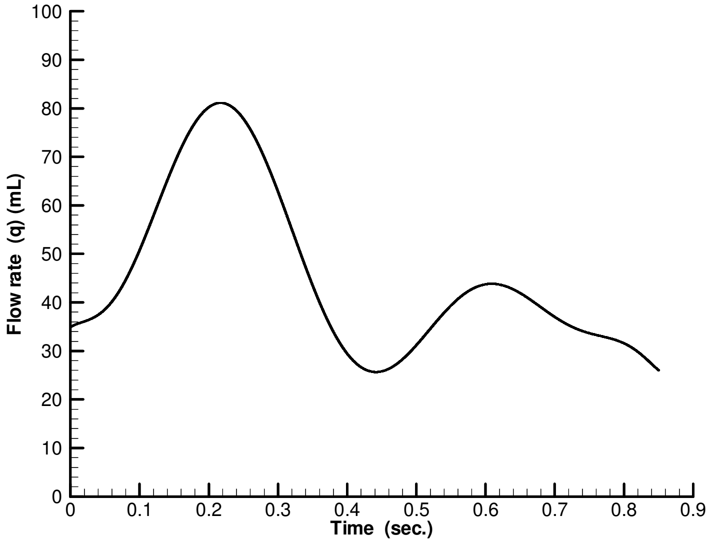

Fig.(3): Physiological flow rate in artery (**Taylor et al 1998)**

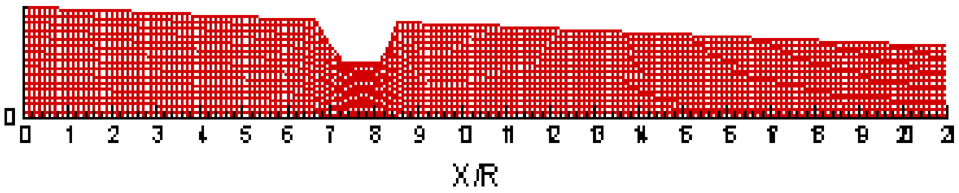

Fig. (4.a): Physical domain

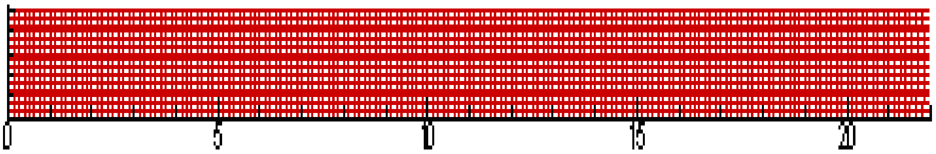

Fig.(4.b): Computational domain.

Fig.(4): Physical and computational domain

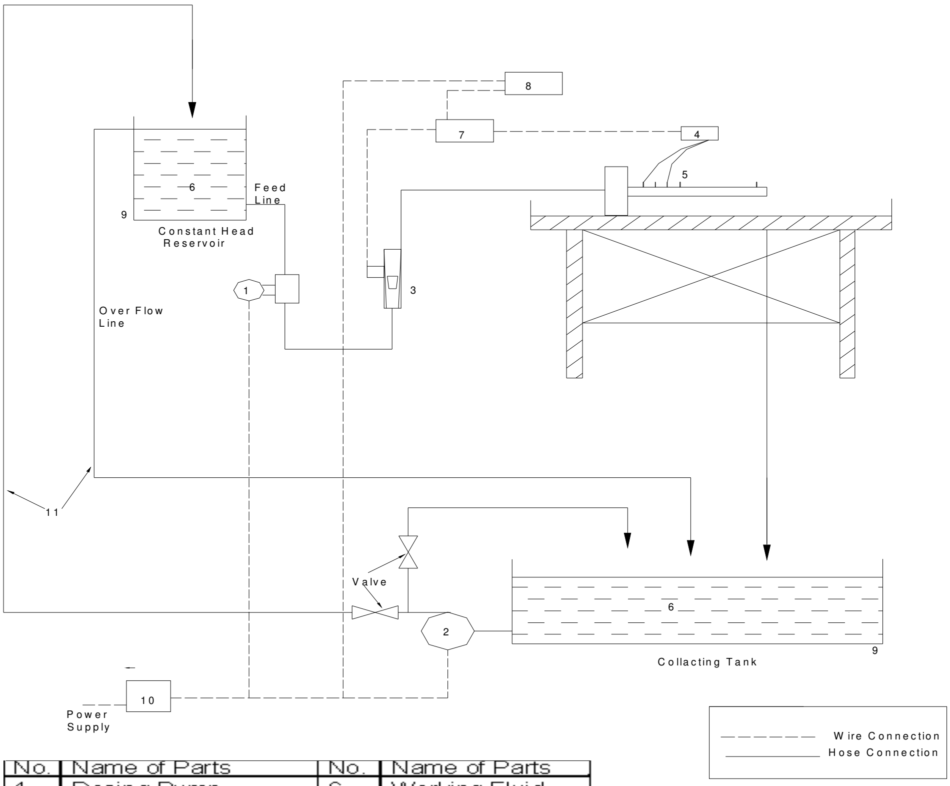

No.	Name of Parts	No.	Name of Parts
1	Dosing Pump	6	Working Fluid
2	Centrifugal Pump	7	Interface Card
3	Flow Meter	8	Computer
4	Pressure Transducer	9	Tank
5	Test Section	10	Stabilizer
11	Hose Connection		

Fig.(5): Experimental rig

Fig.(6): Location of pressure tapes

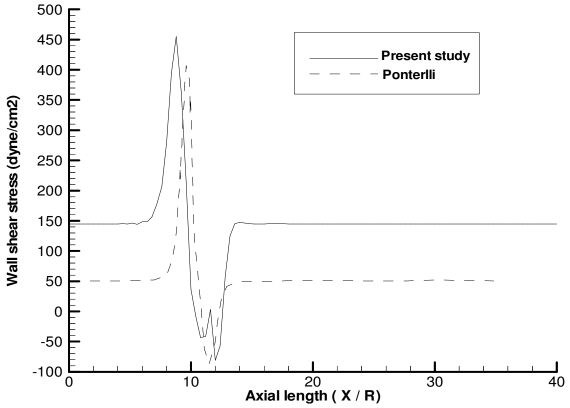

Fig.(7): Comparison of numerical results of wall shear stress (Newtonian fluid) with **(Ponterlli 1999)**.

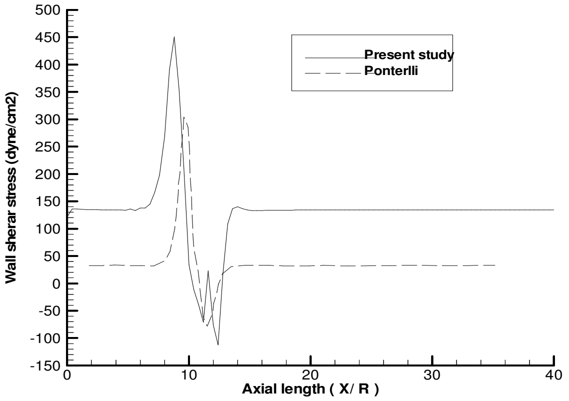

Fig.(8): Comparison of numerical results of wall shear stress (Non Newtonian fluid) with **(Ponterlli 1999)**.

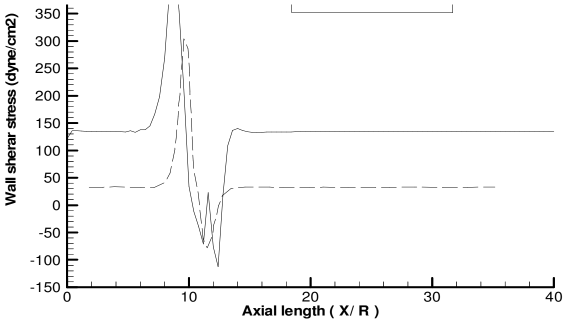

Mesh for taper vessel ,1.5 deg. ,with 75% stenosis

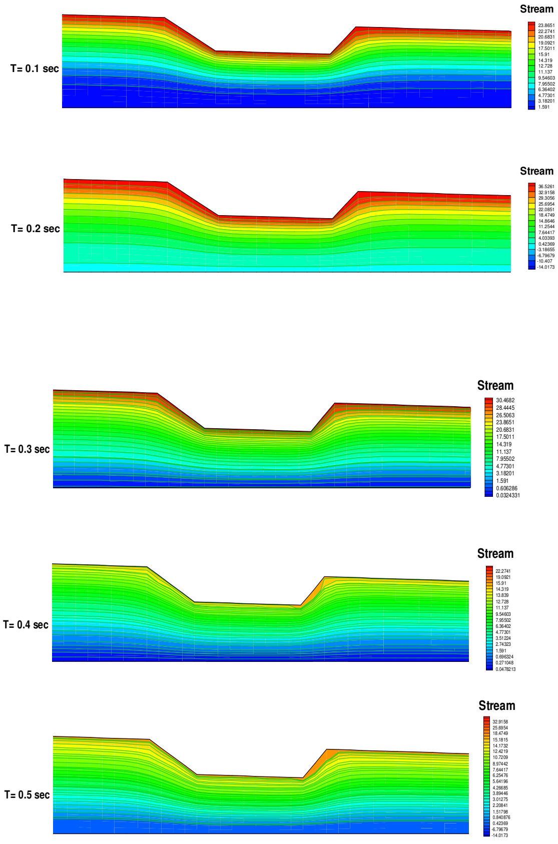

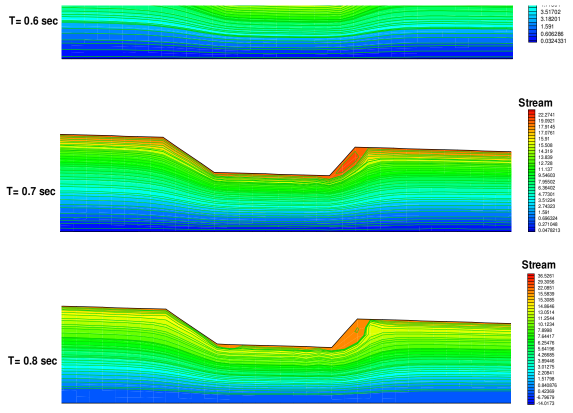

Fig.(9): Instantaneous streamline pattern at different time steps in pulsate flow, for 1.5^{o} taper vessel with 75% stenosis

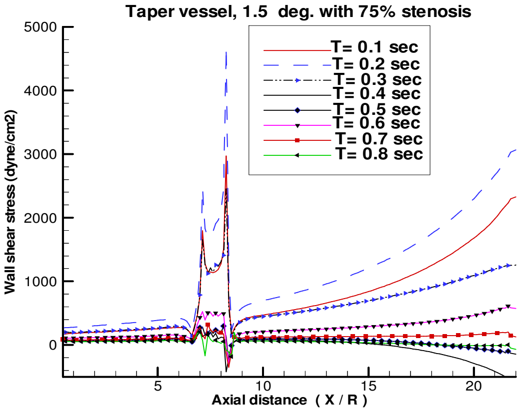

Fig.(10): Wall shear stress at different time steps ,for 1.5^{o} taper vessel with 75% stenosis.

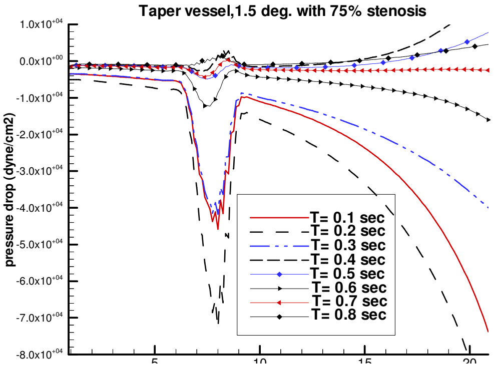

Fig.(11): Pressure drop at different time steps, for 1.5 ^{o} taper vessel with 75% stenosis.

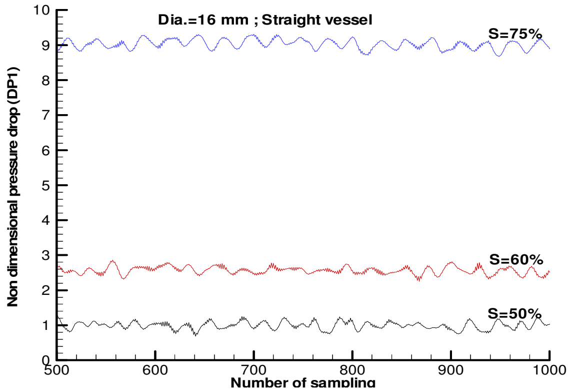

Fig(12): effect of stenosis percent on pressure drop in vessel at flow rate 50ml/s

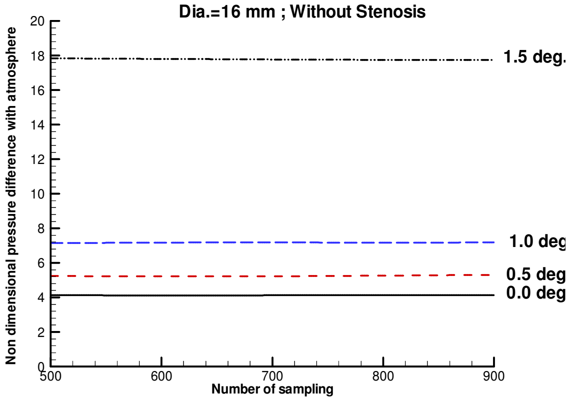

Fig.(13): Effect of tapering angles on pressure in vessel at flow rate 50 ml/sec

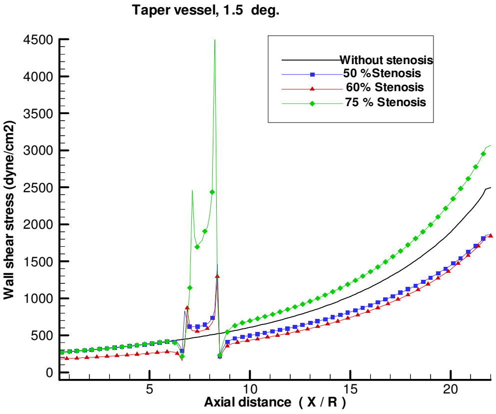

Fig.(14): Effect of stenosis percent on wall shear stress at time step 0.2 sec

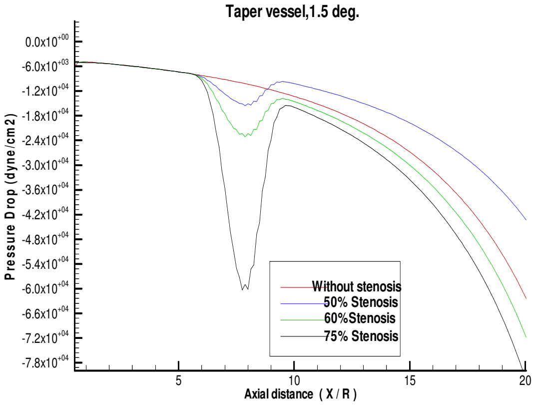

Fig.(15): Effect of stenosis percent on pressure drop at time step 0.2 sec 1.5^{o} taper vessel.

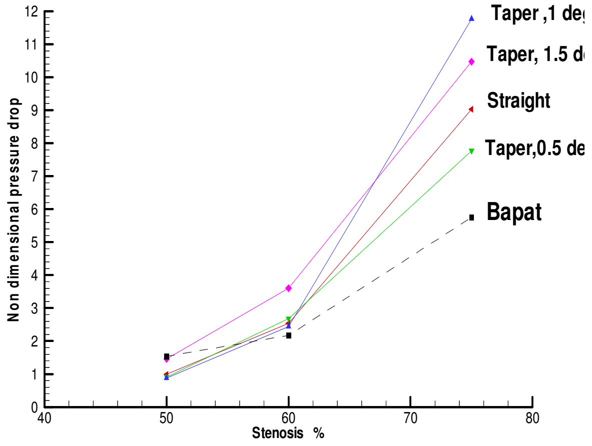

Fig.(16): Comparison of experimental results for different stenosis percent with experimental results of **(Bapat 2005)**.

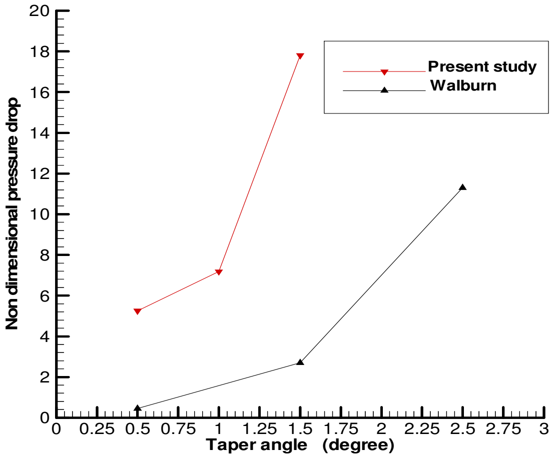

Fig.(17): Comparison of experimental results for tapering angles with experimental results of **(Walburn and Stein 1981)**

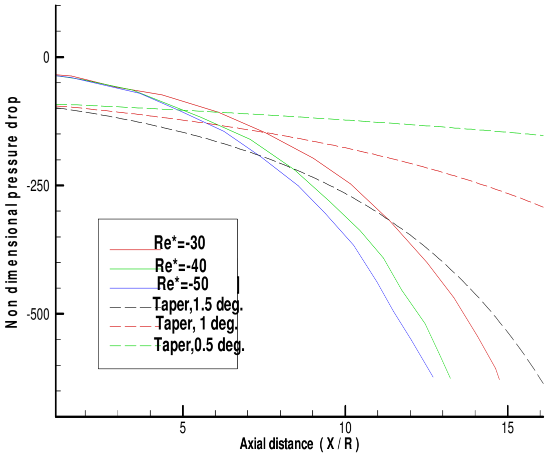

Fig.(18): Comparison of numerical results for tapering angles with numerical results of (**Kimmel and Dinnar 1983**) .

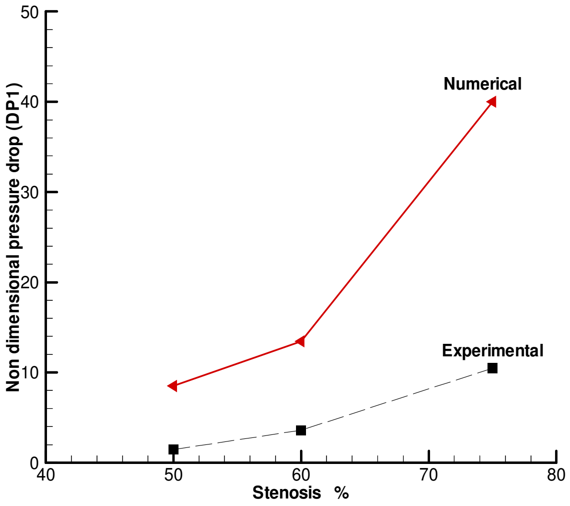

Fig.(19): Comparison of numerical results for different stenosis percent with experimental results for taper vessel 1.5 degree.

NOMENCLATURES

symbol	Meaning	Units
D	Diameter	m
e	Strain rate	1/s
L	length	m
P	Pressure	N/m^2
q	Flow rate	ml/s
r	r-coordinate	
R	Radius	m
Re	Reynolds number $\rho VR/\mu$	
u	Velocity component in x-direction	m/s
v	Velocity component in r-direction	m/s
V	Velocity vector	m/s
x	X-coordinate	
α	Transformation parameter in grid generation	
β	Transformation parameter in grid generation	
γ	Transformation parameter in grid generation	
$\dot{\gamma}$	Shear rate $\dot{\gamma} = \frac{\partial u}{\partial r}$	1/s
δ	$\delta = \frac{\eta_0}{\eta_\infty}$ ratio of asymptotic viscosities at zero to infinity	
ζ	Coordinate in the transformed domain	
η	Coordinate in the transformed domain	
$\mathrm{\eta}$	Shear viscosity	N/m^2
θ	Taper angle	deg.
λ	Weromsly No.=R$\sqrt{\frac{f}{\nu}}$ ratio of transient inertia force to viscose force	
Λ	Material constant	s
μ	Dynamic viscosity	kg/m.s
ν	Kinematics viscosity	m^2/s
ρ	Fluid density	kg/m^3
τ	Shear stress	N/m^2
ϕ	General dependent function	
$\dot{X}$	Non-dimensional viscosity	
ψ	Stream function	m^2/s
ω	Vorticity	1/s
$\Delta\zeta$	Grid step distance in ζ -direction	
$\Delta\eta$	Grid step distance in η -direction	

NUMERICAL STUDY FOR A THREE DIMENSIONAL LAMINAR NATURAL CONVECTION HEAT TRANSFER FROM AN ISOTHERMAL HEATED HORIZONTAL AND INCLINED SQUARE PLATE AND WITH A CIRCULAR HOLE

Yasmeen Hameed Abd
Department of Mechanical Engineering
University of Technology

Dr. Ikhlase M.Fayed
Department of Mechanical Engineering
University of Technology

ABSTRACT

A theoretical study for a three-dimensional natural convection heat transfer from an isothermal horizontal , vertical and inclined heated square flat plates (with and without circular hole) has been done in the present work. The study involved the numerical solution of the transient Navier-Stokes and energy equations by using finite deference method (F.D.M.). The complete Navier-Stokes equation are transformed and expressed in terms of vorticity-vector potential. The Energy and Vorticity equations were solved by using an Alternating Direction Implicit (ADI) method because they are transient equations of parabolic portion, and the Vector potential is solved by using an equations Successive Over-Relaxation (S.O.R) method because it is from elliptic portion. The numerical solution is capable of calculating the Vector potential, three components of Vorticity and temperature field of the calculation domain. The numerical results were obtained in rang of Grashof number ($10^3 \leq Gr \leq 5x10^4$) with Prandtl number of (0.72) for square flat plate and the other consist a circle hole with ratio 0.6 and 0.8 diameter of the hole to main square side length.

The numerical results showed that the main process of heat transfer is conduction for Grashof number less than 10^3 and convection for Grashof number larger than 10^3 and the results of local Nusselt number show fairly large dependence on inclination angle. For horizontal plate facing upward and downward, average Nusselt number is proportional to one-fifth power of Rayleigh number, and there is a significant difference in heat transfer rates between the upward and downward cases. For horizontal plate with circle hole facing upward for Grashof number 10^4, the effect of core portion caused a limited increment in the heat transfer rate, where as for the facing downward case, the effect was larger and the maximum value of heat transfer rates is be for square flat plate with circle hole by ratio 0.6 for all inclination angles. With the increase of Grashof number to 5x104 heat transfer rates decrease except the square horizontal flat plate with circle hole by ratio 0.6 .

The average Nusselt number increases with the increase of inclination of plates facing upward to reach to the higher average Nusselt number at vertical position then decrease with increase of inclination of plates. And the maximum value of average Nusselt number is depended on the ratio of diameter of the hole to main square side length, showed that the maximum temperature gradient occurs at the external edge of the horizontal plate (with and without circle hole) facing upward and at the lower external edge in inclined case. The numerical results was made through comparison with a previous numerical and experimental work, the agreement was good.

المستخلص

يقدم هذا البحث دراسة نظرية لانتقال الحرارة ثلاثي الأبعاد للحمل الحر من صفيحة مربعة و أخرى ذات ثقب دائري أفقية و عمودية و مائلة عن الأفق مسخنة بثبوت درجة الحرارة. تضمنت الدراسة ، الحل العددي لمعادلات الزخم الكاملة والطاقة الانتقالية باستخدام طريقة الفروق المحددة . معادلات الزخم الكاملة تم تحويلها والتعبير عنها بدلالة الدوامية و متجه الجهد الكامن. تم حل كل

من معادلة الطاقة و معادلة دالة نقل الدوامية باستخدام طريقة (الاتجاه المتناوب الضمني)، وذلك لكونها معادلات انتقالية من نوع القطع المكافئ، و حل معادلة متجه الجهد الكامن بطريقة فوق التراخي المتعاقبة لكونها معادلات من نوع قطع ناقص. يتضمن الحل العددي حساب كل من متجه الجهد الكامن والمركبات الثلاث للدوامية ودرجة الحرارة لمنطقة الحساب. النتائج التي حصل عليها لحدود رقم كراشوف ($10^3 \le Gr \le 5x10^4$) مع رقم براندتل(0.72) للصفيحة المربعة و الصفيحة المثقبة بنسبة قطر الثقب الدائري إلى طول ضلع الصفيحة المربعة مساوٍ إلى 0.6 و 0.8 .

بينت النتائج العددية إن العملية الرئيسية لانتقال الحرارة هي التوصيل لرقم كراشوف 10^3 و الحمل لرقم كراشوف أعلى من 10^3 و إن رقم نسلت الموضعي يعتمد كليا على زاوية الميلان. في حالة الصفيحة الأفقية وجهها المسخن إلى الأعلى والأسفل، متوسط رقم نسلت يتناسب مع رقم رالي للأس (1/5) ، كذلك هنالك اختلاف واضح في معدلات انتقال الحرارة بين الوضع الأفقي الموجه للأعلى والأسفل. يسبب تأثير قطر الثقب لرقم كراشوف 10^4 زيادة محدودة في معدلات انتقال الحرارة في حالة الصفيحة المثقبة وجهها المسخن إلى الأعلى بينما تكون اكثر تأثيرا في حالة الصفيحة المثقبة وجهها المسخن إلى الأسفل و ان أقصى قيمة لمعدل انتقال الحرارة تكون للصفيحة المربعة المثقبة بنسبة تثقيب 0.6 و لزوايا الميل المختلفة. بزيادة رقم كراشوف إلى $5x10^4$ يقل معدل انتقال الحرارة ما عدا الصفيحة المربعة الأفقية وجهها المسخن إلى الأسفل حيث يكون أقصى قيمة عند نسبة تثقيب 0.6 . تزداد قيم متوسط رقم نسلت بزيادة زاوية ميل الصفيحة المربعة وجهها المسخن إلى الأعلى لتصل إلى أعلى قيمة لها عند الوضع العمودي وبعدها تقل بزيادة ميلان الصفيحة، و إن أقصى قيمة لمتوسط رقم نسلت تعتمد على نسبة التثقيب، و إن أقصى انحدار لدرجة الحرارة يكون عند الحافة الخارجية للصفيحة المربعة و المثقبة الأفقية المسخنة إلى الأعلى و عند الحافة السفلى الخارجية في حالة الميلان . تم مقارنة نتائج الدراسة الحالية مع نتائج عددية و عملية لدراسات سابقة و كان التوافق بينها جيد .

KEY WORDS
Square Plate, Circular Hole, Natural Convection, Three-Dimensional

المقدمة

شهدت العقود الماضية ، اهتمام كبير لعملية انتقال الحرارة بالحمل الحر، هذا الاهتمام المتزايد هو انعكاس قلقنا المتزايد بالطاقة و البيئة لما لها من أهمية في التطبيقات الصناعية و المدنية حيث قام الباحثان**Aziz & Hellums (1967)** بدراسة عددية باستخدام طريقة الفروقات المحددة لحل معادلات الحركة لحالة الجريان ثلاثي الأبعاد و حالة الجريان الثنائي الأبعاد و الحصول على المعادلات اللابعدية (معادلات الدوامية ودالة المتجه الكامن) بتحويل معادلات نفير ستوك بطريقة (Alternating Direction Implicit Method) لحل معادلات القطع المكافئ (Parabolic Equation) و بطريقة فوق التراخي المتعاقبة (Successive Over Relaxation)(SOR) لحل معادلات القطع الناقص (Elliptical Equation) عند رقم براندتل $Pr=1$ ولحدود رقم رالي $2500 \le Ra \le 3500$ و درس الباحثان الفرق بين الجريان الثنائي والثلاثي الأبعاد و لاحظا توزيع درجة الحرارة في حالة الاستقرار يكون اقل للجريان ثلاثي الأبعاد ، و ان زمن الاستقرار يقل بزيادة رقم كراشوف . و استخدم الباحثان**(Suriano & Yang 1968)** طريقة الفروقات المحددة العددية (Numerical Finite-Difference Scheme) لحل معادلات الزخم والطاقة والإستمرارية **(المعادلات الحاكمة)** لانتقال الحرارة بالحمل الحر الطباقي من صفائح أفقية و عمودية مسخنة لشرط ثبوت درجة الحرارة لمدى رقم رالي $0<Ra<300$ و رقم براندتل $Pr=0.72\&10$. وجد الباحثان ان العملية الرئيسة لانتقال الحرارة هي التوصيل لرقم رالي أقل من 50 و الحمل لرقم رالي أعلى من 50 عندما يكون رقم براندتل 0.72 و عند ثبوت رقم رالي و زيادة رقم براندتل الى 10 يزداد متوسط رقم نسلت لحدود رقم رالي من 0 الى50 و يقل متوسط رقم نسلت لرقم رالي اكبر من 100 و حصلا على توافق جيد عند مقارنه النتائج العددية مع بحوث عملية سابقة. اما الباحثان **(Pera & Gebhart 1973)** فدرسا عملياً و عددياً جريان الطبقة المتاخمة لإنتقال الحرارة بالحمل الحر الطباقي من أسطح أفقية غير محددة و مائلة بزوايا صغيرة عن الأفق لشرطي ثبوت درجة الحرارة و الفيض الحراري باستخدام الطريقة العددية لحل المعادلات الحاكمة عند رقم براندتل $Pr=0.7$ في حالة التسخين لشرط ثبوت درجة الحرارة، وعند حدود رقم براندتل $0.1 \le Pr \le 10$ في حالة التسخين لشرط ثبوت الفيض الحراري ، و توصلا الى ان أي إمالة للصفيحة الأفقية المسخنة لشرط ثبوت درجة الحرارة يؤثر بدرجة كبيرة على توزيع السرعة و بدرجة قليلة على توزيع درجة الحرارة وعند زيادة رقم براندتل في حالة الصفيحة الأفقية المسخنة لشرط ثبوت الفيض الحراري يؤدي الى نقصان السرعة وتقليل سمك الطبقة الحرارية . الباحثان بينا ان عملية انتقال الحرارة في الصفيحة العمودية غير المحددة هو أعلى بمقدار 80% من نظيره في الصفيحة الأفقية عند رقم كراشوف الموضعي 10^5 عند نفس ظروف العمل من درجة الحرارة و نوع المائع المستخدم.أما عمليا فقد استخدما تقنية التصوير بمقياس **(Mach-Zehnder)** لدراسة انتقال الحرارة لصفائح من الألمنيوم مستطيلة ذات أبعاد cm 0.35x0.43وسمك 0.025cm و كانت النتائج العددية أعلى من النتائج العملية لحدود رقم كراشوف $Gr<10^4$ بينما كانت أقل لحدود رقم كراشوف $Gr>10^4$.

و أجرى الباحثان **(Cairnie & Harrison 1982)** دراسة نظرية وعملية لجريان الطبقة المتاخمة لانتقال الحرارة بالحمل الحر من صفيحة عمودية مسخنة بثبوت درجة الحرارة و لفارق درجة الحرارة بين المحيط والصفيحة كبير جداً ، حيث درجة حرارة المحيط 295K و الصفيحة مسخنة لمدى من درجات الحرارة مقدارها $T_W = 674,574,473 \ \& \ 373$ K. نظرياً استخدما طريقة الفروقات المحددة لحل المعادلات الحاكمة أما عملياً فقد استخدما صفيحة مستطيلة ذات طول 0.5 m و عرض 0.25m و سمك 0.00127 m و بينت القياسات الابتدائية ان السطح ذات درجة حرارة 473 K و 623 K يكون اضطرابي لرقم كراشوف $4x10^8$ و $3x10^8$ بالترتيب و خواص المائع عند درجة حرارة (bulk temperature) في حين هذه القيمة الحرجة تتغير كثيراً لو تم إختيار (film temperature) أو أي درجة حرارة اخرى . الباحثان حصلا على توافق جيد بين نتائجه العملية و النظرية. قام الباحثان **(Goldstein & Lau 1983)** بدراسة عددية و عملية لإنتقال الحرارة بالحمل الحر الطباقي من صفائح افقية مربعة بأشكال (مع أسطح امتداد أو عدمها) مختلفة لحالتين الأولى وجهها المسخن إلى الأعلى والثانية وجهها المسخن إلى الأسفل لشرط ثبوت درجة الحرارة ، تضمنت الدراسة النظرية حل

المعادلات الحاكمة بطريقة الفروقات المحددة ضمن حدود رقم رالي $40<Ra<8x10^{3}$ ورقم براندتل $Pr=0.7$ ،وجدا ان ثبوت رقم رالي وزيادة رقم براندتل الى 2.5 يؤدي الى زيادة معامل إنتقال الحرارة بمقدار 7.5% وهذه النتيجة تتفق مع الدراسة التحليلية للمصدر **(Pera & Gebhart 1973)** أما الدراسة العملية تضمنت أجراء تجارب إنتقال الكتلة لقطعة مربعة من النفثالين يتراوح طول الضلع من 0.0258m الى 0.203m معرضة للهواء ضمن حدود رقم رالي $0<Ra<4.8x10^{3}$ و كانت نتائج معامل انتقال الحرارة أعلى من النتائج العددية في حالة الصفيحة وجهها المسخن إلى الأعلى .

أجرى الباحث **(Mustafa 2001)** دراسة عددية و عملية لإنتقال الحرارة بالحمل الحر من سطوح دائرية أفقية وجهها المسخن إلى الأعلى لشرط ثبوت درجة الحرارة ، النتائج العددية التي حصل عليها من الحل العددي كانت بأستخدام طريقة الفروقات المحددة البينية لقرص و حلقات بنسبة قطر داخلي $0.2\leq m\leq 0.9$ من القطر الخارجي و وجد ان العملية الرئيسة لإنتقال الحرارة هي التوصيل لرقم كراشوف أقل من 10^{3} و الحمل لرقم كراشوف أعلى من 10^{3} ضمن مدى رقم كراشوف $10^{3}\leq Gr\leq 10^{7}$ و ان أقصى قيمة لمعدل انتقال الحرارة الكلي يكون عند الحلقات التي لها نفس القطر الخارجي للقرص و بنسبة القطر الداخلي الى القطر الخارجي تتراوح بين (0.2-0.3) و تأثير الإنفصال الحراري على معامل انتقال الحرارة الموضعي يقل بازدياد رقم كراشوف و الريشة تكون اشد بازدياد رقم كراشوف في حالة القرص اما في حالة الحلقات فمعامل انتقال الحرارة الموضعي يزداد بازدياد رقم كراشوف مع زيادة نسبة القطر الداخلي الى الخارجي.
أجرت الباحثة **(Rafah 2002)** دراسة عملية لانتقال الحرارة بالحمل الحر لسطوح مستوية أفقية مربعة الشكل وجهها المسخن للأعلى لشرط ثبوت درجة الحرارة و ذات ثقب مربع الشكل نسبة الطول الداخلي تكافئ 0.25 من الطول الأصلي للمربع وكلاهما بطول خارجي 0.096m و سمك 0.0096m من الألمنيوم لمدى رقم كراشوف $0.5x10^{6}<Gr<6.28x10^{6}$ و لمدى من درجات الحرارة مقدارها $T_W=40,61,82.5,112.8C^{o}$ وجدت ان قيمة معامل انتقال الحرارة الموضعي للصفيحة المستوية المربعة تكون اكبر ما يمكن عند الحافة بسبب الانحدار الكبير في توزيع درجة الحرارة الناتجة عن جريان الطبقة المتاخمة في تلك المنطقة، تقل القيمة عند الاقتراب من مركز الصفيحة نتيجة الانحدار القليل في توزيع درجة الحرارة الناتجة من الانفصال الحراري قرب المركز و ان قيمة متوسط معامل انتقال الحرارة للصفيحة المربعة ذات الثقب أعلى منه للصفيحة المربعة بنسبة 32.1% و سمك الطبقة المتاخمة يقل بزيادة رقم كراشوف ضمن المدى .

أجرى الباحث **(Hassan 2003)** دراسة نظرية عددية لإنتقال الحرارة بالحمل الحر من أقراص وحلقات مائلة بزوايا $\Phi=0^{o},30^{o},45^{o},60^{o},90^{o},120^{o},135^{o},150^{o}\&180^{o}$ عن المستوى الأفقي، وجهها المسخن الى الأعلى والى الأسفل لشرط ثبوت درجة الحرارة باستخدام طريقة الفروقات المحددة لحل المعادلات الحاكمة، النتائج العددية التي حصل عليها ضمن حدود رقم كراشوف $10^{3}\leq Gr\leq 5x10^{4}$ مع رقم براندتل $Pr=0.72$ و توصل إلى ان رقم نسلت الموضعي يعتمد كلياً على زاوية الميلان و متوسط رقم نسلت يتناسب مع رقم كراشوف للأس 1/5 في حالة الوضع الأفقي للقرص مسخن إلى الأعلى كما ان تأثير القطر الداخلي يسبب زيادة محددة في معدلات انتقال الحرارة في حالة الحلقات المسخنة إلى الأعلى بينما تكون أكثر تأثيراً في حالة الحلقات مسخنة إلى الأسفل. وبينت الدراسة ان متوسط رقم نسلت يزداد بزيادة كل من زاوية الميلان عن الأفق ونسبة القطر الداخلي إلى الخارجي للحلقات المائلة المسخنة إلى الأعلى وان أقصى قيمة لمتوسط رقم نسلت لا يعتمد على زاوية الميلان بل يكون تغيره معتمداً على نسبة القطر الداخلي إلى الخارجي لتلك الحلقات.
اهتم البحث الحالي نظرياً بدراسة عملية انتقال الحرارة بالحمل الحر الطباقي لصفيحة مربعة و أخرى ذات ثقب دائري و ذات أسطح امتداد (Extension surface) مسخنة بثبوت درجة حرارة السطح و في حالات مختلفة أفقية و عمودية و مائلة عن الافق بزوايا مختلفة ، حيث يكون الوجه المسخن نحو الأعلى عند الزوايا $0^{o}\leq\Phi<90^{o}$ و يكون الوجه المسخن نحو الأسفل عند الزوايا $90^{o}<\Phi\leq180^{o}$. يتم في هذا البحث حل المعادلات الحاكمة باستخدام الحل العددي الثلاثي الأبعاد وحساب كل من دالة نقل الدوامية و متجه الجهد الكامن و درجة حرارة السطح اللابعدية و إيجاد توزيع رقم نسلت الموضعي ومن ثم إيجاد قيمته المتوسطة بالاعتماد على الطول المميز للصفيحة و تم اختياره ليكون طول ضلع الصفيحة المربعة ، و دراسة تأثير منطقة الانفصال الحراري على معدل انتقال الحرارة وذلك للصفيحة المربعة و للصفيحة ذات الثقب الدائري و إيضاح الفرق بينهما .

المعادلات الحاكمة

لغرض دراسة مسألة انتقال الحرارة يجب ان نحصل أولا على معادلات حفظ الكتلة و الزخم و الطاقة للمائع القابل للأنضغاط **(Torrance 1985)** :

$$C.E. \qquad \frac{\partial\rho}{\partial t}+\nabla(\rho\vec{q})=0 \tag{1}$$

$$M.E. \qquad \rho\frac{D\vec{q}}{Dt}=\mu\nabla^{2}\vec{q}-\nabla P_{L}+\rho\vec{g} \tag{2}$$

$$E.E. \qquad \rho cp\frac{DT}{Dt}-\beta T\frac{DP}{Dt}=\nabla(k\nabla T)+\mu\phi+q'''_{gen} \tag{3}$$

حيث ان

$\frac{D}{Dt}=\frac{\partial}{\partial t}+\vec{q}.\nabla$: the substantial derivative, $\vec{q}=q(u,v.w)$:velocity vector, $\mu\phi$: viscous dissipation function, q'''_{gen} : heat generation , $\rho\vec{g}$: body force.

لغرض اشتقاق المعادلات الأساسية للمسألة قيد البحث ،استخدمت الفرضيات التالية : درجة الحرارة ثابتة لكل من السطح المستوي (T_W) و المحيط (T_∞)،جريان المائع طباقي و غير قابل للأنضغاط، لا يوجد توليد حرارة $q'''_{gen} = 0$ ، المائع خاضع لقوانين نيوتن ، خواص المائع ثابتة عدا خاصية الكثافة في حد قوة الطفو حيث الكثافة في هذا الحد هو الذي يسبب حركة المائع، اهمال دالة الانتشار $\mu\phi$ بسبب السرعة الصغيرة جدا للمائع ، اهمال المقدار $\frac{DP}{Dt}$ لأنه صغير جدا للغازات . ان الطول المميز للمسألة قيد الدراسة هو طول ضلع للصفيحة المربعة (H) ، ولغرض كتابة المتغيرات و المعادلات الاساسية للمسألة بصيغ لابعدية تعرف المقادير اللابعدية التالية كما في **(Hassan 2003)** والمصدر **(Chow,Wilely & Sons 1979)** .

الزمن	$\tau = t(\alpha / H^2)$	**الاحداثيات المتعامدة**	$X = x/H , Y = y/H , Z = z/H$
الضغط	$\mathrm{P} = (P/\rho_\infty)(H/\alpha)^2$	**السرعة**	$U = uH/\alpha , V = vH/\alpha , W = wH/\alpha$
درجة الحرارة	$\Theta = (T - T_\infty)/(T_W - T_\infty)$	**رقم كراشوف**	$Gr = g\beta(T_W - T_\infty)H^3 / \upsilon^2$
رقم براندتل	$\Pr = \upsilon / \alpha$	**رقم رالي**	$Ra = g\beta(T_W - T_\infty)H^3 / \alpha\upsilon$

باستخدام هذه المقادير اللا بعدية يمكن كتابة معادلات حفظ الكتلة و معادلات الزخم و معادلة الطاقة بالصيغة اللابعدية التالية :

$$C.E. \qquad \frac{\partial U}{\partial X} + \frac{\partial V}{\partial Y} + \frac{\partial W}{\partial Z} = 0 \tag{4}$$

$$\text{M.E In X-Component} \quad \frac{1}{\Pr}\left[\frac{\partial U}{\partial \tau} + U\frac{\partial U}{\partial X} + V\frac{\partial U}{\partial Y} + W\frac{\partial U}{\partial Z}\right] = Ra\sin(\Phi)\Theta - \frac{1}{\Pr}\frac{\partial P}{\partial X} + (\nabla^2 U) \tag{5}$$

$$\text{M.E In Y-Component} \quad \frac{1}{\Pr}\left[\frac{\partial V}{\partial \tau} + U\frac{\partial V}{\partial X} + V\frac{\partial V}{\partial Y} + W\frac{\partial V}{\partial Z}\right] = -\frac{1}{\Pr}\frac{\partial P}{\partial Y} + (\nabla^2 V) \tag{6}$$

$$\text{M.E In Z-Component} \quad \frac{1}{\Pr}\left[\frac{\partial W}{\partial \tau} + U\frac{\partial W}{\partial X} + V\frac{\partial W}{\partial Y} + W\frac{\partial W}{\partial Z}\right] = Ra\cos(\Phi)\Theta - \frac{1}{\Pr}\frac{\partial P}{\partial Z} + (\nabla^2 W) \tag{7}$$

$$\text{E.E.} \qquad \frac{\partial \Theta}{\partial \tau} + U\frac{\partial \Theta}{\partial X} + V\frac{\partial \Theta}{\partial Y} + W\frac{\partial \Theta}{\partial Z} = \nabla^2\Theta \tag{8}$$

معادلات نقل الدوامية و دالة متجه الجهد الكامن

إن المعادلات التي وضعت في الجزء السابق من البحث هي معادلات بدلالة المتغيرات $[U, V, W, P, \Theta]$ و التي تسمى المتغيرات الأساسية او المعتمدة و يمكن التخلص من حدود الضغط (P) عن طريق مفاضلة معادلات الزخم بشكل متعاكس و طرحها للحصول على معادلات تدعى معادلات نقل الدوامية(vorticity transport equation) :

$$\frac{1}{\Pr}\left[\frac{\partial \Omega_1}{\partial \tau} + U\frac{\partial \Omega_1}{\partial X} + V\frac{\partial \Omega_1}{\partial Y} + W\frac{\partial \Omega_1}{\partial Z} - \Omega_1\frac{\partial U}{\partial X} - \Omega_2\frac{\partial U}{\partial Y} - \Omega_3\frac{\partial U}{\partial Z}\right] =$$
$$Ra\frac{\partial \Theta}{\partial Y}\cos\Phi + \left[\frac{\partial^2 \Omega_1}{\partial X^2} + \frac{\partial^2 \Omega_1}{\partial Y^2} + \frac{\partial^2 \Omega_1}{\partial Z^2}\right] \tag{9}$$

$$\frac{1}{\Pr}\left[\frac{\partial \Omega_2}{\partial \tau} + U\frac{\partial \Omega_2}{\partial X} + V\frac{\partial \Omega_2}{\partial Y} + W\frac{\partial \Omega_2}{\partial Z} - \Omega_1\frac{\partial V}{\partial X} - \Omega_2\frac{\partial V}{\partial Y} - \Omega_3\frac{\partial V}{\partial Z}\right] =$$
$$Ra\left[\frac{\partial \Theta}{\partial Z}\sin\Phi - \frac{\partial \Theta}{\partial X}\cos\Phi\right] + \left[\frac{\partial^2 \Omega_2}{\partial X^2} + \frac{\partial^2 \Omega_2}{\partial Y^2} + \frac{\partial^2 \Omega_2}{\partial Z^2}\right] \tag{10}$$

$$\frac{1}{\Pr}\left[\frac{\partial \Omega_3}{\partial \tau} + U\frac{\partial \Omega_3}{\partial X} + V\frac{\partial \Omega_2}{\partial Y} + W\frac{\partial \Omega_3}{\partial Z} - \Omega_1\frac{\partial W}{\partial X} - \Omega_2\frac{\partial W}{\partial Y} - \Omega_3\frac{\partial W}{\partial Z}\right] =$$
$$Ra\left[-\frac{\partial \Theta}{\partial Y}\sin\Phi\right] + \left[\frac{\partial^2 \Omega_3}{\partial X^2} + \frac{\partial^2 \Omega_3}{\partial Y^2} + \frac{\partial^2 \Omega_3}{\partial Z^2}\right] \tag{11}$$

يمكن كتابة المعادلات أعلاه بالصيغة التالية:

$$\frac{1}{\Pr}\left[\frac{\partial\Omega}{\partial\tau}+(\vec{q}\cdot\nabla)\vec{\Omega}-(\vec{\Omega}\cdot\nabla)\vec{q}\right]=Ra\begin{bmatrix}\frac{\partial\Theta}{\partial Y}\cos\Phi\\ \frac{\partial\Theta}{\partial Z}\sin\Phi-\frac{\partial\Theta}{\partial X}\cos\Phi\\ -\frac{\partial\Theta}{\partial Y}\sin\Phi\end{bmatrix}+\nabla^2\vec{\Omega} \qquad (12)$$

حيث ان:

$$\Omega_1=\frac{\partial W}{\partial \mathrm{Y}}-\frac{\partial V}{\partial Z},\quad \Omega_2=\frac{\partial U}{\partial \mathrm{Z}}-\frac{\partial W}{\partial \mathrm{X}},\quad \Omega_3=\frac{\partial V}{\partial \mathrm{X}}-\frac{\partial U}{\partial \mathrm{Y}}$$

لحل المعادلات التفاضلية الجزئية بطريقة الفروقات المحددة قسمت منطقة الحسابات إلى عدد من المناطق المحددة وتعيين النقاط العقدية باستخدام الدليل (i) باتجاه المحور (x) و الدليل (j) باتجاه المحور (y) و الدليل (k) باتجاه المحور (z) و أعطت لكل عقدة الإحداثيات التالية **(Aziz & Hellums 1967)** :

$$;\quad R_n=R_n(i,j,k)=R\ (\mathrm{X}_i,\mathrm{Y}_j,\mathrm{Z}_k,t_n)\ \mathrm{X}_i=i\Delta\mathrm{X}\quad;\quad \mathrm{Y}_j=j\Delta\mathrm{Y}\quad;\quad \mathrm{Z}_k=k\Delta\mathrm{Z}\quad;\quad t_n=n\Delta t$$

$$\nabla_x R_n=\frac{R_n(i+1,j,k)-R_n(i-1,j,k)}{2(\Delta\mathrm{X})} \qquad (13)$$

$$\nabla_x^2 R_n=\frac{R_n(i+1,j,k)-2R_n(i,j,k)+R_n(i-1,j,k)}{(\Delta\mathrm{X})^2} \qquad (14)$$

و بالصيغة نفسها يمكن إيجاد كل من $\nabla_y,\nabla_y^2,\nabla_z,\nabla_z^2$

يمكن كتابة معادلة الطاقة (8) و معادلات نقل الدوامية (9)، (10) و(11) بالصورة التالية:

$$\frac{\partial\Theta}{\partial\tau}=\frac{\partial^2\Theta}{\partial\mathrm{X}^2}-U\frac{\partial\Theta}{\partial\mathrm{X}}+\frac{\partial^2\Theta}{\partial\mathrm{Y}^2}-V\frac{\partial\Theta}{\partial\mathrm{Y}}+\frac{\partial^2\Theta}{\partial Z^2}-W\frac{\partial\Theta}{\partial Z} \qquad (15)$$

$$\frac{\partial\Omega_1}{\partial\tau}=\Pr\frac{\partial^2\Omega_1}{\partial\mathrm{X}^2}-U\frac{\partial\Omega_1}{\partial\mathrm{X}}+\Pr\frac{\partial^2\Omega_1}{\partial\mathrm{Y}^2}-V\frac{\partial\Omega_1}{\partial\mathrm{Y}}+\Pr\frac{\partial^2\Omega_1}{\partial Z^2}-W\frac{\partial\Omega_1}{\partial Z}+S_1 \qquad (16)$$

$$S_1=\Pr Ra\left(\frac{\partial\Theta}{\partial\mathrm{Y}}\cos\Phi\right)+\Omega_1\frac{\partial U}{\partial\mathrm{X}}+\Omega_2\frac{\partial U}{\partial\mathrm{Y}}+\Omega_3\frac{\partial U}{\partial Z} \qquad (17)$$

$$\frac{\partial\Omega_2}{\partial\tau}=\Pr\frac{\partial^2\Omega_2}{\partial\mathrm{X}^2}-U\frac{\partial\Omega_2}{\partial\mathrm{X}}+\Pr\frac{\partial^2\Omega_2}{\partial\mathrm{Y}^2}-V\frac{\partial\Omega_2}{\partial\mathrm{Y}}+\Pr\frac{\partial^2\Omega_2}{\partial Z^2}-W\frac{\partial\Omega_2}{\partial Z}+S_2 \qquad (18)$$

$$S_2=\Pr Ra\left(\frac{\partial\Theta}{\partial Z}\sin\Phi-\frac{\partial\Theta}{\partial\mathrm{X}}\cos\Phi\right)+\Omega_1\frac{\partial V}{\partial\mathrm{X}}+\Omega_2\frac{\partial V}{\partial\mathrm{Y}}+\Omega_3\frac{\partial V}{\partial Z} \qquad (19)$$

$$\frac{\partial\Omega_3}{\partial\tau}=\Pr\frac{\partial^2\Omega_3}{\partial\mathrm{X}^2}-U\frac{\partial\Omega_3}{\partial\mathrm{X}}+\Pr\frac{\partial^2\Omega_3}{\partial\mathrm{Y}^2}-V\frac{\partial\Omega_3}{\partial\mathrm{Y}}+\Pr\frac{\partial^2\Omega_3}{\partial Z^2}-W\frac{\partial\Omega_3}{\partial Z}+S_3 \qquad (20)$$

$$S_3=\Pr Ra\left(-\frac{\partial\Theta}{\partial\mathrm{Y}}\sin\Phi\right)+\Omega_1\frac{\partial W}{\partial\mathrm{X}}+\Omega_2\frac{\partial W}{\partial\mathrm{Y}}+\Omega_3\frac{\partial W}{\partial Z} \qquad (21)$$

الشكل العام للمعادلات أعلاه يصاغ كالتالي :

$$\frac{\partial R}{\partial\tau}=(\delta_x+\delta_y+\delta_Z)R+S \qquad (22)$$

يمثل المتغير R كل من $\Theta,\Omega_1,\Omega_2,\Omega_3$

$$\delta_x=\frac{\partial^2}{\partial\mathrm{X}^2}-U\frac{\partial}{\partial\mathrm{X}}\ ,\ \delta_y=\frac{\partial^2}{\partial\mathrm{Y}^2}-V\frac{\partial}{\partial\mathrm{Y}}\ ,\ \delta_z=\frac{\partial^2}{\partial Z^2}-W\frac{\partial}{\partial Z}$$

و باستخدام طريقة (ADI method) تصبح المعادلة (22) بالصورة التالية :

$$(\delta_x-\frac{2}{\Delta\tau})R_{n+1}^{*}=-(\delta_x+2\delta_y+2\delta_z+\frac{2}{\Delta\tau})R_n-2S \qquad (23)$$

$$(\delta_y-\frac{2}{\Delta\tau})R_{n+1}^{**}=\delta_y R_n-\frac{2}{\Delta\tau}R_{n+1}^{*} \qquad (24)$$

$$(\delta_z-\frac{2}{\Delta\tau})R_{n+1}=\delta_z R_n-\frac{2}{\Delta\tau}R_{n+1}^{**} \qquad (25)$$

يتم اشتقاق معادلات متجه الجهد الكامن من معادلات نقل الدوامية في الملحق E ولحل معادلات Ψ يمكن استخدام طريقة فوق التراخي المتعاقب (Iterative successive over relaxation) عند أي خطوة زمنية كما في المصدر (1982) F.Geoola et al. ، اذ يتم تعويض قيمة متجه الجهد الكامن عند الفترة الزمنية $\tau+\Delta\tau$ لحساب القيمة الجديدة لمتجه الجهد الكامن . إذا كانت $\Psi^{n}_{(i,j,k)}$ هي القيمة عند أي نقطة فان بعد عدد من التكرارات مقداره (s) فان التكرار اللاحق يكون (s+1) . يمكن الحصول على مركبة X لمتجه الجهد الكامن بالشكل التالي :

$$\Psi^{n}_{1(i,j,k)}=\frac{1}{bb_1}[a_{x1}(\Psi^{n}_{1(i+1,j,k)}+\Psi^{n}_{1(i-1,j,k)})+a_{y1}(\Psi^{n}_{1(i,j+1,k)}+\Psi^{n}_{1(i,j-1,k)})+ \\ a_{z1}(\Psi^{n}_{1(i,j,k+1)}+\Psi^{n}_{1(i,j,k-1)})+\Omega^{n(s)}_{1(i,j,k)}] \qquad (26)$$

و ان مقدار التكرار او التعاقب w_{ψ}

يمكن ان يعرف :

$$(27)\quad \Psi^{n(s+1)}_{1(i,j,k)}=\Psi^{n(s)}_{1(i,j,k)}+w_{\psi}(\Psi^{n}_{1(i,j,k)}-\Psi^{n(s)}_{1(i,j,k)})$$

ان المقدار (s) يشير إلى عدد نقاط التكرار عند الخطوة الزمنية (n^{th}) و المقدار $\Psi^{n(s+1)}_{1(i,j,k)}$ يمثل قيمة Ψ_1 عند الخطوة الزمنية (n^{th}) بعد (s+1) من التكرار. ان قيمة $\Psi^{n(s+1)}_{1(i,j,k)}$ تعوض في المعادلة (26) بعد ذلك تحل مع المعادلة (27) حتى تحقق المقدار التقريبي التالي :

$$\sum(\Psi^{n(s+1)}_{1(i,j,k)}-\Psi^{n(s)}_{1(i,j,k)})\le\varepsilon_{\Psi} \qquad (28)$$

ان قيمة المقدار التقريبي في البحث الحالي $\varepsilon_{\Psi}=10^{-3}$ و يكون مقدار التكرار w_{ψ} ضمن حدود (1-2) فتم اختيار قيمته (1.75) بالتجربة و الخطأ .

و يمكن الحصول على مركبة Y لمتجه الجهد الكامن Ψ_2 كما يلي:

$$\Psi^{n}_{2(i,j,k)}=\frac{1}{bb_2}[a_{x2}(\Psi^{n}_{2(i+1,j,k)}+\Psi^{n}_{2(i-1,j,k)})+a_{y2}(\Psi^{n}_{2(i,j+1,k)}+\Psi^{n}_{2(i,j-1,k)})+ \\ a_{z2}(\Psi^{n}_{2(i,j,k+1)}+\Psi^{n}_{2(i,j,k-1)})+\Omega^{n(s)}_{2(i,j,k)}] \qquad \mathbf{(29)}$$

و مقدار التكرار كما يلي :

$$\Psi^{n(s+1)}_{2(i,j,k)}=\Psi^{n(s)}_{2(i,j,k)}+w_{\psi}(\Psi^{n}_{2(i,j,k)}-\Psi^{n(s)}_{2(i,j,k)}) \qquad (30)$$

ان قيمة $\Psi^{n(s+1)}_{2(i,j,k)}$ تعوض في المعادلة (29) ويحل مع المعادلة (30) حتى تحقق المقدار التقريبي التالي :

$$\sum(\Psi^{n(s+1)}_{2(i,j,k)}-\Psi^{n(s)}_{2(i,j,k)})\le\varepsilon_{\Psi} \qquad (31)$$

و مركبة Z لمتجه الجهد الكامن Ψ_3 كما يلي:

$$\Psi^{n}_{3(i,j,k)}=\frac{1}{bb_3}[a_{x3}(\Psi^{n}_{3(i+1,j,k)}+\Psi^{n}_{3(i-1,j,k)})+a_{y3}(\Psi^{n}_{3(i,j+1,k)}+\Psi^{n}_{3(i,j-1,k)})+ \\ a_{z3}(\Psi^{n}_{3(i,j,k+1)}+\Psi^{n}_{3(i,j,k-1)})+\Omega^{n(s)}_{3(i,j,k)}] \qquad (32)$$

و مقدار التكرار كما يلي :

$$\Psi^{n(s+1)}_{3(i,j,k)}=\Psi^{n(s)}_{3(i,j,k)}+w_{\psi}(\Psi^{n}_{3(i,j,k)}-\Psi^{n(s)}_{3(i,j,k)}) \qquad (33)$$

ان قيمة $\Psi^{n(s+1)}_{3(i,j,k)}$ تعوض في المعادلة (34) و تحل مع المعادلة (35) حتى تحقق المقدار التقريبي التالي :

$$\sum(\Psi^{n(s+1)}_{3(i,j,k)}-\Psi^{n(s)}_{3(i,j,k)})\le\varepsilon_{\Psi} \qquad (36)$$

الظروف الابتدائية و الحدية للمسألة

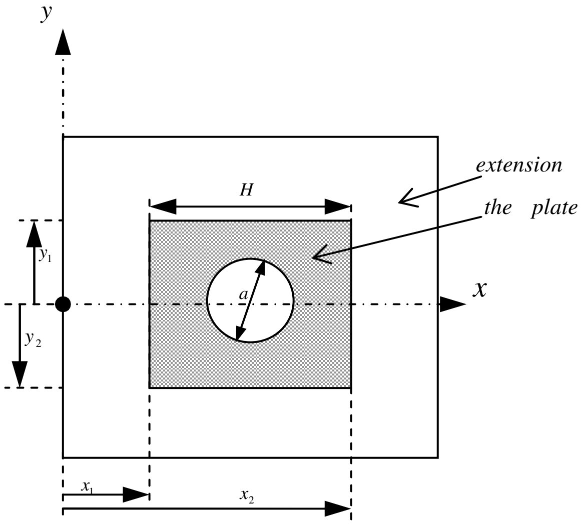

ان الظروف الابتدائية المستخدمة لحل كـل مـن معادلة درجة الحرارة و دالة نقل الدوامية و متجـه الجهد الكامن تؤخذ عند زمن τ=0 حيث ان :

$$\begin{bmatrix}\Theta=0\\ \Theta_W=1\end{bmatrix}\quad\begin{bmatrix}U=0\\ V=0\\ W=0\end{bmatrix}\begin{bmatrix}\Omega_1=0\\ \Omega_2=0\\ \Omega_3=0\end{bmatrix}\begin{bmatrix}\Psi_1=0\\ \Psi_2=0\\ \Psi_3=0\end{bmatrix}$$

اما الظروف الحدية للمسالة و لزمن τ>0 فانها موضحة كما موضح في الشكل (1)

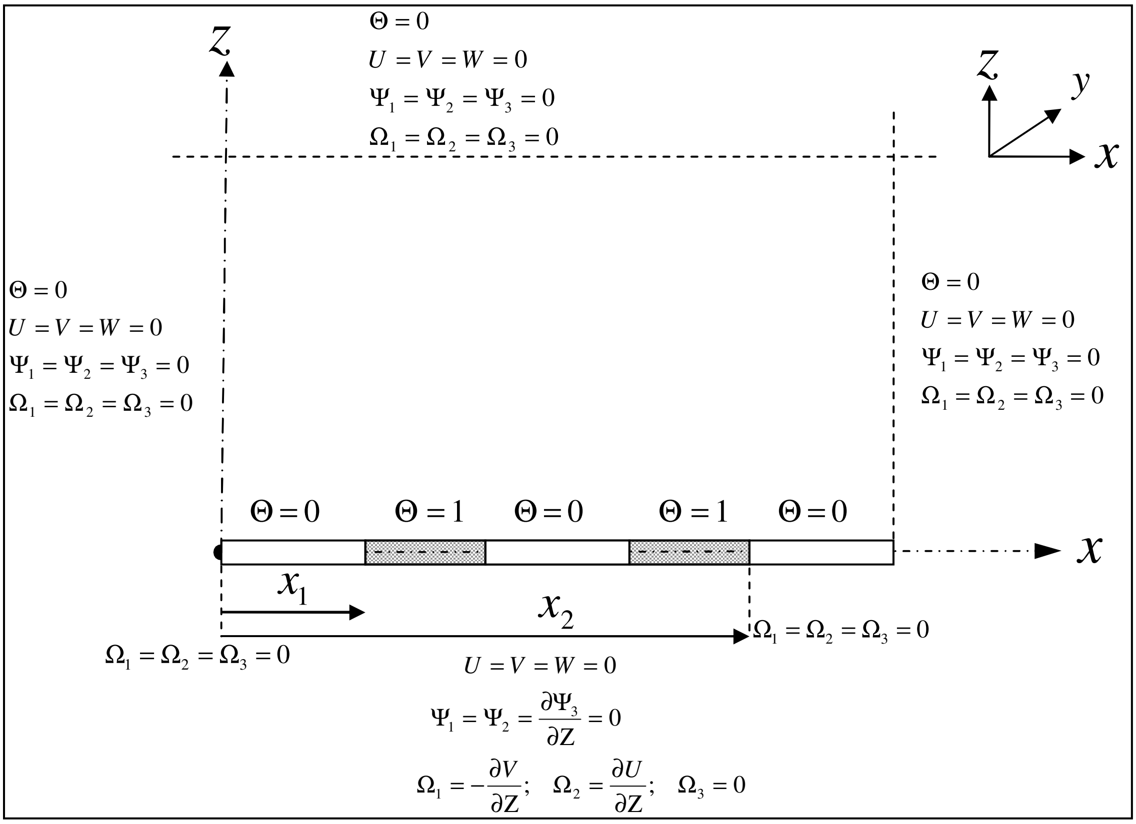

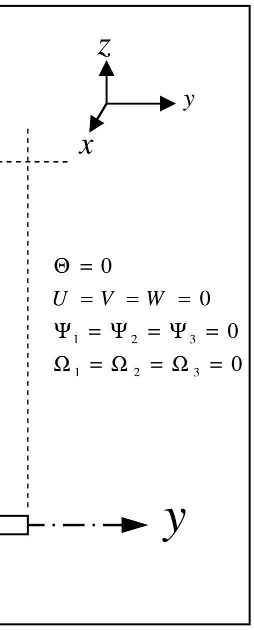

الشكل (1) االظروف الحدية للمسالة

النتائـج و المناقشـة

تـم التوصـل مـن خـلال النتـائج العدديــة الــى شـكل كـل مـن خطـوط ثبوت درجـة الحرارة و خطوط دالة نقل الدواميــة و متجـه الجهـد الكـامن اللابعديـة فـي حالـة التطـور و الاستقرار علـى سـطح الصفيحـة المربعـة و الصفيحـة ذات الثقب الـدائري بنسبتي تثقيـب 0.6و 0.8 لحالة التسخين لثبوت درجة الحرارة لمختلف زوايـا الميل $\Phi=0^o,30^o,60^o,90^o,120^o,150^o\&180^o$ كما في الشكل (2). و جميع النتائج العددية عند رقم براندتل $Pr=0.72$ و لمدى رقم كراشوف $10^3 \leq Gr \leq 5x10^4$.

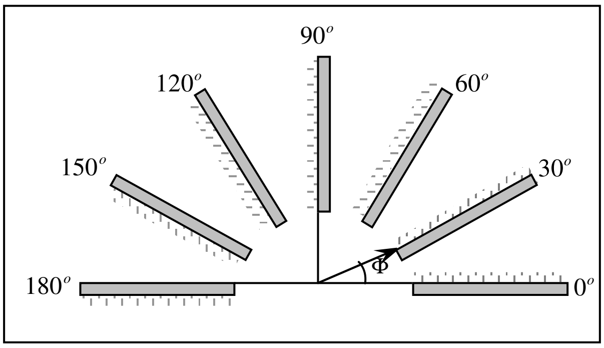

شكل(2) حالة تسخين الصفيحة لزوايا ميل مختلفة

تحديد حجم الشبكة العددية

استخدمت في الحل العددي شبكة منتظمة (Uniform grid) في الاتجاهات x، y و z . تم حسـاب النتائـج للصفيحة المربعـة ذات أسطح امتداد عند الحافة لها طول مساوي نصف طول الصفيحة ، البعد باتجاه المحور x يكون $X=2$ و تكون الحسابات لنصف الصفيحة باتجاه المحور y نظراً لوجود التناظر فيكون البعد $Y=1$. عدد النقاط العقدية باتجاه i تكون $m=21$ و عليه عـدد النقاط العقدية باتجاه j تكون $n=11$ ، (ان زيادة عدد النقاط العقدية يزيد من دقة الحل إلا انه في الوقت نفسه يزيد من زمن الوصول إلى حالة استقرار الحل العددي). و لمعرفة حجم الشبكة المناسب تم اختبار عدد من النقـاط العقدية للبعد العمـودي (اتجاه k) ولتكن ($l=11,21,31,41\&51$) كما مبينة في الشكل (3) . كما تم اختبار أربعة أبعاد عمودية للشبكة ولتكن ($Z=1,1.5,2,2.5$) مع الحفاظ على المسافة بين العقد (Grid spacing) متساوية و تكون في البحث الحالي ($\Delta Z = 0.05$) كما مبين في الشـكل (4). تم اختيار عدد النقاط العقدية باتجاه k وهي $l=41$ لان نسبة الخطأ لمتوسط رقم نسلت تقل بزيادة عدد العقد و تكون حوالي (% 1.66) بين العقدة 41 و 51 كما في الشكل (3)اما البعد العمودي فيكون $Z=2$ حيث نلاحظ من الشكل (4) ان اقل نسبة خطأ لمتوسط رقم نسلت تكون بين الارتفاع 2 و الارتفاع 2.5 و مقداره (% 0.00017) . و بذلك يكون حجم شبكة الحل العـددي ($X,Z =2$ & $Y =1$) لجميع الحـالات و عـدد النقـاط العقديــة المستخدمــة فـي الحـل (21x11x41) . وتـم تحديد أقصـى قيمـة للخطـوة الزمنيـة ($\Delta\tau max=0.000667$) والتي عندها يحقق الاستقرار للحل العددي بتشغيل البرنامج لمرات عدة وبقيم مختلفة من الخطوة الزمنية وتعاد العملية لقيم مختلفة من رقم كراشوف .

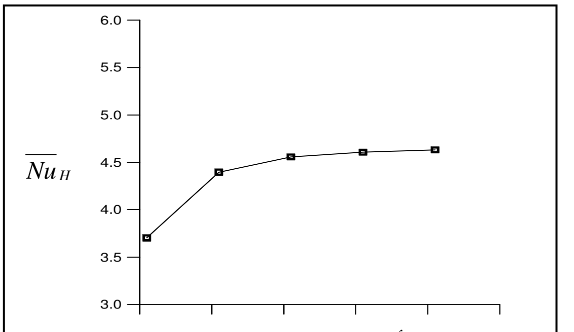

شكل (3) تأثير عدد العقد باتجاه الإحداثي Z على متوسط رقم نسلت لرقم كراشوف $Gr=10^4$.

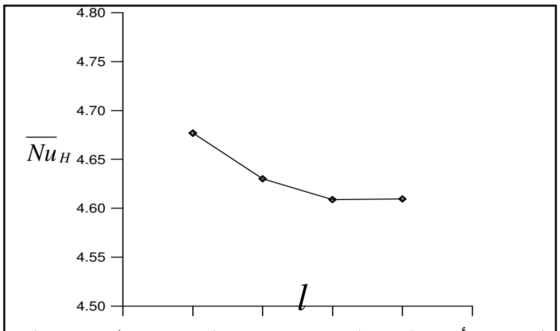

شكل (4) تأثير البعد العمودي Z على متوسط رقم نسلت عندما $\Delta Z= 0.05$ لرقم كراشوف $Gr=10^4$.

الصفيحة المربعة

الشكل (5) يبين حالة الاستقرار لخطوط ثبوت درجة الحرارة اللابعدية لرقم كراشوف 10^3 و النمط المهيمن لانتقال الحرارة يتمثل بالتوصيل R.F.Boehm & D.Kamyab(1977)، و يلاحظ انحراف الخطوط قليلاً عن المركز نحو الحافة العليا للصفيحة المائلة . و بزيادة رقم كراشوف يظهر تأثير الحمل واضحاً و تتكون الريشة (Plume) (حدوث الانفصال الحراري) حيث ترتفع جزيئات المائع الساخنة الأقل الكثافة لتحل محلها جزيئات المائع الباردة الأكثر الكثافة و القادمة من منطقة الاستطالة لرقم كراشوف 10^4 . و نظراً لهبوط الجزيئات المرتفعة يحدث ضغط على خطوط ثبوت درجة الحرارة اللابعدية في منطقة تكون الريشة ليحدث تخصر فيها و هذا واضح لرقم كراشوف $5x10^4$ ، حيث جزيئات المائع عند المركز تمتلك أعلى درجة حرارة على السطح فتكون كثافتها اقل من الجزيئات المجاورة فترتفع بسرعة اكبر محدثة تخلخل في الضغط عند المركز فتندفع الجزيئات المجاورة لتحل محلها بحركة أفقية فيزداد بذلك سمك الطبقة المتاخمة الحرارية بزيادة رقم كراشوف للصفيحة الأفقية المسخنة إلى الأعلى .

إن تأثير زاوية إمالة الصفيحة واضح على خطوط ثبوت درجة الحرارة اللابعدية في حالة الاستقرار لرقمي كراشوف 10^4 و $5x10^4$ حيث يحدث الانفصال الحراري فوق الحافة العليا للصفيحة المائلة و تنضغط الخطوط لتقترب من سطح الصفيحة المائلة بزيادة زاوية الميل و تنضغط اكثر بزيادة رقم كراشوف ، سمك الطبقة المتاخمة الحرارية يقل بزيادة رقم كراشوف للصفيحة المائلة. تكون خطوط ثبوت درجة الحرارة اللابعدية فوق الصفيحة الأفقية وجهها المسخن إلى الأسفل اقل ارتفاعاً من تلك فوق الصفيحة الأفقية وجهها المسخن إلى الأعلى لان حركة الجزيئات الساخنة القليلة الكثافة تكون قريبة إلى سطح الصفيحة المسخنة إلى الأسفل فلا يحدث الانفصال الحراري انظر الشكل (5) .

حالة استقرار خطوط ثبوت دالة الدوامية Ω_1 و Ω_2 لرقم كراشوف 10^3 مبينة في الشكل (6) و نلاحظ انتشار خطوط دالة الدوامية بالتناظر فوق الصفيحة الأفقية في المستويين Z-X و Z-Y ولكن في حالة الصفيحة المائلة وجهها المسخن إلى الأعلى فان قيم دالة الدوامية Ω_1 في المستوي Z-Y تقل حيث تختفي الدوامة السالبة بالتدريج لتحل محلها الدوامة الموجبة مع وصول زاوية الميل90^o لان جزيئات المائع الساخنة القليلة الكثافة ترتفع من فوق حافة الصفيحة ليحدث تخلخل في الضغط فتدخل جزيئات المائع الباردة الى وسط الصفيحة لتحل محلها. أما في المستوي Z-X فان صفة الانتشار هي الغالبة على دالة الدوامية .

و يلاحظ زيادة في شدة الدوامية و أيضاً زيادة في ارتفاعها بسبب زيادة سرعة المائع الساخن (زيادة قوة الطفو) و يزداد ارتفاع الدوامات عند زيادة رقم كراشوف $5x10^4$ مع ظهور دوامات متعددة في الطبقات العليا البعيدة عن سطح الصفيحة الأفقية وجهها المسخن إلى الأعلى و اندفاع خطوط ثبوت دالة الدوامية باتجاه المائع الساخن لحالة الصفيحة المائلة و زيادة في شدتها بسبب زيادة سرعة المائع .

الشكل (7) يبين حالة استقرار متجه الجهد الكامن لرقم كراشوف 10^3 نلاحظ الارتفاع البسيط في قيم متجه الجهد الكامن و تناظر انتشار الخطوط و ابتعاد مركز الحركة عن سطح الصفيحة الأفقية . بزيادة رقم كراشوف إلى 10^4 ترتفع قيم متجه الجهد الكامن بمقدار خمس مرات عن قيم متجه الجهد الكامن لرقم كراشوف 10^3 و تتقارب الخطوط في منطقة الريشة ،لان المائع المسحوب من فوق الاستطالة لا يستمر بالدخول إلى وسط الصفيحة بل يبدأ بالارتفاع قبل أن يصل إلى مركز الريشة (زيادة قوة الطفو بسبب زيادة رقم كراشوف) . عند إمالة الصفيحة تقل قيم متجه الجهد الكامن Ψ_1 مقارنة مع الصفيحة الأفقية وجهها المسخن الى الأعلى . تزداد قيم متجه الجهد الكامن Ψ_2 فوق الصفيحة المائلة وجهها المسخن الى الأعلى ، بزيادة زاوية الميلان يقترب مركز الحركة من سطح الصفيحة مع زيادة في كثافة الخطوط قرب سطح الصفيحة و فوق الاستطالة وصولاً للصفيحة وجهها المسخن الى الأسفل حيث يكون مركز الحركة فوق الاستطالة و قيم متجه الجهد الكامن Ψ_2 تكون اقل . ان قيمة متجه الجهد الكامن لرقم كراشوف $5x10^4$ تزداد مع تقارب اكثر للخطوط في منطقة الريشة و في الطبقة العليا البعيدة عن الصفيحة الأفقية المسخنة إلى الأعلى لارتفاع جزيئات المائع الساخنة بسرعة عالية وانحدار جزيئات المائع الباردة بسرعة عالية إلى الأسفل من جهة الاستطالة.

الصفيحة المثقبة

الشكل (8) يبين حالة استقرار درجات الحرارة اللابعدية و خطوط دالة نقل الدوامية و متجه الجهد الكامن، نلاحظ زيادة في انحدار درجات الحرارة اللابعدية على السطح المسخن و يظهر ارتفاع للريشة فوق منتصف الصفيحة المثقبة الأفقية المسخنة إلى

الأعلى حيث اكبر قوة طفو و يكون الانحدار اكبر عند الحافة الخارجية لكبر محيط الصفيحة الخارجي. و بزيادة نسبة التثقيب يزداد الانحدار فوق سطح الصفيحة كما يلاحظ نقصان في سمك الطبقة المتاخمة فوق الحافة الخارجية للصفيحة المثقبة بزيادة زاوية الميلان.و من ملاحظة خطوط دالة نقل الدوامية Ω_1 و Ω_2 للصفيحة المثقبة بنسبة تثقيب 0.6 نجد ان مركز الدوامات اقل شدة من الدوامات فوق الصفيحة المربعة و تقل أيضاً بشكل بسيط بزيادة نسبة التثقيب كما يلاحظ كثافة في خطوط متجه الجهد الكامن Ψ_1 و Ψ_2 قرب أسطح التبادل الحراري للصفيحة المثقبة بنسبة تثقيب 0.6 و 0.8 بسبب زيادة سرعة المائع لزيادة قوة الطفو.

رقم نسلت الموضعي

الشكل (9) يوضح تغير رقم نسلت الموضعي بزيادة زاوية الميل و زيادة رقم كراشوف عند خط التناظر، و نلاحظ ان رقم نسلت الموضعي يكون اكبر ما يمكن عند حافتي الصفيحة الأفقية حيث الانحدار الكبير في درجة الحرارة (سمك الطبقة المتاخمة قليل) وعند الاقتراب من المركز نجد توزيع درجة الحرارة اللابعدية يتغير نتيجة للانفصال الحراري الذي يحدث بالقرب من المركز مما يؤدي إلى انحدار قليل في درجة الحرارة اللابعدية عند سطح الصفيحة الأفقية و المسبب في انحدار معامل انتقال الحرارة الموضعي. و للصفيحة المثقبة نلاحظ ارتفاع قيمة رقم نسلت الموضعي بزيادة نسبة التثقيب. إن قيمة نسلت الموضعي عند الحافات الداخلية للصفيحة الأفقية المسخنة إلى الأعلى تكون اقل من الحافات الخارجية بسبب جريان الطبقة المتاخمة الحرارية عند الحافات الخارجية و الذي ينتج عنه انحدار كبير في درجة الحرارة و يزداد الفرق بينهما بزيادة رقم كراشوف .عند مقارنة قيم رقم نسلت الموضعي للصفيحة المربعة المثقبة و الصفيحة المربعة نجد إنها أعلى للصفيحة المثقبة و ترتفع بزيادة نسبة التثقيب و نلاحظ أيضاً ان الصفيحة العمودية تملك أعلى قيم لرقم نسلت الموضعي .

يمكن كتابة معادلة رقم نسلت الموضعي بالقيم اللابعدية :

$$Nu_H = -\left.\frac{\partial\Theta}{\partial Z}\right|_{z=0} \qquad (37)$$

و تحل المعادلة (37) بطريقة الفروقات المحددة الأمامية لأربع نقاط :

$$Nu_H = \frac{1}{(6\Delta Z)}(11\Theta_{(i,j,1)} - 18\Theta_{(i,j,2)} + 9\Theta_{(i,j,3)} - 2\Theta_{(i,j,4)}) \qquad (38)$$

العلاقة الرياضية بين متوسط رقم نسلت و رقم رالي

نحصل على متوسط رقم نسلت للصفيحة المربعة من تكامل معادلة رقم نسلت الموضعي كما يلي :

$$(39)\ \overline{Nu}_H = \frac{1}{A}\int_A Nu_H\, dA = \frac{1}{\left(1-\frac{\pi}{4}\ r^2\right)}\int_0^H\int_0^H -\frac{\partial\Theta}{\partial \mathrm{Z}}\ d\mathrm{X}\ \ d\mathrm{Y}$$

ان التكامل أعلاه يمكن ان يُنفّذ باستخدام التكامل العددي بالقاعدة الرباعية (trapezoidal rule) كما في المصدر(**Gerald 1970**) .

يمكن تمثيل متوسط رقم نسلت مع رقم رالي للصفيحة المربعة و الصفيحة المثقبة لمختلف زوايا الميلان بالمعادلة التالية : $\overline{Nu}_H = c_1 Ra^b$ حيث ان c_1 ثابت تعتمد قيمته على زاوية الميل للصفيحة و الثابت b هو أس رقم رالي و قيمته 0.2 ، و قيمة الثابت c_1 مبينة في الجدول (1) و نلاحظ ان أعلى قيمة للثابت c_1 يكون عند الوضع العمودي و تقل وصلاً إلى الوضع الأفقي. و تم استنتاج علاقة يعتمد فيها متوسط رقم نسلت على رقم رالي مرفوع إلى الأس b=0.25 للصفيحة المائلة في حالتي التسخين إلى الأعلى و إلى الأسفل و حسب المعادلة التالية : $\overline{Nu}_H = c_2(Ra\ \sin\ \Phi)^b$ ان الثابت c_2 في علاقات الصفيحة المثقبة يكون أعلى من الصفيحة المربعة و يزداد بزيادة نسبة التثقيب . قيم الثابت c_2 مبينة في الشكل (10) .و تم ايجاد علاقة متوسط رقم نسلت مع رقم رالي للصفيحة المربعة و للصفيحة المثقبة في حالتي التسخين إلى الأعلى و إلى الأسفل لزوايا الميل المختلفة بتأثير نسبة التثقيب r و حسب المعادلة التالية : $\overline{Nu}_H = (c_2 + c_3 r)(Ra\sin\Phi)^b$

للصفيحة المسخنة الى الاعلى : $\overline{Nu}_H = (0.597 + 0.413r)(Ra\sin\Phi)^{0.25}$

للصفيحة المسخنة الى الاسفل : $\overline{Nu}_H = (0.604 + 0.423r)(Ra\sin\Phi)^{0.25}$

جدول (1) يبين قيم الثابت c_1

زاوية الميل	للصفيحة المربعة	للصفيحة المربعة ذات الثقب الدائري 0.6	للصفيحة المربعة ذات الثقب الدائري 0.8
0^o	0.784	1.012	1.230
30^o	0.837	1.117	1.369
60^o	0.924	1.231	1.498
90^o	0.962	1.277	1.553
120^o	0.935	1.246	1.521
150^o	0.856	1.158	1.429
180^o	0.780	1.085	1.361

تأثير نسبة التثقيب (r) على متوسط رقم نسلت

الشكل (11) يوضح تغير متوسط رقم نسلت مع نسبة التثقيب ولحالات الميل المختلفة لرقمي كراشوف 10^4 و $5x10^4$ ، نلاحظ في الأشكال زيادة قيمة متوسط رقم نسلت بزيادة نسبة التثقيب وذلك لان بوجود الثقب يتم التخلص من منطقة الانفصال الحراري التي تتكون عند مركز الصفيحة المربعة و يتم الاقتراب إلى جريان الطبقة المتاخمة عند حافات الصفيحة التي تؤدي إلى زيادة متوسط رقم نسلت . و بزيادة زاوية الميلان للصفيحة المربعة و المثقبة تزداد قيمة متوسط رقم نسلت في حالة التسخين إلى الأعلى و يصل إلى أعظم قيمة له عند الوضع العمودي و يقل متوسط رقم نسلت بزيادة زاوية الميلان في حالة التسخين إلى الأسفل . نلاحظ ان قيم متوسط رقم نسلت تكون أعلى للصفيحة المائلة المثقبة في حالة التسخين إلى الأسفل لكون منطقة الانفصال صغيرة جداً وتختفي عند الزاوية 180^o.

تأثير نسبة التثقيب (r) على معدل انتقال الحرارة اللابعدية الكلي

الشكل (12) يبين معدل انتقال الحرارة اللابعدية الكلي لرقمي كراشوف10^4 و $5x10^4$ مع نسبة التثقيب ، يلاحظ إن أقصى كمية حرارة منتقلة تكون عند نسبة التثقيب r=0.6 لزوايا الميل المختلفة و تقل عند نسبة التثقيب 0.8 بالرغم من الزيادة في متوسط رقم نسلت و ذلك بسبب النقصان في مساحة الصفيحة و ان هناك تساوٍ لكمية الحرارة المنتقلة عند زاويتي الميل 30^o و 180^o لنسبة التثقيب 0.6 . بزيادة رقم كراشوف يزداد تأثير الانفصال الحراري حيث يلاحظ تأثير زيادة رقم كراشوف $5x10^4$ على كمية الحرارة المنتقلة من الصفيحة المربعة اذ تقل بزيادة نسبة التثقيب بخلاف الزاوية 180^o حيث تكون أقصى كمية حرارة منتقلة عند نسبة التثقيب r=0.6 . ان أقصى قيمة لانتقال الحرارة من الصفيحة المربعة أو المثقبة عند الوضع العمودي .

مقارنة نتائج البحث الحالي مع نتائج بحوث سابقة

شكل (13) يبين مقارنة متوسط رقم نسلت للبحث الحالي مع الدراسة العددية و العملية لكل من R.J.Goldstein & Kei-Shun Lau,1983 و الدراسة العملية للباحثة Rafah Aziz , 2002 للصفيحة الأفقية وجهها المسخن إلى الأعلى حيث يلاحظ ارتفاع قيم متوسط رقم نسلت للبحث الحالي عن الباحثان R.J.Goldstein & Kei-Shun Lau,1983 بنسبة فارق اقل من 6% للنتائج العملية و بنسبة لا تتجاوز 20% للنتائج العددية و يعود ذلك لدراسة الباحثان عملية انتقال الحرارة بالكتلة باستخدام صفيحة مربعة بدون أسطح امتداد . والشكل (14) يبين مقارنة متوسط رقم نسلت للبحث الحالي لصفيحة مربعة وجهها المسخن إلى الأسفل مع الباحثان R.J.Goldstein & Kei-Shun Lau,1983 حيث ترتفع قيم متوسط رقم نسلت بنسبة 33% .

الشكل (15) يبين مقارنة متوسط رقم نسلت للصفيحة المربعة الأفقية المثقبة بنسبة تثقيب r=0.6 مع الدراسة العددية للباحث Ahmad W.Mustafa, 2001 و الباحث Ayad K.Hassan , 2003 لحلقة أفقية وجهها المسخن إلى الأعلى. قورن البحث الحالي مع الدراسة العددية لحلقة مائلة للباحث Ayad K.Hassan , 2003 لحالة التسخين إلى الأعلى (كما مبين في الشكل (16)) وجد ان الفارق بين النتائج لم يتجاوز 11% .

الاستنتاجات

من النتائج العددية التي تم الحصول عليها من الحل العددي لكل من الصفيحة المربعة و الصفيحة ذات الثقب الدائري تم التوصل إلى الاستنتاجات التالية :

1. قيم متوسط رقم نسلت للصفيحة المثقبة أعلى من القيم في حالة الصفيحة المربعة وتزداد بزيادة نسبة التثقيب.
2. اكبر قيمة لرقم نسلت الموضعي تكون عند الحافة السفلى للصفيحة المربعة المائلة بزاوية 60^o و 90^o .
3. تزداد قيم متوسط رقم نسلت بزيادة زاوية ميل الصفيحة المربعة وجهها المسخن إلى الأعلى لتصل إلى أقصى قيمة لها عند الوضع العمودي وبعدها تقل بزيادة ميلان الصفيحة .

4. أقصى قيمة لمعدل انتقال الحرارة الكلي يكون للصفيحة المثقبة بنسبة تثقيب 0.6 لرقم كراشوف 10^4 ولزوايا ميل مختلفة و بزيادة رقم كراشوف إلى $5x10^4$ يقل معدل انتقال الحرارة ما عدا الصفيحة المربعة الأفقية وجهها المسخن إلى الأسفل حيث يكون أقصى قيمة عند نسبة تثقيب 0.6 .
5. يتساوى معدل انتقال الحرارة الكلي من الصفيحة المائلة عند الزاويتين 30^o و180^o المثقبة بنسبة تثقيب 0.6 لرقم كراشوف 10^4 .
6. توافق جيد بين النتائج العددية للبحث الحالي مع البحوث السابقة.

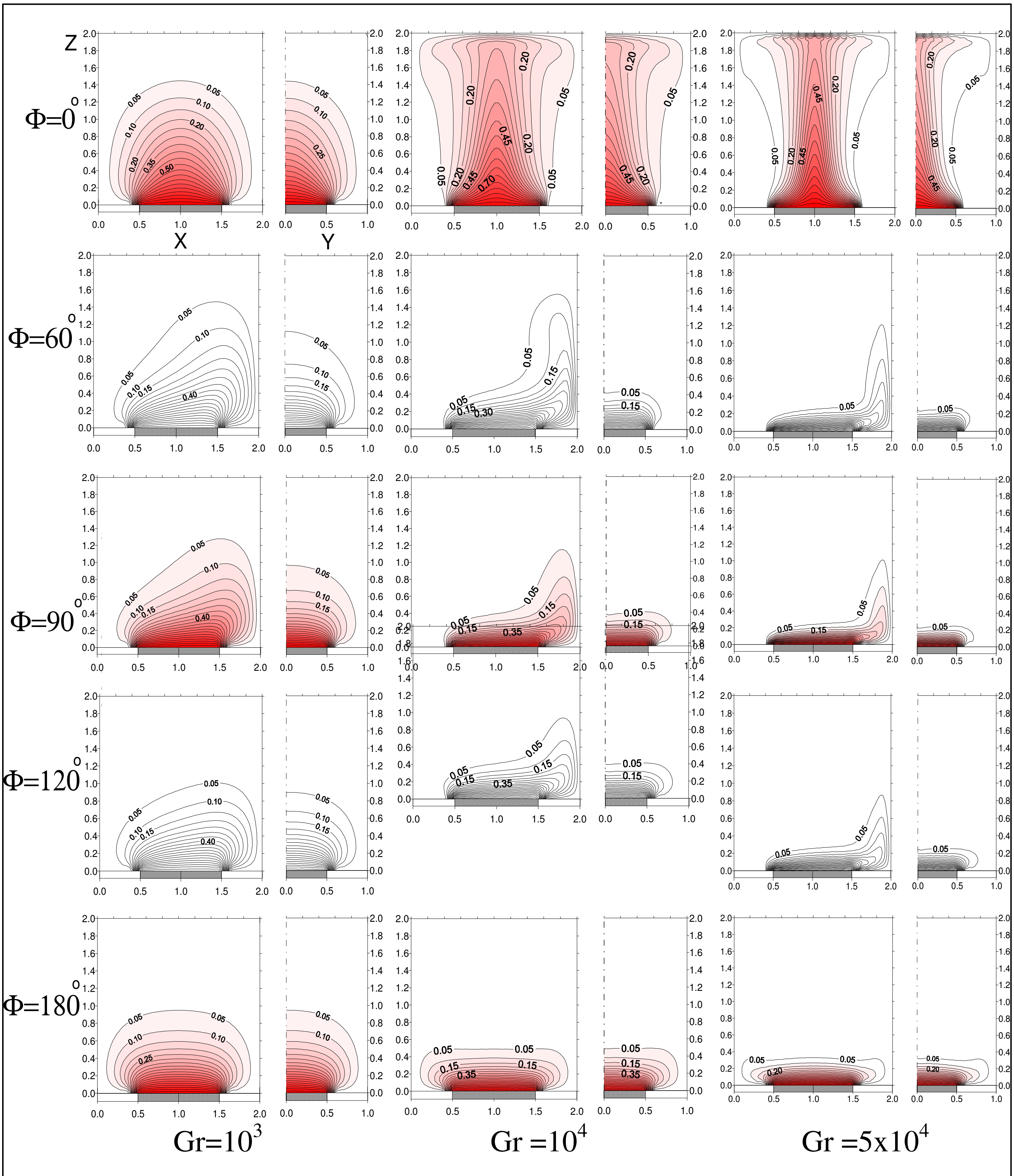

شكل (5) حالـــة الاستقرار لخطوط ثبوت درجـــة الحرارة اللابعدية لرقم كراشوف 10^3 ، 10^4 و $5x10^4$

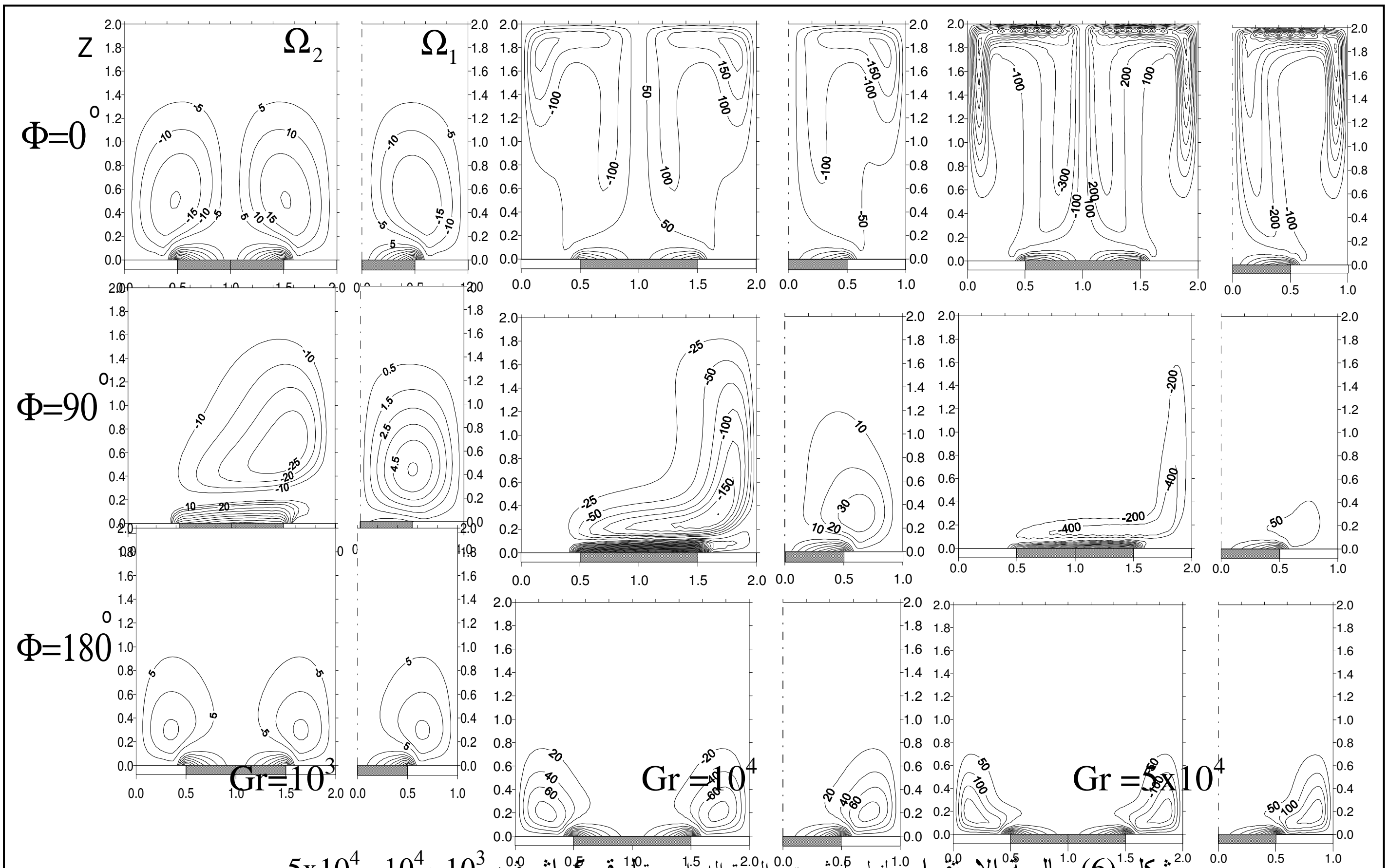

شكل (6) حالـــة الاستقرار لخطوط ثبوت دالـــة الدواميـــة لرقم كراشوف 10^3 ، 10^4 و $5x10^4$.

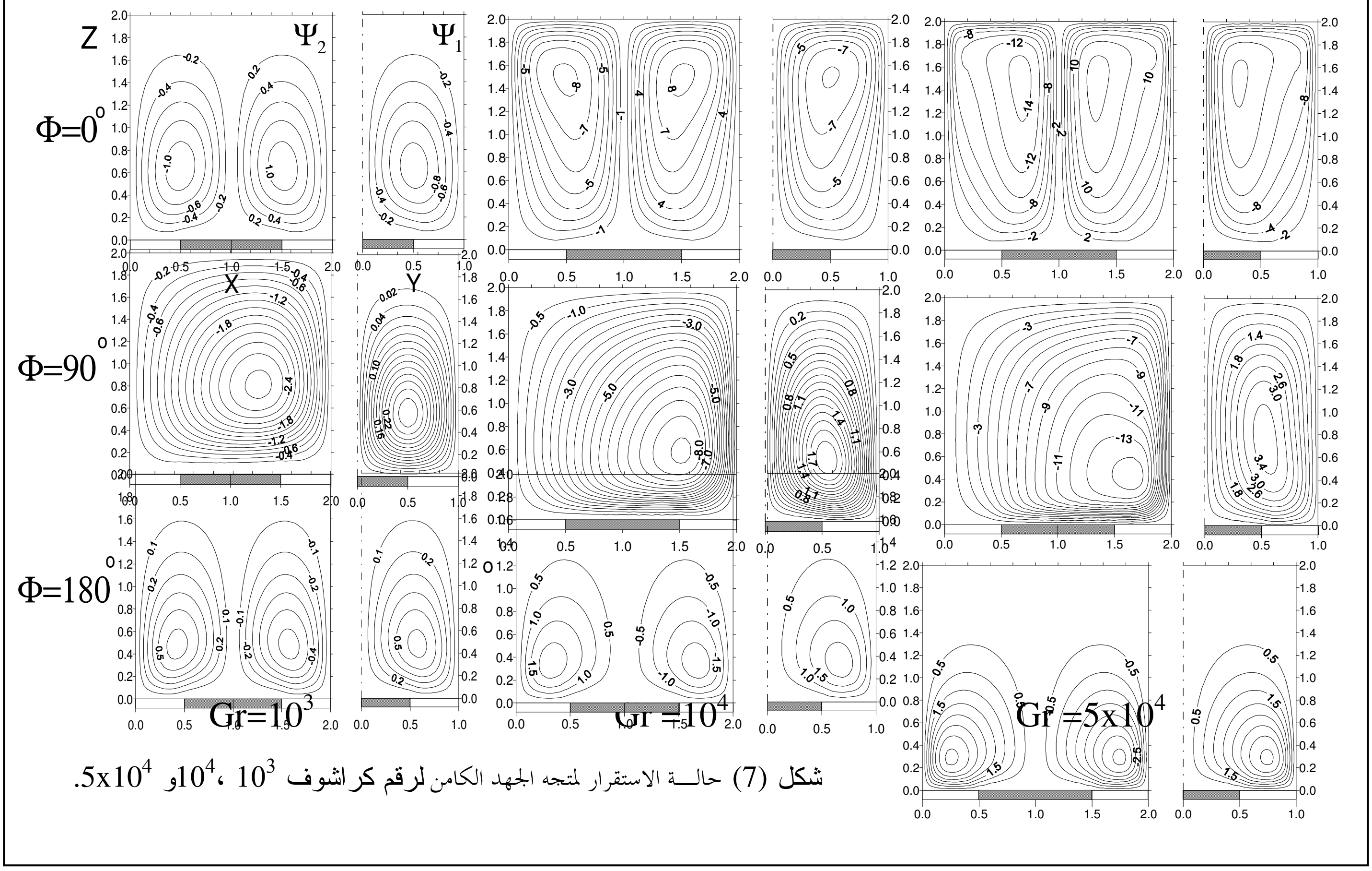

شكل (7) حالـــة الاستقرار لمتجه الجهد الكامن لرقم كراشوف 10^3 ، 10^4 و $5x10^4$.

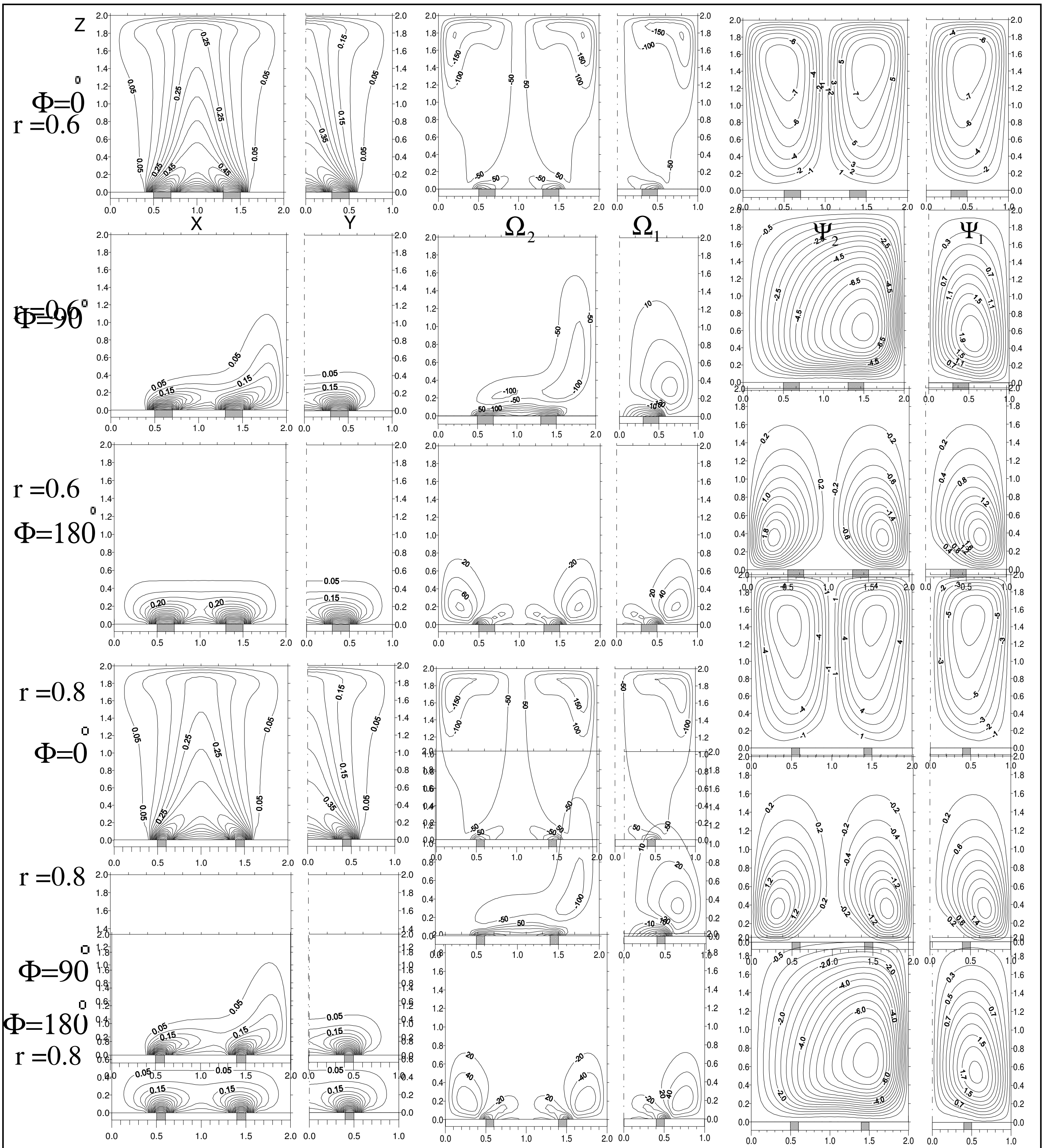

شكل (8) حالـــة الاستقرار لخطوط ثبوت درجـــة الحرارة اللابعدية و لدالة نقل الدواميةو لمتجه الجهد الكامن لرقم كراشوف 10^4 للصفيحة المثقبة بنسبتي تثقيب 0.6 و 0.8

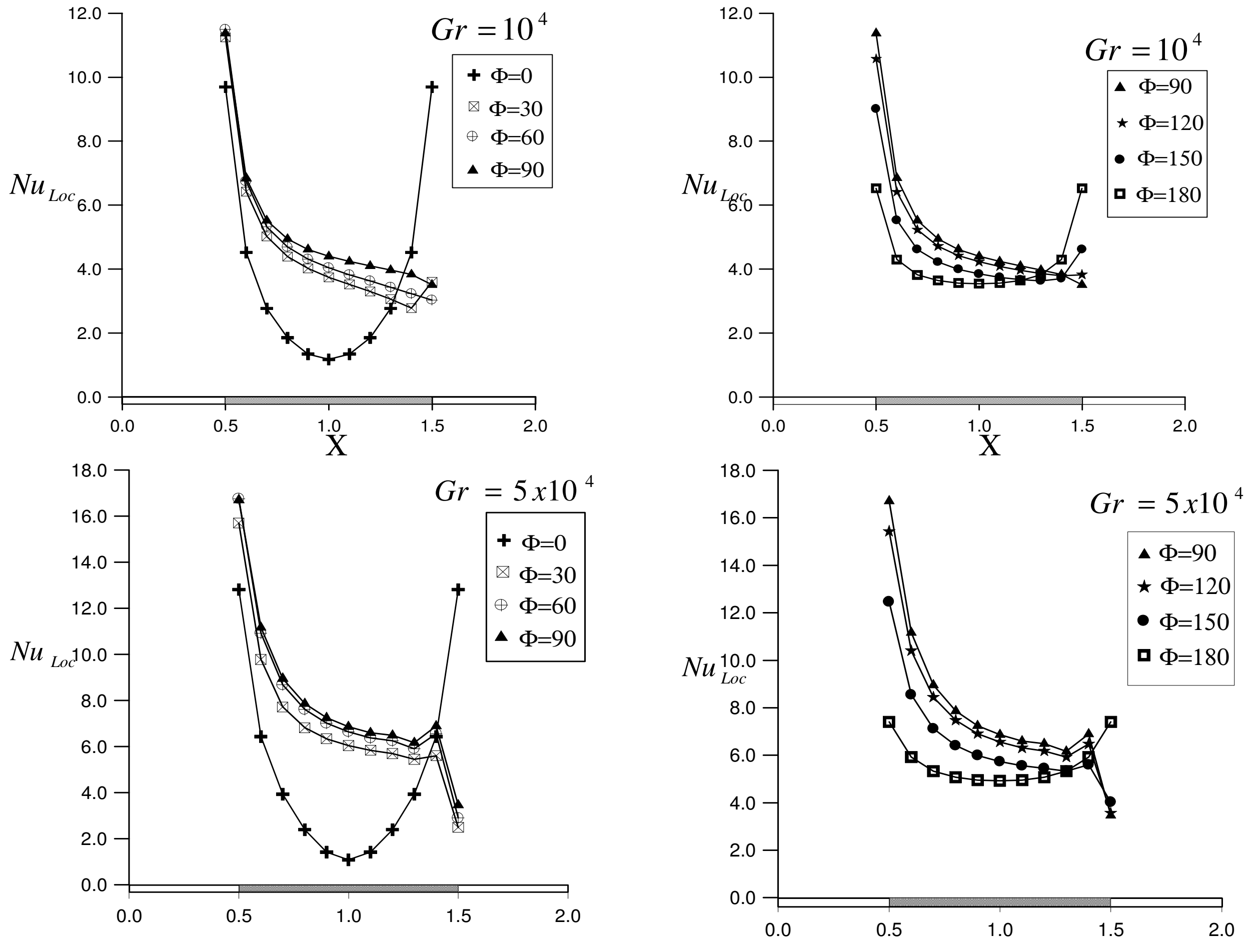

للصفيحة المربعة

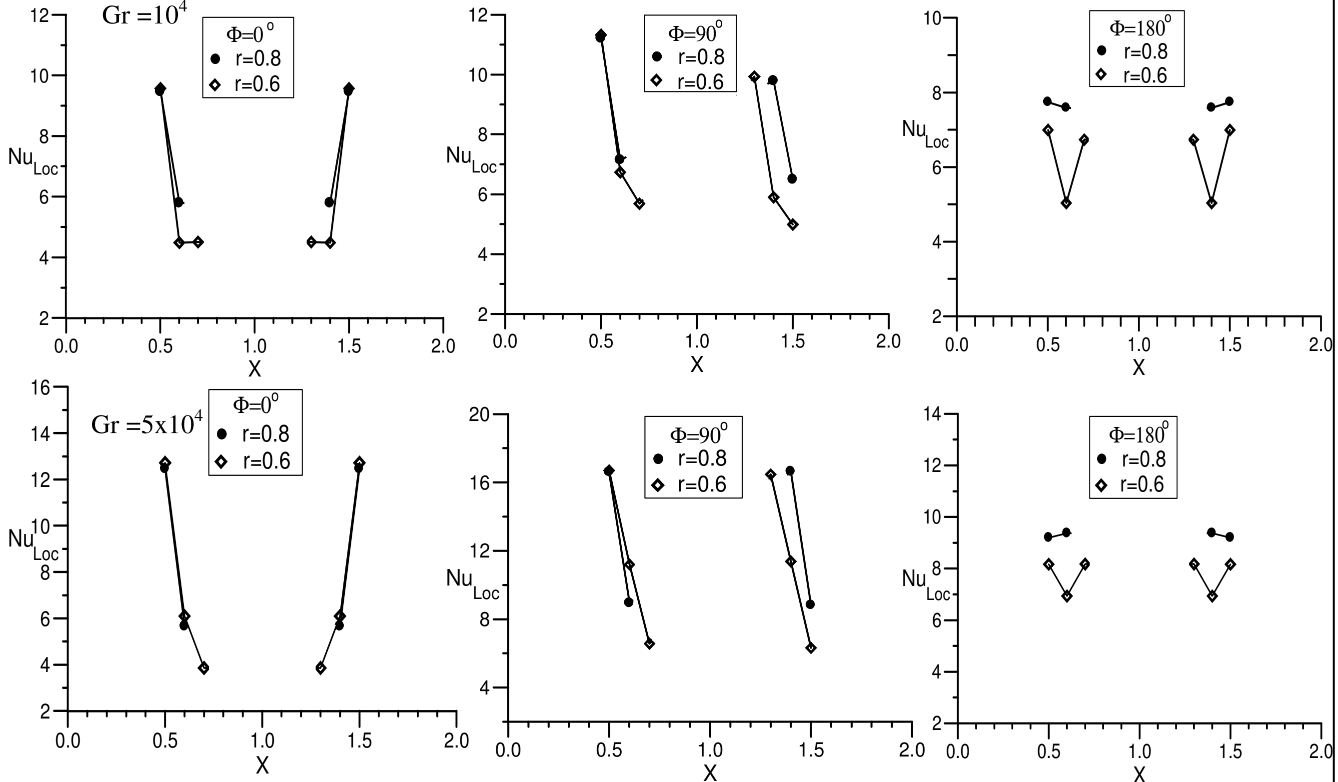

للصفيحة المثقبة

كل (9) رقم نسلت الموضعي للصفيحة المربعة و الصفيحة ذات الثقب الدائري بنسبتي تثقيب 0.6 و 0.8 لرقم كراشوف 10^4 و $5x10^4$

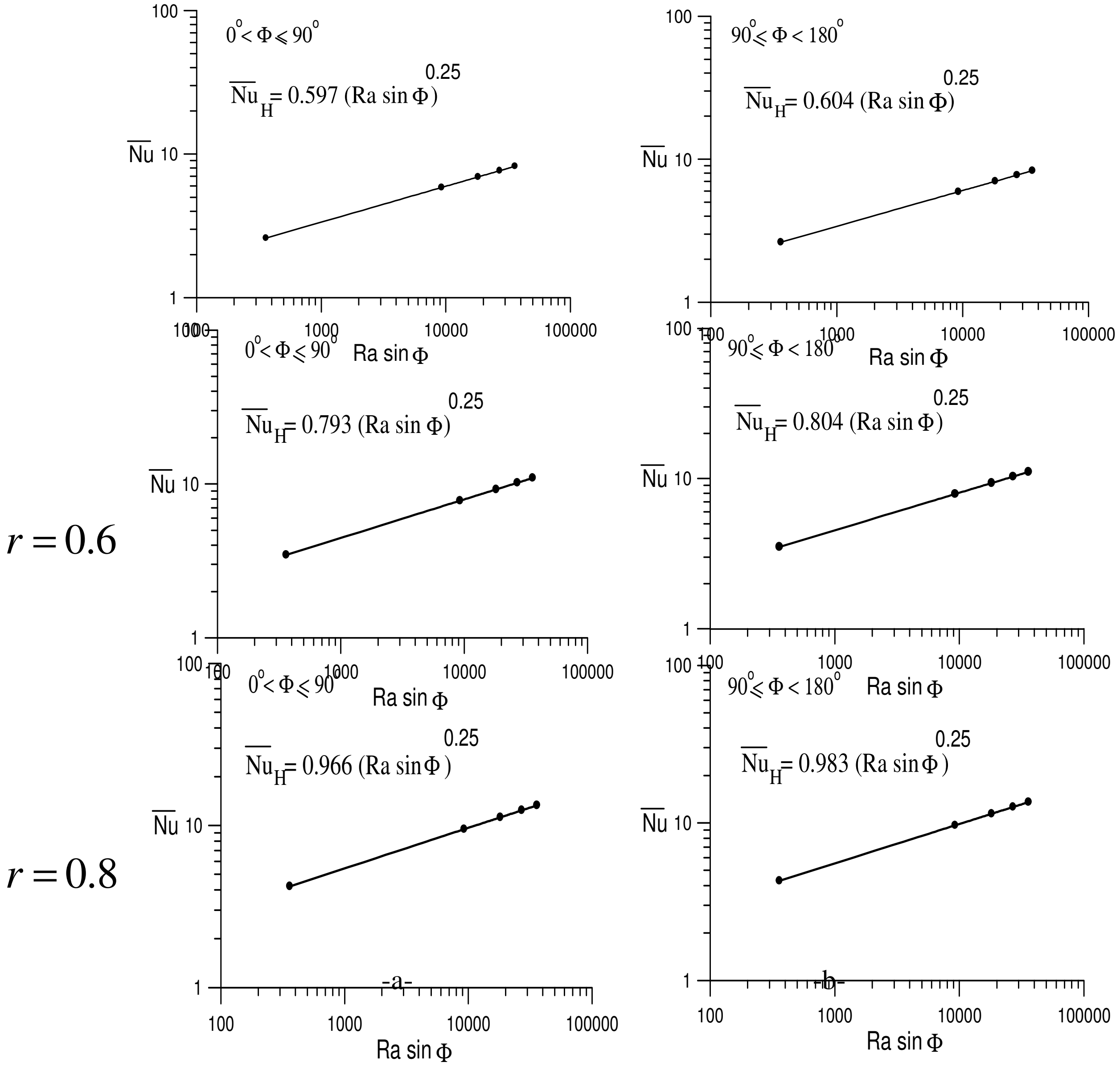

شكل (10) علاقة متوسط رقم نسلت مع Ra sin Φ للصفيحة المربعة و لصفيحة ذات الثقب الدائري المسخنة : -a- إلى الأعلى -b- إلى الأسفل

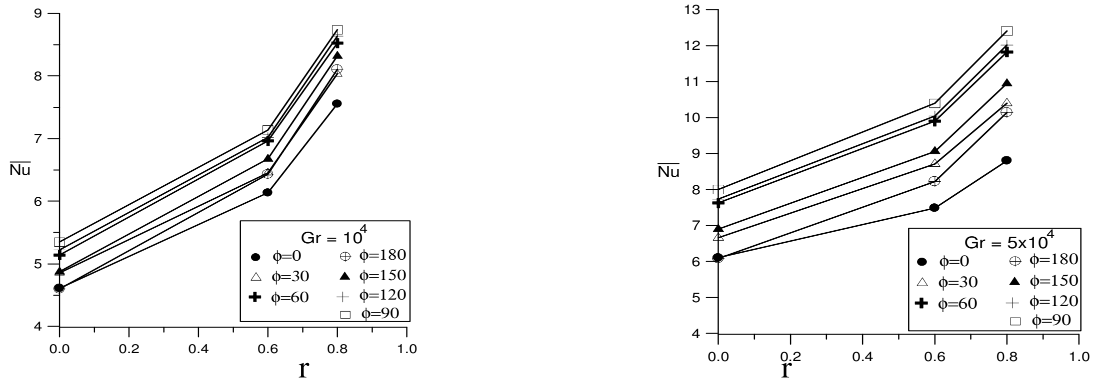

شكل (11) تأثير نسبة التثقيب r على متوسط رقم نسلت لرقم كراشوف10^4 و $5x10^4$

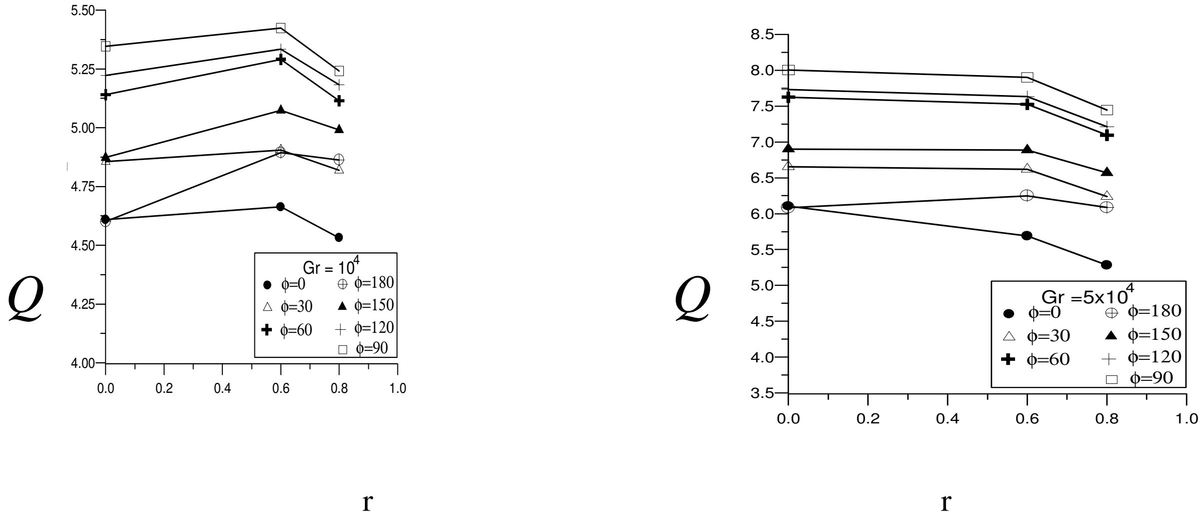

شكل (12) تأثير نسبة التثقيب r على كمية الحرارة المنتقلة لرقم كراشوف10^4 و $5x10^4$

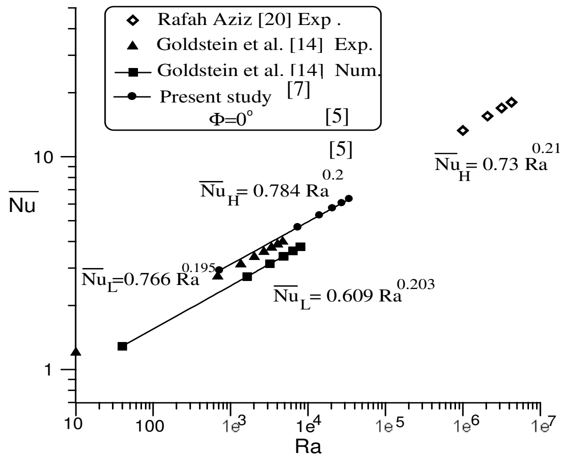

شكل (13) مقارنة متوسط رقم نسلت للبحث الحالي مع دراسة عملية و عددية سابقة لصفيحة مربعة لحالة التسخين الى الاعلى

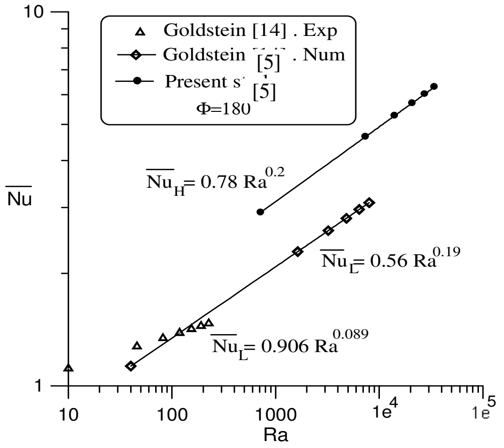

شكل (14) مقارنة متوسط رقم نسلت للبحث الحالي مع دراسة عملية و عددية سابقة لصفيحة مربعة لحالة التسخين إلى الأسفل

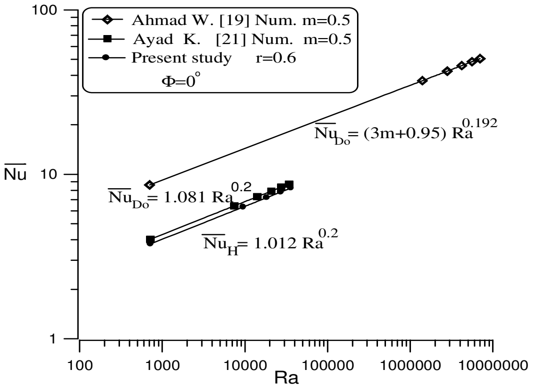

شكل (15) مقارنة متوسط رقم نسلت للصفيحة المربعة الأفقية المثقبة بنسبة تثقيب r=0.6 مع دراسة عددية سابقة لحلقة أفقية لحالة التسخين إلى الأعلى.

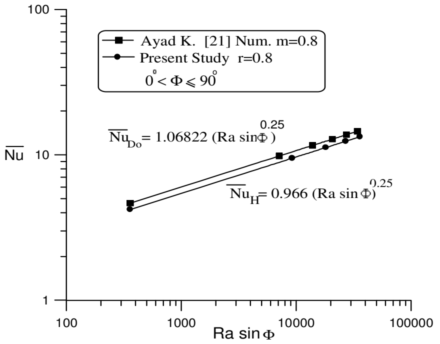

شكل (16) مقارنة متوسط رقم نسلت للصفيحة المربعة المثقبة المائلة مع دراسة عددية سابقة لحلقة مائلة لحالة التسخين إلى الأعلى .

المصـــادر

Ahmad W.Mustafa, 2001, "Numerical and Experimental Study of Natural Convection Heat Transfer from Isothermal Horizontal Disks and Rings". M. Sc. Thesis Univ. Technology.

Ayad K.Hassan , 2003,"Prediction of Three Dimensional Natural Convection from Heated Disks and Rings at Constant Temperature ". J. Eng. & Technology. Vol. 22, No.5, PP. 229-248 .

C.F.Gerald 1970. "Applied Numerical Analysis" Addison-Wesley Publishing Company.

Chuen-Yen Chow, Jone Wilely & Sons, 1979,"An Introduction to Computational Fluid Mechanics."

F.Geoola&A.R.H.Cornish.1982"Numerical Simulation of Free Connective Heat Transfer From a Sphere" Int. J.Heat&Mass Transfer. Vol. 25, No. 11, PP. 1677-1687.

Francis J.Suriano & Kwang-Tzu Yang ,1968 ,"Laminar Free Convection About Vertical And Horizontal Plates At Small And Moderate Grashof Numbers". Int. J.Heat & Mass Transfer.Vol. 11, PP.473-490.

7. K. Aziz & J.D.Hallums, 1967,"Numerical Solution of The Three-Dimensional Equations of Motion for Laminar Natural Convection ". The physics of fluids .Vol. 10, No. 2 , PP.314-325.

8. K.E.Torrance ,1985,"Numerical Method In Heat Transfer". Handbook of Heat Transfer Fundamentals, McGraw-Hill, 2nd Edition.

Luciano Pera & Benjamin Gebhart , 1973,"Natural Convection Boundary Layer Flow Over Horizontal And Slightly Inclined Surfaces".Int.J.Heat & Mass Transfer. Vol. 16, PP. 1131-1145.

L.R.Cairnie & A.J.Harrison,1982,"Natural Convection Adjacent To a Vertical Isothermal Hot Plate with a High Surface-To-Ambient Temperature Difference ".Int. J.Heat & Mass Transfer. Vol. 25, No. 7, PP. 925-934.

R.F.Boehm&D.Kamyab. May,1977,"Established Stripwise Laminar Natural Convection on Horizontal Surfaces".Transactions of the Asme. Vol. 99, PP. 294-299.

R.J.Goldstein & Kei-Shun Lau,1983,"Laminar Natural Convection From A Horizontal Plate And The Influence of Plate-Edge Extensions ". J.Fluid Mech. Vol.129 , PP.55-75.

Rafah Aziz , 2002,"Instructional System To Study Free Convection Heat Transfer from Isothermal Horizontal Square Flat Surfaces ".M. Sc.Thesis Univ. Technology.

قائمة الرموز

الرمز	تعريفه	وحداته	الرمز	تعريفه	وحداته
c_1,c_2,c_3	ثوابت في علاقة متوسط رقم نسلت مع رقم رالي	----	x_1, x_2	حدود لابعدية للصفيحة على المحور x	------
g	التعجيل الارضي	m/s^2	y_1, y_2	حدود لابعدية للصفيحة على المحور y	------
H	طول الصفيحة	m	ΔX	المسافة اللابعدية بين نقطتين في الشبكة باتجاه x	------
h	معامل انتقال الحرارة الموضعي	$W/m^2.^oC$	ΔY	المسافة اللابعدية بين نقطتين في الشبكة باتجاه y	------
$\overline{h}$	متوسط معامل انتقال الحرارة	$W/m^2.^oC$	ΔZ	المسافة اللابعدية بين نقطتين في الشبكة باتجاهz	------
n,m,l	عدد نقاط الشبكة باتجاه x,y,z	-------	α	الانتشارية الحرارية	m^2/s
P	الضغط الديناميكي	N/m^2	β	معامل التمدد الحجمي	1/K
P_L	الضغط الموضعي	N/m^2	Φ	زاوية ميلان الصفيحة عن المستوى الافقي	degree
P	الضغط اللا بعدي	-------	Ø	زاوية ميلان الصفيحة عن المستوى العمودي	degree
Q	الحرارة المنتقلة بالحمل اللابعدية	--------	υ	اللزوجة الكينماتية	m^2/s
r	نسبة التثقيب(نسبة قطر الثقب إلى طول ضلع الصفيحة r=a/H)	-------	ρ	كثافة المائع	kg/m^3
T	درجة الحرارة	^oC	τ	الزمن اللابعدي	------
T_∞	درجة حرارة الهواء المحيط	^oC	$\Delta\tau$	الخطوة الزمنية اللابعدية	------
T_W	درجة حرارة السطح المسخن	^oC	Ψ	متجه الجهد الكامن اللابعدي	------
t	الزمن	s	Ω	الدوامية اللابعدية	------
U,V, W	السرعة اللابعدية باتجاه x,y,z	-------	$\vec{\Omega}$	متجه الدوامية	------
u,v,w	السرعة باتجاه x,y,z	m/s	Θ	درجة الحرارة اللابعدية	------
X,Y,Z	الاحداثيات اللابعدية	-----	ϕ	دالة الانتشار	$1/s^2$
x,y,z	الاحداثيات المتعامدة	m	μ	اللزوجة المطلقة	kg/m.s

رموز السفلى		الرموز العليا	
av	القيمة المتوسطة	--	المتوسط
Loc	القيمة الموضعية	*,**	القيمة الوسطية المستخدمة في طريقة ADI
L	يستند على الطول المميز	n	الخطوة الزمنية (n)th
H	يستند على طول الصفيحة المربعة	n+1	الخطوة الزمنية (n+1)th
Do	يستند على القطر الخارجي للصفيحة الدائرية	s	التكرار (s)th
∞	المحيط	s+1	التكرار (s+1)th
w	السطح		
1	المركبة باتجاه المحور x		
2	المركبة باتجاه المحور y		
3	المركبة باتجاه المحور z		
(i,j,k)	نقاط الشبكة باتجاه (x,y,z)		

BLUNDER DETECTION TECHNIQUES IN ADJUSTMENT COMPUTATIONS

Mr. Bashar Saleem
Dept.of Surveying.
College of Engineering.
University of Baghdad

Mr. Hussein Alwan
Dept.of Surveying.
College of Engineering.
University of Baghdad

Mr. Jareer Jabir
Dept.of Surveying.
College of Engineering.
University of Baghdad

ABSTRACT

In adjustment of geodetic and photogrammetric networks, the surveying engineer faces many problems, such as errors of blunder nature in the observations (when comparing the homogeny of precision) make these observations odd from the result, and effecting directly on observation values after adjustment, and the statistical results after analysis as, adjusted coordinates of points, standard deviations, and ellipse of errors.

The research is deal with some of the most common usage of statistical methods to detect these odds observations to confirm which best method is, by studying the advantages and disadvantages of each method to geodetic network.

Three statistical methods will use in the analysis, these are:-

1. Standardized residuals method
2. F-t test
3. Robust estimation method

The adjustments were accomplished by preparing a Matlab program with the three blunder detection methods and the results were evaluated and some scientific conclusions were reached.

It was found that the robust estimation method represent the better blunder detection technique due to its ability in what is called (multi-blunder detection) , and the resulted higher accuracy indices.

الخلاصة

عند تصحيح الشبكات الجيوديسية وشبكات التثليث الجوي تعترض مهندس المساحة جملة من الأمور منها وجود أخطاء ذات طابع غلطي في بعض الارصادات (عند مقارنة تجانس الدقة) تجعل من هذه الارصادات شاذة عن البقية ,وتؤثر بصورة مباشرة على قيم الارصادات بعد التصحيح والنتائج الاحصائية بعد التحليل كالإحداثيات المصححه للنقاط والانحرافات المعيارية اضافة الى الشكل الاهليليجي للأخطاء الناتجة.

يتناول البحث مجموعة من الطرق الإحصائية الشائعة والمستخدمة للكشف عن هذه الرصدات الشاذة لاقرار الطريقة الافضل من خلال دراسة محاسن و مساوئ كل طريقة لشبكة جيوديسية .حيث اختيرت ثلاثة طرق احصائية متمثلة بالاتي:

1. طريقة البواقي القياسية (Standardized residuals method)
2. طريقة اختبار (F-t) test
3. طريقة التخمين المتين (Robust estimation method)

وباعداد برنامج بلغة (Matlab) تم اجراء التصحيح وتخمين النتائج للحصول على بعض الاستنتاجات العلمية والكشف عن الرصدات الشاذة بتطبيق الطرق الثلاث أعلاه.

وقد وجد ان طريقة التخمين المتين (Robust estimation method) تمثل أفضل تقنيه في الكشف عن الرصدات الشاذة استنادا إلى قابلية الطريقة في الكشف المتعدد للرصدات الشاذة (multi –blunder detection) وبسبب الدقة العالية التي توفرها هذه الطريقة مقارنة مع الطريقتين الأخريين.

KEY WORDS

Blunder detection, Geodetic Networks, Robust Estimation, Standardized Residual.

INTRODUCTION

When computing and adjusting geodetic networks, It is quiet important to ensure that the considered observations are free of blunders and systematic errors, and therefore the results are only affected by the random errors which presented in every measuring process.

Obviously, precaution in the observation process has to be the first step to avoid undesirable error appearance. Moreover, an adequate data filtering previous to the adjustment, checking reciprocal observations, and closures even with more detailed schemes is a suitable routine to be adopted in order to detect and eliminate the wrong observations.

Blunders or mistakes could be defined as obviously incorrect data points or results that are not reasonably close to the expected value. Some blunder or systematic errors may slip into the adjustment process. So it would be interested to deal with the subject that deals with the blunder detection.

BLUNDER DETECTION METHODS

The used methods for blunder detection will be explained theoretically and mathematically as follows:

Standardized Residual

The detection of blunder among the observations was treated using a technique pioneered by the geodesist Baarda (1968). In Baarda's method a statistical test which is called as *Standardized residuals* used to detect blunder [Baarda, 1968].

Blunders will affect the observations badly and produce incorrect estimations of the unknowns and their covariance matrix. If the blunders are detected by a statistical test, then those contaminated observations are removed, the network is re-adjusted, and we obtain the final results.

This method of standardized residuals, detect one blunder in every iteration and remove it from the observations, and readjust the network with the original observations, the iterations continued until remove all blunders and until the chi square test (χ^2) passed depend upon the significance level, variance and the degree of freedom. The method also depends on computing the variance-covariance matrix of residuals Σ_{vv} .

The standardized residuals are computed as:

$$\bar{v}_i = \frac{v_i}{\sqrt{q_{ii}}} \tag{1}$$

Where $\bar{v}_i$ is the standardized residual,

v_i is the residual, and

q_{ii} is the diagonal element of the Σ_{vv} matrix.

Since a computed parameter divided by its standard deviation which is a random normal variable, we can compute a (t) value as:

$$t_i = \frac{v_i}{S_0\sqrt{q_{ii}}} = \frac{v_i}{S_{v_i}} = \frac{\bar{v}_i}{S_0} \qquad (2)$$

However, this equation should be based on "good "value for the reference variance since a blunder automatically affects the value of S_0, the method summarized as follows:

1) Locate all measurements that qualify for rejection.
2) Reject the single observation with the largest standardized residuals.
3) Repeat adjustment 1& 2 until all observations qualify for rejection are rejected, and until (goodness of fit) pass.

Robust estimation method

The method is the latest method for blunders detection, that was obtained by scientist Huber in 1981 [Huber, 1981] and developed in 1990's [Francis, 2004]. The basics of this method are depending upon the original weights of observations.

Ordinary Least square adjustment is not sensitive to the blunder in the observation. From the Figure (1) below, it could be noticed how the regression line of least square dropped to the blunder points ,and affect the regression line by this amount ,but if we use the method of robust estimation that resistant to blunder the problem will be very different .

The regression line by both ordinary least square method, and robust line fit shown, and it could be noticed how the blunder point could not affect the regression line of the robust estimation method, and how affects on the least square line regression.

Robust estimation method will treat the blunder from a new view of point, which will compute a weight through a special function upon the scientific function which detect blunder and give a correct result, then treat the blunder.

One can notice how the blunder points dropped the least square line towards the blunder points, how the regression line of robust estimation is canceled the blunder point and how resistant the dropping of the blunder point and did not let it to affect the line of regression.

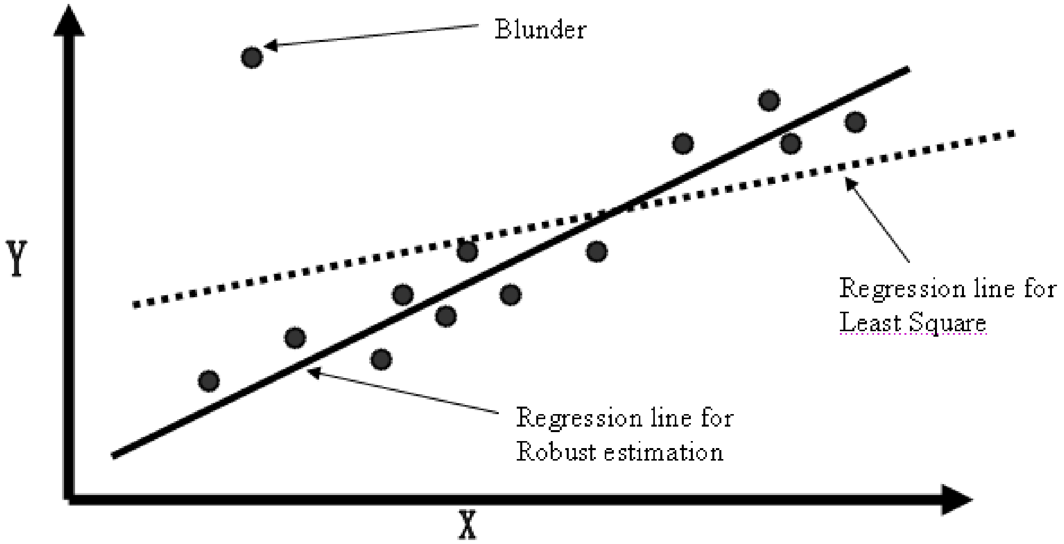

Fig (1). robust regression line and ordinary least square regression line (with one blunder).

Specifies a weight function, a tuning constant, and the presence or absence of a constant term. The weight function can be any of the names listed in the following Table (1).

Table (1). Weight function used in robust estimation function**.**

Tune constant	Meaning	Weight function
1.339	$W = (abs(r)) \times \sin(r)/r$	Andrew
4.685	$W = (abs(r)) \times (1 - r^2)^2$	Bisquare
2.385	$W = 1/(1 + r^2)$	Cauchy
1.400	$W = 1/(1 + abs(r))$	Fair
1.345	$W = 1/(abs(r))$	Huber
1.205	$W = \tanh(r)/r$	Logistics
2.795	$W = 1/(abs(r))$	Talwar
2.985	$W = \exp(r^{-2})$	Welsech

Procedure for robust estimation method could be summarized as follow:

1) Solve as ordinary least square method

2) Solve for hat matrix $\hat{H}$ (covariance of observations)

Where:

$$H = B \times (B^t \times B)^{-1} \times B^t \tag{3}$$

3) Compute r

$$r_i = \frac{V_i}{tune \times s \times \sqrt{(1 - h_{ii})}} \tag{4}$$

Where:

V_i : the residuals of observation i,
tune: the tuning constant from table (1),
s: an estimate of the standard deviation of the error term. s = MAD/0.6745, and
h_{ii} : the vector of leverage values (diagonal element of the hat matrix H).

The quantity MAD is the median absolute deviation of the residuals. The constant 0.6745 makes the estimate unbiased for the normal distribution.

4) If the value of r_i is greater than rejection level, then this observation is considered as a blunder, and it must be down weighted to a new weight according to the weight function in the table above.

5) Readjust according to the new weight.

F-T TEST METHOD

It is one of the traditional methods for detecting blunders; it was presented by the researcher Xu Pieliang. The basic of this method depends upon the tests *F-t*. Initially *F* test used for the global test and then *t* test to check for each blunder immediately after an *F* test. The *U* statistics here is actually the χ^2 statistics given by Stefanovic [Xu Pieliang, 1987].

Compared with an *F* test or (χ^2) test, this method is convenient for testing each blunder after the global test, and makes it possible to discuss the relationship of significance levels between the global test and the test of each blunder.

Let the mathematical model be:

$$L = B\Delta + V \tag{5}$$

Where

B: the design matrix,
L: the observational vector with the weight matrix W,
Δ: the vector with *u* unknown parameters, and
V: the normally distributed error vector.

If there are blunder in (l), eq. (5) is rewritten as:

$$l_1 = B_1\Delta + V_1 \tag{6}$$

$$l_2 = B_2\Delta + \Delta l_2 + V_2 \tag{7}$$

Where:

B_1: a matrix with full column rank,
l_1: a no-blunder observational error,
l_2: may be considered to be a vector containing some blunders (Δl_2) after the initial identification, and
V₁ and *V₂* are the normally distributed error vectors of (l_1) and (l_2), respectively.

The ordinary least square solutions are:

$$\Delta = (B_1^t W_1 B_1)^{-1}(B_1^t W_1 l_1) \tag{8}$$

$$\Sigma_{xx} = (B_1^t W_1 B_1)^{-1}\ \sigma^2 \tag{9}$$

$$\hat{\sigma}^2 = V_1^t W_1 V_1 / (n - m - u) \tag{10}$$

$$V_1 = B_1\Delta + l_1 \tag{11}$$

Where

W_1: the weight matrix of (l_1), and
n: total number of observations,

The predicted vector ($\hat{l}_2$) of (l_2) is:

$$\hat{l}_2 = B_2.\hat{\Delta} = B_2(B_1^t.W_1.B_1)^{-1}B_1^tW_1l_1 \tag{12}$$

For each element ($\hat{l}_2$) of (l_2) (i > *n*-*m*):

$$\hat{l}_i = B_i(B_1^tW_1B_1)^{-1}B_1^tW_1l_1 \tag{13}$$

Where

B_i: a row vector of B_2.

The predicted residuals vector is therefore (denoted by$\hat{V}_2$)

$$\hat{V}_2 = l_2 - \hat{l}_2 = l_2 - B_2\Delta \tag{14}$$

For each element of $\hat{V}_2$

$$\hat{V}_i = l_i - B_i\Delta \tag{15}$$

If (l_1) and (l_2) are unrelated, (l_2) is unrelated to Δ, thus we can get from eq. (14) and (15)

$$\Sigma_{vv} = D(l_2) + D(\hat{l}_2)$$

$$\sum_{vv} = \left[W_2^{-1} + B_2(B_1^tW_1B_1)^{-1}B_2^t\right]\sigma^2 \tag{16}$$

$$\Sigma_{vv} = [W_i^{-1} + B_i(B_1^tW_1B_1)^{-1}B_i^t]\sigma^2 \tag{17}$$

To test if blunders exist in $\hat{V}_2$ we test the zero hypotheses:

$$H_o = \Delta L_2 = 0 \tag{18}$$

When a priori value of the unit weight variance is known, the quadratic form:

$$U = \hat{V}_2^t\Sigma_{vv}^{-1}\hat{V}_2 \sim \chi^2(\delta) \tag{19}$$

If eq. (18) is correct the noncentral parameter (*δ)* of *U* is equal to zero; otherwise,

$$\delta = \Delta L_2^tD^{-1}(\hat{V}_2)\Delta L_2. \tag{20}$$

In fact statistics U is Stefanovic's χ^2 tests.

Now we further establish two statistics, denoted by *F* and *t*, respectively [Xu Pieliang, 1987]:

$$F = U/m/\hat{\sigma}^2/\sigma^2$$

$$F = \hat{V}_2{}^t[W_2{}^{-1} + B_2(B^t{}_1W_1B_1)\ {}^1B_2{}^t]\ {}^1\hat{V}_2/m\hat{\sigma}^2 \tag{21}$$

~F (m, n-m-t)

Using eq. (21) we can conveniently test whether (l_2) contain some blunders. When the zero hypotheses are rejected, further testing is needed to determine which (l_2) is responsible.

Therefore establish the zero hypotheses for each elements of (l_2):

$$H_o = \Delta L_2 = 0 \tag{22}$$

It is clear that when eq. (21) is correct,

$$t = \hat{v}\sqrt{\Sigma_{vv}} / \sqrt{\hat{\sigma}^2 / \sigma^2} \tag{23}$$

~t (n-m-t)

After the *F* test, the *t* test can therefore be used to detect blunder in (l_2). It is not difficult to see that a (*t*) test makes it easy to test each element (l_i) of (l_2).

The steps according to this method may be summarized as follow:

1) Initial identification of blunders.

2) Division of model in eq. (5) into two parts–the adjustment model in eq.(6) and the prediction model in eq.(7) according to the initial identification and then solving for Δ in eq. (8), the predicted residuals vector $\hat{V}_2$ from eq. (16) and its variance-covariance matrix.

3) Use of the *F* test for the global test. If the zero hypotheses are rejected, further investigation (a *t* test) is needed to determine which (l_i) is responsible.

APPLICATION TO ACTUAL NETWORK:

For mathematical verification, a combined (Hybrid) geodetic net were chosen, which was adjusted by [Ghilani, 1994]. The systematic errors are corrected and the observed distances are reduced to mean see level. Goodness of fit test for this net after ordinary least square adjustment was failed which means that blunders exist, so the net was suitable to check our methods for blunders detection.

The specifications of this network were as follows [Ghilani, 1994]; (see appendix A)

-Two control points (2000, 2001).

-11 unknown points.

-19 distance observations, and 17 angles. Fig (2) shows the configuration of the net.

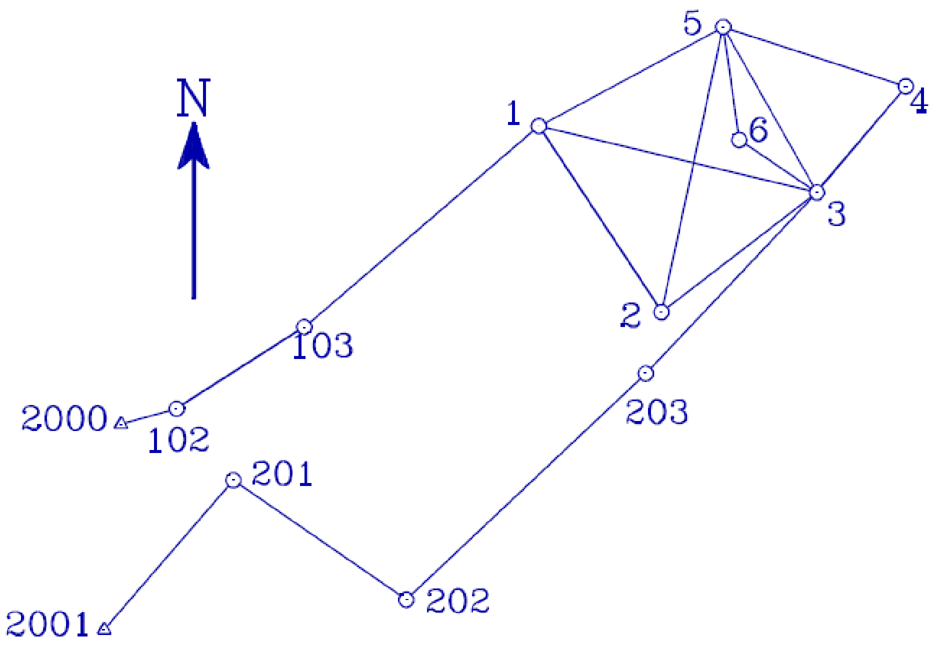

Fig (1). Configuration of the geodetic net

RESULTS AND DISCUSSIONS

After performing the least square adjustment, each method was checked for blunders detection in the observation. The results had been summarized in the Table (2)

Table (2) Comparison between blunder detection methods used for adjusting the geodetic network.

Method	Iteration	χ^2 test	±σ	Blundered observations	Redundancy
Standardized residuals method	3	Pass	1.162	2	12
Robust estimation method	1 (One step)	Pass	0.983	2	14
F-*t* test method	1 (Two steps)	Pass	1.165	2	12

The adjustment of the above network by using 1st method (Standardized residuals) was done by [Ghilani, 1994], while this research adjust the same network by using the two other methods.

It was found that the robust estimation method represent the better blunder detection technique due to its ability in what is called (multi-blunder detection), and the resulted higher accuracy indices, this is obvious from the comparing the values of (±σ).

CONCLUSIONS

It could be concluded the following:

1. It is clear that standardized residuals method, Robust estimation method and F-t test method are all effective in blunder detection.
2. A disadvantage on standardized residuals method was noticed, in that it is an iterative procedure or a single blunder detection technique. Robust estimation and F-t test has the advantage in that it is a multiple blunder detection techniques.
3. From the two applications discussed, it is quite evident that Robust estimation technique gives a lower value for the final variance of unit weight ($\hat{\sigma}_0^2$) and also for the standard deviations of the adjusted unknown, which indicates that Robust estimation is the best blunder detection method.

   This lower value of variance could be explained in that the redundancy (n-u) remain fixed while in the standardized residuals method and F-t test method the redundancy decreased each time a blunder detected and removed

4. Among all the weight functions used in robust estimation method it is highly recommended to use the (Cauchy) weight function.

REFERENCES

Baarda, W. (1968), A Testing Procedure for Use in Geodetic Networks, Netherlands Geodetic Commission Publ. On Geodesy, New series 2, No. 5, Delft 1968

Francis, W.O.Adoul (2004), Robust Geodetic Parameter Estimation under Least Square through Weighting on the Basis of the Mean Square Error, Netherlands Geodetic Commission, publication on Geodesy ,New Series ,Vol.2,No.5,Delft, 2004.

Huber, P.J., (1981), Robust Statistics, John Wiley& Sons, New York.

Wolf & Ghilani (1994), Adjustment Computations, John Wily & Sons, New York.

Wolf, Paul R.(1982), Elements of Photogrammetry, 2nd edition, John Wily & Sons, New York

Xu Pieliang (1987) A test method for many outliers, ITC journal, No.4, 1987.

APPENDIX (A)

Blunder detection example
===========================

Number of Control Stations = 2
Number of Unknown Stations =11
Number of Distance observations = 19
Number of Angle observations = 17

Initial approximations for unknown stations

Station	X	Y
1	2 477 233.88	420 353.62
2	2 477 497.99	419 951.98
3	2 477 832.67	420 210.17
4	2 478 023.86	420 438.88
5	2 477 630.64	420 567.44
6	2 477 665.36	420 323.31
102	2 476 454.17	419 743.39
103	2 476 728.88	419 919.69
201	2 476 576.25	419 589.24
202	2 476 948.76	419 331.29
203	2 477 463.90	419 819.56

Control Stations

Station	X	Y
2000	2 476 334.60	419 710.09
2001	2 476 297.98	419 266.82

Distance Observations

Station Occupied	Station Sighted	Distance	S
1	3	615.74	0.02
1	2	480.71	0.02
3	1	615.74	0.02
3	4	298.10	0.02
3	6	201.98	0.02
3	5	410.44	0.02
3	2	422.70	0.02
5	2	629.58	0.02
5	1	450.67	0.02
5	6	246.61	0.02
5	4	397.89	0.02
5	3	410.46	0.02
102	103	327.37	0.02
103	1	665.79	0.02
201	202	453.10	0.02
202	203	709.78	0.02
203	3	537.18	0.02
2000	102	125.24	0.02

2001	201	425.90	0.02

Angle Observations

Station Back sighted	Station Occupied	Station Fore sighted	Angle	S
2	1	3	316° 48' 00.5"	6.3"
2	3	4	167° 32' 28.0"	14.5"
2	3	6	71° 42' 51.5"	15.1"
2	3	5	98° 09' 36.5"	10.3"
2	3	1	51° 07' 11.0"	7.2"
203	3	2	8° 59' 56.0"	6.5"
2	5	3	318° 20' 54.5"	7.0"
1	5	3	268° 49' 32.5"	9.8"
6	5	3	338° 36' 38.5"	10.7"
3	5	4	324° 17' 44.0"	8.1"
2000	102	103	162° 58' 16.0"	28.9"
102	103	1	172° 01' 43.0"	11.8"
2001	201	202	263° 54' 18.7"	9.7"
201	202	203	101° 49' 55.0"	8.1"
202	203	3	176° 49' 10.0"	8.4"
102	2000	2001	109° 10' 54.0"	25.5"
2000	2001	201	36° 04' 26.2"	7.4"

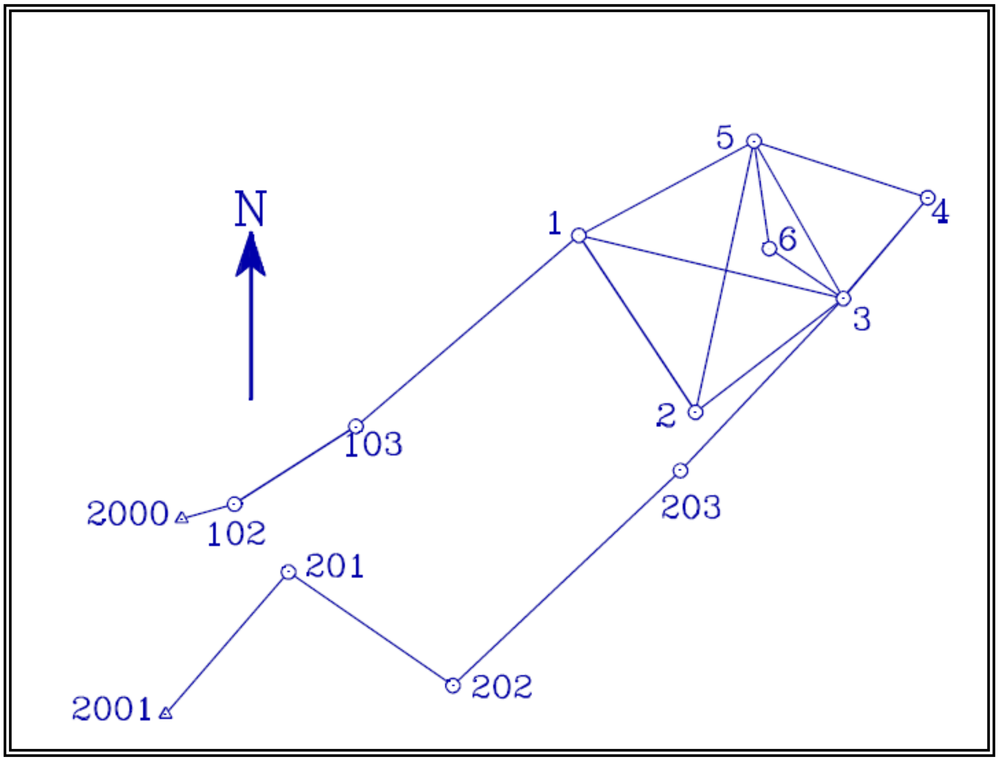

SOLUTION

Adjusted stations

```
                                 Error ellipse confidence level at 0.950
 Station    X              Y             Sx         Sy         Su          Sv      t
=======================================================================================
   1   2,477,236.78    420,351.57    26.138     27.582     95.745      40.382 137.21°
   2   2,477,500.02    419,949.06    18.862     32.883     95.031      41.414 158.93°
   3   2,477,835.61    420,206.18    22.972     41.726    124.575      38.036 155.07°
   4   2,478,007.59    420,410.17    28.839     47.264    145.573      41.617 151.30°
   5   2,477,631.63    420,566.15    32.636     36.320    127.266      40.399 138.75°
   6   2,477,667.20    420,320.89    26.259     37.620    118.995      39.741 147.78°
 102   2,476,455.42    419,742.35     9.931      6.023     27.726      15.494  75.95°
 103   2,476,731.25    419,918.44    14.445     13.310     40.980      34.721 120.10°
 201   2,476,576.61    419,589.00     8.329      9.077     27.541      19.397  37.62°
 202   2,476,948.76    419,330.06    12.410     16.494     46.100      32.569  16.98°
 203   2,477,465.47    419,816.79    15.649     30.287     85.777      36.510 163.29°
```

Adjusted Distance Observations

```
   Station    Station
   Occupied   Sighted     Distance       V          S       Std.Res.      Red.#
=====================================================================================
         1          3       616.23     0.495      5.356       26.05      0.746
         1          2       480.95     0.243      5.921       13.29      0.689
         3          1       616.23     0.495      5.356       26.05      0.746
         3          4       266.81   -31.287      6.525    -1802.59      0.622*
         3          6       203.77     1.789      6.889      106.83      0.579
         3          5       413.76     3.317      5.059      171.47      0.773
         3          2       422.77     0.069      5.459        3.67      0.736
         5          2       630.97     1.394      6.012       76.87      0.679
         5          1       449.39    -1.281      7.192      -79.16      0.541
         5          6       247.83     1.225      7.100       74.85      0.553
         5          4       407.04     9.153      7.819      614.84      0.458
         5          3       413.76     3.297      5.059      170.43      0.773
       102        103       327.25    -0.121     10.056      -17.16      0.103
       103          1       665.70    -0.087     10.048      -12.18      0.105
       201        202       453.37     0.268     10.526       92.01      0.017
       202        203       709.85     0.075     10.051       10.51      0.104
       203          3       537.24     0.060     10.056        8.53      0.103
      2000        102       125.05    -0.188     10.138      -28.72      0.089
      2001        201       425.95     0.048     10.063        6.82      0.102
```

Adjusted Angle Observations

Station Back Sighted	Station Occupied	Station Fore Sighted	Angle	V	S	Std. Res.	Red. #
2	1	3	316°49'53.8"	113.32"	2334.36	28.07	0.411
2	3	4	167°35'29.5"	181.54"	5764.13	22.07	0.322
2	3	6	71°43'01.5"	10.01"	5660.17	1.05	0.397
2	3	5	97°55'08.5"	-868.02"	2793.81	-101.88	0.684
2	3	1	51°06'18.6"	-52.42"	2462.81	-10.32	0.498
203	3	2	8°59'35.6"	-20.36"	3049.99	-13.36	0.055
2	5	3	318°25'19.8"	265.26"	1871.66	45.52	0.693
1	5	3	268°58'58.7"	566.22"	3246.9	79.45	0.529
6	5	3	338°42'49.1"	370.61"	4309.5	62.85	0.304
3	5	4	322°04'20.0"	-8004.04"	3222.81	-1745.41	0.321*
2000	102	103	162°23'46.9"	-2069.09"	10624.86	-110.49	0.420
102	103	1	171°57'47.3"	-235.73"	5605.07	-112.46	0.032
2001	201	202	263°58'29.6"	250.90"	4536.27	104.48	0.061
201	202	203	101°52'55.9"	180.90"	3608.54	58.03	0.148
202	203	3	176°50'15.3"	65.26"	3819.12	23.14	0.113
102	2000	2001	109°40'20.8"	1766.77"	9348.51	106.51	0.423
2000	2001	201	36°07'53.9"	207.69"	3440.52	104.46	0.072

Adjustment Statistics

```
            Iterations = 4
          Redundancies = 14

    Reference Variance = 232,981.728
          Reference So = ±482.7

       Failed to pass X² test at 95.0% significance level!
                      X² lower value = 5.63
                      X² upper value = 26.12
  Possible blunder in observations with Std.Res. > 1,588
                Convergence!
```

Then the problem be as following:-

Number of Control Stations = 2
Number of Unknown Stations = 11
Number of Distance observations = **18** (It was 19)
Number of Angle observations = 17

After that readjustment will be done.